12-1999

Innovative approaches to selective detection and remote analysis : developments in surface-enhanced raman scattering (sers)-based and separations-based fiberoptic chemical sensors

David L. Stokes

Follow this and additional works at: https://trace.tennessee.edu/utk_graddiss

To the Graduate Council:

I am submitting herewith a dissertation written by David L. Stokes entitled "Innovative approaches to selective detection and remote analysis : developments in surface-enhanced raman scattering (sers)-based and separations-based fiberoptic chemical sensors." I have examined the final electronic copy of this dissertation for form and content and recommend that it be accepted in partial fulfillment of the requirements for the degree of Doctor of Philosophy, with a major in Chemistry.

Michael J. Sepaniak, Major Professor

We have read this dissertation and recommend its acceptance:

Tuan Vo-Dinh, James Q. Chambers, Earl L. Wehry, Robert N. Compton

Accepted for the Council:

Carolyn R. Hodges

Vice Provost and Dean of the Graduate School

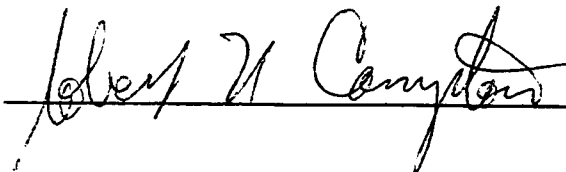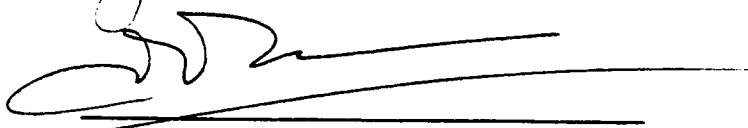(Original signatures are on file with official student records.)

To the Graduate Council:

I am submitting herewith a dissertation written by David L. Stokes entitled "Innovative Approaches to Selective Detection and Remote Analysis: Developments in Surface-Enhanced Raman Scattering (SERS)-Based and Separations-Based Fiberoptic Chemical Sensors." I have examined the final copy of this dissertation for form and content and recommend that it be accepted in partial fulfillment of the requirements for the degree of Doctor of Philosophy, with a major in Chemistry.

Dr. Michael J. Sepaniak, Major Professor

We have read this dissertation
and recommend its acceptance:

Accepted for the Council:

Associate Vice Chancellor and
Dean of The Graduate School

INNOVATIVE APPROACHES TO SELECTIVE DETECTION AND REMOTE ANALYSIS: DEVELOPMENTS IN SURFACE-ENHANCED RAMAN SCATTERING (SERS)-BASED AND SEPARATIONS-BASED FIBEROPTIC CHEMICAL SENSORS

A Dissertation

Presented for the

Doctor of Philosophy

Degree

The University of Tennessee, Knoxville

David L. Stokes

December, 1999

DEDICATION

This dissertation is dedicated to my father

The Reverend George Ellis Stokes, Jr.

and in memory of my mother

Nancy Thomas Stokes

for their encouragement, attention, and good example.

ACKNOWLEDGMENTS

ABSTRACT

This two-part study investigates the feasibility of selective detection in remote analysis based on 1) surface-enhanced Raman scattering (SERS), and 2) separations-based fiberoptic sensing (SBFOS).

For the first case, the extremely sharp spectral features of Raman scattering can sometimes allow the analysis of multicomponent samples without complicated sample pretreatment steps. Furthermore, the giant signal-enhancing effect of SERS can enable trace level detection. A solid, surface-based metallic substrate approach is taken for the development of a practical SERS technology. Various substrates are described, including silver-coated alumina, silver-coated TiO_2, and silver islands. These substrates are economical and easy to fabricate with a high degree of reproducibility. Furthermore, they are readily integrated with fiberoptic sensors for remote SERS detection. Three fiberoptic SERS sensor systems are described in this work. The surface-based substrates are also applied to the detection of organic vapors.

In the latter case, the high separation efficiency of capillary electrophoresis is coupled with laser-induced fluorescence (LIF) detection in the development of a fiberoptic sensor. Although LIF can offer exceptional detectability, its application to the analysis of complex samples can be difficult due to the broadband nature of fluorescence. It often requires sample pretreatment steps such as separations. In the SBFOS approach, separations can be performed remotely. Several complications are associated with the development of CE-based SBFOSs and are described in this work. Four SBFOS designs are described and applied to analysis environmentally and biomedically significant samples.

Publications

The major part of the material presented in this dissertation has been or will be published in the scientific literature:

Bello, J. M.; Stokes, D. L.; Vo-Dinh, T. "Titanium dioxide based substrate for optical monitors in surface-enhanced Raman scattering analysis" *Anal. Chem.* **61**, 1779 (1989).

Bello, J. M.; Stokes, D. L.; Vo-Dinh, T. "Silver-coated alumina as a new medium for surface-enhanced Raman scattering analysis" *Appl. Spectrosc.* **43**,1325 (1989).

Bello, J. M.; Stokes, D. L.; Vo-Dinh, T. "Direct characterization of phthalic acid isomers in mixtures using surface-enhanced Raman analysis" *Anal. Chem.* **62**, 1349 (1990).

Bello, J. M.; Narayanan, V. A.; Stokes, D. L.; Vo-Dinh, T. "Fiber-optic remote sensor for in situ surface-enhanced Raman scattering analysis" *Anal. Chem.* **62**, 2437 (1990).

Narayanan, V. A.; Bello, J. M.; Stokes, D. L.; Vo-Dinh, T. "Determination of *p*-aminobenzoic acid in Presun-15 lotion using surface-enhanced Raman analysis" *Analusis* **19**, 307 (1991).

Narayanan, V. A.; Begun, G. M.; Stokes, D. L.; Sutherland, W. S.; Vo-Dinh, T. "Normal Raman and surface-enhanced Raman scattering (SERS) spectra of some fungicides and related chemical compounds" *J. Raman Spectrosc.* **23**, 281 (1992).

Vo-Dinh, T.; Stokes, D. L. "Surface-enhanced Raman vapor dosimeter" *Appl. Spectrosc.* **47**, 1728 (1993).

Pal, A.; Stokes, D. L.; Alarie, J. P.; Vo-Dinh, T. "Selective surface-enhanced Raman spectroscopy using a polymer-coated substrate" *Anal. Chem.* **67**, 3154 (1995).

Stokes, D. L.; Alarie, J. P.; Vo-Dinh, T. "Surface-enhanced Raman fiberoptic sensors for remote monitoring" *Proc. SPIE-Int. Soc. Opt. Eng.* 2504 (Environmental Monitoring and Hazardous Waste Site Remediation), 552 (1995).

Sepaniak, M. J.; Vo-Dinh, T.; Stokes, D. L.; Tropina, V.; Dickens, J. E. "Demonstration of an integrated capillary electrophoresis-laser-induced fluorescence fiber-optic sensor" *Talanta* **43**, 1889 (1996).

Stokes, D. L.; Sepaniak, M. J.; Vo-Dinh, T. "Development of a new capillary electrophoresis-based fibre-optic sensor" *Biomed. Chromatogr.* **11**, 187 (1997).

Sepaniak, M. J.; Vo-Dinh, T.; Tropina, V.; Stokes, D. L. "Evaluation of a separation-based fiber-optic sensor in a micellar electrokinetic capillary chromatography mode of operation" *Anal. Chem.* **69**, 3806 (1997).

Stokes, D. L.; Vo-Dinh, T. "Development of an integrated single-fiber SERS sensor" *Sensor Actuat. B-Chem.* (1999) in press.

Stokes, D. L.; Narayanan, V. A.; Vo-Dinh, T. "Evaluation of a chemical vapor dosimeter using polymer-coated SERS substrates" *Anal. Chim. Acta.* (1999) in press.

Stokes, D. L.; Sepaniak, M. J.; Vo-Dinh, T. "Demonstration of a separations-based fiberoptic sensor for bioanalysis" *Anal. Chim. Acta.* (1999) in press.

TABLE OF CONTENTS

xiii

LIST OF TABLES

LIST OF FIGURES

FIGURE   **PAGE**

NOMENCLATURE

Part I Symbols:

b	Number of chemical bonds in a given molecule
cm^{-1}	Wavenumber
C	Analyte concentration
C_{AVC}	Estimated analyte concentration in air vapor chamber
C_0	Bulk analyte concentration
C_{inj}	Analyte concentration of solution injected for air vapor generation
C_s	Analyte concentration at a substrate surface
d	Major dimension of scattering particle
$\dfrac{dC}{dx}$	Concentration gradient
$d\tau$	Indication of integration over all space
D	Diffusion constant
D_b	Bond dissociation energy
D_p	Detection zone diameter
D_s	Diameter of distributed sample spot on substrate surface
E_{in}	Electric field of incident radiation
$E_{in}(t)$	Electric field of incident radiation with respect to time.
E_{in}^n	Electric field of "natural" (unpolarized) incident radiation
E_{in}^p	Electric field of polarized incident radiation
E_0	Maximum incident electric field
$\left| \mathbf{E}_{sc} \right|$	Magnitude of scattered electric field
E_{sc}	Electric field of scattered radiation

$E_{sc}^{p}(\phi)$	Irradiance of polarized scattered radiation with respect to scattering angle, ϕ (between orientation of polarized E_{in} and scattered radiation)
$\overline{E}_{sc}$	Average magnitude of induced electric field
$\overline{E}_{x}, \overline{E}_{y}, \overline{E}_{z}$	Magnitude of the electric field vector on a given axis, x, y, or z
f	Bond force constant (general)
f_{e}	Bond force constant near potential energy minimum
F	Force required to move an atom a given distance from the equilibrium position
F_{AVC}	Air flow rate through air vapor chamber
h	Planck constant (6.62618 x 10-34 J/s)
$I_{\parallel}$	Scattering intensity due to parallel polarized radiation
$I_{\parallel}(\theta)$	Scattering intensity due to parallel polarized light at angle, θ (with respect to the axis of propagation of the incident light beam)
$I_{\perp}$	Scattering intensity due to perpendicular polarized radiation
$I_{sc}(\Phi)$	Scattering intensity at angle, Φ (with respect to the induced dipole axis)
I_{sc}^{n}	Scattering intensity for natural (unpolarized) incident radiation
$I_{sc}^{n}(\theta)$	Scattering intensity for natural (unpolarized) incident radiation at angle, θ (with respect to the axis of propagation of the incident radiation beam)
I_{sc}^{p}	Scattering intensity for polarized incident radiation
I_{r}^{n}	Intensity of Raman scattering for "natural" (unpolarized) incident radiation
I_{r}^{p}	Intensity of Raman scattering for polarized incident radiation

$I_{r,as}$	Intensity of anti-Stokes Raman scattering
$I_{r,st}$	Intensity of Stokes Raman scattering
$I_{r,st}^{p}$	Intensity of Stokes Raman scattering for polarized incident radiation
J	Molecular flux
k	Designation for vibrational mode
	OR
	Designation for constant as defined in text
k'	k^2, where $k = \dfrac{\pi}{\varepsilon_0}$ (SI units) (with reference to electric field calculations)
L	Length of diffusion tube (with reference to SERS dosimeter)
m	Reduced mass (general)
$\lvert m \rangle$	Original stationary vibrational energy level of a Raman transition (or resultant vibrational energy level of a Rayleigh transition)
M	Mass of analyte collected at a substrate surface
mw	Molecular weight
n	Number of atoms in a given molecule
n_1	Number of terminal atoms in a given molecule
$\lvert n \rangle$	Resultant vibrational energy level of a Raman transition
N	Number of trials for statistical calculations
N_t	Total number of molecules deposited on substrate surface
N_d	Estimated number of detected molecules
P_{sc}	Rate of Raman scattering (in all directions)

q	Ratio of dielectric core radius to silver coating sphere radius for SERS-active microparticles
Q_k	Displacement of an atom from equilibrium position for a given vibrational mode, k
$Q_k(t)$	Displacement of an atom from equilibrium position for a given vibrational mode, k, with respect to time
Q_k^0	Maximum displacement of an atom from equilibrium position for a given vibrational mode, k
$\langle n|Q_k|m \rangle$	Average displacement of an atom from equilibrium position for the k-th vibrational mode of the transition, $|m\rangle \rightarrow |n\rangle$
r	Distance from a source (surface or point) of scattering OR Internuclear separation (with reference to Raman transition moment)
r_e	Bond length (with reference to Raman transition moment)
$|r\rangle$	Unperturbed energy level in Raman scattering process
R	Raman transition moment
R_{inj}	Rate of analyte solution injection for air vapor generation
S	Effective cross-sectional area of diffusion tube channels (with reference to SERS dosimeter)
t	Time (general)
T	Time required to establish concentration gradient across diffusion tube (with reference to SERS dosimeter)
V	Potential energy of a diatomic molecule
V	Molar volume of gas-phase analyte

x	Position of an atom at a given time during harmonic oscillation
x_0	Maximum displacement of an atom from equilibrium position
$x-y-z$	Coordinate axes of a fixed external frame of reference
$x'-y'-z'$	Principal axes of a polarizability ellipsoid
α	Molecular polarizability
$\underline{\alpha}$	Molecular polarizability tensor
$\overline{\alpha}_{ii}$	Time-average molecular polarizability for diagonal elements of the polarizability tensor (anisotropic molecule)
$\overline{\alpha}_{ij}$	Time-averaged molecular polarizability for off-diagonal elements of the polarizability tensor (anisotropic molecule)
$\alpha_{mn}(t)$	Molecular polarizability with respect to time for the transition, $\lvert m\rangle \rightarrow \lvert n\rangle$
$\left(\alpha'_{mn}\right)_k$	First-order molecular polarizability for the k-th vibrational mode of the transition, $\lvert m\rangle \rightarrow \lvert n\rangle$
$\langle \alpha \rangle$	Mean molecular polarizability (with reference to eigenvalues of the principal axes, x', y' and z')
$\langle \alpha'_k \rangle$	First-order derived mean molecular polarizability of the k-th vibrational mode
$\langle n\lvert\alpha\rvert m\rangle$	Mean molecular polarizability for the transition, $\lvert m\rangle \rightarrow \lvert n\rangle$.
$\alpha_1, \alpha_2, \alpha_3$	Eigenvalues of three orthogonal eigenvectors of α
γ	Anisotropy of a given molecule
γ'_k	First-order anisotropy for the k-th vibrational mode of a given molecule
ε_0	Dielectric constant in vacuum
η	Index of refraction

θ	Scattering angle with respect to the propagation axis of the incident radiation beam
λ	Wavelength
λ_{sc}	Wavelength of scattered radiation
λ_{in}	Wavelength of incident radiation
μ	Induced dipole moment
$\overline{\mu}$	Time-averaged induced dipole for all possible orientations of a given molecule
$\mu(t)$	Induced dipole moment with respect to time
μ°	Maximum induced dipole moment
μ_r	Reduced mass of molecule (with reference to Raman scatter intensity calculations)
v	Frequency (vibration or radiation)
v_{in}	Frequency of incident radiation
v_k	Frequency of a vibrational mode, k
v_{sc}	Frequency of scattered radiation
ρ	Depolarization ratio
ρ^n	Depolarization ratio for "natural" unpolarized incident radiation
ρ^p	Depolarization ratio for polarized incident radiation
σ	Cross section for photophysical transition
σ_{sc}	Cross section for Raman scattering
ϕ	Angle between the orientation of the incident electric field (polarized) and the direction of scattered radiation.
Φ	Scattering angle with respect to oscillating dipole axis
ψ	Wavefunction for a given energy state

φ Phase angle (with reference to harmonic oscillation)

Symbols for vibrational modes

γ	Out-of-plane vibration
δ	Scissoring vibration
v	Stretching vibration
ρ	Rocking vibration
τ	Twisting vibration
ω	Wagging vibration

Part II Symbols:

C	Electronic charge of counterion
D_M	Diffusion constant for solute in mobile phase
E	Electric field strength applied in electrophoresis (voltage/length of separation medium)
H	Height equivalent of a theoretical plate
k'	Capacity factor
K	Boltzmann constant (1.38066×10^{-23} J/K)
L	Effective length of separation medium
L_T	Total length of separation medium
n_x	Index of refraction for medium, x
N	Number of trials for statistical calculations
N	Separation Efficiency
P	Probability of finding counterion at given distance from the inner boundary of the diffuse region of an electrical double layer

P_0	Probability of finding counterion at the inner boundary of the diffuse region of an electrical double layer
q	Ionic charge
r	Ionic radius of solute
Rs	Resolution between adjacently-eluting bands
t_0	Retention time of unretained solute, or elution time of neutral solute in CZE
t_{mc}	Micelle elution time
t_r	Solute band retention or elution time
Δt_r	Difference in band retention or elution times for adjacently-eluting solutes
$\bar{t}_r$	Average band retention or elution time for adjacently-eluting solutes
T	Temperature
T_r	Solute band retention or elution time
V	Total applied voltage in electrophoresis
W_b	Baseline width of eluting band
δ	Electrical double layer thickness
ε	Dielectric constant for the buffer solution
ζ	Zeta potential
η	Viscosity of buffer solution
θ_0	Acceptance angle of an optical fiber
θ_x	Incident light ray angle in medium, x, with respect to the normal of the interface between two mediums of different refractive indices (including medium, x)

μ_e	Electrophoretic mobility of analyte solute
$\bar{\mu}_e$	Average electrophoretic mobility for adjacently-eluting solutes
μ_{eo}	Electroosmotic mobility
μ_{mc}	Micelle electrophoretic mobility
v	Linear velocity (general)
v_b	Total solute linear velocity
v_e	Migration velocity
v_{elec}	Electrophoretic flow contribution to total solute linear velocity
v_{eo}	Linear velocity of electroosmotic flow
v_{hy}	Gravity-driven hydrostatic flow velocity contribution to total solute linear velocity
v_r	Solute linear velocity
$\bar{v}_r$	Average linear velocity of adjacently-eluting solutes
Δv_r	Difference in linear velocities of adjacently-eluting solutes
σ	Standard deviation
σ^2	Variance
σ_L^2	Variance in band profile in time units
σ_t^2	Variance in band retention time
ψ	Electric potential at a given distance from the inner boundary of the diffuse region of an electrical double layer
ψ_0	Electric potential at the interface between the capillary wall and the buffer solution
ψ_d	Electric potential at the interface between the compact and diffuse regions of an electrical double layer

LIST OF ABBREVIATIONS

General Terms:

AE	Additional Enhancement
AOTF	Acousto-optic tunable filter
APD	Avalanche photodiode
Ar	Argon ion (reference to lasers)
CCD	Charge-coupled device
CE	Capillary electrophoresis
CID	Charge injection device
CZE	Capillary zone electrophoresis
DOE	Department of Energy
EOF	Electroosmotic flow
EPA	Environmental Protection Agency
f/n	f-number
FT	Fourier transform
FT-IR	Fourier transform- infrared
FT-Raman	Fourier transform- Raman
FWHM	Full width at half maximum
(Ga,Al)As	Gallium-aluminum-arsenide (reference to lasers)
GHF	Gravity-driven hydrostatic flow
HeNe	Helium-neon (reference to lasers)
IR	Infrared
Kr	Krypton (reference to lasers)
LCTF	Liquid crystal tunable filter

.

LIF	Laser-induced fluorescence
LOD	Limit of detection
MECC	Micellar electrokinetic capillary chromatography
NA	Numerical Aperture
Nd:YAG	Neodymium-doped yttrium-aluminum-garnet (reference to lasers)
OPO	Optical parametric oscillator (reference to lasers)
ORNL	Oak Ridge National Laboratory
PMT	Photomultiplier tube
RAI	Random access integration
RE-ICCD	Red-enhanced charge-coupled device
RSD	Relative standard deviation
SBFOS	Separations-based fiberoptic sensing
SCM	Scanning multichannel method
SEM	Scanning electron microscope
SERgen probe	Surface-enhanced Raman gene probe
SERS	Surface-enhanced Raman Scattering
SIT	Silicon-intensified target
S/N	Signal-to-noise ratio
UTK	University of Tennessee, Knoxville
UV	Ultraviolet
UV-VIS	Ultraviolet-visible

Concentration Terms:

M	Molar (mole/liter)
%	percent

ppt	parts-per-thousand
ppm	parts-per-million
ppb	parts-per-billion
wt/wt	Weight/weight
wt/vol	Weight/volume

Chemicals and Reagents:

2-AP	2-aminopyrimidine
3AP	3-aminopyrene
BA	Benzoic acid
BCB	Brilliant Cresyl Blue
CFV	Cresyl Fast Violet
CD	Cyclodextrin
DNA	Deoxyribonucleic acid
DNP	2,4-dinitrophenol
EDTA	Ethylenediaminetetraacetic acid
FITC	Fluorescein isothiocyanate
HQS	8-hydroxyquinoline-5-sulfonic acid
MC	Methyl cellulose
NBD	4-nitrobenzofurazan
NBD-Cl	7-chloro-4-nitrobenzofurazan
PABA	*p*-aminobenzoic acid
PEO	Polyethylene oxide
PVA	Polyvinyl alcohol
PVPL	poly(vinylpyrrolidone)
SDS	sodium dodecyl sulfate

TBE	TRIS-boric acid-EDTA (reference to buffers)
TEMED	N,N,N',N'-tetramethylethylenediamine
TiO_2	Titanium Dioxide
TPA	Terephthalic acid
TRIS	*Tris*-(hydroxymethyl)aminomethane

PART I

DEVELOPMENTS IN SURFACE-ENHANCED RAMAN SCATTERING-BASED TECHNIQUES FOR SELECTIVE REMOTE DETECTION

PREFACE

Raman spectroscopy has become an increasingly popular analytical technique in recent years. The Raman effect was first discovered in 1928 by C.V. Raman (Raman, 1928a,b; Raman and Krishnan, 1928a,b), for which he was awarded the Nobel prize for physics in 1930. Based on vibrational transitions, the fine structure inherent in Raman spectra enables the elucidation of molecular structure and is often considered the complement to infrared (IR) spectroscopy. Raman bands are typically <0.1 nm wide and thereby not only provide enhanced spectral selectivity relative to luminescence spectroscopies, but also allow the potential for multicomponent sample analysis. It is readily applicable to solid, liquid and gaseous samples. Furthermore, the Raman effect does not require the absorption of incident radiation at specific polar bond frequencies, thereby making it applicable to the analysis of highly symmetric molecules (a characteristic not shared by IR absorption spectroscopy).

Raman spectroscopy is certainly a potentially versatile technique. Even so, the intrinsically low intensity of Raman scattered radiation had limited its use until the development of high-powered gas lasers in the late 1960's. More recently, the development of more compact and less expensive lasers and spectrometers has made Raman spectroscopy a more accessible technology. A great deal of effort has been devoted towards the development of fiberoptic sensors for remote detection, making Raman-based sensing an especially attractive analytical tool in environmental studies. Another major contribution to the renewed interest in Raman scattering was the discovery of a giant enhancement (up to 10^8) in Raman signal when molecules are adsorbed on or near roughened metallic surfaces (Fleischmann, 1974). There has been considerable debate

2

over the theoretical basis of "surface-enhanced Raman scattering" (SERS). Nevertheless, simplified electromagnetic as well as chemical models have been adopted and have become the basis in the development of a practical SERS technology in the last twenty years. The first part of this dissertation describes some of the SERS-enabling substrates which have been developed in our laboratory, incorporated in fiber optic sensors, and applied towards environmental applications.

CHAPTER 1

INTRODUCTION TO MOLECULAR SCATTERING

Raman scattering spectroscopy is a very powerful diagnostic tool for the elucidation of molecular structure of solid, liquid or gaseous samples. Based on vibrational transitions, it is considered a complementary technique to IR absorption spectroscopy. While both techniques yield fine spectral features, the selection rules and relative intensities of IR and Raman peaks are dissimilar. Simply stated, IR absorption results from a change in molecular dipole moment, thus requiring absorption of radiation at specific vibrational mode frequencies. Raman scattering, by contrast, requires a change in molecular polarizability. The resulting spectral features, usually expressed in wavenumber (cm^{-1}) shifts, represent absolute energy differences between vibrational eigenstates of a molecule. As such, wavenumber shifts are independent of incident radiation wavelength. Furthermore, the wavelength-independent Raman shift frequencies correspond to IR absorption frequencies, thereby allowing functional group identification in Raman as well as IR spectroscopy.

While IR spectroscopy requires a continuous excitation source in the 4000-100 cm^{-1} range (2.5-100 µm), Raman scattering spectroscopy can be performed with intense, monochromatic laser excitation sources in the visible through near infrared region. Table 1.1 illustrates the electromagnetic spectrum and corresponding applicable regions for various spectroscopic techniques for comparison. As will be discussed below, the intensity of scattered radiation is inversely proportional to λ^4 of incident radiation. This advantage is offset, however, by the increased probability of interfering

Table 1.1 Regions of electromagnetic spectrum

Spectral Region	Wavelength Range (λ)	Frequency Range (ν)	Wavenumber/Energy Range	Transition
γ-Ray	<0.005 nm	>6 x 10^{19}	>2.5	Nuclear
X-Ray	0.005-10 nm	3.0 x 10^{16} - 6.0 x 10^{19}	124-2.5 x 10^5 ev	K- and L shell electrons
Vacuum UV	10-180 nm	1.7 x 10^{15} - 3.0 x 10^{16}	7-124 ev	Middle shell electrons
Near UV	180-350 nm	8.6 x 10^{14} - 1.7 x 10^{15}	3.6-7 ev	Valence electrons
Visible	350-770 nm	3.9 x 10^{14} - 8.6 x 10^{14}	1.6-3.6 ev	Valence electrons
Near IR	770-2500 nm	1.2 x 10^{14} - 3.9 x 10^{14}	12,900-4000 cm^{-1}	Molecular vibrations
Middle IR	2.5-50 μm	6.0 x 10^{12} - 1.2 x 10^{14}	4000-200 cm^{-1}	Molecular vibrations
Far IR	50-1000 μm	3.0 x 10^{11} - 6.0 x 10^{12}	200-10 cm^{-1}	Molecular rotations
Microwave	1-200 mm	1.0 x 10^9 - 3.0 x 10^{11}		Molecular rotations
Radio wave	>300 mm	<1 x 10^9		Electron and nuclear spin

luminescence processes at shorter wavelengths, thus explaining increasing interest in Raman scattering in the near IR. Raman spectra generally cover the 0-4000 cm^{-1} Raman shift range, usually covering only the shifts to smaller wavenumbers (lower energy). The following sections are an introduction to radiation scattering and are a general compilation of theories that can be found with more in-depth treatments in the literature (Placzek, 1934; Long *et al.*, 1954; Kerker, 1969; Chu, 1974; Long, 1977; van de Hulst, 1981; Schrader, 1995).

RADIATION SCATTERING

The nature of radiation scattering is dependent on both size and refractive indices of the scattering particles. For cases in which the scattered radiation of the same frequency as incident radiation occurs, elastic scattering, the result is Mie, Debye and Rayleigh scattering with decreasing particle size. Table 1.2 lists particle sizes and refractive indices for the three processes. In general, for particles $>0.05\lambda$ multiple scattering points exist on a single particle thereby leading to destructive and constructive interference and a non-uniform scattering intensity distribution about the particle. Forward scattering is favored for both Mie and Debye scattering.

Rayleigh scattering occurs for particles $<0.05\lambda$. This condition applies to molecules, which can be considered as point sources with more uniform forward and backscattering intensity distributions. Furthermore, these point sources can be considered as being in a homogeneous electric field of the incident light, E_{in}. Implementing the classical theory of light scattering, and assuming monochromatic incident light, the incident radiation induces an oscillating dipole, μ, in the molecule, which will re-emit radiation at the frequency of the dipole oscillation $\left(v_{sc}\right)$[Hz]:

Table 1.2. General classes of scattering

Type of scattering	Refractive index[a]	Particle size[b]
Rayleigh	$I(\eta_r - 1)I \ll 1$	$d_s < 0.05\ \lambda$
Debye	$I(\eta_r - 1)I \approx 0.1$	$0.05\ \lambda < d_s < \lambda$
Mie	$(\eta_r - 1) \gg 0$	$d_s > \lambda$

[a] η_r, Relative refractive index, where η_s = refractive index of the scattering particle, and η_m = refractive index of the medium.

[b] d_s, Major dimension of the scattering particle.

Source: Ingle, J. D., Jr.; Crouch, S. R. *Spectrochemical Analysis*, Prentice Hall, Englewood Cliffs, NJ, p.495, 1988.

$$\mu(t) = \mu^\circ \cos(2\pi v_{sc}t) \qquad\qquad (1.1)$$

where $\mu(t)$ is the magnitude of the dipole moment at time t, and μ° is the maximum induced dipole moment. The induced dipole moment can also be approximated based on the polarizability of the molecule, α:

$$\mu(t) = \alpha E_{in}(t) \qquad\qquad (1.2)$$

The molecular polarizability, α (SI units: $C^2\,m^2\,J^{-1}$), is a measure of the ease with which molecular orbitals can be disturbed by an external electric field can distort molecular orbitals. This factor generally increases with the volume of molecular orbitals.

The induced dipole may be composed of a variety of harmonic frequency components. For the case when the scattering radiation is of the same frequency as the incident radiation $\left(v_{sc} = v_{in}\right)$, the result is Rayleigh scattering. Otherwise, frequency components not equivalent to the incident radiation give rise to Raman scattering. A more detailed discussion for Raman scattering is described later.

Polarization Considerations

An advantage of Raman scattering spectroscopy over IR is the fact that, in addition to the information offered by vibrational frequency peaks observed in spectra, scattering offers further structural information based on the depolarization ratio, ρ:

$$\rho = \frac{I_{\parallel}}{I_{\perp}}$$

(1.3)

where $I_{\parallel}$ and $I_{\perp}$ are scattering intensities due to parallel and perpendicular polarized light, respectively (measured at a fixed scattering angle). Depending on the nature of a molecular vibration during scattering, there will be a characteristic polarization shift produced on incident linearly polarized light. For spherical molecules, or for cases where molecular vibrations are highly symmetric, the depolarization ratio approaches zero. Such molecules are described as isotropic. By contrast, for unsymmetric molecules or symmetric molecules which are distorted during vibrations, the increasing ρ is a measure of molecular anisotropy and approaches 0.75 for totally nonsymmetric vibrations. A better understanding of the observation of polarization shifts during scattering processes can be gained from a detailed discussion of scattering by isotropic and anisotropic molecules.

Scatter from Isotropic Molecules

Isotropic molecules are highly symmetric molecules for which the dipole induced by linearly polarized light is independent of molecular orientation with respect to the incident electric field, E_{in}. This condition requires two properties for all possible molecular orientations with respect to E_{in}.

1) μ is always aligned parallel to E_{in}, and
2) $|\mu|$ is constant for given $|E_{in}|$.

9

Considering the scattered electric field, E_{sc}, the magnitude varies with distance, r, as derived from Maxwell's equations (van de Hulst, 1981; Hecht, 1987):

$$|\mathbf{E}_{sc}(t)| = k\left(\frac{|\mu(t)|}{r\lambda_{sc}^2}\right)\sin\Phi \qquad (1.4)$$

where $|\mathbf{E}_{sc}(t)|$ and $|\mu(t)|$ are, respectively, magnitudes of the scattered electric field and induced dipole moments at time, t; $k = \dfrac{\pi}{\varepsilon_0}$ [SI units] or $4\pi^2$ [cgs units]; Φ is the scattering angle with respect to the oscillating dipole axis (see Figure 1.1); and λ_{sc} is the wavelength of scattered radiation. In this initial assumption, only Rayleigh scattering intensity distributions $(\lambda_{sc} = \lambda_{in})$ will be considered. For this case, a time-independent (time-average) expression for irradiance, E [W • m^{-2}], is derived, which is proportional to $\mathbf{E}^2$:

$$E_{sc}^p(\phi) = k'\left(\frac{\alpha^2}{r^2\lambda_{in}^4}\right)E_{in}^p\sin^2\phi \qquad (1.5)$$

where $k' = k^2$, α is the polarizability of the scattering molecule; λ_{in} is the wavelength of incident radiation; and ϕ is the scattering angle between E_{in} and Rayleigh scatter. Note that since an isotropic molecule is considered, $\phi = \Phi$ in the previous equation. The superscript p denotes polarized incident and scattered light. The more familiar scattering intensity (I_{sc}^p) [W • sr^{-1}] is defined by the following expression:

$$I_{sc}^p = k'\left(\frac{\alpha^2}{\lambda_{in}^4}\right)E_{in}^p\sin^2\phi \qquad (1.6)$$
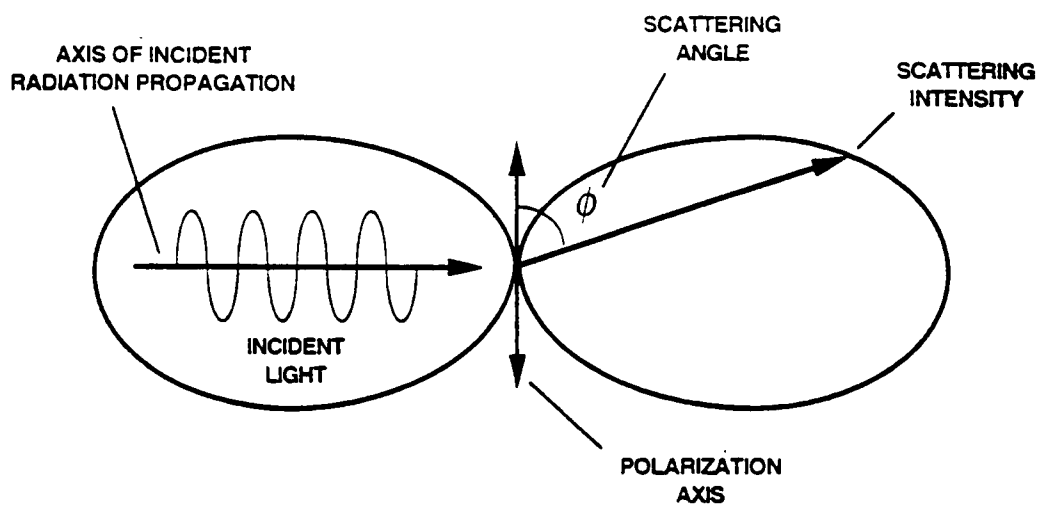
Figure 1.1. Scattering intensity diagram of linearly polarized radiation from an isotropic molecule as a function of angle, ϕ, from the incident polarization axis.

since $I = Er^2$. As the equations demonstrate, the observed scattered light intensity for polarized incident light is zero at 0° with respect to incident polarization. Figure 1.1 illustrates a 2-dimensional scattering intensity distribution plot for linearly polarized light incident upon an isotropic particle or molecule. The corresponding donut-shaped, three-dimensional plot can be envisioned by rotating the plot about the dipole axis. A polarization state plot in three planes perpendicular to coordinate axes for polarized incident light scattered by an isotropic particle or molecule is illustrated in Figure 1.2.

While the scattered light intensity estimations described by above expressions are based on polarized incident light, similar expressions can also be derived for unpolarized or "natural" incident light. While Equation 1.6 still applies, E_{in} fluctuates and therefore the induced dipole and scattered electric field vectors fluctuate with time. For a given point, unpolarized incident light can be considered to be composed of two major orthogonally-oriented polarization components of equal magnitude. Using Equation 1.6, intensity distributions can be estimated for the corresponding major polarization components of the scattered light, $I_{\parallel}$ and $I_{\perp}$. With the scattering plane defined by the incident and scattered light rays, the parallel scatter component, $I_{\parallel}$, is composed of light whose polarization is in the scattering plane, while the perpendicular component, $I_{\perp}$, has polarization perpendicular to the scattering plane. With the scattering angle, θ, defined with respect to the axis of propagation of the incident light beam (see Figure 1.3), the intensities are calculated as follows:

$$I_{\parallel}(\theta) = k' \left(\frac{\alpha^2}{\lambda_{in}^4} \right) \frac{E_{in}^n}{2} \cos^2 \theta \qquad\qquad (1.7)$$

12

$\phi = 0°$
$\theta = 90°$

$\phi = 90°$
$\theta = 0°$

POLARIZATION OF
INCIDENT RADIATION

ISOTROPIC
MOLECULE

$\phi = 90°$
$\theta = 90°$
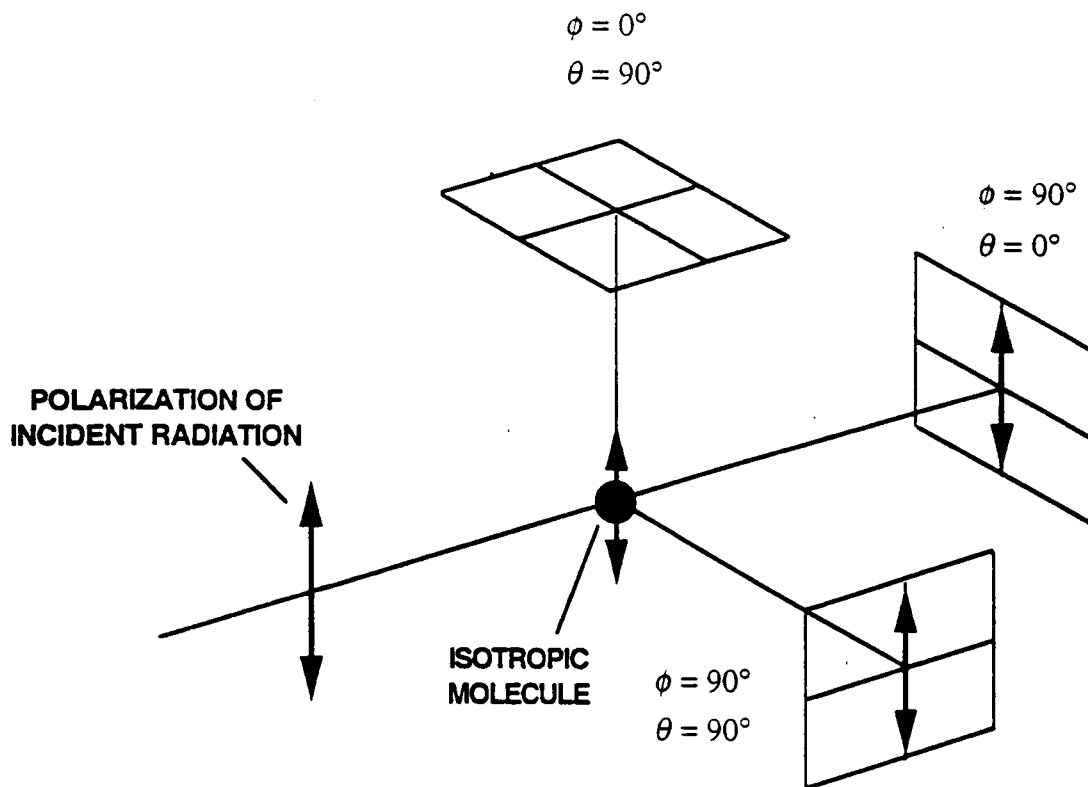
Figure 1.2. Polarization of scattered radiation in three planes perpendicular to the coordinate axis for an isotropic molecule and polarized incident radiation.

ISOTROPIC MOLECULE

UNPOLARIZED
INCIDENT RADIATION

SCATTERING
ANGLE

ϕ

$I_{\parallel}$

$I_{\perp}$

$I_{\parallel} + I_{\perp}$
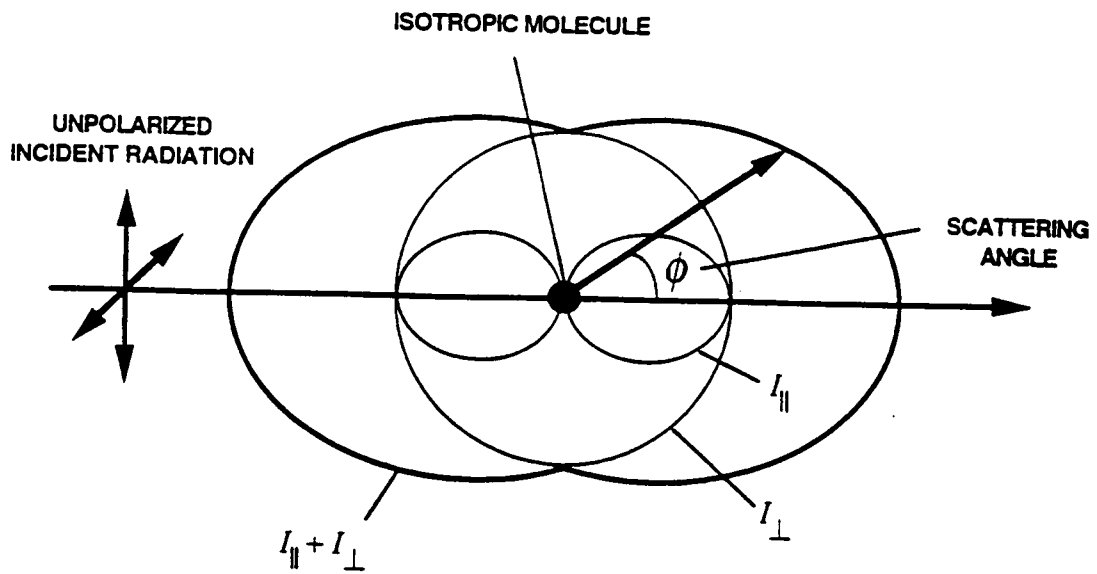
Figure 1.3. Scattering intensity diagram of unpolarized radiation from an isotropic molecule as a function of angle, θ, from the axis of propagation of the incident radiation.

$$I_\perp = k'\left(\frac{\alpha^2}{\lambda_{in}^4}\right)\frac{E_{in}^n}{2} \qquad\qquad (1.8)$$

where $I_{\parallel}(\theta)$ is the parallel component of scattered light at the angle, θ, and E_{in}^n corresponds to the "natural" or unpolarized incident electric field. As demonstrated by the equation, the intensity of the perpendicular scattering component is independent of the scattering angle. While the perpendicular component intensity remains constant, the parallel component intensity reduces to zero at $\theta = 90°$, thus explaining the depolarization ratio of 0 observed for isotropic molecules. A 2-dimensional representation of scattering intensity distributions for parallel and perpendicular components is demonstrated in Figure 1.3. Also shown in the figure is the combined intensity plot, which is determined as a simple addition of the two components:

$$I_{sc}^n(\theta) = I_{\parallel}(\theta) + I_\perp \qquad\qquad (1.9)$$

or

$$I_{sc}^n(\theta) = \frac{k^2}{2}\left(\frac{\alpha^2}{\lambda_{in}^4}\right)E_{in}^n\left(1 + \cos^2\theta\right) \qquad\qquad (1.10)$$

where $I_{sc}^n(\theta)$ is the intensity of "natural" scattered radiation at angle, θ.

Scatter from Anisotropic Molecules

The distinguishing property of anisotropic molecules is that there is a parallel component of scattered light ($\theta = 90°$) in any direction relative to the incident light

15

axis of unpolarized light. Furthermore, for polarized light incident on anisotropic molecules, scattered light is observed at ϕ = 0° and 180° (angles with respect to the axis of polarization). By contrast, unpolarized incident radiation scattered from isotropic molecules is completely linearly polarized at θ = 90°, and eliminated for ϕ = 0° and 180°.

An example of projected polarizations of radiation scattered from an anisotropic medium in the three planes perpendicular to the coordinate axes is illustrated in Figure 1.4. As demonstrated by the figure, the orientation of the induced dipole, μ, is not aligned with E_{in}. Both the polarization and the magnitude of E_{sc} shift with respect to incident polarized light. This effect arises from unequal polarizabilities for different planes of the medium or molecule. The induced dipole is therefore better represented as a tensor:

$$\begin{pmatrix} \mu_x \\ \mu_y \\ \mu_z \end{pmatrix} = \begin{bmatrix} \alpha_{xx} & \alpha_{xy} & \alpha_{xz} \\ \alpha_{yx} & \alpha_{yy} & \alpha_{yz} \\ \alpha_{zx} & \alpha_{zy} & \alpha_{zz} \end{bmatrix} \bullet \begin{pmatrix} E_x \\ E_y \\ E_z \end{pmatrix} \qquad (1.11)$$

or

$$\mu = \underline{\alpha} \bullet E_{in} \qquad (1.12)$$

For the purpose of simplified demonstration of the importance of a molecule's orientation relative to an incident field, the tensor can be conceived as a polarizability ellipsoid (Figure 1.5), expressed by the following equation:

$$\frac{x^2}{\alpha_{xx}^2} + \frac{y^2}{\alpha_{yy}^2} + \frac{z^2}{\alpha_{zz}^2} + \frac{2xy}{\alpha_{xy}^2} + \frac{2yz}{\alpha_{yz}^2} + \frac{2zx}{\alpha_{zx}^2} = 1 \qquad (1.13)$$
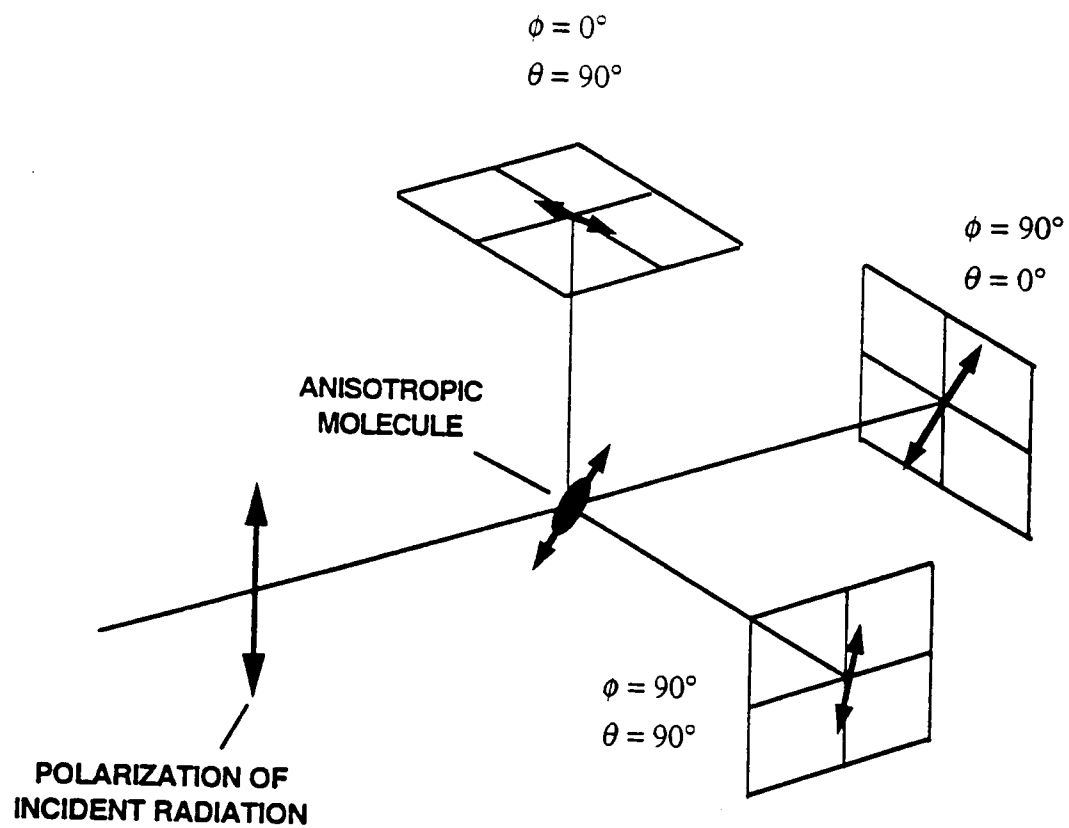
Figure 1.4. Polarization of scattered radiation in three planes perpendicular to the coordinate axis for an anisotropic molecule and polarized incident radiation.
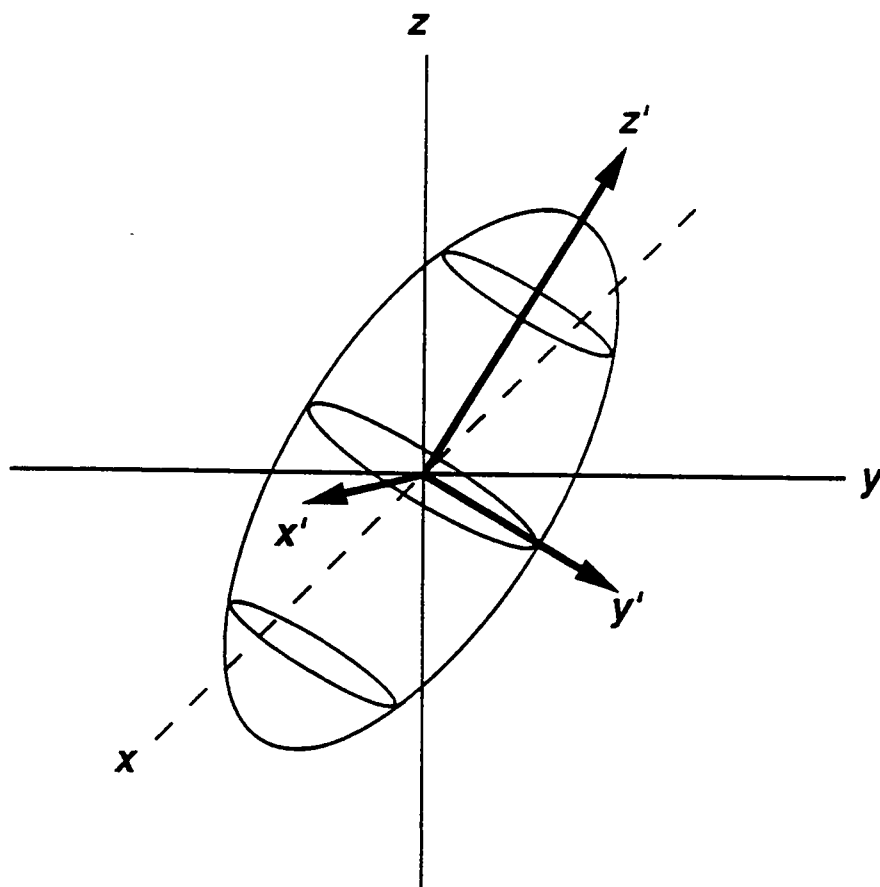
Figure 1.5. Illustration of a polarizability ellipsoid for an anisotropic molecule.

18

The principal axes of the polarizability ellipsoid correspond to the $x' - y' - z'$ axes in the figure. Considering an applied electric field aligned with any of the coordinate $(x - y - z)$ axes as a fixed external frame of reference, it is clear that the value of each element of α, and thus the induced dipole, μ, will change as the orientation of an anisotropic molecule changes. It is interesting to note that when the applied field is aligned with any of the principal axes $(x' - y' - z')$ of the polarizability ellipsoid, the off-diagonal elements of the polarizability are eliminated, and Equation 1.13 is reduced to:

$$\left(\frac{x'}{\alpha_1}\right)^2 + \left(\frac{y'}{\alpha_2}\right)^2 + \left(\frac{z'}{\alpha_3}\right)^2 = 1 \qquad (1.14)$$

where α_1, α_2 and α_3 correspond to the eigenvalues of the three orthogonal eigenvectors of α. The induced dipole is aligned with E_{in}. There are therefore three orientations of anisotropic molecules relative to incident light in which the molecule mimics an isotropic molecule (e.g., linearly polarized light vanishes at $\phi = 0°$ and $180°$). Furthermore, it is evident from the equation that when α_1, α_2 and α_3 are equivalent, the ellipsoid is reduced to a spheroid, in which case the magnitude of the induced dipole, μ, is independent of molecular orientation with respect to E_{in}. The molecule is isotropically polarizable.

As was mentioned above, the magnitude and alignment of the induced dipole of an anisotropic molecule by incident light depend on the orientation of the molecule with respect to incident field. Therefore, the orientation and magnitude of μ can be expected to be variable for gaseous or liquid molecules which are free to rotate. As a result, for a given fixed point in space at a distance, r, from a rotating dipole, the angle with respect

to the induced dipole axis, Φ, will vary with time. Equation 1.4, used to determine the magnitude of the induced electric field, $\mathbf{E}_{sc}(t)$ must therefore be modified with an average induced dipole, $\bar{\mu}$, for all possible orientations of the molecule:

$$\overline{\mathbf{E}}_{sc} = k\left(\frac{\bar{\mu}}{r\lambda_{sc}^2}\right)\sin\Phi \qquad (1.15)$$

where Φ represents the angle at the fixed point with respect to a time-averaged orientation of the induced dipole axis. The corresponding intensity at angle, Φ, is expressed as

$$I_{sc}(\Phi) = k'\left(\frac{\bar{\mu}^2}{\lambda_{sc}^4}\right)\sin^2\Phi \qquad (1.16)$$

It is also possible, and more convenient, to express the intensity of radiation scattered from an anisotropic molecule in terms that are independent of the molecular orientation with respect to incident radiation. While the elements of α change as the molecule rotates, the eigenvalues (α_1, α_2 and α_3) corresponding to the three orthogonal eigenvectors (the principal axes, $x' - y' - z'$, in Figure 1.5) remain constant. These eigenvalues are used to determine two invariant tensor properties: the mean polarizability, $\langle\alpha\rangle$, and the anisotropy, γ:

$$\langle\alpha\rangle = \frac{1}{3}(\alpha_1 + \alpha_2 + \alpha_3) \qquad (1.17)$$

$$\gamma^2 = \frac{1}{2}\left[(\alpha_1 - \alpha_2)^2 + (\alpha_2 - \alpha_3)^2 + (\alpha_3 - \alpha_1)^2\right] \qquad (1.18)$$

Furthermore, although the elements of α vary with molecular orientation, average values of the elements, $\overline{\alpha}$, are derived for all orientations, as off-diagonal and diagonal expressions, in terms of the polarizability invariants:

off-diagonal elements; $i \neq j$:
$$\overline{\alpha_{ij}^2} = \frac{1}{15}\gamma^2 \qquad (1.19)$$

diagonal elements, $i = j$:
$$\overline{\alpha_{ii}^2} = \frac{1}{45}\left(45\langle\alpha\rangle^2 + 4\gamma^2\right) \qquad (1.20)$$

Finally, the intensity of polarized radiation scattered from an anisotropic molecule can be expressed in terms of the average polarizability elements described above. The point of observation is at 90° with respect to the incident light beam, which for this example, propagates along the y coordinate axis. Considering only the induced dipole components in the $y - z$ plane, the induced dipole components of interest, $\overline{\mu}$, are as follows:

$$\overline{\mu}_y = \overline{\alpha}_{xy}\overline{E}_x + \overline{\alpha}_{zy}\overline{E}_z \qquad (1.21)$$

$$\overline{\mu}_z = \overline{\alpha}_{xz}\overline{E}_x + \overline{\alpha}_{zz}\overline{E}_z \qquad (1.22)$$

Note the absence of the E_y-containing factors due to the lack of electric field vector along the axis of propagation. By applying the appropriate average polarizability elements to equations 1.21 and 1.22, and then substituting the average dipole expressions into Equation 1.16, the following intensity expression is derived for incident unpolarized (natural) radiation scattered by an anisotropic molecule:

$$I_{sc}^n = \frac{k'}{45}\left(\frac{45\langle\alpha\rangle^2 + 13\gamma^2}{\lambda_{in}^4}\right)E_{in}^n \qquad (1.23)$$

21

For linearly polarized radiation with polarization aligned with the z-axis, $E_x = E_y = 0$. After redetermination of the average dipole expressions and substitution in Equation 1.16 the following expression is yielded for the intensity of scattered radiation resulting from polarized incident radiation, I_{sc}^p:

$$I_{sc}^p = \frac{k'}{45}\left(\frac{45\langle\alpha\rangle^2 + 7\gamma^2}{\lambda_{in}^4}\right)E_{in}^p \qquad (1.24)$$

It is also clear that by basing parallel and perpendicular polarized scattering components on the average y and z dipole components in equations 1.21 and 1.22, respectively, the depolarization ratio can also be expressed in terms of the polarization invariants for both unpolarized and linearly polarized incident light:

$$\rho^n = \frac{6\gamma^2}{45\langle\alpha\rangle^2 + 7\gamma^2} \qquad (1.25)$$

$$\rho^p = \frac{3\gamma^2}{45\langle\alpha\rangle^2 + 4\gamma^2} \qquad (1.26)$$

RAMAN SCATTERING

Molecular Vibrations

The Raman scattering phenomenon is based on molecular vibrations and rotations. Within a molecule, each atom has three degrees of freedom as it can move independently along each of the axes of the Cartesian coordinate system. For a molecule with n atoms,

there are $3n$ motional degrees of freedom. However, motions which do not affect the distance between atoms have little or no consequence in Raman scattering. These include translational motions in which all atoms move simultaneously in the same direction parallel to the axes of the Cartesian coordinate system (three degrees of freedom), and rotations about the principal axes of a molecule (two and three degrees of freedom for linear and nonlinear molecules, respectively). There are therefore $3n$-5 and $3n$-6 normal vibrational modes for linear and nonlinear molecules, respectively. These modes can change the distance between atoms by periodically altering bond lengths or angles.

The energy associated with a molecular vibration is dependent on bond strength, masses of the inclusive atoms, and the magnitude of displacement from the equilibrium position of the inclusive atoms. A very simplified model applies Hooke's Law to the stretching vibration of a diatomic molecule:

$$F = -f \bullet x \qquad\qquad\qquad (1.27)$$

where F is the force required to move the atom a distance, x, from the equilibrium position, and f represents the force constant analogous the bond strength. For reference, typical force constants for single, double, and triple carbon-carbon bonds are 4.5, 9.4, and 15.7 N/cm, respectively. Force, as defined by Newton's Second Law, is also proportional to mass, m, and acceleration, d^2x/dt^2:

$$F = m \bullet \frac{d^2x}{dt^2} \qquad\qquad\qquad (1.28)$$

The two expressions for force can be combined to yield the following equation:

$$m \bullet \frac{d^2x}{dt^2} = -f \bullet x \qquad\qquad (1.29)$$

In Equation 1.29, m denotes the reduced mass of a diatomic molecule:

$$\frac{1}{m} = \frac{1}{m_1} + \frac{1}{m_2} \qquad\qquad (1.30)$$

where m_1 and m_2 represent the atomic masses for the elements of the diatomic molecule.

The expression for a harmonic oscillator can be used to describe the time-dependent value for x:

$$x(t) = x_0 \cos(2\pi vt + \varphi) \qquad\qquad (1.31)$$

where $x(t)$ is the displacement of an atom from the equilibrium position at time, t, x_0 represents the maximum displacement of an atom from the equilibrium position, v is the vibrational frequency, and φ is the phase angle. The second derivative,

$$\frac{d^2x}{dt^2} = -4\pi^2 v^2 x_0 \cos(2\pi vt + \varphi) = -4\pi^2 v^2 x \qquad\qquad (1.32)$$

can be substituted in Equation 29 to yield

$$4\pi^2 v^2 m = f \qquad\qquad (1.33)$$

Rearrangement and replacement of m by the reduced mass expression yields the vibrational frequency, v, of the diatomic molecule:

$$v = \frac{1}{2\pi}\sqrt{f\left(\frac{1}{m_1} + \frac{1}{m_2}\right)}$$

(1.34)

The potential energy, V, of the diatomic molecule as a function of displacement from the equilibrium separation between atoms, r, is obtained by integrating the force expression of Equation 27.

$$V = \frac{1}{2}fr^2$$

(1.35)

When V is plotted as a function of r, the resulting graph, the "harmonic" potential, is a parabola. Actual molecules violate Hooke's law, however, as the force constant for the chemical bond is variable. For example, compression of a bond from the equilibrium length requires more energy than stretching. Likewise, the stretching becomes progressively easier up to limit which is defined by the bond dissociation energy. The resulting plot is a nonsymmetric "anharmonic" potential. An example of an anharmonic function is the Morse function (Morse, 1929):

$$V = D_b\left[1 - \exp\left(-\sqrt{\frac{f_e}{2D_b}}\right)\bullet r\right]^2$$

(1.36)

where D_b is the bond dissociation energy, and f_e represents the bond force constant near the potential minimum.

Classical mechanics accounts for vibrations of any amplitude, r, defined by plots of Figure 1.6. Quantum mechanics, however, limits the molecule to discrete energy states represented by the horizontal lines of the potential energy diagrams. For harmonic oscillators, the energy levels are equidistant. For anharmonic oscillators, the difference between energy levels decreases with increasing energy.

Having discussed molecular vibrations, the focus of ensuing discussions is their role in Raman scattering. Indeed, Raman scattering arises from both molecular rotations and vibrations. However, rotational transitions are of much lower energy than vibrational transitions and result in fine structure superimposed on vibrational bands. For the gaseous state, high resolution spectrometers are required. For solutions, rotational energy levels are broadened and the fine structure becomes obscured. For the topic of analytical chemistry, emphasis devoted exclusively toward vibrationally-induced Raman scattering should be sufficient.

Classical Theory

According to the classical theory of light scatter from a molecule, the intensity is proportional to the dipole moment induced on the molecule in the presence of an incident electric field, E_{in}. The time-dependent dipole, $\mu(t)$ is expressed as follows:

$$\mu(t) = \underline{\alpha}(t)E_{in}(t) \tag{1.37}$$

where $E_{in}(t)$ is represented as a harmonic function:

$$E_{in}(t) = E_0 \cos(2\pi v_{in}t) \tag{1.38}$$

26
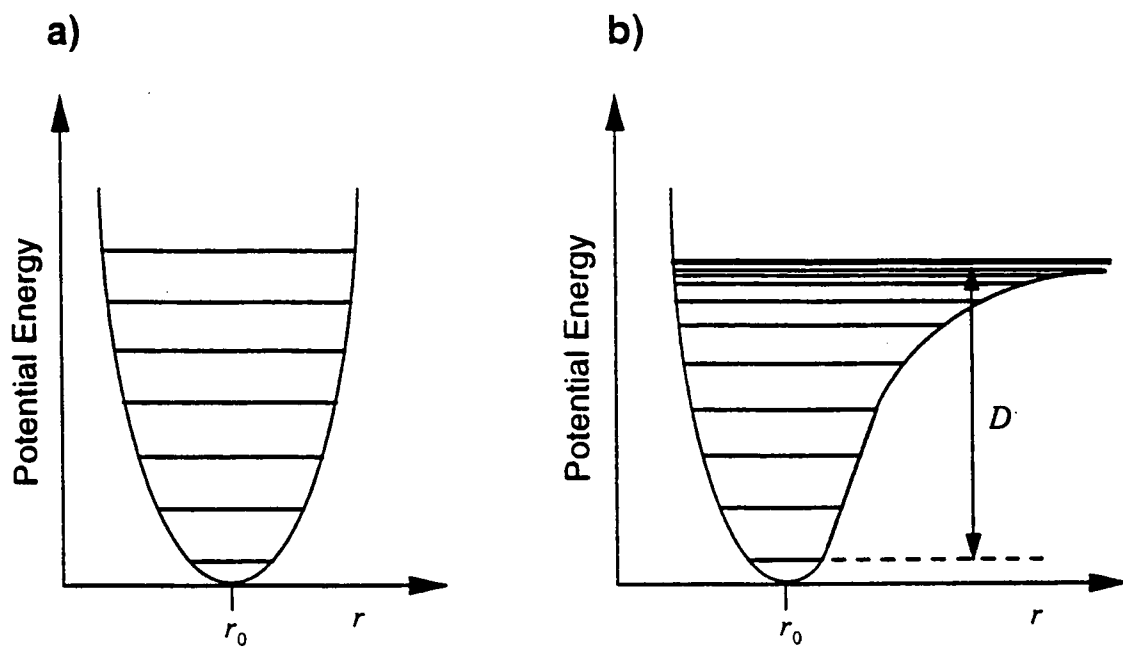
Figure 1.6. Potential energy diagrams for a) harmonic oscillation, and b) anharmonic oscillation.

27

where E_0 is the maximum amplitude of the incident electric field, and v_{in} corresponds to the incident radiation frequency. Because both the polarizability, α, and E_{in} can be represented by harmonic functions, the overall induced dipole, μ, may be composed of several frequency components. In addition to the Rayleigh scattering discussed above, scattering occurs at lower and higher frequencies with respect to the Rayleigh scattering frequency (Wood, 1928). For the higher frequency case, the scattered radiation carries excess energy from the vibrating molecule, resulting in anti-Stokes Raman scattering. In the low frequency case, energy of incident radiation is lost to the molecule, resulting in Stokes Raman scattering. It is noteworthy that the energy shift for a given vibrational mode relative to the Rayleigh scattering frequency is the same for both Stokes and anti-Stokes Raman scattering $\left(hv_{in} \pm hv_{sc}\right)$.

As was discussed above, the polarizability of an anisotropic molecule varies with rotation. Furthermore, the polarizability tensor can vary with changes in molecular shape arising from vibrations for both isotropic and anisotropic molecules. Focusing on the vibrationally-induced Raman scattering, a time-dependent expression for the polarizability tensor elements, α_{ij}, arising from J normal vibration modes is derived from a Taylor expansion:

$$\alpha_{ij}(t) = \alpha_{ij} + \sum_{k=1}^{J}\left(\frac{\partial \alpha_{ij}}{\partial Q_k}\right)_0 Q_k(t) + \frac{1}{2}\sum_{k=1}^{J}\left(\frac{\partial^2 \alpha_{ij}}{\partial Q_k^2}\right)_0 (Q_k(t))^2 + \dots \quad (1.39)$$

For this case the displacement of the atom from the equilibrium position is represented by Q_k $\left(Q_k(t) = Q(t) - Q_{eq}\right)$ which when using the harmonic oscillator model can be expressed as

$$Q_k(t) = Q_k^0 \cos(2\pi v_k t) \qquad\qquad (1.40)$$

where Q_k^0 is the maximum displacement for the k vibrational mode, and v_k is the corresponding frequency. Assuming all but the first two terms of Equation 1.39 are insignificant, and by combining equations 1.37 - 1.40, the following expression demonstrates the effect of molecular vibrations of the induced dipole in the presence of the incident field, E_0:

$$\mu(t) = \underline{\alpha}E_0 \cos(2\pi v_{in}t) + E_0 \cos(2\pi v_{in}t)Q_k^0 \sum_{k=1}^{J}\left(\frac{\partial \alpha}{\partial Q_k}\right)_0 \cos(2\pi v_k) \qquad (1.41)$$

Using the trigonometric identity, $\cos(f_1)\cos(f_2) = \frac{1}{2}\cos(f_1 + f_2) + \frac{1}{2}(f_1 - f_2)$, the following expression is derived:

$$\mu(t) = \underline{\alpha}E_0 \cos(2\pi v_{in}t) + \frac{E_0}{2}Q_k^0 \sum_{k=1}^{J}\left(\frac{\partial \alpha_{ij}}{\partial Q_k}\right)_0 \cos 2\pi(v_{in} + v_k) + ...$$
$$... \frac{E_0}{2}Q_k^0 \sum_{k=1}^{J}\left(\frac{\partial \alpha_{ij}}{\partial Q_k}\right)_0 \cos 2\pi(v_{in} - v_k)t \qquad (1.42)$$

In this expression, the first term represents Rayleigh scattering, while the second and third terms represent anti-Stokes Raman and Stokes Raman scattering, respectively. The following expressions apply to intensities, I_r, of both anti-Stokes and Stokes Raman scattering:

$$I_r^p = \frac{k'}{45}\left(\frac{1}{2}Q_k^0\right)^2 \left(\frac{45\langle\alpha_k'\rangle^2 + 7(\gamma_k')^2}{\lambda_r^4}\right)E_i^p \qquad (1.43)$$

29

$$I_r^n = \frac{k'}{45}\left(\frac{1}{2}Q_k^0\right)^2 \left(\frac{45\langle\alpha_k'\rangle^2 + 13(\gamma_k')^2}{\lambda_r^4}\right)E_i^n \qquad (1.44)$$

In equation 1.44, the superscripts, n and p, correspond to "natural" and polarized incident radiation, respectively. Due to the inversely proportional dependence of scattering to λ^4 expressed by this classical model, one would predict that the intensity of anti-Stokes Raman scattering exceeds that of Stokes Raman scattering for a given vibrational mode. In practice, the opposite is usually true. Quantum mechanics better predicts the relative intensities based on the Boltzmann distribution of molecules among discrete vibrational levels of the ground electronic state. Indeed, the Boltzmann distribution can be used to determine the temperature of a sample based on relative intensities of Stokes and anti-Stokes Raman lines. A more complete discussion of quantum mechanical models for Raman scattering is given below.

Quantum-Mechanical Theory of Raman Scattering

A semiclassical approach to describing the Raman effect has been applied by Plazcek to better account Raman scattering intensity (Plazcek, 1934). In this theory the scattering molecule is considered a quantum object while the electromagnetic radiation is treated classically. The model is valid for conditions where the excitation frequency differs considerably from those of electronic and vibrational transitions.

A quantum mechanical representation of the scattering process is illustrated in Figure 1.7. Central to the figure is a time-dependent virtual vibrational energy level arising from perturbation produced by the incident radiation. Unperturbed energy levels are

30

$|r\rangle$

$|r\rangle$

VIRTUAL VIBRATIONAL
ENERGY LEVEL

V_{in} V_{st} V_{in} V_{as}

$|m+1\rangle$

$|m\rangle$

$|m-1\rangle$
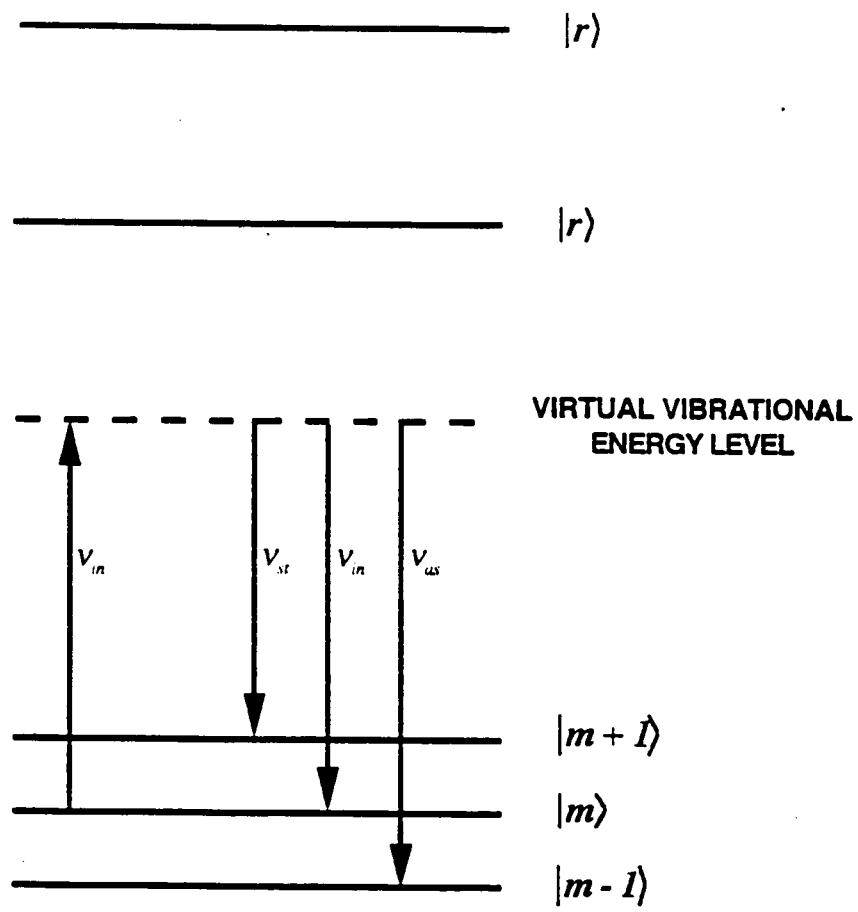
Figure 1.7. Quantum-mechanical representation of molecular scattering processes.

3 1

represented by $|r\rangle$. Transitions can originate from any stationary state $|m\rangle$. Any transition which results in no change in energy (e.g., $|m\rangle \rightarrow |m\rangle$) yields elastic Rayleigh scatter ($v_{sc} = v_{in}$), while inelastic Raman scatter results from any transition, $|m\rangle \rightarrow |n\rangle$. Transitions that terminate in a higher ground state vibrational energy level ($|m\rangle \rightarrow |m+1\rangle$) yield Stokes Raman scatter ($v_{sc} < v_{in}$). Transitions to a lower ground state vibrational energy level ($|m\rangle \rightarrow |m-1\rangle$) yield anti-Stokes Raman scatter ($v_{sc} > v_{in}$), and are usually much less likely to occur (see below).

Theoretical semiclassical expressions for the intensities of Raman scattering have been derived based on perturbation theory and the time-dependent Schrodinger equation (Blokhintsev, 1964; Davydov, 1965). A more practical approach in terms of estimating Raman scattering intensity utilizes Placzek's semiclassical polarizability theory (Placzek, 1934). With this approach, the first two terms of the Taylor series of Equation 1.39 represents the time-dependent polarizability tensor components as follows:

$$\alpha_{mn}(t) = \langle n|\alpha|m\rangle + \sum_k (\alpha'_{mn})_k \langle n|Q_k|m\rangle \qquad (1.45)$$

where the summation includes all k vibrational modes which result in the $|m\rangle \rightarrow |n\rangle$ transition. As before, the first term applies to Rayleigh scatter. Pauling and Wilson (Pauling and Wilson, 1935) have defined the second term for both Stokes and anti-Stokes scatter as follows:

$$n^k = m^k + 1; \quad \langle n|Q_k|m\rangle = \frac{1}{2}Q_k^0 = \sqrt{\frac{(m^k+1)h}{8\pi^2\mu_r v_k}} \; ; \text{(Stokes)} \qquad (1.46)$$

$$n^k = m^k - 1; \quad \langle n|Q_k|m \rangle = \frac{1}{2} Q_k^0 = \sqrt{\frac{m^k h}{8\pi^2 \mu_r \nu_k}} \quad ; \text{ (anti-Stokes)} \qquad (1.47)$$

where m^k and n^k are quantum numbers for the stationary vibrational states, $|m\rangle$ and $|n\rangle$, of the k-th vibrational mode; and μ_k and ν_k correspond to the reduced mass and frequency of the k-th vibrational mode, respectively. Reviewing Equations 1.43 and 1.44, it is clear that classical theory predicts near equal magnitudes of Stokes and anti-Stokes Raman scattering. With the quantum mechanical approach, the Boltzmann distribution predicts that the Stokes scatter will be stronger than the anti-Stokes scatter. For example, the probability, P, that a molecule exists in the ground vibrational state is

$$P\left(m^k = 0\right) = 1 - \exp\left[-\frac{h\nu_k}{kT}\right] \qquad (1.48)$$

where k is Boltzmann's constant, and T is the Kelvin temperature. It is clear that at room temperature most of the molecules will occupy the lowest vibrational level, from which no anti-Stokes Raman scattering is possible. Substituting the term for $\frac{1}{2} Q_k^0$ from Equation 1.46 into Equation 1.43, and further adding the probability term of Equation 1.48, Equation 1.43 can now be expressed as follows for Raman scatter from the lowest vibrational energy level:

$$I_{r,st}^p = \frac{k'}{45}\left(1 - \exp\left[-\frac{h\nu_k}{kT}\right]\right)\left(\frac{h}{8\pi^2 \mu_r \nu_k}\right)\left(\frac{45\langle \alpha_k' \rangle^2 + 7(\gamma_k')^2}{\lambda_k^4}\right)E_{in}^p \qquad (1.49)$$

33

where the equation applies to the case of linearly polarized incident radiation and a detection angle of 90°. The term, μ_r, represents the reduced mass of the molecule. While the expression would need to be modified for different detection angles or ranges of detection angles, the following expression generally describes the ratio of Stokes and anti-Stokes Raman scattering intensities under similar conditions:

$$\frac{I_{r,st}}{I_{r,as}} = \left(\frac{v_0 - v_k}{v_0 + v_k}\right)^4 * \exp\left(\frac{hv_k}{kT}\right) \qquad (1.50)$$

Selection Rules for Raman Scattering

While it is straightforward to calculate the number of vibrational modes of a molecule, defining such modes in a Raman scattering spectrum is more complex. Although generally weak, normal vibrational mode combinations or overtones may be manifested in a spectrum. Also, not all of the normal vibrational modes may be represented by a Raman spectrum as a result of degeneracy (two or more vibrational modes of the same frequency) or the existence of Raman-inactive modes.

The Raman activity of a vibrational mode depends on the symmetry of the molecule. More specifically, there must be a change in polarizability, α during a vibration as demonstrated in the following expression for the Raman transition moment, R:

$$R = \int \psi_m^* \left[(r - r_e)\left(\frac{\partial \alpha}{\partial r}\right)_e\right] \psi_n d\tau \qquad (1.51)$$

where r and r_e represent internuclear separation and bond length, respectively, and ψ represents the wavefunction for the given energy state. The $d\tau$ term indicates the integration over all space. Furthermore, Raman scattering for the fundamental vibrational modes require the transition condition: $\Delta v = \pm 1$. Overtones transitions (e.g., $\Delta v = \pm 2$) also occur but usually result in very weak scattering. For $R = 0$, the transition is forbidden. An effective method of predictive Raman activity of a given vibrational mode is to use group theory (Harris and Bertolucci, 1978) while considering the symmetry properties of the transition states and the polarizability. For the integral in Equation 1.51 to be nonzero, the product of the ground state, the polarizability and the excited stated symmetry must be totally symmetric.

Alternative steps can be taken to predict Raman activity. In terms of above discussions, it is clear that when all elements of the polarizability tensor are zero, the Raman mode is inactive. For cases where it is possible to envision a polarizability ellipsoid, changes in the ellipsoid shape arising from a vibrational mode can be used to determine Raman activity (Tobias, 1967; Banwell, 1971). Finally, one can consider the symmetry classes of the polarizability tensor elements and that of the excited vibrational levels of a given mode. The symmetry class of the excited vibrational level must match the symmetry class of at least one of the polarizability tensor elements (Wilson *et al.*, 1955; Harris and Bertolucci, 1978).

In general, Raman-active vibrations arise from totally symmetric vibrations. It is noteworthy that Raman scattering is widely considered as the complementary phenomenon to IR absorption. IR transitions, by contrast, require a change in dipole moment which generally involves unsymmetrical vibrations. For centrosymmetric

molecules, there are no common Raman and IR active modes. For noncentrosymmetric molecules, there may be several vibrational modes manifested by both Raman scattering and IR absorption spectra. For the extreme case where there is no symmetry (C_1), all vibrations are both Raman and IR active. A comparison of group frequencies in both Raman and IR techniques has been compiled (Tobin, 1971). In closing, while above discussions about Raman scattering intensity have been based on the perturbation of the polarizability of the entire molecule, attempts have been made to base some observed Raman intensities on the polarizability between individual atoms of a vibrating molecule (Long *et al.*, 1954; and Hester, 1967).

A Summary of Rules Concerning Vibrations

- The number of vibrational degrees of freedom for nonlinear molecules of n atoms is $3n - 6$.

- The number of vibrational degrees of freedom for linear molecules of n atoms is $3n - 5$.

- For a nonlinear, noncyclic molecule with b chemical bonds, the number of stretching degrees of freedom is b.

- For a nonlinear, noncyclic molecule with b chemical bonds and n_1 terminal atoms, the number of bending degrees of freedom is $4b - 3n + n_1$.

- For a nonlinear, noncyclic molecule the number of torsions corresponds to the number of nonterminal bonds, $b - n_1$.

- Normal vibrations are a linear combination of the degrees of freedom.

- Combinations of normal vibrational modes are possible, including harmonics, sum and difference tones.

- If vibrational modes of differing frequencies are coupled, the low frequency is shifted lower while the high frequency is shifted higher.

- Vibrations can be localized to regions of a molecule where bonds or functional groups give rise to vibrational frequencies significantly different from those of adjacent groups. This effect yields characteristic frequencies which can aid in functional group identification or bond order determination.

- Characteristic vibrations and symbols:

  Stretching vibration of XY group- $\nu(XY)$

  Scissoring vibration of XY_2 or XY_3- $\delta(XY_2); \delta(XY_3)$

  Wagging vibration of XY_2- $\omega(XY_2)$

  Rocking vibration of XY_2- $\rho(XY_2)$

  Twisting vibration of XY_2- $\tau(XY_2)$

  Out-of-plane vibrations of XY- $\gamma(XY)$

SURFACE-ENHANCED RAMAN SCATTERING (SERS)

Since its Nobel Prize-winning discovery in 1928 (Raman, 1928a,b; Raman and Krishnan, 1928a,b), Raman scattering has been recognized as a valuable tool in the structural elucidation of molecules. Based on vibrational transitions, the technique yields very sharp spectral features in comparison to those observed with luminescence and UV-Vis absorption spectroscopies. Even with the advent of lasers in the 1960's, the acceptance of Raman scattering as a practical analytical tool has been deterred largely due to its low cross section relative to other spectroscopic processes commonly applied to analytical chemistry.

The low cross-section of the Raman scattering process is due in part to the inefficiency of promoting a molecule to the virtual state. The cross section for Raman scattering, σ_{sc}, is defined as the ratio of rate of generation of scattered photons to the irradiance of incident light:

$$\sigma_{sc} = \frac{P_{sc}}{E_{in}} \qquad (1.52)$$

where P_{sc} and E_{in} are expressed in W and W*m^{-2}, respectively. Having the units m^2, the cross-section can be envisioned as the effective area covered by the molecule for scattering incident photons. The rate of scattering (in all directions), P_{sc}, can be calculated from the scattering intensity as follows:

$$P_{sc} = 2\pi \int_0^{\pi} I_{sc}(\theta) \cos \theta d\theta \qquad (1.53)$$

where $I_{sc}(\theta)$ has been defined in for both Rayleigh and Raman scattering in previous sections. Table 1.3 lists typical cross-sections for molecular absorption (UV-Vis and IR), fluorescence, Rayleigh scatter and Raman scatter. The competitive processes of molecular absorption and fluorescence are often ten orders of magnitude more likely to occur than Raman scattering.

Despite the inherently low cross-section of Raman scattering, photophysical phenomena have been observed to significantly enhance Raman signals, such as resonance Raman scattering (RRS) and surface-enhanced Raman scattering (SERS). Resonance Raman scattering occurs when the excitation radiation frequency coincides with the frequency of an electronic transition of a molecule. In this case the excited electronic state

Table 1.3. Cross-sections for various photophysical processes

Process	σ (cm^2)
UV Absorption	10^{-18}
IR Absorption	10^{-20}
Fluorescence[a]	10^{-19}
Rayleigh Scatter	10^{-26}
Raman Scatter	10^{-29}

[a]Cross-section strongly dependent on environmental factors.

Source: C. L. Stevenson, and T. Vo-Dinh, "Signal expressions in Raman spectroscopy" In: *Modern Techniques in Raman Spectroscopy*, Laserna, J. J. (Ed.), John Wiley and Sons, Chichester, p.22, 1996.

contributes strongly to the character of the virtual state, thus greatly enhancing the probability that the transition will result in Raman scatter. However, there may be a dramatic increase in interfering fluorescence as well. Procedures that can be taken to offset the fluorescence interference in RRS include temporal discrimination and environmental quenching. Enhancements due to RRE can be as high as 10^6. When the excitation radiation comes within the high- or low-frequency wings but not within the vibrational structure of the an electronic absorption band, an effect called pre-resonance Raman scattering also occurs. While enhancements of 10-100 are observed for this effect, fluorescence interference may be insignificant. For either of the resonance effects, the range of molecules for which enhancement could be observed would be very limited without the use of a tunable excitation source or multiple fixed-excitation sources. Furthermore, only the vibrational modes associated with the chromophoric region of a molecule are enhanced. The reader is referred to the literature for more detailed theories of RRE effects (Kramers and Heisenburg, 1925; Dirac, 1927; Albrecht, 1961; Tang and Albrecht, 1970; Behringer, 1974; Lee and Heller, 1979; Myers and Mathies, 1987).

SERS is an important Raman scattering enhancement phenomenon with the potential for more far reaching applications. The SERS effect was first observed in 1974 by Fleischmann and coworkers who reported strongly enhanced Raman scatter from pyridine molecules adsorbed on electrochemically roughened silver electrodes (Fleischmann *et al.*, 1974). While they attributed the effect to increased surface area of the roughened surface, later reports by the teams of Jeanmaire and Van Duyne (Jeanmaire and Van Duyne, 1977), and Albrecht and Creighton (Albrecht and Creighton, 1977) not only confirmed the enhancement, but attributed the enhancement to more complex surface enhancement processes. Furthermore, the signal enhancement of

adsorbed molecules relative to gas phase molecules was determined to be 10^6-10^8 times. Since then, there has been renewed interest in Raman scattering as an analytical tool in many application areas, as is indicated by a large number of papers and review articles in the literature (Furtak and Rayes, 1980; Otto, 1980; Yamada, 1981; Birke and Lombardi, 1982; Dornhaus, 1982; Chang and Furtak, 1982; Ueba et al., 1982; Aussenegg et al., 1983; Otto, 1983; Kerker, 1984; Pockrand, 1984; Schatz, 1984; Wokaun et al. 1984; Efrima, 1985; Moskovits, 1985; Weitz et al., 1986; Barlett and Cooney, 1987; Cotton, 1988; Creighton, 1988; Garrell, 1989; Vo-Dinh, 1989; Kneipp, 1990; Aroca and Kovacs, 1991; Pemberton, 1991; Cotton and Brandt, 1992; Otto et al., 1992; Vo-Dinh, 1995; Ruperez and Laserna, 1996). Highlights of SERS in recent years have included reports of further Raman scattering enhancements. Near-field SERS measurements have demonstrated enhancements on the order of 10^{13} (Zeisel et al., 1998; Deckert et al., 1998). In fact, single molecule detection studies have been pursued with Raman enhancements reported to be on the order of 10^{14}-10^{15} for specific sites in SERS-active media, referred to as "hot spots" (Nie, 1997; Kneipp et al., 1997; Kneipp et al., 1998a; Kneipp et al., 1998b).

SERS Theories

While the development of SERS-inducing media and applications of SERS have been far reaching, a full theoretical basis for the surface-enhancement mechanism has not yet been proposed. Instead, several component models based on electromagnetic and chemical effects have been independently proposed. A full discussion of these models is beyond the scope of this chapter. More detailed reviews are found in the literature (Chang and Furtak, 1982; Kerker, 1984; Pockrand, 1984; Schatz, 1984; Wokaun et al., 1984;

Moskovits, 1985; Creighton, 1986; Creighton, 1988; Otto *et al., 1992*; Kambhampati *et al.,* 1998, Vo-Dinh, 1998).

As was discussed before, the transition electric dipole is proportional to the polarizability of the molecule, α, and the magnitude on the incident electric field E_{in}:

$$\mu = \alpha \bullet E_{in} \qquad\qquad (1.54)$$

It is therefore clear that enhancement of either the molecular polarizability α or the magnitude of the incident electric field E_{in} can enhance the Raman scattering intensities. Electromagnetic models have been proposed to account for an enhancement of the factor, E_{in}. These models are independent of the adsorbed analyte molecule, thereby predicting enhancements for a broad range of chemicals. Likewise, chemical models have been proposed for the enhancement of the factor, α. In contrast to electromagnetic models, chemical models are less understood at this point and are highly specific in terms of both the adsorbed molecules and the nature of the metallic surface (see below).

Electromagnetic models for SERS- the E_{in} factor. According to classical electromagnetic theory, molecules on or near metal surfaces will experience enhanced electric fields relative to that of the incident radiation. Indeed, six-fold enhancements are possible even with smooth metallic surfaces (Moskovits, 1985). For roughened metallic surfaces, the enhancement can be on the order of 10^6-10^7. A major contribution to this enhancement is provided by surface plasmons (Ritchie, 1957). When a metallic surface is irradiated by an incident field, conduction electrons are displaced into an oscillation of equal frequency to the incident light. These oscillating electrons in turn produce a secondary electric field which adds to the incident field.

When these oscillating electrons become spacially confined, as is the case for isolated metallic spheres or otherwise roughened metallic surfaces, there is a characteristic frequency (the plasmon frequency) at which there is a resonant response of the collective oscillations to the incident field, thus producing intense localized fields which can in turn interact with molecules within the fields (a relatively long range effect in comparison to chemical effects). It is also notable that the Raman scatter from the adsorbed molecule can further stimulate surface plasmons in the metallic substrate (the image effect), thus providing even further enhancement (Gertsan and Nitzan, 1980; Schatz and Van Duyne, 1980; Otto, 1978). In a similar enhancement effect, the Fresnel reflection effect, the oscillation dipole and/or quadrupole of the vibrating molecule can interact with surface electrons to produce Raman-shifted reflection of light (Gertzen and Nitzan, 1980; Schatz and Van Duyne, 1980; Otto, 1978; Zeman and Schatz, 1987). Finally, electric field lines may be concentrated to provide field enhancements at high curvature points of a metallic feature, the "lightning rod" effect. It is interesting to note that image, Fresnel reflection, and "lightning rod" effects are independent of incident radiation fields.

The magnitude of an enhanced field decreases with the cube of the distance, r, from the center of the metallic feature. Likewise, the resulting Raman scatter intensity increases with the square of the enhanced field applied to the molecule, E_{in}. In light of these conditions, it is clear that the variation in the enhanced field with distance from the source could be used to determine the proximity of molecules to the metallic surface. In addition, because a localized field is highest in the direction normal to the metallic surface, it may be possible to determine orientation of the molecule with respect to the metallic surface because vibrational modes comprising variations in the molecular

polarizability perpendicular to the metallic surface will be selectively enhanced. Creighton has provided a detailed summary of adaptations in fundamental Raman scattering selection rules which take this effect into consideration (Creighton, 1988).

In order to fully utilize the electromagnetic enhancement due to the surface plasmon contribution, various parameters must be optimized to match the plamson frequency to the frequency of the intended excitation source. These factors include the metal used as well as the size and shape of the metallic feature. For the visible region, silver, copper and gold provide the strongest enhancements in the order given. Silver and gold based substrates have also been reported for use in the near-infrared region (Ibrahim et al., 1996). Despite the popularity of the precious metals, other materials have been investigated for use in SERS substrates, including Pt (Chang and Furtak, 1982; Zeman and Schatz, 1987), Pd (Zeman and Schatz, 1987), Ni (Chang and Furtak, 1982), Li (Moskovitz et al., 1982), Na (Lund et al., 1982), Al (Wood and Klein, 1980; Zeman and Schatz, 1987), Zn (Zeman and Schatz, 1987), Cd (Loo, 1981; Zeman and Schatz, 1987), Ga (Zeman and Schatz, 1987) and In (Zeman and Schatz, 1987).

The size of a metallic surface feature is a very important factor in the plasmon frequency. For simplicity, a spherical metallic particle is considered in this discussion. Wokaun et al. have reported theoretical calculations which indicate that the field enhancement predicted by the particle plasmon model is limited by radiation damping (Wokaun et al.; 1982). The size range of surface features is limited at the upper end by radiation damping, while the lower end is limited by surface scattering resulting from energy losses of conduction elections caused by collisions with the particle surface. The effects of radiation damping and dynamic depolarization have been considered by several investigators (Schatz, 1984; Barber et al., 1983 a,b; Meier and Wokaun, 1983).

According to a theory developed by Kerker for silver spheres (Kerker, 1984), a maximum enhancement value of 10^6 occurs for 5-nm radius particles and 382 nm excitation. As particle size increases, the plasmon frequency bandwidth increases and shifts toward the red, and the enhancement decreases (e.g., 50-nm radius: 10^4, 500-nm radius: 10-100).

While particle plasmon-based theories discussed above apply to solid metallic spheres, it is interesting to briefly note that theoretical models have also been developed for concentric spheres comprised of dielectric cores and metallic outer layers (Kerker and Blatchford, 1982), prolate spheroids (Barber *et al.*, 1983a,b) and ellipsoids (Gertzen and Nitzan, 1980). For concentric silver-coated spheres, it was demonstrated that enhancements in the 10^5-10^6 range are achievable throughout the visible range by varying the ratio (q) of the dielectric core radii (dielectric constant of 2.25) to the silver coating sphere radii. However, it was shown that the excitation bandwidth for maximum enhancement was quite narrow for any given ratio. Wavelength maxima ranged from approximately 350 nm for q=0, to about 375 nm for q=0.5, to 650 nm for q = 0.9. For prolate spheroids, enhancements as high as 10^5 have been calculated for the infrared region of the spectrum.

Chemical models for SERS- the α factor. In contrast to the electromagnetic enhancement component of SERS, the chemical effect is much more specific. It involves the overlap of metal and adsorbate electronic wavefunctions, which in turn leads to light-induced charge transfer processes which can increase the apparent value of the molecular polarizability (Chang and Furtak, 1982; Zeman and Schatz, 1987; Burstein *et al.*, 1979; Furtak, 1983; Pandey and Schatz, 1984; Adrian, 1982; Persson, 1981). As such, the effect is short-range relative to the electromagnetic effect (0.1-0.5 nm).

Furthermore, as will be discussed below, the mechanisms can depend on atomic-scale features of the metallic surface, the geometry of possible bonding between the adsorbate and the metallic surface, and the energy levels of the adsorbate molecule. Obviously, the magnitude of the effect is extremely variable for a broad range of chemicals, but it can be quite large for specific adsorbate-surface systems, with enhancements ranging from approximately 10 to 1000 (Pandey and Schatz, 1984; Adrian, 1982; Persson, 1981). In general, chemical effects are considered minor contributions to the SERS effect relative to electromagnetic effects. While chemical models are limited at this time, two models are commonly cited: the charge-transfer model and the "adatom model".

In the charge transfer model, upon stimulation by an incident photon, an electron from the metal surface tunnels into a charge-transfer excited state of the adsorbed molecule. The result is an ionized adsorbate molecule with an equilibrium geometry differing from that of the original neutral adsorbate, hence a change in polarizability. Subsequently, the molecule relaxes upon the return of the electron to the metal surface. This relaxation step in turn produces a vibrationally excited neutral adsorbate molecule which finally relaxes with the emission of a Raman-shifted photon.

In the "adatom model", there are interactions between the adsorbate molecules and specific atomic-scale active sites in the metallic surface. When such interactions facilitate the charge transfer process described above, the result can be additional chemical enhancement for very specific molecules (Zeman and Schatz, 1987; Furtak, 1983, Otto et al., 1980). The enhanced Raman scattering could be attributed to the additional momentum available for scattering of electron-hole pairs at atomic scale roughness, or by the relaxation of momentum by the presence of the adatom site to which

the adsorbate is bound. It is interesting to note that an adatom active site is probably associated with clusters no larger than five or six atoms.

RAMAN INSTRUMENTATION

General Instrumental System

The instrumentation required for Raman and SERS include a) a monochromatic excitation source, b) a high-resolution dispersive element, such as a monochromator or a polychromator, and c) an appropriate single-channel or multichannel detector. The excitation light source is usually a laser. The laser radiation is generally passed through optical filters to reject unwanted plasma lines and directed to the sample. Selection of the laser polarization may affect the intensity of the observed SERS signal. The SERS emission from the sample is collected through appropriate optics and focused onto the entrance slit of a dispersive element. There are three basic classes of Raman spectrometers for which very general schematic diagrams are illustrated in Figure 1.8. The first class includes single-channel scanning instruments which generally use a double-grating monochromator coupled to a photomultiplier tube (PMT). The second class includes multichannel instruments which use a polychromator interfaced to a multichannel detector, such as a vidicon, a photodiode array, or a charge-coupled device (CCD). The final class includes imaging instruments which utilize dispersive devices with imaging capability along with two-dimensional array detectors such as CCDs. These and other types of instrument systems and components are discussed in the following sections, with emphasis on milestone developments towards practical instrumentation.

47
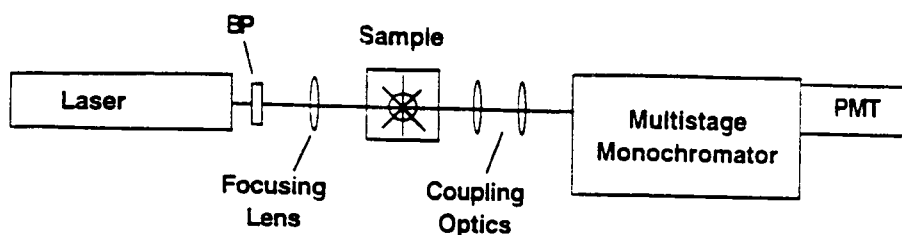
Single-Channel Scanning Instrument
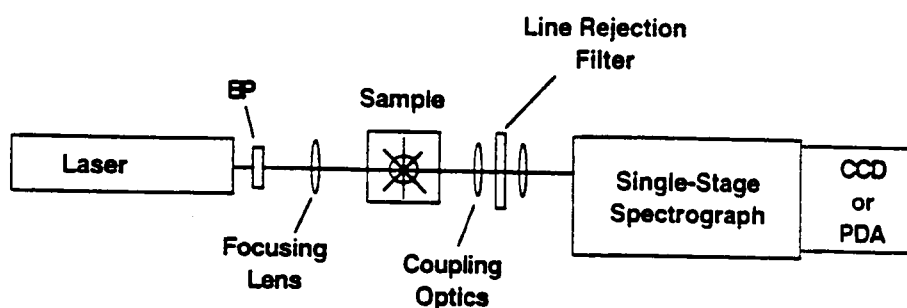
Multichannel Instrument
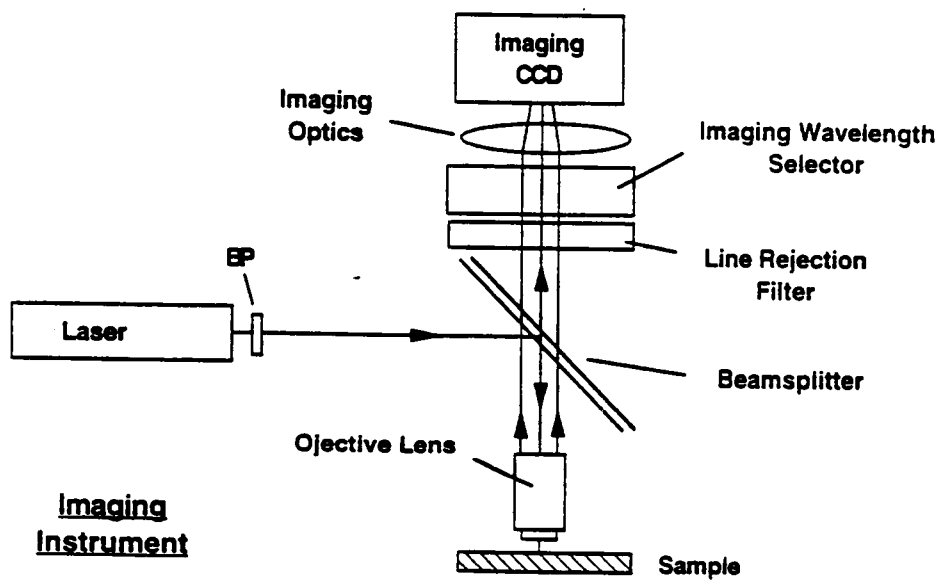
Imaging Instrument

Figure 1.8. General instrumental approaches for Raman scattering detection.

48

Excitation Sources

Lasers. Even though Raman scattering was discovered in 1928, its use as a routine laboratory technique had to wait until the development of laser light sources in the 1960s. The Raman effect is relatively weak compared to other forms of light scattering. Stimulation of Raman scattering to a detectable level requires intense excitation sources with narrow bandwidths, which can be provided by lasers. Since Raman scattering does not require a tunable excitation source, measurements of Raman spectra of molecules were reported soon after the first lasers were in use. The active medium of a laser, in which the stimulated emission occurs, may consist of various types of materials. The first laser used ruby as the active medium (Maiman, 1960; Collins *et al.*, 1960; Maiman *et al.*, 1961). Today, solid-state lasers are made from semiconductors and metal-doped sapphires, garnets and glasses. Gas lasers are also commonly used and are based on a variety of atomic and molecular gases as the amplification medium.

In the laboratory, large high-power lasers have traditionally been used as excitation sources for Raman instrumentation. These sources have included both continuous wave (cw) lasers such as argon ion (Ar: 488 nm, 514.5 nm), krypton ion (Kr: 647.1 nm), and helium-neon (HeNe: 632.8 nm), as well as pulsed sources, such as the Nd-doped yttrium-aluminum-garnet (Nd:YAG: 1064 nm, 532 nm). Some intense lasers can be coupled to dye heads, frequency doublers or optical parametric oscillators (OPOs) to extend the wavelength range of these lasers or permit tunability for resonance Raman or other nonlinear Raman techniques. With the exception of helium-neon and some argon ion lasers, these laser systems are bulky, and require intense power supplies and external cooling sources. They are generally not well-suited for portable instrumentation.

For portable Raman instrumentation, diode lasers [(Ga,Al)As] emitting in the 640-840 nm range (i.e. red-to-near-IR range) are a suitable alternative to the previously-described lasers (Angel *et al.* 1995a). The first diode lasers were reported in 1962, but their use in Raman spectroscopy has become popular more recently, probably due to the improved power, wavelength stability and coherence of the more recently-developed diode lasers. The development of improved photodiode-based detectors for better response in the red to near-IR spectral region is probably another factor. As the diode laser technology stands, it offers several advantages over the larger gas laser systems. They are much cheaper, require much less power to operate, are very compact, and have some inherent tuning capability (30nm). High power diode lasers suitable for Raman (e.g., 100-500 mW) require cooling and thermal stability. Nevertheless, compact integrated thermoelectric coolers are suitable for the task. The most significant persistent disadvantages include the decreased wavelength stability, decreased coherence, and higher beam divergence. An external cavity with a grating (Angel *et al.* 1995b) or a distributed Bragg reflector (Cooper *et al.*, 1995) can greatly increase the wavelength stability. The decreased Raman cross section in the near-IR due to the direct proportionality of the scattering process with v^4 is a disadvantage, but it is largely offset by the decrease in fluorescence interference. Nevertheless, blue-green emitting diodes may make their appearance in the near future from wide-bandgap II-VI semiconductor compounds. Diode lasers have been used in many recent applications and appear to be well-suited for development of compact Raman instrumentation.

Pen ray lamps. There has been some renewed interest in mercury pen ray lamps as Raman excitation sources in the UV (Pelletier, 1992). In comparison to laser sources for the UV (typically high powered pulse lasers), the mercury lamps are much less

expensive, are simple to operate and maintain, and are less noisy. However, tunability is not an option, and many interfering atomic emission lines need to be rejected. Some examples of strong atomic emission lines that could become more common in Raman spectroscopy include the mercury 253.7-nm and 184.9-nm lines, the zinc 213.9-nm line, and the cadmium 228.8-nm line.

Spectrometer Systems

Single-channel scanning spectrometers. The detection of Raman scattering places vigorous demands on the spectrometers in terms of both resolution and, more importantly, stray light rejection. Because the Rayleigh (elastic) scattering can exceed the Raman (inelastic) scattering by several orders of magnitude, the detection of the weak Raman bands close to the excitation line, especially within 50-100 nm of the Rayleigh wavelength (depending on the excitation wavelength), is very challenging due to a high likelihood of stray light in the spectrometer. Traditionally, multiple stage scanning monochromators have been used for Raman spectroscopy with single channel detectors such as photon counting PMTs.

A PMT coupled with a double-grating monochromator is the most commonly used Raman spectrometer. The spectral resolution and the sensitivity of the spectrometer are strongly dependent on the characteristics of the monochromator and the PMT. Modern holographic gratings generally offer excellent stray light rejection. The photon counting method is often used for detection since it has proved to have several advantages over analog methods, especially for low-level signal detection (Malmstadt *et al.*, 1972; Vo-Dinh and Wild, 1973, 1974). PMTs are widely used for their high spectral sensitivity, wide operating range, low cost, and relatively simple electronics.

The recent development of notch filters, which consist of crystalline arrays of polystyrene spheres, has given rise to filters with very high rejection efficiency of laser lines (Asher *et al.*, 1986) and has eased the demands placed on spectrometers. As a result, there has recently been more common use of single-stage spectrographs with multichannel detectors such as photodiode arrays and CCDs. Nevertheless, progress in single-channel scanning spectrometers continues to be reported. For example, a conventional scanning Raman spectrometer has been modified for near-IR excitation (1064 nm) yielding results comparable to Fourier transform (FT)- Raman instruments (Engert *et al.*, 1991). The instrument has been used to record spectra of gases excited at 1064 nm for the first time. Nevertheless, the sensitivity has been estimated to be three orders of magnitude lower then for gas spectra excited at 514 nm.

The development of high dispersion holographic gratings and compact detectors has helped miniaturize scanning single-channel instruments. Until recently, single-channel scanning instruments for Raman spectroscopy have generally used large spectrometers (e.g., 1-m path length) and bulky PMTs, often operated in the photon counting mode. The recently developed silicon avalanche photodiodes (APDs) are relatively compact and exhibit good response in the visible through near-IR region. Bypassing the multiple dynode stages used with PMTs, the power requirement for operation of APDs is relatively low (+12V, +5V, and -5V). Furthermore, the response time of the detector is commendable, with a single photon timing resolution of 3 ns rms. Photon counting of up to 10^6 photons/s is possible. By exploiting these recent developments, Sutherland *et al.* have developed a portable single-channel scanning instrument (Sutherland *et al.*, 1994). The spectrometer featured a 0.125-m double grating monochromator with gold-coated gratings for enhanced throughput towards the

red spectral region. Despite its small size, the resolution of the monochromator was 12 cm^{-1}, which was later demonstrated to be adequate for the analysis of mixtures (Sutherland *et al.*, 1995). A small 9-mW HeNe laser was the excitation source. The detector, a 1.5" x 1.25" x 4" APD, was cooled with an integrated thermoelectric cooling module for highly regulated, relatively low dark noise (typically 250 ± 5 counts/s). The system was used in conjunction with SERS substrate technology to detect 11-pg samples of 3-aminopyrene. Use of fiberoptic probes for remote detection was also demonstrated. The entire optical system occupied less than 1.5 cubic feet and weighed less than ten pounds. The suitcase instrument has since been marketed by Gamma-Metrics (San Diego, CA).

Filter-based systems. The recent use of narrow line rejection filters has therefore enabled the development of much more compact Raman spectrometers. Furthermore, elimination of Rayleigh scattering by line rejection filters (e.g., holographic notch filters) has permitted the exploitation of the multiplex advantage via the development of FT-Raman instruments. Compact single-stage spectrographs are a recent generation of Raman instruments, springing largely from the recent development of holographic notch filters, which largely utilize concurrently developed scientific CCD detectors. Clearly, the development of line rejection filters has had a dramatic effect on the development of Raman instrumentation. Such filters have come in the forms of absorptive filters (Britow, 1979; Hirschfeld and Chase, 1986; Schulte *et al.*, 1991), thin-film interference filters (Tobin, 1959; Puppels *et al.*, 1990) holographic filters (Carrabba *et al.*, 1990; Pelletier, 1991; Yang *et al.*, 1991), crystalline colloid filters (Flaugh *et al.*, 1984) and atomic vapor filters. (Rasetti, 1930; Pelletier, 1992) The recent commercial availability of Raman holographic notch filters have made them a very popular line rejection device, with rejection bandwidths of as little as 320 cm^{-1}, with

absorbances as high as 5. Furthermore, the typical 75% transmission of Raman scattered radiation is very attractive in comparison to conventionally-used triple-stage monochromators. Examples of some recent developments of other line rejection filter technologies are described below.

The atomic vapor filter was first introduced in 1930 for UV Raman spectroscopy (Rasetti, 1930, Nuovo Cimento). The absorbance of this mercury vapor was 3 for the 253.7-nm line. More recently, a mercury vapor filter was reported to have an absorbance of greater than 5.5 over a bandwidth of only a few wavenumbers centered at 253.7 nm. Transmittance of Raman scattering is typically 95% for atomic vapor line rejection filters (Pelletier, 1992). This line rejection filter has permitted the use of a mercury pen ray lamp as a Raman excitation source. The small size, simplicity, low maintenance, low cost and low noise are particularly attractive features of pen ray lamps in the development of more practical, compact spectrometers. Other vapor filters have been proposed for the near-IR region (e.g., Rb: 780.0 nm and 794.8 nm; Cs: 852.1 nm and 894.4 nm; K: 766.5 nm and 769.9 nm)(Pelletier, 1992). In fact, a Rubidium atom vapor filter has been reported with an absorbance of 4 at 780 nm. (Sabbaghzadeh *et al.*, 1995)

Chevron-type dielectric filters continue to be applied toward the development of compact Raman spectrometers and microscopes. Puppels and coworkers reported using a chevron-type line rejection filter with a rejection bandwidth of only 60 cm^{-1} (FWHM) and an absorbance of 8 (Puppels *et al.*, 1994). Furthermore, it allowed 70% transmission of Raman scattered radiation. Futamata later reported use of dielectric filters with an absorbance of merely 5, but a 90% transmittance of the Raman scatter, which could be measured down to a spectral distance of 50 cm^{-1} from the Rayleigh line

(Futamata, 1996). This reported throughput is approximately 20% greater than for typical notch filters; and 8-9 times better than triple stage monochromators.

Interferometric and FT-Raman spectrometers. Since low-intensity signals are frequently observed in Raman measurements, it is desirable to improve the sensitivity of detection by recording the entire spectrum simultaneously. FT spectroscopy is an example of frequency division multiplexing. All wavelengths of interest strike a single detector simultaneously. Spectral information is encoded by a Michelson interferometer which generates a complex time-dependent pattern of multiple sine waves which are converted to the frequency domain. There is no dispersion and instruments are slitless. As a result, there is a throughput (Jacquinot) advantage in addition to the multiplex (Felgett) advantage, which together may yield exceptional S/N values in comparison to scanning instruments with comparable acquisition times. Because the multiplex advantage is most fully realized for detector noise-limited applications, FT spectroscopy is most commonly used in the IR. The Felgett and Jacquinot advantages were exploited by FT-IR absorption spectroscopy in the 1970's, but the application towards Raman spectroscopy were delayed because of several potential disadvantages.

Unlike IR absorption which is mainly detector noise-limited, Raman detection is almost always shot noise-limited. After the transform to the frequency domain, this noise is distributed throughout the entire spectrum. Furthermore, the high intensity of coexistent Rayleigh scattering in comparison to Raman scattering virtually eliminates the throughput advantage. The recent development of high quality line rejection filters for rejection of Rayleigh scatter has therefore renewed an interest in FT-Raman spectroscopy. An important development in FT-Raman spectroscopy was reported in 1986 by Hirschfeld and Chase who observed both the throughput and multiplex

advantages, while sample fluorescence and decomposition was also minimized (Hirschfeld and Chase, 1986). Since then, a multitude of FT-Raman works have been reported. Parker and coworkers reported the use of an inexpensive, bench top FT-IR spectrometer for acquiring Raman spectra in 1988 (Parker *et al.*, 1988). Adapting the instrument with a Nd:YAG laser (1064 nm) and a triplet set of corresponding dielectric line rejection filters (56 = 3 each), high quality spectra of pure rubrene, anthracene and calomel were recorded with up to 3 cm^{-1} resolution. Acquisition times were as low as 2 min. Soon afterward, Archibald *et al.* reported modifying a commercial FT-IR instrument with 6-m optical fiber probes for remote detection of pure liquids and solids (Archibald *et al.*, 1988). Both single and dual fiber probe geometries were investigated. Using 1-W,1064-nm excitation from a Nd:YAG laser, typical acquisition times were as low as 9 min. Zimba and Rabolt also reported FT-Raman detection over a 2-m bifurcated fiberoptic probe (Zimba and Rabolt, 1991). Furthermore, they reported spectra acquired with a relatively compact prototype diode-bar-pumped Nd:YAG laser operated at a few hundred milliwatts.

Although a Michelson interferometer is a compact instrument in comparison to grating dispersion devices commonly used for Raman spectroscopy, resolution is proportional to the length of travel covered by the translating mirror. Such travel requires a high degree of precision which can be adversely affected by constant or jarring movement of the instrument. As a result, compact Michelson FT-Raman instrumentation may not be suitable for a portable device. A possible alternative form of FT-Raman instrumentation utilizes a common path Sagnac interferometer with no moving parts (Takahashi *et al.*, 1993). The resulting 2-dimensional fringe pattern is projected onto a CCD for multichannel FT spectroscopy (MCFT). The resolution of these instruments is limited by pixel dimensions of the CCD. Zhao and McCreery have reported 25 cm^{-1} resolution

using this type of system (Zhao and McCreery, 1996). Integration times for full Raman spectra were as low as 5 s for a 135-mW 830-nm laser.

Multichannel Systems. The use of monochromators helps minimize the stray light often encountered in Raman measurements. However, only one spectral resolution element, or channel, can be monitored at a time with scanning monochromators. Detectors that permit the recording of the entire spectrum simultaneously are known as multichannel detectors. A well-known example of a multichannel detector is the photographic plate. More modern multichannel detectors comprise the vidicon, the diode array, and charge transfer devices such as the charge-injection device (CID) (Michon and Burke, 1973; Sims and Denton, 1983) or the CCD (Talmi, 1975; Campion and Woodruff, 1987; Alarie *et al.*, 1992). In multichannel spectrometers, the detector is placed at the focal plane of a polychromator, which is a monochromator with the exit slit removed. As a result, the radiation dispersed at all spectral elements defined by the polychromator is detected simultaneously. The simultaneous detection of all the dispersed radiation using n spectral resolution elements reduces the measurement time by a factor of $\sqrt{n}$ in the case of an S/N (signal-to-noise)-limited measurement, or improves the S/N level by a factor of $\sqrt{n}$ in the case of a time-limited measurement.

Several types of multichannel detectors are currently available. One device is the vidicon, which is essentially a television-type device comprised of an array of microscopic photosensitive diode junctions that are grown upon a single silicon crystal wafer. These diode junctions provide individual microelements that are used to simultaneously detect all radiation elements dispersed by the polychromator. Vidicons are capable of integrating radiation intensity over multiple scanning cycles due to their charge storage capabilities. Sensitivity can be further enhanced by incorporating an

image-intensification module in front of the vidicon to yield a silicon-intensified target (SIT) vidicon.

Another multichannel detector is the diode array, which also utilizes photodiodes as detection elements. Recording of the signal is performed with direct on-chip circuitry rather than with a scanning electron beam. Signal amplification is achieved by a microchannel plate image intensifier. Gated detection with down to 5-ns time resolution can be performed with the intensified diode array.

Recently, other types of devices, such as CIDs and CCDs, have received increasing use due to their high quantum yield, two-dimensional imaging capability, and very low dark current. There are significant differences in the operation modes and performance characteristics between these two detectors. With CIDs, each detection element of this two-dimensional array detector consists of n-doped silicon with an overlayer of two crossed electrodes: one "collection" electrode, and one "sense" electrode. A major drawback of CIDs is their high read noise (Bilhorn et al., 1987). Nevertheless, averaging multiple signals can significantly reduce read noise (Bilhorn and Denton, 1990). Relative to CCDs, CIDs are very highly resistant to charge blooming, thereby allowing a relatively large linear dynamic range per detection element. Furthermore, the signal integration times can be varied for different elements of the detector array in a mode called random access integration. This feature further expands the linear dynamic range of the detector as a whole and thereby allows signal integration of both intense and weak spectral features in a single exposure (Bilhorn et al., 1987; Bilhorn and Denton, 1989; Bilhorn and Denton, 1990). To date, applications of CIDs in analytical spectroscopy have been limited mostly to atomic emission spectroscopy (Bilhorn et al., 1987; Bilhorn and Denton, 1989; Bilhorn and Denton, 1990). Their

58

limited use could be due to the low quantum efficiency (QE) relative to CCDs (e.g., peak QE = 47% and 90% for typical CIDs and CCDs, respectively, at 500 nm) (Sweedler et $al.$, 1988). A complete review of applications of both CIDs and CCDs in chemical analysis has been summarized by Sweedler (Sweedler, 1993).

The introduction of the scientific-grade CCD has had a dramatic effect on the development of practical, compact spectrometers. CCDs are compact, solid-state sensors with integrated circuit technology. They are two-dimensional array detectors composed of pixels (metal-oxide-semiconductor capacitors) of typically <30-μm diameter. As such, they may offer a high resolution which fully exploits the Raman spectral selectivity, even with relatively small spectrometers. In addition to exhibiting high quantum efficiency in the visible and near-IR range, CCDs produce relatively low dark current, thus allowing long integration times. The potential advantages of CCDs in Raman spectroscopy were first exploited in the late 1980s with introduction of the first CCD-based Raman spectrometers (Murray and Dierker, 1986; Pemberton and Sobocinski, 1989; Wang and McCreery, 1989) Wang and McCreery reported a CCD-based instrument for near-IR Raman spectroscopy in which compact 782 nm and 830 nm diode lasers were used (Wang and McCreery, 1989). Full 400-3200 cm^{-1} spectra were reported for several compounds with integration times as low as 10 s. Fluorescence suppression in the near-IR allowed observation of Raman bands from highly fluorescent compounds such as Rhodamine 6G and nylon. Furthermore, a 2-mM detection limit was reported for benzene in CCl_4.

A drawback of CCD use in spectrometry has been a limited spectral range, defined not by the response of the device, but by a combination of the linear dispersion of gratings and optical path lengths of spectrometers. This limitation has been partially offset by the

59

scanning multichannel method (SCM), in which several partial spectra can be acquired and recombined with data acquisition times still relatively short in comparison to single-channel scanning methods (Knoll *et al.*, 1990). The combination of a CCD with a double monochromator using the SCM technique was first reported by Deckert and Kiefer in 1992 (Deckert and Kiefer, 1992). Exceptionally high resolution has been reported for near-IR Raman (Panitz *et al.*, 1994). Using this system with 780-nm laser powers of 150-250 mW, 200-1800 cm^{-1} spectra of pure liquids and solids were acquired with 0.2 - 1 cm^{-1} resolution over acquisition periods of up to 1700 s. In general, 10-factor improvements in resolution were associated with 100-factor increases in acquisition time for equal S/N.

An alternative to the SCM approach exploits the two-dimensional array format of the CCD by coupling this detector to an echelle grating spectrometer for simultaneous acquisition of multiple partial spectra distributed over both dimensions of the detector. CCD use has been reported with an f/1.9, 0.1-m echelle spectrograph for 2 cm^{-1} resolution over a range of roughly 5000 cm^{-1} (Pelletier, 1990). The echelle-type geometry allowed acquisition of 25 simultaneous partial spectra with a 1-s signal integration time. S/N values of 85 were observed for cyclohexane bands, but required 200 mW laser power. Yet another approach has been the combined use of relatively low dispersion gratings and more recently-available oblong CCDs which are better formatted for spectrographs. Hoffman *et al.* used this approach in the development of a compact 30 cm X 50 cm spectrometer for combined Raman and fluorescence spectrometry (Hoffman *et al.*, 1992). However, the reported 26 cm^{-1} resolution was quite low in comparison to other CCD-based systems. Nevertheless, isomers of xylene (neat) were fully discriminated with this system when using 1-W, 488-nm excitation and a 22-s signal integration time.

CCD-based Raman spectrometers have also been used with fiberoptic probes for remote detection. A CCD-based imaging spectrometer equipped with a commercially-available fiberoptic probe was first reported by Newman and coworkers in 1992 (Newman *et al.*, 1992). Spectra were taken for liquids inside glass vials with acquisition times of as low as 30 s. Furthermore, use of a 783-nm excitation source allowed the observation of Raman scattering from otherwise fluorescent compounds. Likewise, a red-enhanced CCD-based spectrometer coupled to a 20-m long optical fiber probe was described for SERS measurements at 514.5 nm (Alarie *et al.*, 1992). The giant signal-enhancing SERS effect combined with fiberoptic probes demonstrated the potential for remote detection of compounds at low concentrations. Furthermore, the CCD detection format allowed particularly short data acquisition times. For example, a 69-ng sample of *p*-aminobenzoic acid was detected using the 20-m fiberoptic probe with 100-mW laser power and only 9-ms acquisition time.

CCD-based Raman spectrometers have also been developed for remote detection without optical fibers. Angel *et al.* have described a portable instrument for line-of-sight detection of samples located at distances of up to 20 m (Angel *et al.*, 1992). Argon ion (488 nm) and diode (809 nm) lasers of 23- to 100-mW powers were used in conjunction with an f/4, 0.25-m spectrograph equipped with a liquid nitrogen-cooled CCD. Typical Raman signal integration times for the detection of various pure powders and neat liquids were in the 1-2 min range for a 2000 cm^{-1} spectrum with 10 cm^{-1} resolution. An instrument for noninvasively monitoring powders inside amber vials was described by McCreery *et al.* (McCreery *et al.*, 1998). A dispersive spectrometer was used with a 785-nm laser and a CCD to acquire spectra of the pure compounds in the 1 - 60 s acquisition time range, even though there was a 60% loss in signal caused by the

vials. The instrument also featured an on-line library of 309 compounds with library search software capability. The fidelity of compound identification by the unassisted search software was 88-96% for 26 random samples. The 785-nm excitation source produced significant fluorescence background in only approximately 10% of the samples comprising the library.

Hadamard transform system for multiplexed Raman detection. In addition to the spectral multiplex advantage offered by Fourier transform instruments or multichannel detectors such as CCD and photodiode arrays, an additional time-saving method of Hadamard transform can allow the simultaneous acquisition of multiple spectra from spatially-separated samples or separated positions within a given sample. A general Hadamard transform method, based on a simple mathematical function that requires little computer time, has been described by Belton and Wright which may be particularly well-suited for IR and FT-Raman spectroscopy (Belton and Wright, 1994).

Acousto-optic tunable filter (AOTF)-based Raman devices. An attractive tool for wavelength selection in compact, portable spectrometers is the acousto-optic tunable filter (AOTF). These compact, solid-state devices are used to spectrally filter light, with a bandpass on the order of 1-10 Å, through the interaction of acoustic waves and optical waves in a birefringent crystal. The acoustic waves are launched into the crystal from piezoelectric transducers coupled to the crystal, forming regions of compression and rarefaction in the crystal which form a refractive index grating which propagates at the speed of the launched acoustic wave. Because the acoustic wave velocity is on the order of 10^5 times less than the speed of light in the medium, the grating is virtually stationary from the perspective of the optical wave front.

Tuning the filter is accomplished by simply adjusting the frequency of the acoustic wave. Random wavelength access or sequential scanning is possible with interim periods merely on the order of microseconds required between wavelength changes. In addition to being relatively compact, the AOTF has no moving parts, thereby making it a rugged instrument for which repetitive calibration procedures are not necessary. These large aperture devices (limited by the size of the crystal) use no slits, and acceptance angles can be up to 20°. As a result there is high optical throughput and imaging ability. Tuning ranges from UV through IR are possible, depending on the crystal material (e.g., quartz, collinear, 255-800 nm; TeO_2, noncollinear, 350-4500 nm; $CaMoO_4$, collinear, 400-4500 nm; and $LiNbO_3$, collinear, 400-4500 nm.) No other dispersive device encompasses all of these abilities. As a result, AOTFs have recently been used in the development of several novel spectrometers for the UV-vis, near-IR and mid-IR ranges (Kurtz *et al.*, 1987; Shipp *et al.*, 1976; Smith, 1987; Hueber *et al.*; 1995; Moreau *et al.*, 1996a, 1996b; Campiglia *et al.*, 1997) An astronomical photometer and polarimeter (Smith and Smith, 1991; Kradjel and Fresenius, 1991) and a near-IR microscope (Treado *et al.*, 1992a) have been developed. An AOTF-based Raman imaging microscope was even reported by Treado *et al.* in 1992 (Treado *et al.*, 1992b). The device used a noncollinear TeO_2 AOTF capable of a 2-nm bandpass at 700 nm. A CCD was used to record the images. A detailed description of a more refined AOTF-based, high-fidelity Raman imaging microscope for acquiring both large format Raman images and complete Raman spectra from 1-µm diameter samples was later published by Goldstein *et al.* (Goldstein *et al.*, 1996).

The feasibility of an AOTF-based scanning Raman spectrometer was first reported be Lewis *et al.* in 1993 (Lewis *et al.*, 1993). The instrument utilized the noncollinear

TeO_2 AOTF used in previous AOTF-based Raman microscopes (Treado *et al.*, 1992). However, the newer instrument utilized an APD, rather than a CCD, for rapid data acquisition. The compactness of both the AOTF and APD were particularly well-suited for portability. Excluding the laser source, the instrument measured 12" X 7". Using a 50-mW, 647.1-nm laser line from a krypton ion laser, a 650-3200 cm^{-1} Raman spectrum of neat benzene was acquired in 204 s. However, the observed resolution was only 50 cm^{-1}. A quartz collinear AOTF-based scanning Raman spectrometer was later reported for measurements of explosives (Gupta and Fell, 1997). Excluding the laser source and electronic controller unit, the instrument measured 10" x 4" x 1.5" (despite the use of a PMT) and weighed slightly less than 4 lb. A 50-500 mW, 514.5-nm line from an argon ion laser was used for the acquisition of 58-3600 cm^{-1} spectra with an improved (yet still moderate) resolution of 7.4 cm^{-1}. 20-ms detection times were used for each spectral point. Typical scan times were 6 min, including 10 accumulations for S/N enhancement.

Liquid crystal tunable filter (LCTF) devices. A possible alternative to the AOTF for wavelength selection with a no-moving-parts device is the compact LCTF. LCTFs are electronically tunable from the visible to IR region. As with the AOTF, the tuning response time of the LCTF can be on the order of milliseconds for both sequential spectral scanning and random access of desired bandpass wavelengths. Furthermore, bandpass widths of as small as 7.5 cm^{-1} (FWHM) are possible with LCTFs, making them comparable to a single-stage dispersive monochromator. Unfortunately, the throughput of LCTFs are typically 40% lower than those for AOTFs. Nevertheless, the spatial resolution offered by LCTFs is typically 2.5 times better than for AOTFs. making them better suited for imaging applications. A Fabry-Perot LCTF-based Raman microscope was first reported by Christensen *et al.* in 1995 (Christensen *et al.*, 1995). However,

the low resolution (25 cm^{-1}-bandpass, FWHM), low stray light rejection ($<10^3$), small acceptance angle and susceptibility to thermal-induced spectral bandpass drift were all factors that made it rather unsuitable for Raman imaging. Such characteristics are also nonconducive to the development of portable instrumentation.

The use of a Lyot-type LCTF (Lyot, 1933; Masterson et al., 1989) in a Raman microscope was described by Morris et al. in 1996 (Morris et al., 1996). The Lyot-type filter provided higher stray-light rejection, broader free spectral range, higher acceptance angle and more stable computer tunability (1.6 cm^{-1} increments with 0.38 cm^{-1} repeatability) than the previously-described Fabry-Perot LCTF-based Raman microscope. Furthermore, the device yielded nearly diffraction-limited spatial resolution. The microscope was designed for use with the 514.5-nm line of an argon ion laser. The spectral range of the instrument was -564 cm^{-1} to 4052 cm^{-1}, with a transmittance range of 6.7 to 16.3%. The detector was a slow-scan, thermoelectrically-cooled CCD. Used in conjunction with a 250-mW defocused laser beam, full-field image acquisition times of as high as five minutes were required. Using the same system, Raman spectra were generated with similar quality to that of a 0.5-m, 7 cm^{-1} bandpass monochromator. However, a 1-s integration time per scanned bandpass step was required.

CHAPTER 2

DEVELOPMENT OF SILVER-COATED MICROPARTICLE-BASED SUBSTRATES FOR SERS ANALYSIS

INTRODUCTION

The acceptance of SERS as a practical analytical tool requires the development of practical SERS substrates. Fabrication should be simple, inexpensive, and reproducible. Many approaches to SERS substrate developed have been taken in the past few decades. As a result, a wide variety of SERS substrates have been developed which range from liquid-based media, to gels and solids. The relative merits of several classes of SERS substrates developed thus far are described below.

Roughened metal electrodes were among the first SERS substrates to be investigated (Jeanmaire and Van Duyne, 1977; Albrecht and Creighton, 1977; Chang and Furtak, 1982; Pettinger *et al.*, 1980; Loo, 1983; Fleischman *et al.*, 1985). These media have been mainly used in laboratory settings. While they have proven very useful in fundamental studies, their acceptance as a practical technology (e.g.,. for use in field studies) has been limited to lack of stability and reproducibility.

Another type of medium where SERS enhancement can be observed is the colloidal solution. Reasons for using colloid sols include ease of production and straightforward characterization of sol solutions by UV-Vis absorption. Silver sols are generally

66

prepared via the reduction of $AgNO_3$ with ice-cold $NaBH_4$. The challenge is acquiring a suitable particle size for the SERS effect. Several procedures for silver sol preparation that will yield suitable particle sizes have been reported (Lee and Meisel, 1982; Silman et al. 1983). Silver colloids have been demonstrated to exhibit enhancements suitable for single molecule detection in recent years (Nie, 1997; Kneipp et al., 1997; Kneipp et al., 1998a). The use of colloidal gold clusters for extremely large SERS enhancement factors has also been reported (Kneipp et al., 1998b). A drawback of colloidal solutions is the tendency for colloids to agglomerate into clusters too large for suitable SERS enhancement. Nevertheless, it has been demonstrated that dilute polymers such as polyvinyl alcohol (PVA) can help stabilize colloidal solutions and extend their shelf life (Lee and Meisel, 1982). Colloids have also been prepared in gel matrices, yielding a relatively stable solid SERS substrate of isolated, nm-scale metal particles (Akbarian et al., 1995; Akbarian et al., 1996; Lee et al., 1997).

Silver-coated quartz posts have proven to be another effective SERS substrate (Liao, 1982; Buncick et al., 1984; Meier et al., 1985; Enlow et al., 1986; Vo-Dinh et al., 1986). The preparation of SiO_2 prolate posts is a multistep procedure that involves thermal deposition of an SiO_2 layer on top of a fused quartz layer, annealing of the crystalline quartz layer to the fused quartz layer, deposition of a 5-nm silver islands mask, and plasma etching of the deposited SiO_2 layer. The fused quartz layer etches much more slowly than the crystalline quartz layer, resulting in a microstructured substrate. The microstructured quartz surface is finally coated with an 80-nm silver layer. The resulting substrate has extremely uniform structures suitable for theoretical studies, but production is laborious and time consuming, and the substrate is fragile.

Another example of a solid surface-based substrate for SERS which is much easier to prepare is the silver island film (Jennings *et al.*, 1984; Berthold, 1987; Freeman *et al.*, 1995; Lacy *et al.*, 1996). In this case, a thin film (7.5-10 nm) of silver is thermally deposited onto a nonroughened dielectric plate such as glass. The sparse deposition of the silver promotes the formation of discontinuous "silver islands", which impart the roughness required for the SERS effect. This type of substrate exhibits competitive enhancement factors, is easy to make, is highly reproducible, and exhibits minimal background. However, these substrates are not sufficiently rugged for practical applications. They are also extremely vulnerable to air oxidation and thus manifest short shelf lives.

A unique approach to SERS substrate technology investigated in our laboratory has involved silver-coated microparticles. A general illustration of this class of substrate is demonstrated in Figure 2.1. Briefly stated, a layer of dielectric microparticles (0.5-5 µm diam.) is applied to a solid support such as glass, filter paper, cellulosic membrane or quartz (Goudonnet *et al.*, 1982; Vo-Dinh *et al.*, 1984; Moody *et al.*, 1987; Alak and Vo-Dinh, 1987, 1989). The microparticle layer is then coated with a 50-150 nm layer of silver by thermal evaporation. All parameters in substrate development, including particle size, particle density on the solid support, and silver thickness are easily controlled, making optimization relatively simple. Furthermore, the resulting optimized substrates are highly reproducible. Prior to the studies reported herein, microparticles used to provide the structure needed for the SERS effect have included polystyrene beads (Goudonnet *et al.*, 1982; Vo-Dinh *et al.*, 1984; Moody *et al.*, 1987; Alak and Vo-Dinh, 1987) and fumed silica particles (Alak and Vo-Dinh, 1989; Vo-Dinh *et al.*, 1988; Vo-Dinh *et al.*, 1989). These substrate have been applied to the detection

A) Microbody - Based Substrate

Induced Field

Surface Plasmon

Silver Layer (750 Å - 1500 Å)

Microbody Layer: (0.1 μm - 0.5 μm)

Materials:
1) Alumina,
2) Titanium Dioxide, or
3) Polystyrene Beads

Glass Support

Incident Laser Beam

B) Silver Islands Substrate

75 Å - 150 Å Silver

Glass Support

C) Filter Paper-Based Substrate

750 Å - 1500 Å Silver

Filter Paper
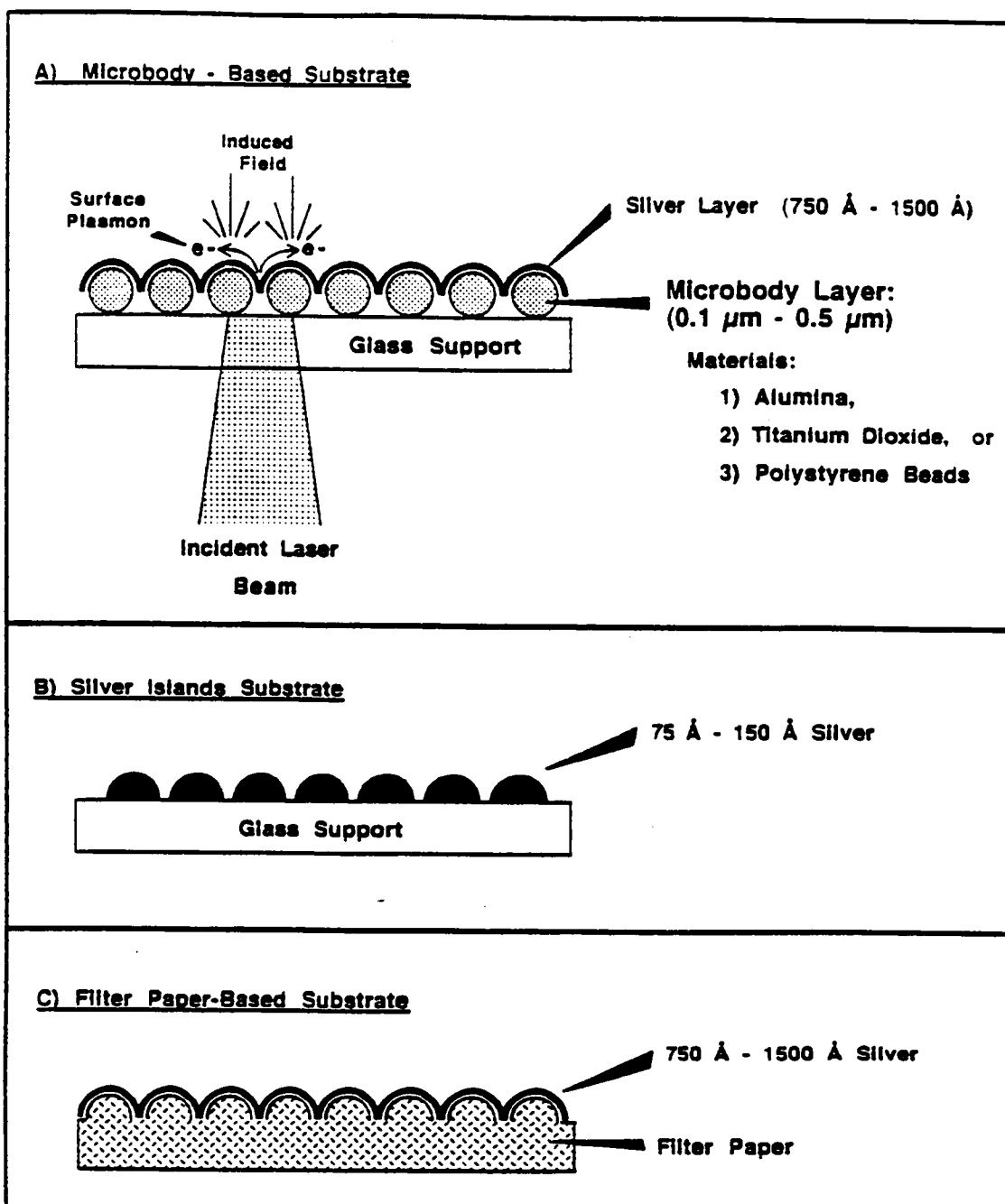
Figure 2.1. Examples of commonly used types of SERS substrate.

of environmentally-significant compounds including chlorinated pesticides (Alak and Vo-Dinh, 1988), organophosphorus compounds (Alak and Vo-Dinh, 1987) and polycyclic aromatic compounds (Vo-Dinh *et al.*, 1984).

The purpose of this chapter is to report the development of SERS substrates based on silver-coated particles of alumina and titanium dioxide (TiO$_2$). These substrates exhibit SERS enhancements competitive to previously developed microparticle-based substrates. In addition, they are cost effective, easy to prepare, and highly reproducible. In order to demonstrate the steps taken in the development of typical microparticle-based substrates, optimization of parameters is discussed in detail for the alumina-based substrate. These include particle size and silver thickness. It is noteworthy to mention that theoretical models have been derived for optimum Raman scatter enhancement with isolated concentric metallic spheres with dielectric cores (Kerker and Blatchford, 1982). Regardless of this fact, such models can not be applied to our substrate development because, in our case, the microparticles are tightly packed with a continuous silver overlayer. Optimization procedures are thus justified in the development of our microparticle-based substrates. Application of the substrates to the detection of both dry and liquid (*in situ*) samples of environmentally significant compounds is demonstrated. The potential for multicomponent analysis is demonstrated with structural isomers of phthalic acid. The application of the microparticle-based substrate technology to the selective determination of chemicals from complex media is also reported.

EXPERIMENTAL

Instrumentation

SERS measurements were conducted with a Spex Model 1403 double grating spectrometer equipped with a gallium-arsenide PMT (Burle Industries, Model C31034, Lancaster, PA) operated in the single-photon counting mode. Data storage and processing were handled with Spex Datamate DM3000 software. A schematic diagram of the auxiliary optical system is illustrated in <u>Figure 2.2</u>. Two excitation sources were used: the 514.5-nm line of an argon ion laser (Coherent, Model Innova 70, Palo Alto, CA) and the 647.1-nm line of a krypton ion laser (Coherent, Model Innova 70, Palo Alto, CA). Unless otherwise stated, the laser power was 50 mW. Appropriate bandpass filters with 5-10 nm bandpasses (FWHM) were used to reject unwanted plasma lines from the laser sources. The laser beams were focused onto the SERS substrates with a 1", f/2 lens. The scattered radiation was collected at 90° with respect to the excitation beam. A 1", f/1 lens was used to collect and collimate the scattered radiation, while an f/7 lens was used to focus the collimated beam onto the spectrometer entrance slit. The monochromator bandpass was 2 cm^{-1}. All spectra were acquired with 2 cm^{-1} increments and 0.4 s integration times.

Chemicals

Agglomerate-free alumina of various nominal particle diameters (0.05-, 0.1-, and 0.3-μm) was provided by Baikowski International Corporation (Charlotte, NC). TiO_2 (Titanox 1000) was provided by N. L. Chemicals (Highstown, NJ) and had a nominal
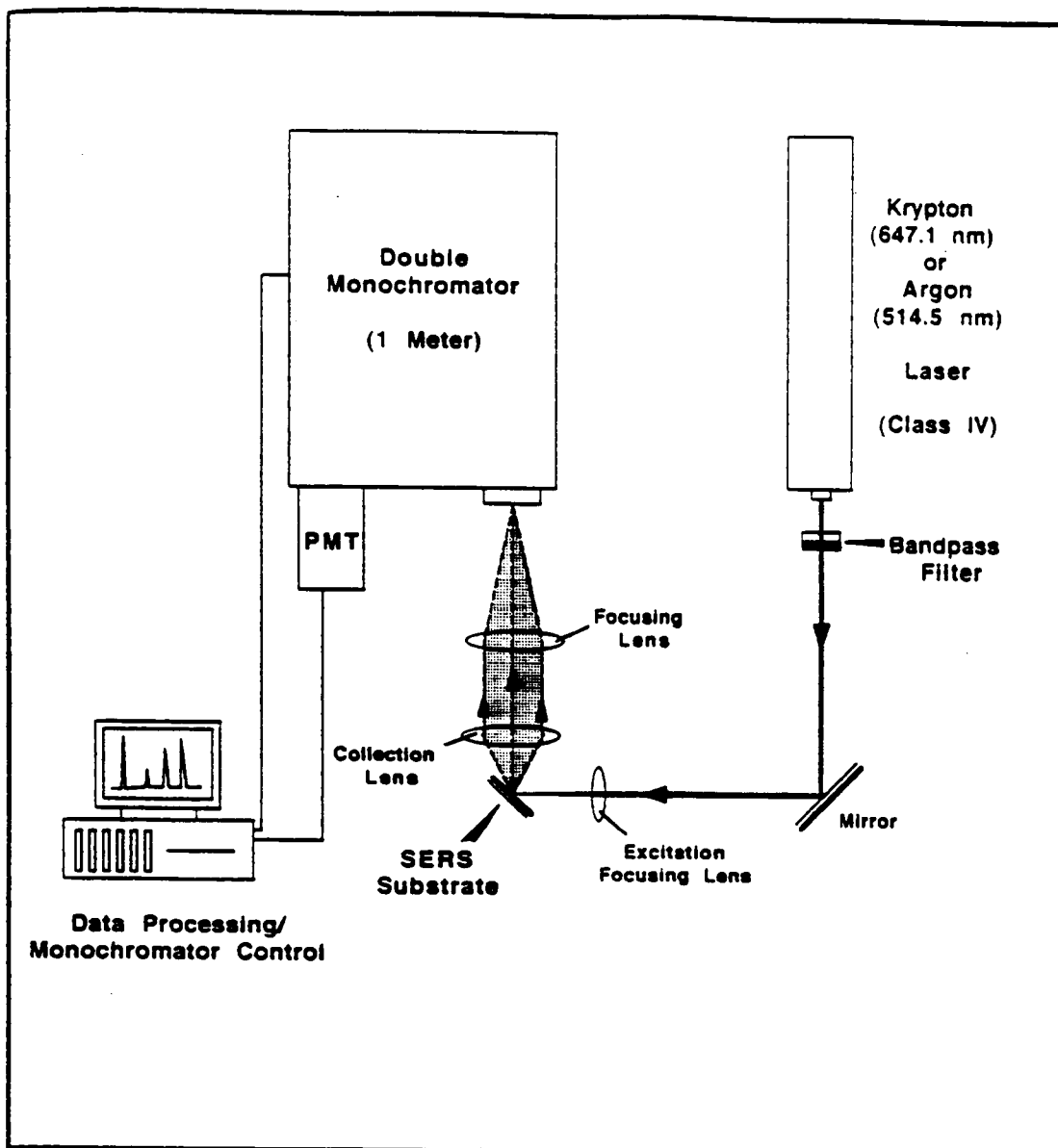
Figure 2.2. General research instrument for Raman scattering detection.

72

particle diameter of 0.2 µm. Benzoic acid (Aldrich, Milwaukee, WI), *p*-aminobenzoic acid (Aldrich), benzo(a)pyrene-tetrol (Midwest Research Institute, Kansas City, MO), pyrene (Aldrich), terephthalic acid (Pfaltz and Bauer, Waterbury, CT), phthalic acid (Aldrich), isophthalic acid (Pfaltz and Bauer), gallic acid (Eastman Kodak, Rochester, NY) were all used as received. Ferbam and Thiram were both obtained from the U. S. Environmental Protection Agency as EPA standards. The Presun-15 sunscreen lotion (Westwood pharmaceuticals) was also used as received. The 20-mesh silver used for coating the SERS substrates is manufactured by CERAC Incorporated (Milwaukee, WI) with 99.999% purity. Ethanolic samples were prepared with spectroscopic-grade ethanol (Warner-Graham Co., Cockeysville, MD) while aqueous samples and microparticle suspensions were prepared with HPLC (high-performance liquid chromatography)-grade water (Burdick and Jackson, Muskegon, MI).

SERS Substrate Preparation

Glass microscope slides were cut into rectangular strips, cleaned with 2 M nitric acid, rinsed with distilled water, and stored in ethanol. The rectangular strips, measuring 2.5 cm X 1.25 cm X 1 mm, were individually dried in a filtered air stream (calcium sulfate and charcoal cartridges) immediately prior to deposition of the microparticle layer. Three drops of aqueous suspensions of the alumina or TiO_2 microparticles were deposited onto the glass strips, which were then individually spun at 2000 rpm for 20 s with a spin-coating device for uniform spreading of the microparticles over the glass surface. The microparticle-coated slides were then mounted in a substrate holder and placed inside a vacuum evaporation system (Cooke, Model CV301, Norwalk, CT). The substrate holder was mounted at a 65° angle with respect to the silver source and rotated during the silver deposition process to ensure uniform coverage. Silver deposition was

performed at a pressure of 2 x 10^{-6} torr with a deposition rate of 1.5 - 2 Å/s. Both deposition rate and thickness was monitored with a microbalance (MaxTech, Model TM-100R, Torrance, CA)

Sample Preparation for SERS Measurement

Unless otherwise stated, SERS spectra were acquired from dry samples. A 1-µl aliquot of the analyte sample solution was deposited onto the SERS substrate surface and allowed to dry. For solution measurements, approximately 1 ml of analyte solution was pipetted into a standard fluorescence cuvette. Then the SERS substrate was inserted directly into the cuvette so that the long edges were supported by diagonal corners of the cuvette.

RESULTS AND DISCUSSION

Alumina-Based Substrate Studies

The alumina used in this study is widely used as a polishing powder, particularly for fiber optics, and is commercially available at a low cost. Powders are available in nominal particle sizes of 0.05, 0.1, 0.3, 1.0, and 3.0 µm diameter. In addition, the alumina powders are available in two forms: agglomerate-free and standard. The agglomerate-free alumina powders are calcined from a higher-purity alum to a purity of 99.99%, and the powders are further processed to break down the large agglomerates or aggregates. In this study, only agglomerate-free alumina powders were investigated for SERS substrate development.

It has been shown that for substrates such as polystyrene beads and fumed silica, several substrate parameters have considerable effect the observed SERS enhancement. Such parameters include particle size, particle density on the glass plate, and silver thickness. Since alumina was a new basis for substrate development, it was necessary to repeat substrate optimization studies. These studies were performed with benzoic acid as the model compound, with the intensity of 1012 cm^{-1} band being used as the reference for comparisons. We based this selection of the extensive data reported with this compound (Vo-Dinh *et al.*, 1984; 1986; Alak and Vo-Dinh, 1989).

Alumina particle size optimization. The first parameter investigated was the particle size which would yield the best enhancement. It has been reported that the optimum particle diameter distribution range for the SERS effect is 0.025-0.5 μm (Moody *et al.*, 1987). Using this report as a guide, alumina powders of 0.05-, 0.1-, and 0.3-μm diameters were selected for this study. A silver layer of 75 nm was used for each particle size in this study. Silver was used as the surface-coating material because previous results have shown that the highest Raman enhancements are obtained with this metal in the visible region (Otto, 1980). The thickness was also selected as a good starting point based on previous studies with particles of similar size (Goudonnet *et al.*, 1982; Vo-Dinh *et al.*, 1984; Moody *et al.*, 1987; Alak and Vo-Dinh, 1987; Alak and Vo-Dinh, 1989; Vo-Dinh *et al.*, 1988; Vo-Dinh *et al.*, 1989). The result of the investigation showed that the SERS intensities of benzoic acid adsorbed on the 0.05-μm and 0.30-μm particle-based substrates were approximately equal. On the other hand, a slightly larger signal was observed for the 0.1-μm particle-based substrate. The remaining studies were therefore performed with the 0.1-μm alumina particles. Nevertheless, it should be pointed out that the other powders did yield excellent Raman

enhancements and probably could also be used to develop a competitive SERS substrate as well.

Silver thickness optimization. Another parameter that has a significant effect on the Raman enhancement is the amount of silver deposited on the roughening agent. The thickness used to coat the 0.1-μm particles was varied between 25 nm and 150 nm. Figure 2.3 illustrates the SERS intensity of the 1012-cm^{-1} band of benzoic acid as a function of the silver thickness. Between 25 and 50 nm silver thickness, a very weak SERS intensity was observed, probably due to incomplete coverage of the alumina microbody layer, or a nonsuitable ratio of the metal layer thickness to the dielectric underlayer. A sharp increase in the SERS intensity was observed over the 50-75 nm range. Beyond 75 nm, the thickness of the silver layer was observed to be non critical for the range studied. It should be pointed out, however, that there should be a point at a thickness greater than 150 nm when the Raman enhancement will begin to decrease due to smoothing of the alumina layer by the silver coating. A 75-nm silver thickness was used in subsequent studies.

Particle density optimization. Yet another important parameter in substrate optimization is the grain of the surface. An easy way to optimize this parameter is by varying the concentration of the alumina suspension used to prepare the substrates. Thirteen suspensions of the 0.1-μm were prepared in the 1% to 25% (w/v) concentration range. Figure 2.4 illustrates that a significant increase in SERS signal from benzoic acid was observed for to 0-5% range. Furthermore, the enhancement was approximately constant for the 5-15% range. However, beyond 15% there was an apparent decrease in SERS signal. The less-than-optimal signal for substrates prepared with alumina suspensions of less than 5% concentration may have been due an
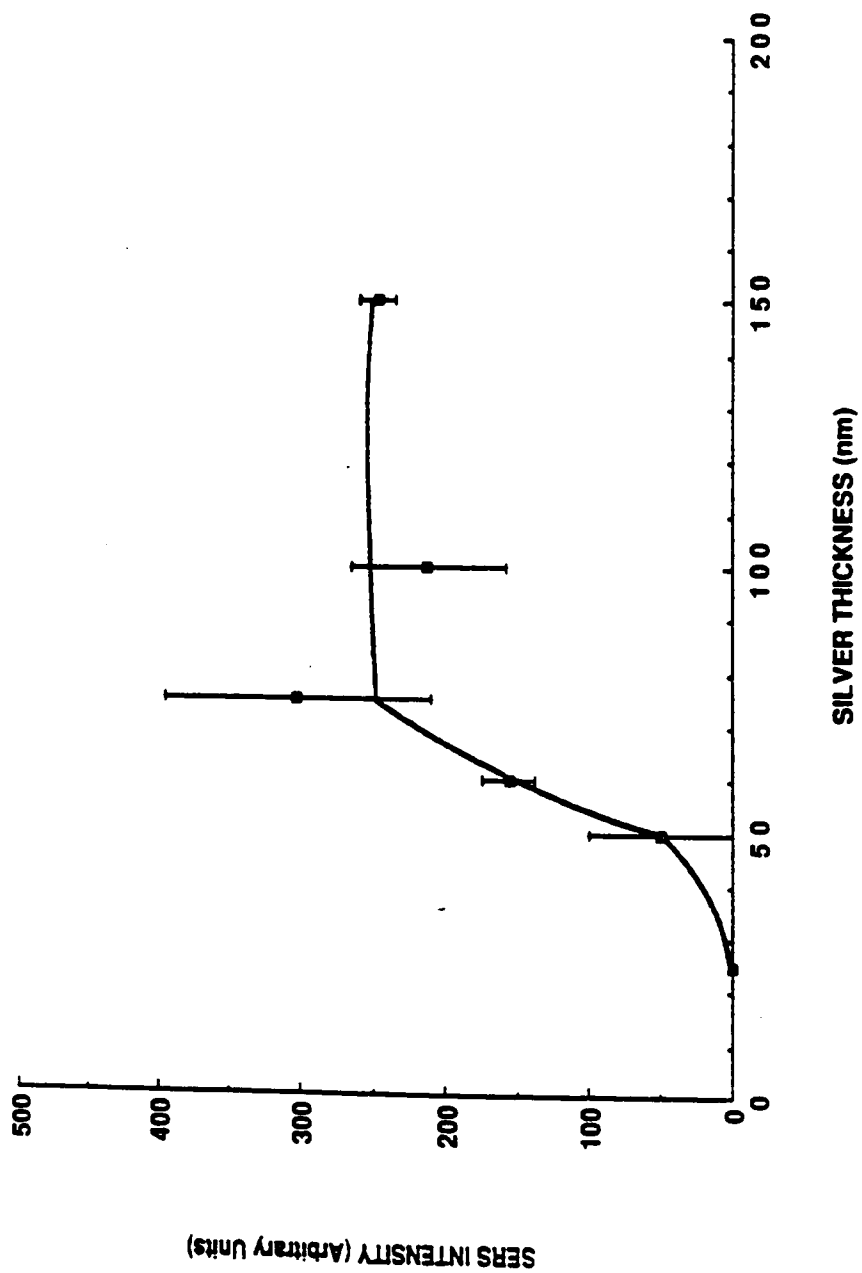
Figure 2.3. Intensity of the SERS signal from benzoic acid (1010 cm^{-1}) as a function of silver thickness used in alumina-based substrate production. Laser: Kr. 647.1 nm, 50 mW.

Source: J. M. Bello, D. L. Stokes, and T. Vo-Dinh, *Appl. Spectrosc.* **43**,1325 (1989).
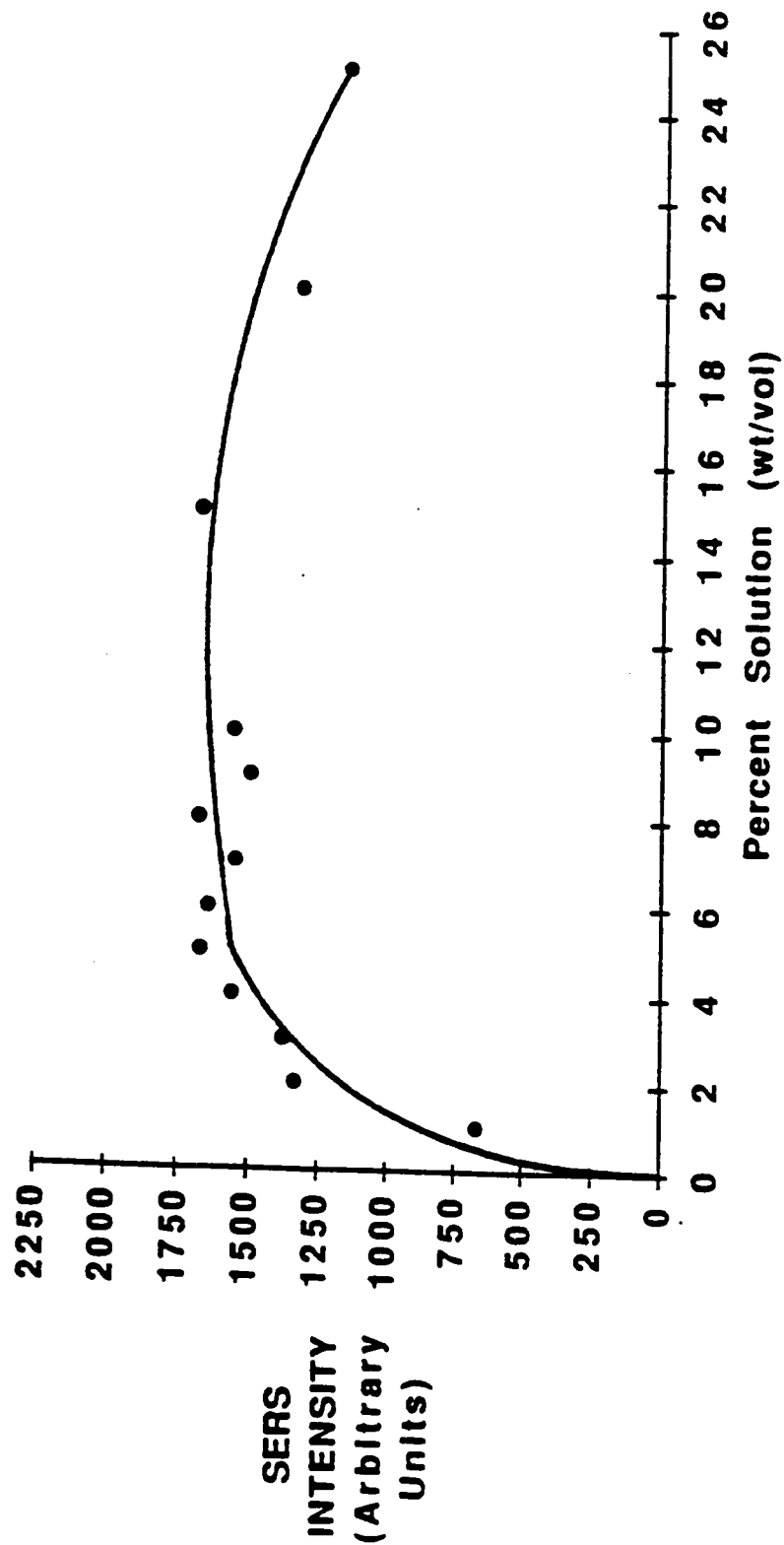
Figure 2.4. Intensity of the SERS signal from benzoic acid (1010 cm^{-1}) as a function of alumina suspension concentration used in substrate production. Laser: Kr. 647.1 nm, 50 mW.

Source: J. M. Bello, D. L. Stokes, and T. Vo-Dinh, *Appl. Spectrosc.* **43**,1325 (1989).

insufficient amount of alumina to provide a uniform layer of microparticles. On the other hand, the apparent decrease in SERS intensity for substrates prepared with alumina suspensions of greater than 15% concentration may have been due to formation of aggregates with dimensions too large for optimum enhancement (e.g., radiation damping). In order to further investigate these possible surface features, scanning electron microscope (SEM) photographs were acquired for substrates prepared with 1%, 10% and 25% alumina suspensions and are illustrated in Figure 2.5. Figures 2.5a and c show the substrate surface features of the substrates prepared with the 1% and 25% alumina suspensions, respectively. The SEM photograph for 1% alumina suspension substrate shows that only a small percentage of the glass support was covered with the 0.1-µm particles. The other extreme is illustrated by the 25% suspension substrate (Figure 2.5c). For this case, although the support was uniformly covered with the alumina particles, it is clear that aggregates were formed which were much larger than the ideal size for the SERS effect. Figure 2.5b illustrates the SEM for the 10% suspension substrate which yielded an optimum SERS signal. In this case, the glass support was uniformly covered by the alumina particles, but only a small percentage of the surface was covered by aggregates.

As a result of these optimization studies, alumina based substrates were prepared with the 5% suspension of 0.1-µm alumina particles and a silver thickness of 100 nm for all subsequent studies.

Investigation of excitation sources. Figure 2.6 illustrates SERS spectra of a 500-ng benzoic acid sample obtained with the optimized alumina-based SERS substrate and two different laser excitation lines. Figure 2.6a was obtained with the 514.5-nm line, while Figure 2.6b was obtained with the 647.1-nm line. With the 514.5-nm line,

79
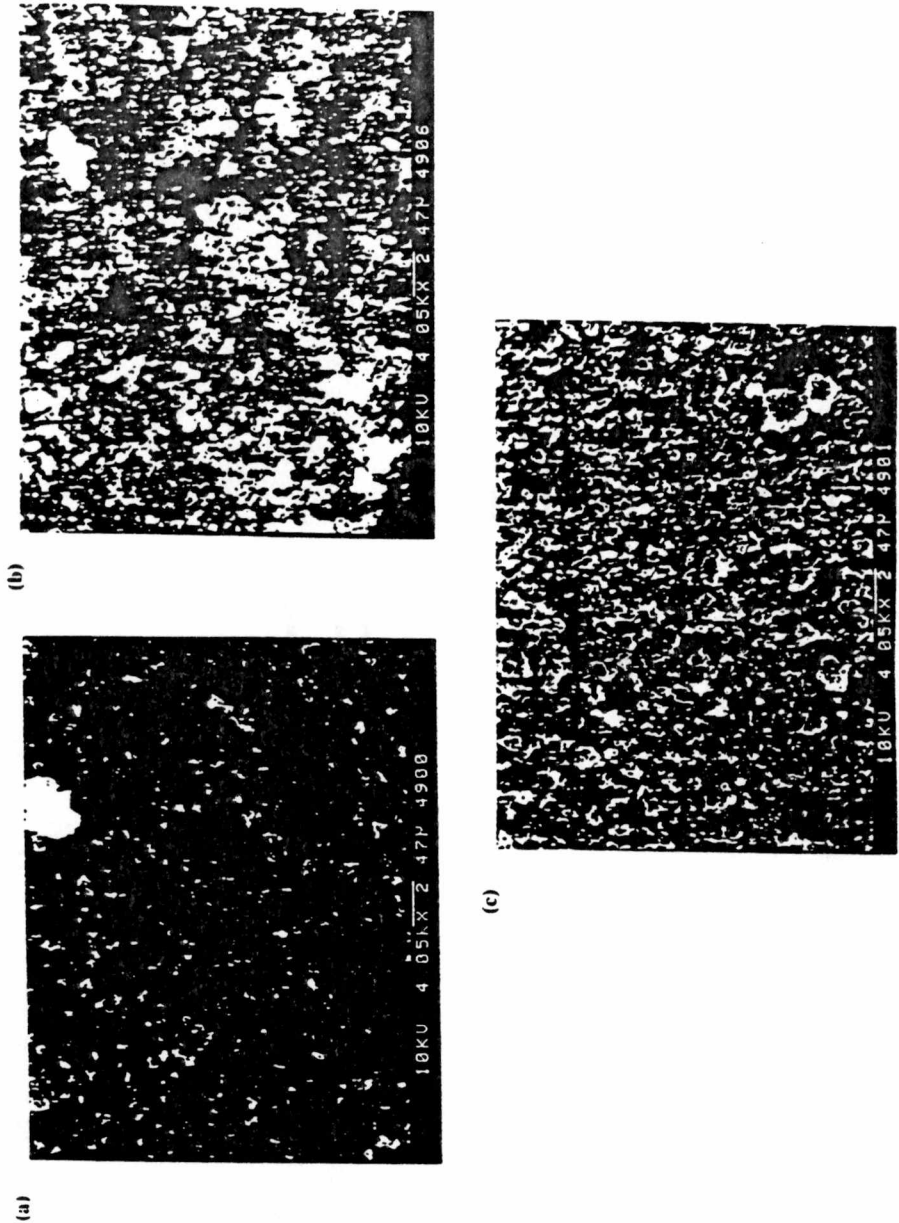
Figure 2.5. SEM photographs of SERS substrate surfaces prepared with a) 1%, b) 10%, and c) 25% alumina suspensions.

Source: J. M. Bello, D. L. Stokes, and T. Vo-Dinh, *Appl. Spectrosc.* **43**,1325 (1989).
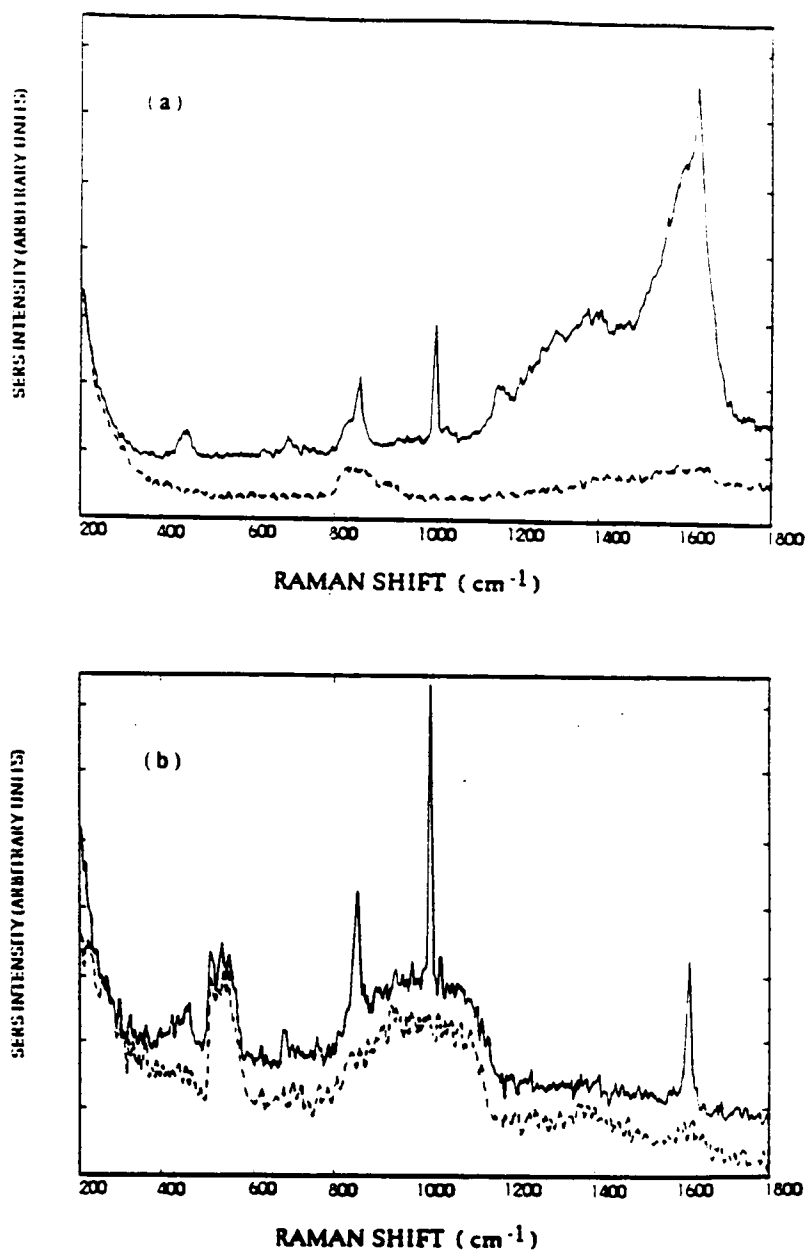
Figure 2.6. SERS spectra of a 500-ng sample of benzoic acid acquired with an optimized alumina-based substrate and with a) 514.5-nm, and b) 647.1-nm excitation radiation. Laser power = 50 mW.

Source: J. M. Bello, D. L. Stokes, and T. Vo-Dinh, *Appl. Spectrosc.* **43**,1325 (1989).

the SERS spectrum of benzoic acid revealed several bands consistent with those reported in the literature (Alak and Vo-Dinh, 1989; Pagannone et al., 1987). However, the presence of a broad band between 1200 and 1600 cm^{-1} was also observed with the 514.5-nm excitation, which could have obscured any analyte bands in this range. For example, it was observed that the 1608 cm^{-1}-band of benzoic acid was partially obscured, yet it is also shown in Figure 2.6a that the alumina-based substrate blank did not exhibit any background between 1200 and 1600 cm^{-1}. The only apparent background from the substrate was a weak broad band between 800 and 900 cm^{-1}. The broad bands centered at 1356 and 1578 cm^{-1} and in the 1200-1600 cm^{-1} region of the benzoic acid SERS spectrum were therefore most likely due to Raman scattering from a graphitic carbon layer created by the laser decomposition of a benzoic acid monolayer (Tsang et al., 1980; Otto, 1978). One way to avoid or minimize graphitization is to use a lower energy excitation line (longer wavelength). Figure 2.6b illustrates the SERS spectrum of benzoic acid obtained with 647.1-nm excitation. As shown by the figure, the broad bands assumed to be due to graphitic carbon were eliminated, and the 1608 cm^{-1} band of benzoic acid was fully visible without any interference. However, a problem associated with the use of the 647.1-nm line is that the alumina-based substrate yields some minor background emissions at 500-600 cm^{-1} and 800-1200 cm^{-1}, as demonstrated by the figure. Nevertheless, these background features did not appear to seriously obscure the SERS bands of benzoic acid, as was evidenced by the presence of well-resolved analyte SERS bands at 846, 1010, and 1032 cm^{-1}.

Another example of the elimination of the graphitic carbon band by using the 647.1-nm excitation line is illustrated by Figure 2.7. Figures 2.7a and b illustrate the SERS spectra of a 500-ng sample of terephthalic acid (TPA) obtained with the 514.5-nm and 647.1-nm lines, respectively. As shown by Figure 2.7a, the Raman bands due to
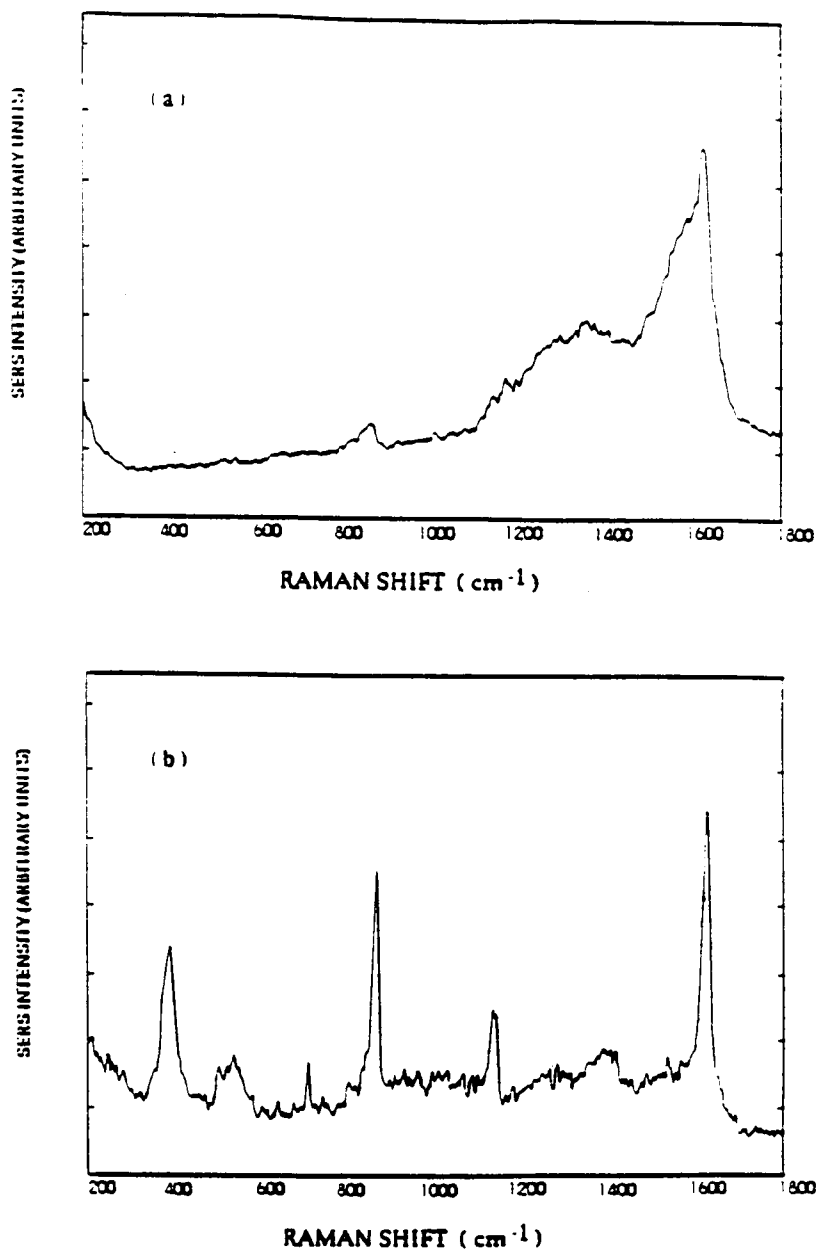
Figure 2.7. SERS spectra of a 500-ng sample of TPA acquired with an optimized alumina-based substrate and with a) 514.5-nm, and b)647.1-nm excitation radiation. Laser power = 50 mW.

Source: J. M. Bello, D. L. Stokes, and T. Vo-Dinh, *Appl. Spectrosc.* **43**,1325 (1989).

graphitic carbon totally obscured the SERS bands from the TPA molecule. The only discernible bands for the 514.5-nm excitation were those at 864 and 1614 cm^{-1}. On the other hand, <u>Figure 2.7b</u> illustrates the elimination of the graphitic carbon bands, resulting in the appearance of the well-resolved bands of the TPA molecules when using the 647.1-nm excitation line.

Analytical figures of merit for the optimized alumina-based substrate. Benzoic acid (500 ng) samples were used to evaluate the reproducibility of the new alumina-based SERS substrate. The excitation line was 647.1 nm. For five identically-prepared substrates, the relative standard deviation of the 1010-cm^{-1} benzoic acid band intensity was approximately 15%. As a demonstration of intra-plate reproducibility, <u>Figure 2.8</u> illustrates the SERS signal profile of a 500 ng spot sample of *p*-aminobenzoic acid (PABA). The profile was obtained by translating the SERS substrate through a 647.1-nm excitation beam and recording the intensity of the 1132 cm^{-1} band as a function of time. The linear dynamic range for the detection of benzoic acid spanned approximately two orders of magnitude, which is typical for surface emission methods. Finally, the limits of detection (LODs) for several compounds obtained with the optimized alumina-based substrate are listed in <u>Table 2.1</u>. The LODs were based on the strongest SERS band of each compound, assuming a minimum detectable signal level to be 3 times the standard deviation of the noise. As demonstrated by the table, LODs yielded by the alumina-based substrate ranged from 2 pg for pyrene to 17 ng for benzoic acid. It is noteworthy that these LODs correspond to total mass distributed on the substrate. The actual detected amount, as determined by the illuminated area of the substrate surface, is much lower. For example, assuming the laser spot and total sample spot sizes to be approximately 100 μm and 10000 μm, respectively, an estimation of the actual detected mass is also included in the table.
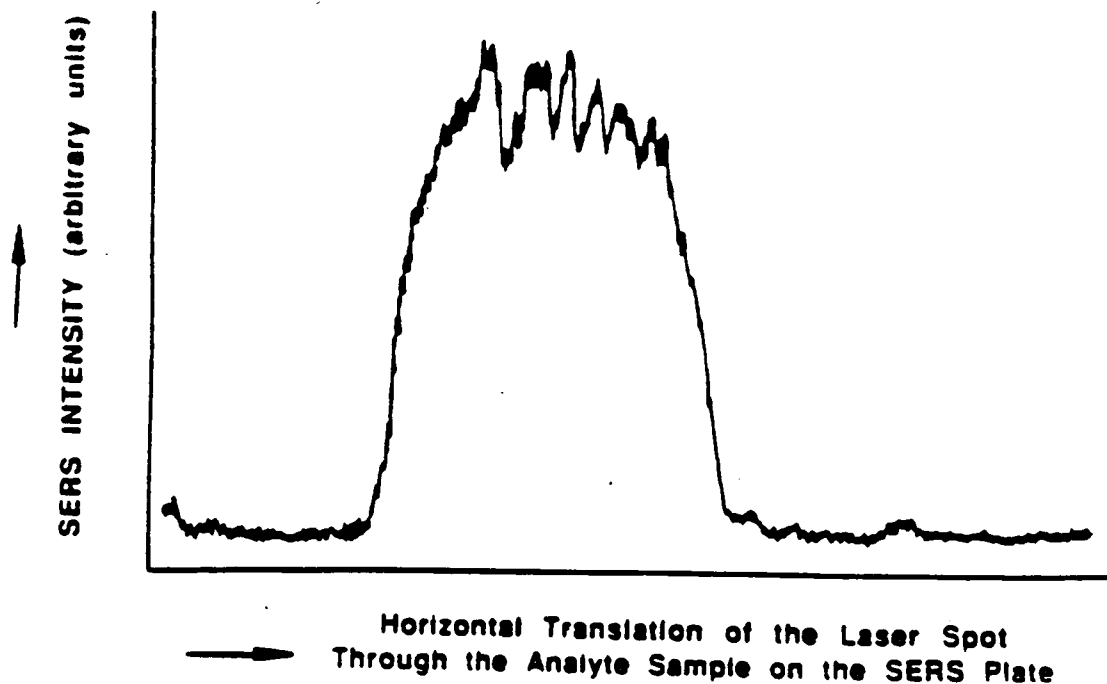
Figure 2.8. SERS signal profile of a 500-ng spot of PABA observed with an optimized alumina-based substrate. Laser: Kr. 647.1 nm, 50 mW; PABA signal at 1464 cm^{-1}.

Source: V. A. Narayanan, J. M. Bello, D. L. Stokes, and T. Vo-Dinh, *Analusis* **19**, 307 (1991).

Table 2.1. LODs of various compounds obtained with alumna-based SERS substrates

Compound	LOD, ng[a] (per delivered sample)	Estimated LOD, pg (per laser spot area)
PABA	1 7	1.7
Benzoic acid	1 7	1.7
Benzo(*a*)pyrene-tetrol	8.0	0.8
Formothion	1 1	1.1
Pyrene	0.0020	0.00020
TPA	1 5	1.5

[a]Relative standard deviation ≈10%

Source: J. M. Bello, D. L. Stokes, and T. Vo-Dinh, *Appl. Spectrosc.* **43**,1325 (1989).

TiO$_2$-Based Substrate Studies

As with the development of the alumina-based studies, the motivation behind the TiO$_2$-based substrate studies was to further demonstrate the development of easily-fabricated, highly-reproducible and inexpensive substrates utilizing the dielectric microparticle approach to surface roughening. As with the alumina studies, several parameters needed to be optimized. However, only a 0.2-µm diameter TiO$_2$ particle size was used in these studies because it was the only size available within the optimum range (0.025-0.5 µm) as defined by previous microparticle-based substrate studies (Moody *et al.*, 1987). In order to illustrate the feasibility of applying the microparticle-based SERS substrate technology to *in situ* studies, all optimization studies were performed with the TiO$_2$-based substrates submerged in analyte solutions. A 50-mW, 514.5 nm excitation line was used for all TiO$_2$-based substrate studies.

Silver thickness optimization. With terephthalic acid (TPA) used as the model compound, the silver thickness needed to coat the 0.2-µm TiO$_2$ particle layer for optimum Raman enhancement was investigated. The determinations of all optimum substrate parameters were performed *in situ* using a 500-ppb solution of the TPA in ethanol. The 1618 cm^{-1} SERS band of the TPA was used as the reference signal for all comparisons. TiO$_2$-based substrates with three different silver coating thicknesses were prepared and used for comparative measurements. The relative SERS intensities of TPA on substrates having silver thicknesses of 25, 125, and 150 nm were determined to be 1.0, 1.1, and 1.1, respectively. Surprisingly, the effect of silver thickness was much less dramatic than observed in the alumina-based substrate studies. All

subsequent TiO_2-based substrate studies were performed with a 120-nm silver thickness.

Particle density optimization. As with the alumina-based substrate optimization studies, the surface coverage of the glass surface by TiO_2 particles was investigated by varying the concentration of the particle suspension used to prepare the substrates. The silver thickness was kept at 120 nm. <u>Table 2.2</u> lists the relative intensities of the 1618 cm^{-1} TPA band obtained from substrates prepared with TiO_2 suspension concentrations of 5%-25% (w/v). TiO_2 suspensions greater than 25% were very viscous and therefore did not spread uniformly on the glass surface during the spin coating process. Suspensions of greater than 25% TiO_2 were therefore not used in these studies. <u>Table 2.2</u> shows that an increase in the SERS intensity of the model compound was observed between the 5% and 20% suspension concentrations. The most intense Raman enhancements were observed for substrates produced with 20% and 25% TiO_2 suspensions.

As a result of these optimization studies, all subsequent TiO_2-based SERS substrates were prepared with 20% suspensions and 120 nm silver coatings.

In situ vs. dry-state sample studies. It was demonstrated with the alumina-based substrate studies that the energy of a 514.5-nm laser beam can produce intense, broad graphitic carbon bands which can severely obscure Raman spectra. It was also demonstrated that this effect can be minimized by using a lower-energy excitation source, such as the 647.1-nm line of a krypton ion laser. In these TiO_2-based substrate studies, it was observed that the graphitization effect was minimized for *in situ*

Table 2.2 *In situ* SERS intensities of a 500 ppb TPA solution in ethanol as a function of TiO_2 suspension concentration used in SERS substrate production

% TiO_2	Relative Intensity[a]	% TiO_2	Relative Intensity[a]
5	1.0	20	3.3
10	2.0	25	2.8
15	2.4		

[a]Results of two determinations.

Source: J. M. Bello, D. L. Stokes, and T. Vo-Dinh, *Anal. Chem.* **61**, 1779 (1989).

measurements relative to dry-state measurements even when using the 514.5-nm excitation source. Figure 2.9a shows the *in situ* spectrum of a 500 ppb ethanol solution of TPA obtained with the TiO_2-based SERS substrate and 514.5 nm excitation. As illustrated, the SERS spectrum of TPA included five sharp bands, with the strongest band at 1618 cm^{-1}. The bands observed at 1618, 1142, 868, and 400 cm^{-1} correspond to A_g mode vibrations of TPA (Boerio and Roth, 1987). On the other hand, the band at 1406 cm^{-1} corresponds to a symmetric OCO stretch (Pagannone *et al.*, 1987). It is also noteworthy that the characteristic CO stretching vibration band at $\approx$1650 cm^{-1} was noticeably absent in the solution spectrum of TPA (Figure 2.9a). This observation demonstrates that the carboxylate form of TPA was adsorbed to the metal surface (Pagannone *et al.*, 1987). In addition, the spectrum for the *in situ* measurement of TPA was very similar to that described in the literature for terephthalate ion adsorbed on metal surfaces (Boerio and Roth, 1987).

Figure 2.9b shows the dry-state SERS spectrum of a 500-ng TPA sample spotted on the TiO_2-based substrate. It is evident that from the figure that the carbon layer Raman scattering was present in the dry-state measurement, thus obscuring some of the TPA bands (1142 and 1406 cm^{-1}) otherwise observed with the *in situ* measurement. For the *in situ* measurement, by contrast, the broad amorphous carbon Raman bands centered at 1336 and 1587 cm^{-1} were noticeably absent. The *in situ* spectra of other compounds that were investigated, such as isophthalic acid (8 ppm) and phthalic acid (8 ppm), respectively shown in parts a and b of Figure 2.10, also did not exhibit the amorphous carbon Raman bands. The characteristic SERS bands of isophthalic and phthalic acid in the 1300-1600 cm^{-1} region were clearly visible in these solution measurements. Several factors may have accounted for the absence of the amorphous carbon bands with *in situ* measurements. One explanation is that any surface heating
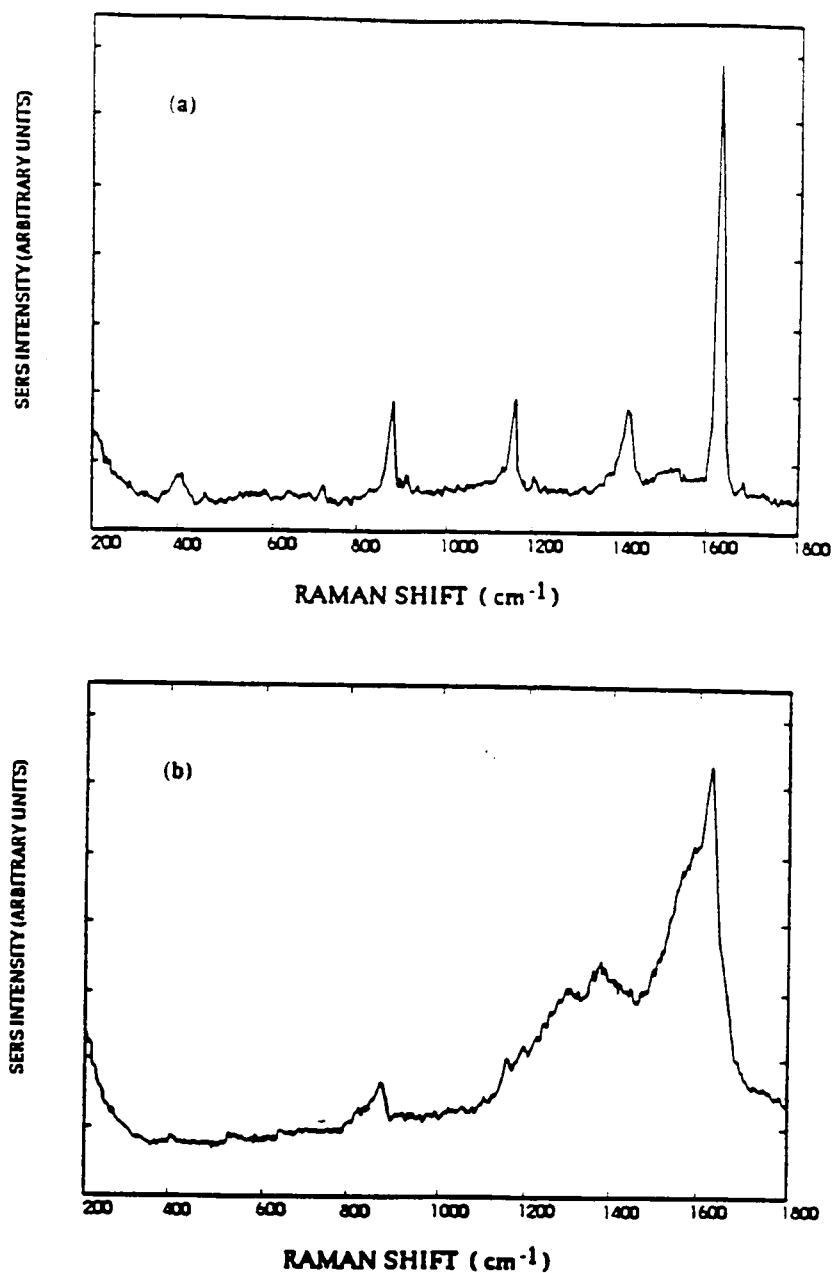
Figure 2.9. SERS spectra of a) solution (500 ppb), and b) dry-state (500 ng) samples of TPA acquired with TiO_2-based substrates and 514.5-nm excitation radiation. Laser power = 50 mW.

Source: J. M. Bello, D. L. Stokes, and T. Vo-Dinh, *Anal. Chem.* **61**, 1779 (1989).
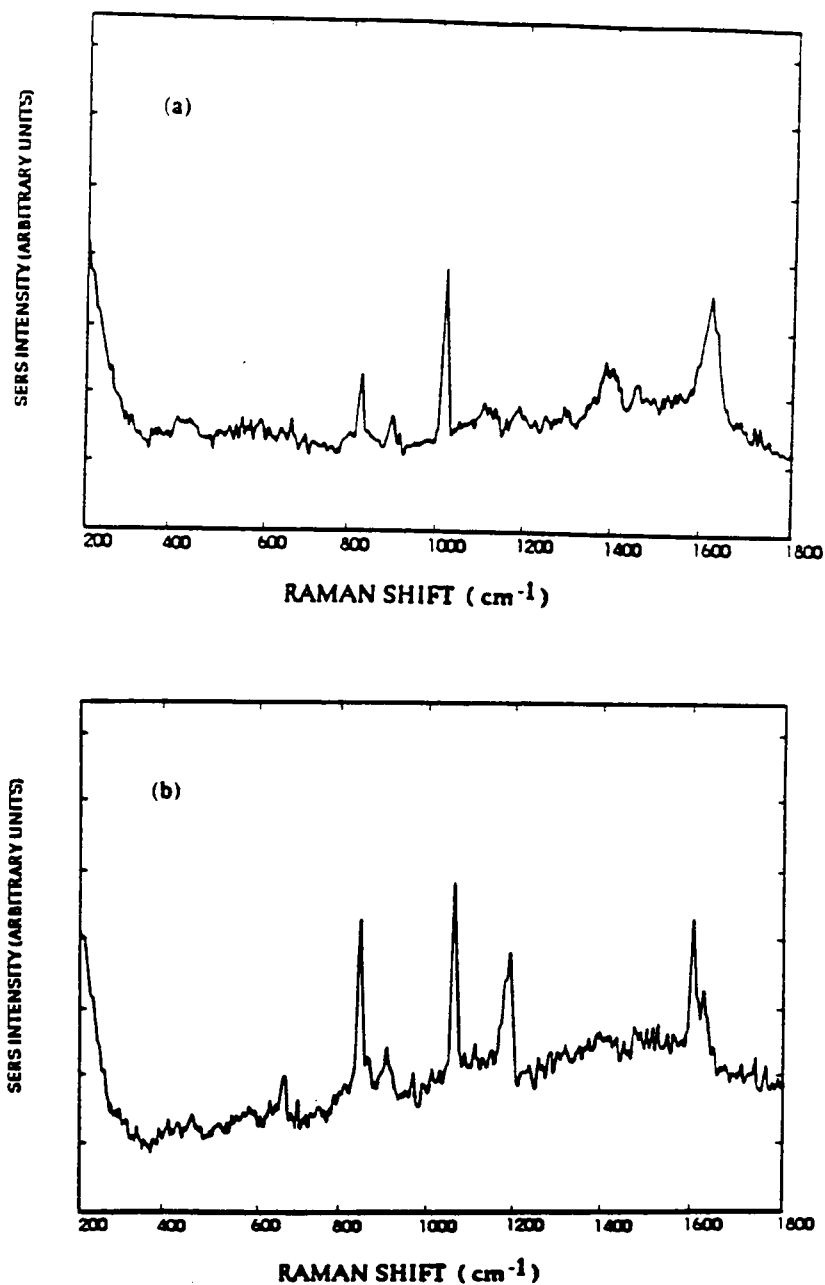
Figure 2.10. *In situ* SERS spectra of solution samples of a) isophthalic acid (8 ppm) and b) phthalic acid (8 ppm) acquired with TiO_2-based substrates and 514.5-nm excitation radiation. Laser power = 50 mW.

Source: J. M. Bello, D. L. Stokes, and T. Vo-Dinh, *Anal. Chem.* **61**, 1779 (1989).

that may have been caused by the incident laser beam could have been dissipated immediately since the substrate was in contact with the liquid medium, which served as an effective heat sink. Alternatively, if any photodecomposition of the TPA sample occurred at the substrate, the decomposed TPA molecules could have diffused into the sample while being replaced by unaltered TPA molecules from the bulk solution.

Investigation of the back-side excitation/collection geometry for *in situ* measurements. An aspect of *in situ* SERS analysis that has a major effect on signal intensity is the geometry of the substrate with respect to the laser beam. Figure 2.11 shows the geometry that was used with the a) *in situ*, and b) dry-state SERS measurements. It was found that directing the laser beam onto the back side of the substrate and collecting the scattered radiation also from the back side of the substrate (Figure 2.11a) increased the SERS intensity observed from solution samples by approximately 11 times. This is an interesting result because dry-state measurements are usually performed by focusing the laser beam onto the silver-coated side of the substrate (Figure 2.11b). Nevertheless, the observation is consistent with those of Jennings *et al.*, who reported that the SERS intensity for copper and zinc phthalocyanine complexes adsorbed on silver-island films was greater if a back-side geometry was used (Jennings *et al.*, 1984). They attributed this effect to the discontinuous nature of the silver film, whereby excitation from the back side of the substrate results in the observed scattering being mainly due to molecules forming the first monolayer of the analyte. Although a 120-nm continuous layer of silver was used in our work, our results suggest that the laser beam was able to penetrate both the TiO_2 and silver layers, and that the Raman radiation could have likewise been transmitted back through these layers. However, it should be emphasized that further studies are still needed to explain

93
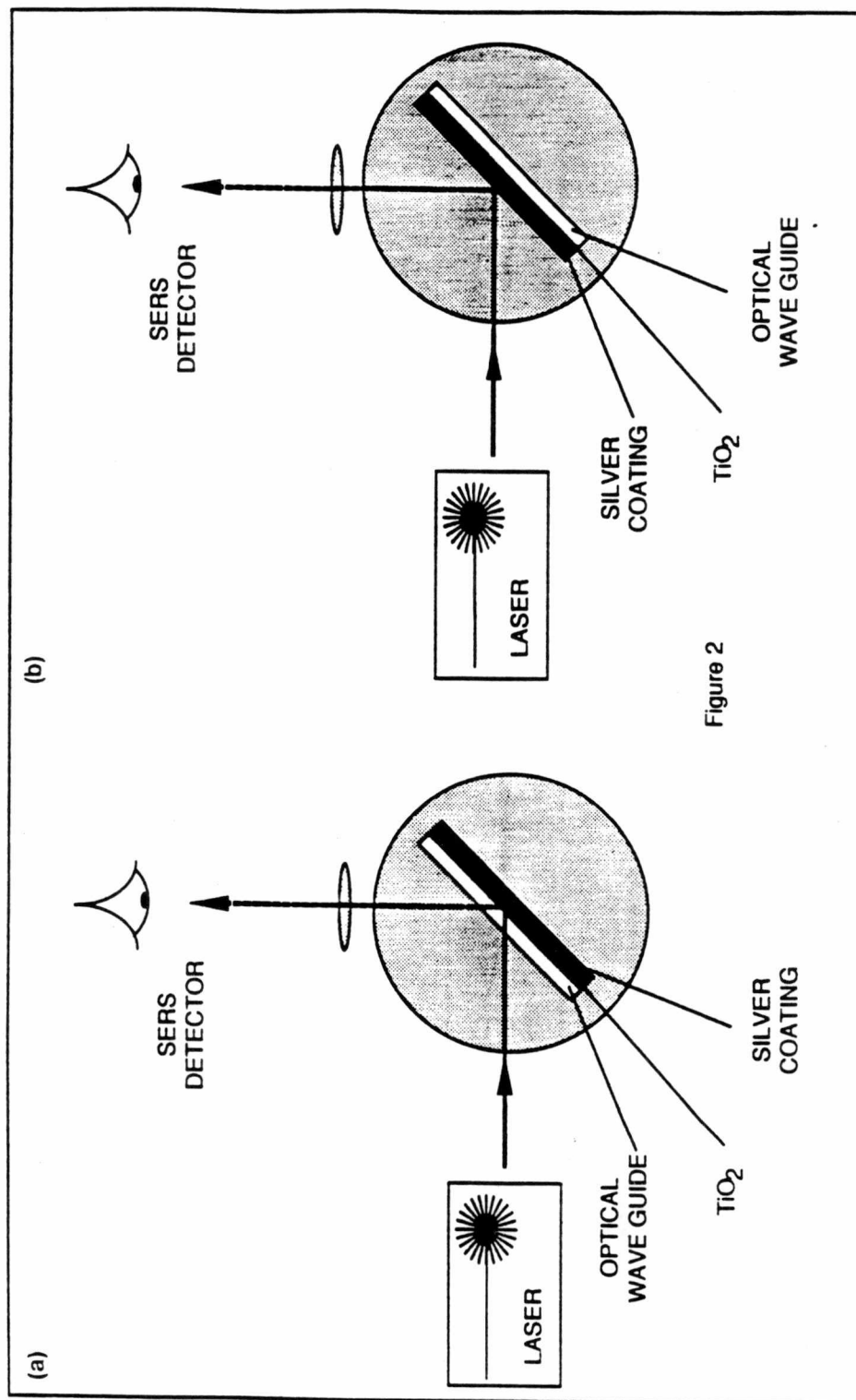
Figure 2.11. Illustrations of the a)backside excitation/collection, and b) frontside excitation/collection geometries implemented for SERS detection with planar SERS substrates.

Source: J. M. Bello, D. L. Stokes, and T. Vo-Dinh, *Anal. Chem.* **61**, 1779 (1989).

94

this back-side enhancement effect. The excitation of the molecules forming the first monolayer may be only one of several contributing factors to the enhancement.

Excitation laser power study. The effect of the excitation laser intensity on the observed Raman enhancement yielded by the optimized TiO_2-based was also investigated. Figure 2.12 shows a plot of the SERS intensity of TPA, measured *in situ*, as a function of laser power. A linear increase in the SERS signal was observed for the 0-50 mW range. At intensities higher than 50 mW, SERS signal intensities increased less dramatically and appeared to level off. The leveling off of signal for laser powers greater than 50 mW was most likely due to thermal decomposition of the molecules at rates too rapid to be compensated for by replacement with unaltered molecules from the bulk solution. It is also noteworthy that analytically useful signals were observed for the TPA sample with laser powers of as low as 5 mW. This is an important aspect of this technique for practical applications because of the possibility of using low-power, compact, and inexpensive lasers for field applications.

Response time and stability of the *in situ* SERS intensity. Response time and stability of the SERS signal are two important analytical parameters involved with *in situ* studies. Figure 2.13a illustrates the rate at which adsorption of TPA molecules on the TiO_2-based substrate comes to equilibrium for a 500 ppb bulk solution concentration. The procedure used to obtain the data illustrated in the figure involved first exposing the sample solution containing the SERS-active substrate to the laser beam (50 mW) for 1 min prior to each measurement, and then blocking the laser beam after each measurement to minimize photodecomposition of the TPA molecules between measurements. The abscissa of Figure 2.13a represents the time elapsed from initial submersion of the substrate in the sample solution. As demonstrated by the figure, the

95
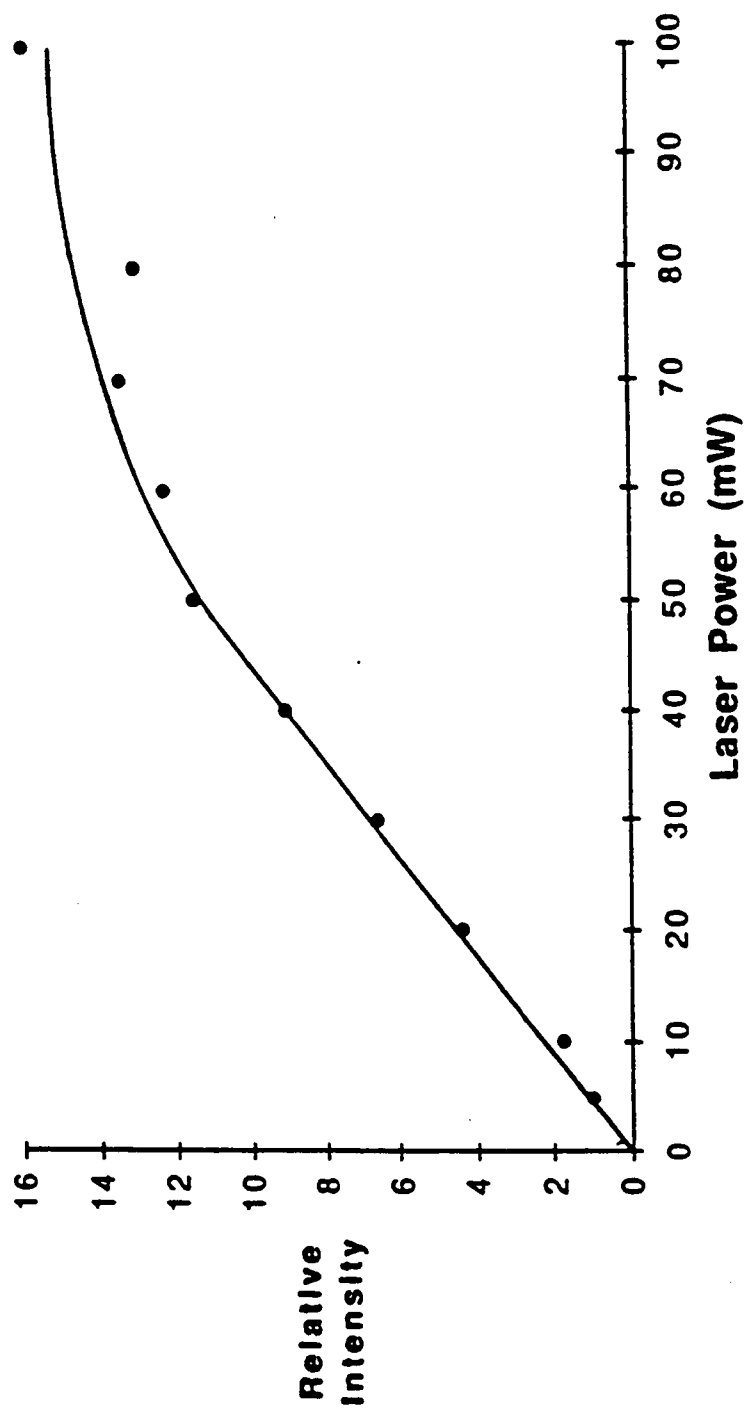
Figure 2.12. SERS intensity plot for the 1618-cm^{-1} band of TPA observed as a function of excitation radiation intensity. TiO$_2$-based substrates. Laser: Ar, 514.5.

Source: J. M. Bello, D. L. Stokes, and T. Vo-Dinh, *Anal. Chem.* **61**, 1779 (1989).
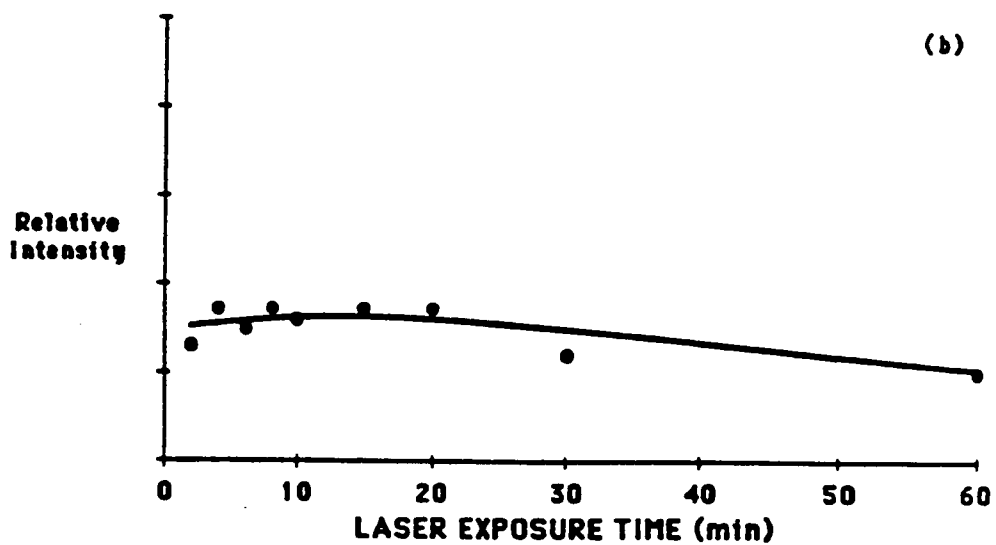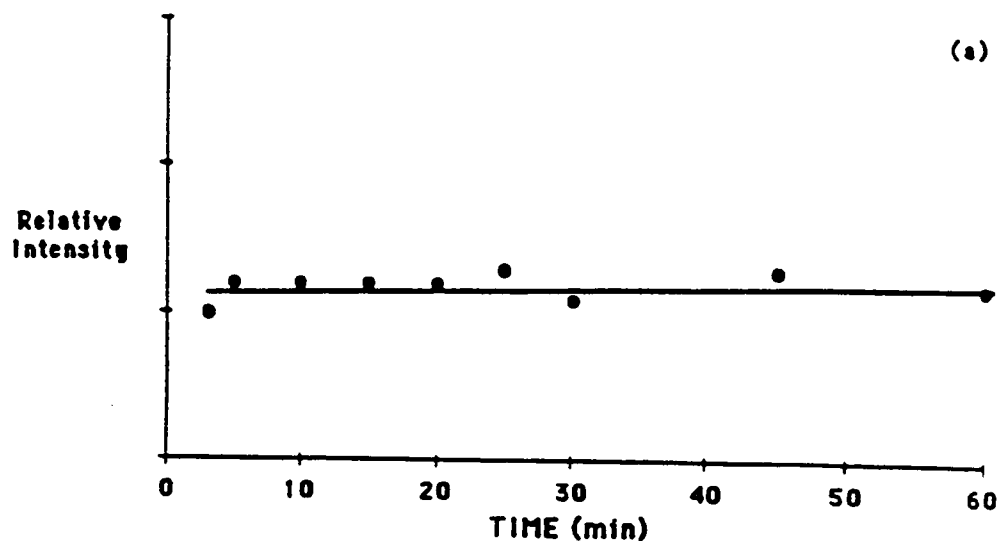
Figure 2.13. SERS intensity plots for the 1618-cm^{-1} band of TPA (500 ppb) illustrating a) response time, and b) sample stability for *in situ* measurements with a TiO_2-based substrate and 50-mW, 514.5-nm excitation radiation.

Source: J. M. Bello, D. L. Stokes, and T. Vo-Dinh, *Anal. Chem.* **61**, 1779 (1989).

97

SERS intensity of TPA was stable throughout the 1-hr experiment. This observation indicates that the rate of equilibrium for adsorption of TPA molecules from the bulk solution onto the metal surface of the SERS substrate was very rapid, since the maximum signal was reached in less than 3 min. Therefore, the analyst needs to wait for only a few minutes prior to data acquisition in order to obtain optimal and stable signal when using this technique.

Figure 2.13b illustrates the photo-stability of the SERS intensity of TPA (500 ppb) in ethanol. To obtain the data in this figure, sample exposure to the 50-mW laser beam and data acquisition was initiated at 10 min after initial submersion of the TiO_2-based substrate in the sample solution. According to the previous equilibrium study, this time interval was more than adequate to allow equilibration of TPA molecules between the bulk solution and the metal surface. It can be seen in Figure 2.13b that the SERS intensity of TPA was stable between 2- and 20-min laser exposures. The signal dropped off only slightly thereafter. This result indicates that TPA molecules were not thermally degraded by the 50-mW laser beam with time, or that any photodegradation was offset by displacement of photodecomposed molecules by unaltered molecules from the bulk solution. Nevertheless, it should be noted that these response times may be compound-dependent.

Analytical figures of merit for the optimized TiO_2-based SERS substrate. Reproducibility of the new TiO_2-based SERS substrate was evaluated *in situ* with a 500 ppb solution of TPA in ethanol. The 1618 cm^{-1} band intensity was measured for 10 different substrates. The resulting relative standard deviation was 10%. Table 2.3 lists *in situ* SERS LODs of five carboxyl aromatic compounds in ethanol obtained with the TiO_2-based substrate. LODs were determined using the most intense spectral features of

Table 2.3. LODs of various carboxyl aromatic compounds obtained from *In Situ* ethanolic solution measurements with TiO_2-based SERS substrates

Compound	LOD[a], ppb	LOD[a], M
PABA	130	9.5×10^{-7}
Isophthalic acid	1000	6.1×10^{-6}
Phthalic acid	980	6.0×10^{-6}
Gallic acid	930	4.1×10^{-6}
TPA	17	1.0×10^{-7}

[a]Relative standard deviation $\approx 10\%$

Source: J. M. Bello, D. L. Stokes, and T. Vo-Dinh, *Anal. Chem.* **61**, 1779 (1989).

each analyte. The results demonstrate excellent detectivity with LODs spanning the low parts-per-billion to low parts-per-million range. The wide range of LODs is most likely due to varying degrees of adsorption to the SERS substrate for the different compounds.

Applications of Microparticle-Based Solid SERS Substrates

Direct characterization of structural isomers in mixtures. Because vibrational spectra provide abundant information on the structure of molecules, SERS could be an excellent tool for the characterization and identification of structurally similar compounds. Furthermore, the sharpness of the spectral features associated with Raman scattering may allow analyses of multicomponent samples due to the likely minimal overlap of bands characteristic of the individual components. In spite of these advantages, the SERS technique has not been widely used for mixture analysis. In this study, *in situ* measurements of ternary synthetic mixtures of phthalic acid isomers were performed using the alumina-based SERS substrate described above. Without prior separation of the three isomers into individual components, it would be very difficult to identify and quantify these isomers in a mixture by using other spectroscopic techniques such as luminescence or UV-Vis absorption.

Figures 2.14a,b, and c illustrate the individual spectra of terephthalic acid (0.5 ppm), phthalic acid (2 ppm), and isophthalic acid (1 ppm), respectively. The spectra were acquired *in situ* using an 80-mW, 647.1-nm laser beam. The SERS spectra of the three isomers are very similar to the conventional Raman spectra of the ionic forms of these acids described in the literature (Boerio and Roth, 1987). As with the TiO_2-based SERS substrate *in situ* studies discussed above, this observation indicates that the carboxylate

100
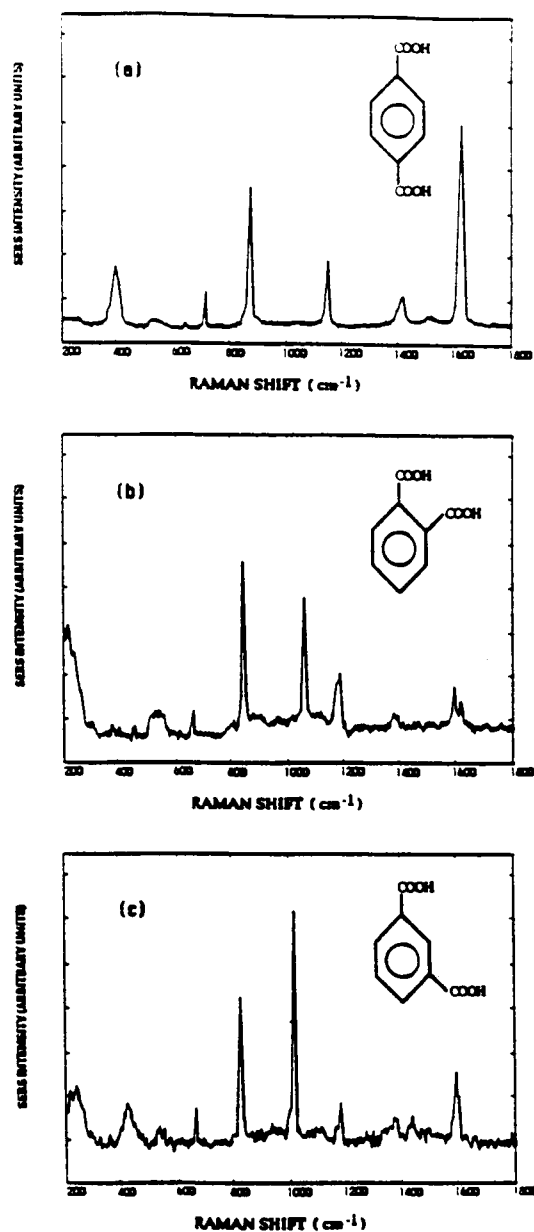
Figure 2.14. SERS spectra of a) TPA (0.5 ppm), b) phthalic acid (2 ppm), and c) isophthalic acid (1 ppm) acquired *in situ* with alumina-based substrates and 647.1-nm excitation radiation (80 mW).

Source: J. M. Bello, D. L. Stokes, and T. Vo-Dinh, *Anal. Chem.* **62**, 1349 (1990).

101

form of the acids were adsorbed to the metallic surface of the alumina-based substrates. The absence of the characteristic CO stretching vibration for the unionized forms of the acids further supports this conclusion.

Figure 2.14a illustrates eight characteristic bands of terephthalic acid. The band at 530 cm^{-1}, which is also present in the SERS spectra for the other two isomers, is a background band from the substrate. The two strongest terephthalic acid bands at 1612 and 862 cm^{-1} and the weak band at 708 cm^{-1} correspond to symmetric CC stretching modes (Arenas and Marcos, 1979). On the other hand, the band at 1406 cm^{-1} and the weak band at 1502 cm^{-1} are those corresponding to symmetric and asymmetric OCO stretching modes, respectively. The 1138-cm^{-1} band corresponds to the symmetric CH bending mode, while the bands at 638 and 392 cm^{-1} can be attributed to OCO bending vibrations. Phthalic acid, on the other hand, shows a total seven SERS bands as illustrated in Figure 2.14b. For this isomer, the bands at 832, 1364 and 1580 cm^{-1} are attributable to symmetric CC stretching vibrations, while the band at 1604 cm^{-1} is due to asymmetric CC stretch (Arenas and Marcos, 1979). Also, the bands at 660 and 1046 cm^{-1} are due to bending vibrations of the OCO and CH groups, respectively. The 1170-cm^{-1} band is due to symmetric stretching of the benzene ring. The SERS spectrum of isophthalic acid, demonstrated in Figure 2.14c also shows several unique bands. The strong bands at 820 and 1598 cm^{-1} are due to symmetric CC stretching vibrations. The other dominant band at 1010 cm^{-1} is due to CC bending vibrations. A symmetric benzene ring vibration is manifested by the 1178-cm^{-1} band. Finally, the 418- and 664-cm^{-1} bands are both attributable to bending vibrations of OCO groups. In general, the *in situ* SERS spectra of the isomers show highly resolved and very narrow bands, many of which do not overlap. Each *in situ* SERS spectrum of the isomers can therefore serve as a "fingerprint" for each compound.

To further evaluate the applicability of the *in situ* SERS technique for the characterization and identification of isomers in a mixture, a ternary mixture of the phthalic acid isomers was analyzed. Figure 2.15 illustrates the SERS spectrum acquired from the three-component mixture. The 647.1-nm excitation line (80 mW) was used for this *in situ* measurement, performed with an alumina-based substrate. Five bands of this spectrum, 392, 708, 862, 1138, and 1612 cm^{-1}, can be attributed unequivocally to terephthalic acid. The discernible bands of phthalic acid occur at 832, 1046 and 1170 cm^{-1}. In addition, the 1580 cm^{-1} band of this isomer appears as a shoulder of the strong 1612-cm^{-1} band of terephthalic acid. There are three discernible bands for the isophthalic acid isomer, occurring at 664, 820, and 1010 cm^{-1}. It is noteworthy that even though the 820 cm^{-1} band of isophthalic strongly overlaps the 832-cm^{-1} band of phthalic acid, this band clearly appears as a peak for isophthalic acid in the three-component mixture. Also, the 1598-cm^{-1} band of isophthalic acid can be seen as a shoulder of the strong 1612-cm^{-1} band of terephthalic acid. In general, all of the SERS bands observed in the ternary mixture spectrum could be assigned to terephthalic acid, phthalic acid or isophthalic acid. Finally, the LODs for terephthalic acid, phthalic acid and isophthalic acid in the ternary mixture were determined to be 24, 180, and 181 ppb, respectively. In conclusion, the highly structured and very narrow bands that are characteristic of a Raman spectrum, coupled with the high detectability offered by the SERS technology, can allow SERS to be an effective method for analyzing mixtures of trace-level components. As this study has demonstrated, such components can be very closely related.

Selective detection and quantitative analysis of complex samples. The ability to selectively detect and perform quantitative analyses of specific trace
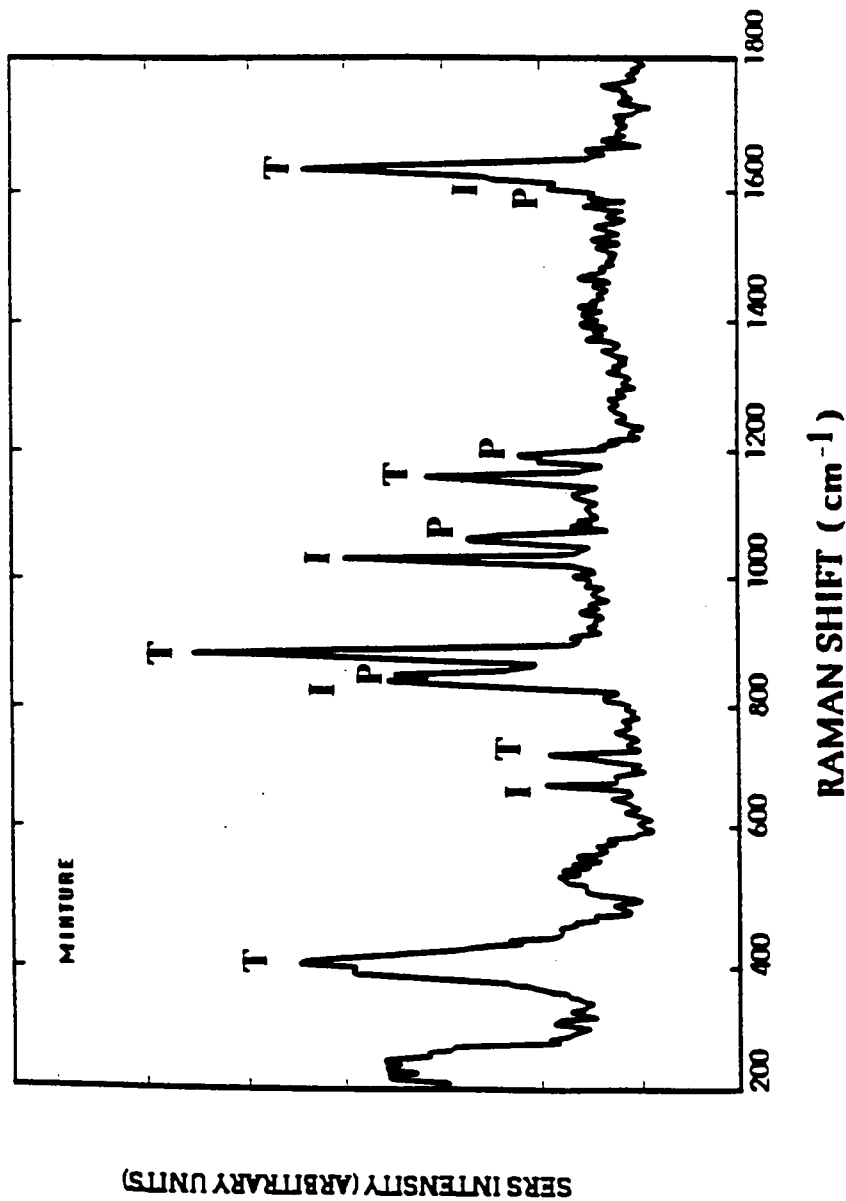
Figure 2.15. SERS spectrum of a ternary mixture of 2 ppm phthalic acid (P), 0.5 ppm terephthalic acid (T), and 1 ppm isophthalic acid (I) acquired *in situ* with an alumina-based substrate and 647.1-nm excitation radiation (80 mW).

Source: J. M. Bello, D. L. Stokes, and T. Vo-Dinh, *Anal. Chem.* **62**, 1349 (1990).

104

compounds in complex samples without pretreatment steps is of obvious value to the analytical chemist. The highly structured and narrow features of typical Raman spectra and the enhanced detectability enabled by the SERS technique may be combined to offer a practical analytical tool for one-step analyses of environmental pollutants, pesticides, carcinogenic agents, and other food additives in complex media. In this study, we demonstrate this potential of SERS by applying the alumina-based substrate technology (described in previous sections) towards the selective detection and quantitative determination of PABA in Presun-15 sunscreen lotion. PABA is an active ingredient in suntan lotions which blocks UV-B radiation. This demonstration could therefore be of value to the quality control pharmaceutical chemist. PABA also occurs widely in plant and animal tissues and is used to raise the salicylate level in the blood.

A spectrum of pure PABA is illustrated in Figure 2.16. A 1-μL aliquot of a 14 ppm solution of PABA in ethanol was spotted on an alumina-based substrate, allowed to dry, and the spectrum was acquired with a 150 mW, 647.1-nm laser beam. The spectrum includes prominent bands at 1132, 1148, 1180, 1390, 1452, and 1600 cm^{-1}. The bands at 1452 and 1600 cm^{-1} are due to benzene ring stretching vibrations, while the 1390-cm^{-1} band is attributable to stretching of the COOH group. The 1180-cm^{-1} peak arises from the out-of-plane CH bending vibration. Likewise, the 1132-cm^{-1} band is due to in-plane CH bending, coupled with the ring stretching mode and an NH_2 twisting vibration at 1148 cm^{-1}. Band assignments are based on various reports in the literature (Dornhaus *et al.*, 1980; Tsang *et al.*, 1983a,b&c; Suh *et al.*, 1983; Laserna *et al.*, 1987; Venkatachalam *et al.*, 1988). The broad background observed for the 200-700 cm^{-1} region of this spectrum is due to silica background from a fiber that was used to transmit the signal from the sample to the spectrometer in this particular example (see Chapter 5). Likewise, a spectrum of Presun-15 lotion diluted in ethanol is
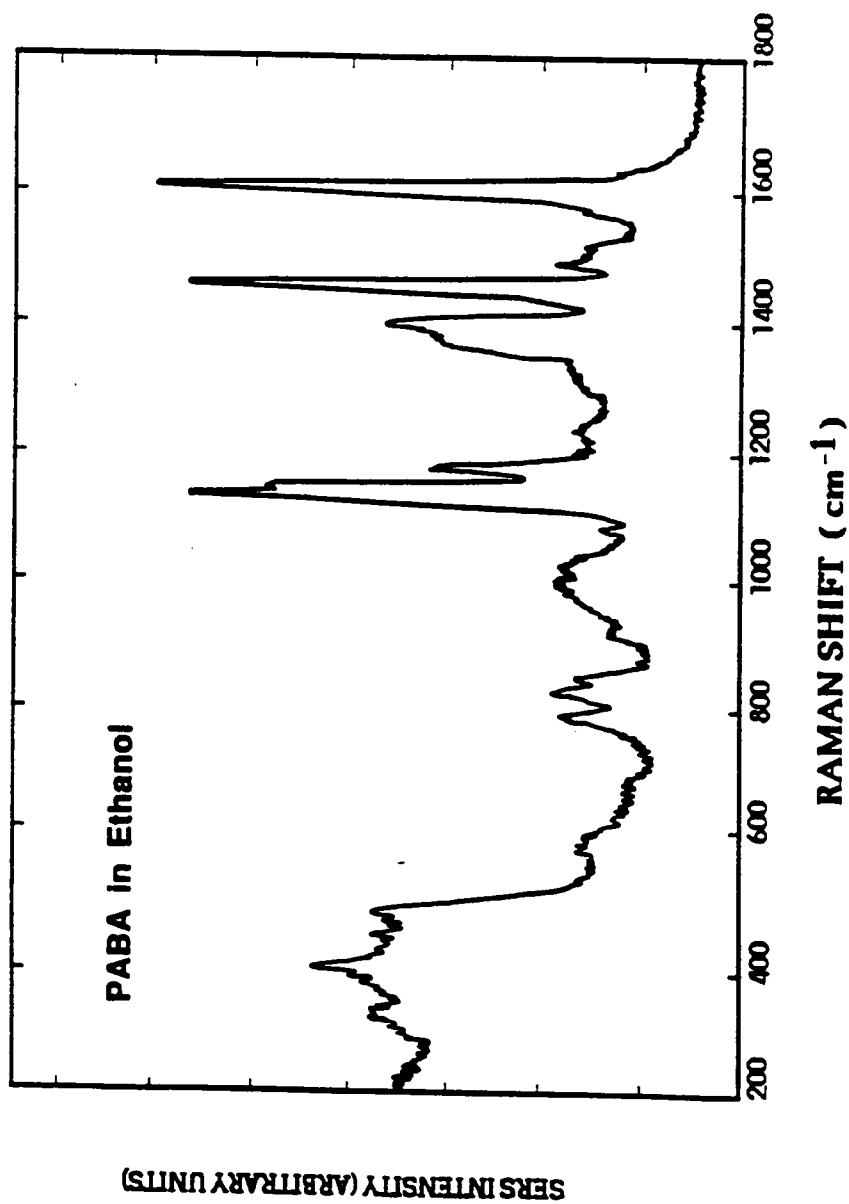
Figure 2.16. SERS spectrum of a 14-ng sample of PABA acquired with an alumina-based substrate and 647.1-nm excitation radiation (150 mW).

Source: V. A. Narayanan, J. M. Bello, D. L. Stokes, and T. Vo-Dinh, *Analusis* **19**, 307 (1991).

demonstrated in Figure 2.17. The spectrum is virtually identical to the pure PABA spectrum with respect to the frequencies of the observed SERS bands. This result indicates that the complex medium of the Presun-15 lotion offers little or no interference to the detection of PABA. As specified by the manufacturer, the active ingredients of the lotion include 5% PABA, 5% octyldimethyl PABA, 3% oxybenzone and 58% SD alcohol 40. Remaining ingredients were not specified. Based on the manufacturer's information, the concentration of PABA in the tested Presun-15 lotion was 14 ppm.

Before performing the quantitative analysis of the Presun-15 lotion, stability of the dry-state samples to the intense 150 mW laser beam was investigated. Figure 2.18 illustrates the SERS intensity of the 1132-cm^{-1} PABA band as a function of laser exposure time for pure samples of PABA spotted from 8 ppm and 16 ppm solutions. Also included in the plot is a stability curve for a Presun-15 lotion sample spotted from a solution estimated to contain 6 ppm PABA. As suggested by the figure, an exposure time of 30 minutes was deemed necessary for adequate stabilization of the PABA signal when using the 150 mW laser power. The 30-min laser exposure was therefore used for all subsequent measurements in the quantitative analysis (e.g., measurements of standard PABA samples for generation of a calibration curve and measurements of the lotion samples). Lotion samples with estimated PABA concentrations of 6 ppm and 14 ppm were measured. Using a calibration for pure PABA, true concentrations of these samples were determined to be approximately 9 ±1 ppm and 12±1 ppm, respectively (both within 3 ppm of the concentration specified by the manufacturer). In closing, it has been demonstrated that PABA can be selectively detected and quantitatively determined
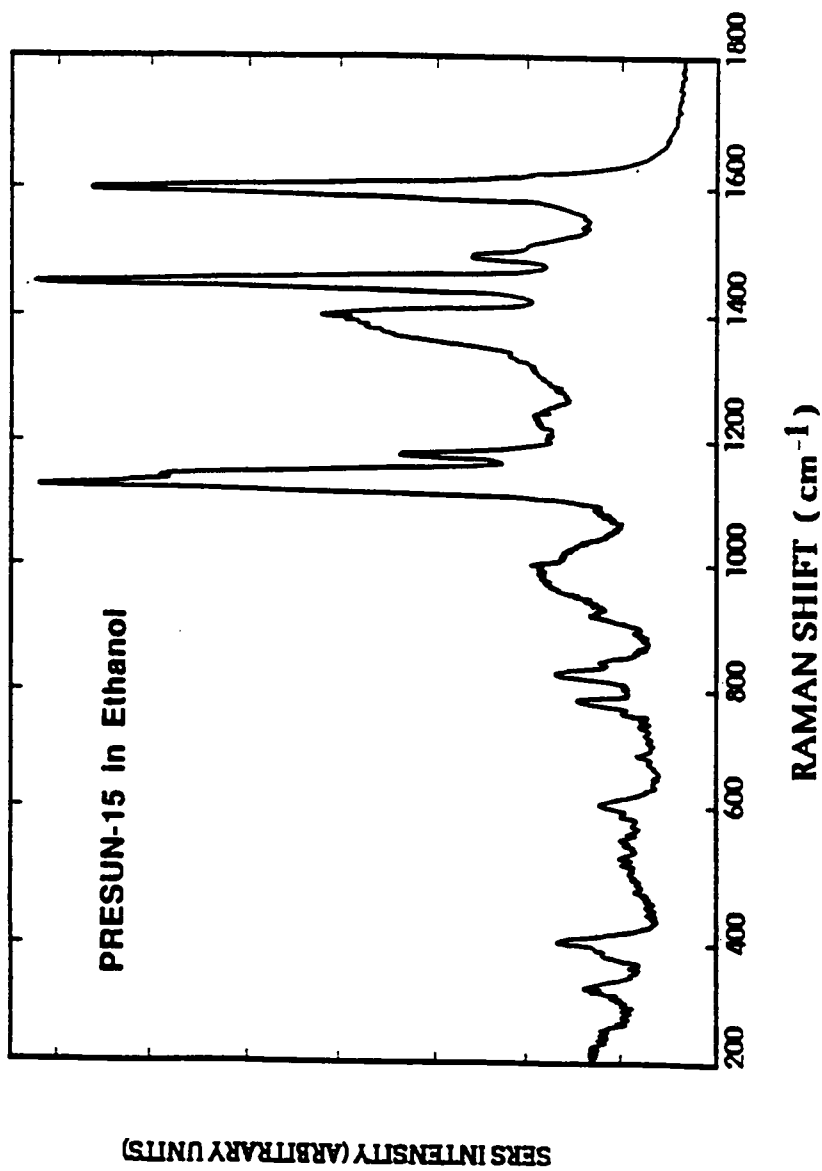
Figure 2.17. SERS spectrum of Presun-15 lotion sample containing 14-ng of PABA, acquired with an alumina-based substrate and 647.1-nm excitation radiation (150 mW).

Source: V. A. Narayanan, J. M. Bello, D. L. Stokes, and T. Vo-Dinh, *Analusis* **19**, 307 (1991).
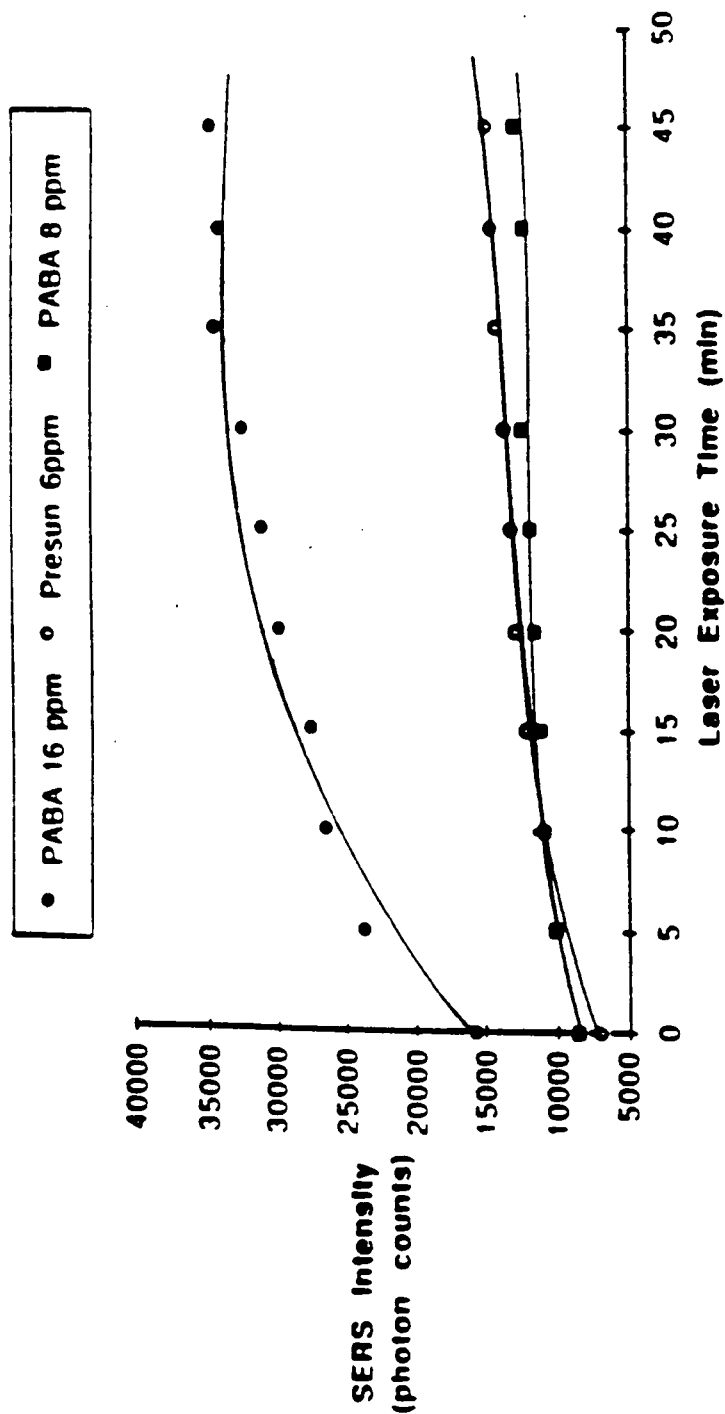
Figure 2.18. Intensity plots for the 1132-cm^{-1} band of PABA as a function of laser exposure time acquired from 8-ppm and 16-ppm pure samples as well as a Presun-15 lotion sample containing an estimated 6 ppm PABA. Laser: Kr, 647.1 nm, 150 mW.

Source: V. A. Narayanan, J. M. Bello, D. L. Stokes, and T. Vo-Dinh, *Analusis* **19**, 307 (1991).

directly from the complex matrix, Presun-15 lotion, when using the SERS technique. Furthermore, determinations can be accurate at the low ppb level.

Detection of fungicides. The ability to detect fungicides and pesticides at trace levels by nondestructive, *in situ* methods is of major importance and a topic of great interest in environmental applications. Such interest can, in part, be attributed to regulations imposed by the US Environmental Protection Agency (EPA). For example, in 1987, the EPA reviewed the use of certain classes of bis-thiocarbamate fungicides and, as a result, issued a preliminary advisory against the use of these fungicides in 45 crop applications (Fed. Regist., 1989). The use of microparticle-based SERS substrates for the detection of organophosphorus chemical agents (Alak and Vo-Dinh, 1987) and chlorinated pesticides (Alak and Vo-Dinh, 1988) has been previously reported. In this study, the SERS detection of the fungicides, Thiram and Ferbam, is demonstrated through use of the alumina-based substrate technology.

The SERS spectra, along with the molecular structures of Thiram and Ferbam, are illustrated in <u>Figures 2.19a and b</u>. For each measurement, a 1-µL aliquot of a 1000 ppm solution was deposited onto an alumina-based substrate. The excitation source was a 150-mW, 647.1-nm laser beam. As would be expected from their molecular structures, the two compounds yield very similar SERS spectra. Nevertheless, subtle differences in the spectra may allow identification with an instrument of suitable spectral resolution, thus further demonstrating the value of SERS as an analytical tool. For Thiram, discernible SERS bands appear at 338, 438, 478, 558, 1136, 1376, 1444, and 1510 cm^{-1}. Similarly, Ferbam SERS bands occur at 344, 434, 556, 1144, 1378, 1444, and 1503 cm^{-1}. Obviously, the two compounds share many common vibrational modes and adsorb to the silver surface with essentially the same chemical
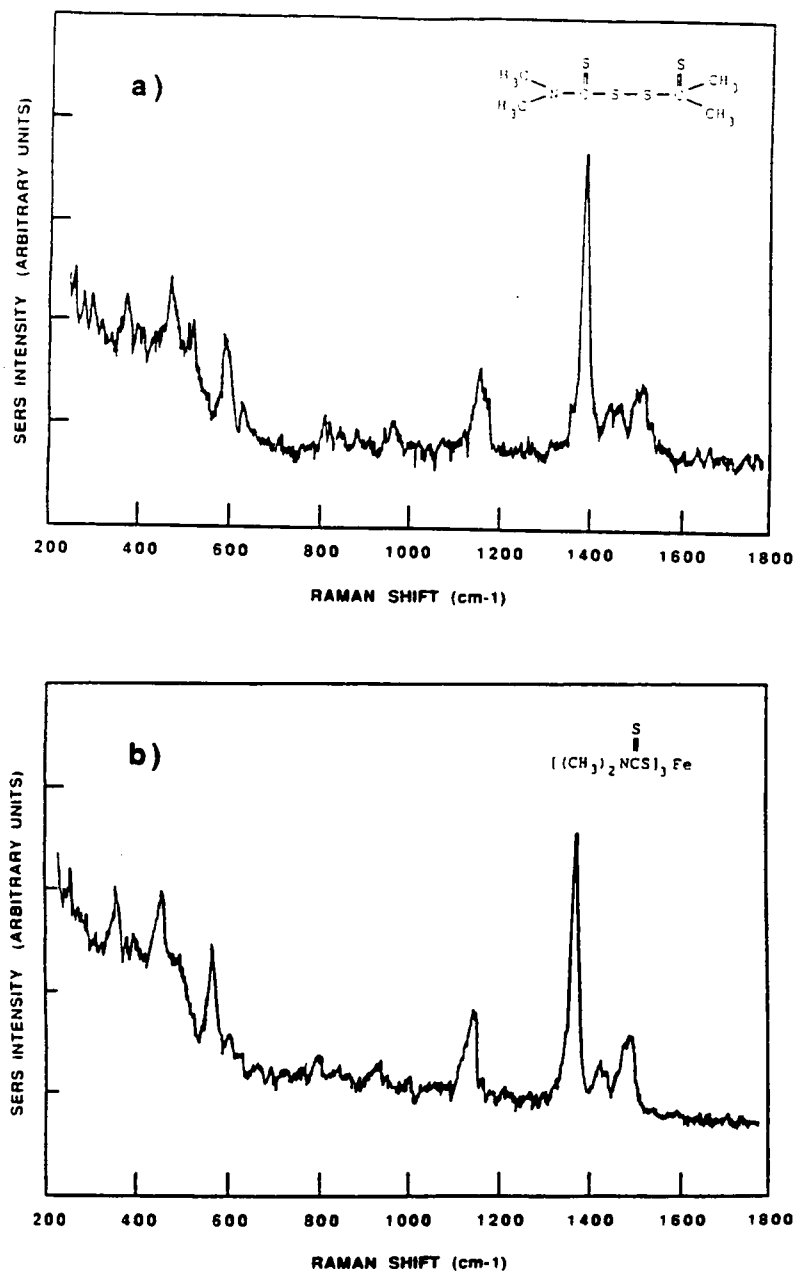
Figure 2.19. SERS spectra of 1000-ng samples of a) Thiram, and b) Ferbam acquired with alumina-based substrates and 647.1-nm excitation radiation (150 mW).

Source: V. A. Narayanan, J. M. Bello, D. L. Stokes, and T. Vo-Dinh, *Analusis* **19**, 307 (1991).

111

groups. For both compounds, bands appearing in the 1100-1510 cm^{-1} range can generally be attributed to C=S stretching modes. These multiple bands arise from coupled vibrational modes which are inherent for thiocarbonyl groups attached to a nitrogen atom (Rao and Venkataraghavan). In addition, the 1376- and 1444-cm^{-1} bands of Thiram, and the corresponding 1378- and 1444-cm^{-1} bands of Ferbam, may also involve CH_3 vibrational modes. The bands at 438 and 478 cm^{-1} for Thiram, and 434 cm^{-1} for Ferbam, can be assigned to mixed modes involving SS stretching vibrations, C=SS scissoring vibrations, and CSS scissoring vibrations. Finally, the broad 558- and 556-cm^{-1} bands of Thiram and Ferbam, respectively, can be attributed to various vibrational modes of the CN, CS, and CNC groups. The broad background observed for the 200-700 cm^{-1} region of this spectrum is due to silica background from a fiber that was used to transmit the signal from the sample to the spectrometer in this particular example (see Chapter 5). In closing, LODs for Thiram and Ferbam were determined to 60 and 50 ppm, respectively, when implementing the alumina-based SERS substrate for Raman detection. These detection levels, coupled with the spectral selectivity offered by Raman scattering, may provide a means of identifying these fungicides by *in situ* trace analysis.

CHAPTER 3

OPTIMIZATION OF SILVER ISLAND FILM-BASED SUBSTRATE FOR USE WITH 632.8-nm RADIATION: APPROACHING SINGLE MOLECULE DETECTION IN SERS DETECTION

INTRODUCTION

In addition to the microparticle-based substrates discussed in Chapter 2, metal island films are a very effective medium for providing giant Raman enhancements (Jennings et al., 1984; Meier et al., 1985; Aroca and Martin, 1986; Vo-Dinh et al., 1986; Berthold et al., 1987; Ni et al., 1990; Van-Duyne et al., 1993; Chen et al., 1995; Freeman et al., 1995; Lacy et al, 1996). These substrates are very easy to produce, essentially requiring a only single step. A thin layer of silver (7.5-10 nm) is simply deposited directly to a clean, smooth solid support, such as glass, under vacuum (e.g., < 10-5 torr). At this thickness, the silver coating is discontinuous, leading to the formation of silver islands. The islands themselves provide the surface roughness required to induce the SERS effect. In fact, the performance of silver islands has been demonstrated to be competitive with that of several other nanostructured materials (Meier et al., 1985;Vo-Dinh et al., 1986). Furthermore, island film surfaces have been well-characterized by atomic force microscopy (Van-Duyne et al., 1993; Chen et al., 1995). Thermal evaporation in vacuum systems is a common method for preparation of silver island films, especially since deposition rates are so easily

113

controlled by this method. Deposition rates have been demonstrated to have significant effects on the degree of aggregation and hence Raman enhancements with silver island films (Chen *et al.*, 1995). Nevertheless, sputter-deposition of thin films for production of SERS-active substrates has also been reported (Ni *et al.*, 1990).

Despite the reported successes of this class of substrate and the amount of interest devoted towards its characterization, a major drawback of this substrate is its short shelf-life. While it may not be practical for field studies, it is well-suited for laboratory-based applications. In this work, we describe the optimization of a silver islands-based substrate specifically for use with a low-power helium-neon laser (632.8 nm). Silver thickness and deposition rates were varied to yield the maximum Raman scattering enhancement. As a result of this optimization study, we have observed an extremely high enhancement which we believe approaches that required for single molecule detection. One motivation for achieving such high detectability in this laboratory is for the enhanced performance of the surface-enhanced Raman gene (SERGen) probe technology (Vo-Dinh *et al.*, 1994; Isola *et al.*, 1998). Silver islands are more compatible with the SERGen technique than microparticle-based substrates.

Single molecule detection has been the object of intense efforts in recent years, as is evidenced by some comprehensive review articles (Barnes *et al.*, 1995; Keller *et al.*, 1996). A majority of these studies have involved fluorescence-based detection techniques. They have been applied towards cryogenic solids (Moerner and Kadar, 1989; Moerner, 1994; Orrit and Bernard, 1990; Orrit *et al.*, 1993), and room temperature solids via near-field microscopy (Betzig and Chichester, 1993; Xie and Dunn, 1994; Ambrose *et al.*, 1994). Fluorescence-based single molecule detection has also been observed for liquid samples via time-gated detection of flowing streams

114

(Nguyen and Keller, 1987; Peck *et al.*, 1989; Mathies *et al.*, 1990; Shera *et al.*, 1990; Wilkerson *et al.*, 1993), or by probing extremely low-volume samples via confocal microscopy (Eigen and Rigler, 1994; Nie *et al.*, 1994) or evanescent wave detection (Xu and Yeung, 1997). Yet another technique involves analyzing micrometer-scale liquid droplets (Whitten *et al.*, 1991; Ng *et al.*, 1992; Barnes *et al.*, 1993). While offering the required sensitivity, the broadband nature of the LIF signal has the drawback of lacking the spectral selectivity offered by the vibrational spectroscopies, such as Raman scattering. Furthermore, the sharpness of Raman peaks offers a larger "capacity" for signals from various molecules within a given spectral window. Simultaneous multicomponent detection of single molecules may therefore be possible with a single excitation source and spectrometer.

In light of all these advantages, single molecule detection utilizing SERS has also been pursued in recent years. Most of the SERS-based studies have involved silver or gold colloidal media (Nie and Emory, 1997; Kneipp *et al.*, 1997, 1998a, b). In one study, individual colloidal nanoparticles, immobilized on a solid support, were screened from a large heterogeneous population for special size-dependent properties. These "hot" particles were used to amplify the spectroscopic signatures of adsorbed molecules (Nie and Emory, 1997). For single Rhodamine 6G molecules adsorbed on the selected nanoparticles, the intrinsic Raman enhancement factors were on the order of 10^{14} to 10^{15}, much larger than the ensemble-averaged values derived from conventional measurements. Single molecule detection was demonstrated by performing a polarization analysis of light scattered from the nonrotating molecules. The observation of single molecules of crystal violet and cyanine dye was also reported with silver and gold colloidal solutions (Kneipp *et al.*, 1997; Kneipp *et al.*, 1998a &b). Spectra observed in a time sequence for an average of 0.6 dye molecules in the

probed volume exhibited the expected Poisson distribution for actually measuring 0, 1, 2 or 3 molecules. In this study, extremely enhanced Raman signals are reported for cresyl fast violet (CFV) and brilliant cresyl blue (BCB) molecules adsorbed onto a silver islands substrate. This solid medium offers an attractive alternative to colloidal solutions or immobilized colloids because the silver islands produce a very uniform surface roughness. The low detection limits reported herein for CFV and BCB are particularly encouraging because they are dyes used for DNA labeling in the SERGen probe technology (Vo-Dinh *et al.*, 1994; Isola *et al.*, 1998).

EXPERIMENTAL

Chemicals

CFV was purchased from Fluka (Buchs, Switzerland) at standard purity for microscopy. BCB was purchased from Pharmaceutical Laboratories (National Aniline Division, New York, NY) at 68% percent purity. PABA was purchased from Aldrich (Milwaukee, WI). 10^{-4} M stock solutions of the dyes were prepared in absolute ethanol (Aaper Alcohol and Chemical Co., Shelbyville, KY). An ethanolic solution of PABA was similarly prepared at 10^{-3} M concentration. Subsequent dilutions (in 10-ml volumes) were performed serially down to 10^{-11} M with the ethanol, with accurate volume transfers being performed with appropriate Gilsen Pipetman® (France) dispensers (5000 or 1000 µl). Nitric acid was purchased from Baker (Phillipsburg, NJ). Any water used in this study was purified from tap with a Waters Milli-Q+ filtration system.

SERS Substrates

Glass microscope slides (Corning Glass Works) were cut into 1 cm x 2.5 cm rectangles with 1-mm thickness. The glass portions were bathed in 2 M nitric acid before being stored in ethanol. Immediately prior to substrate preparation, the glass portions were dried in a stream of dry air. The air stream had been filtered by activated charcoal and calcium sulfate (Drierite) cartridges. Once dried, the glass bases were placed in a vacuum evaporation system (Cooke, CV-301) for application of the silver layer. The silver deposition was performed at approximately 2×10^{-6} Torr.

Instrumentation

A schematic diagram of the optical system used for this study is demonstrated in <u>Figure 3.1</u>. The 5-mW excitation at 632.5 nm was supplied by a helium-neon laser (Spectra-Physics, Model 106-1). A 10-nm bandpass filter (Corion) was used to reject laser plasma lines. The laser beam was expanded with a 20X objective lens. The expanding beam was collimated with a 1" f/1 biconvex lens. The resulting beam diameter was approximately 0.5 cm. A holographic beam splitter (Kaiser Optical Systems, Inc., Model HB-633-1.0) directed the excitation beam through a 100X, 0.90-numerical aperture (NA) objective lens (Nikon, Part No. 230327) onto the sample, which was placed atop a mirror for enhanced signal collection. Sample SERS signals were collected with the same objective lens. The 0° excitation-to-collection separation geometry was enabled with the use of the holographic beam splitter, which allowed the collected analytical signal to pass towards the additional collection optics while the unwanted Rayleigh scatter was deflected back towards the excitation source.

117
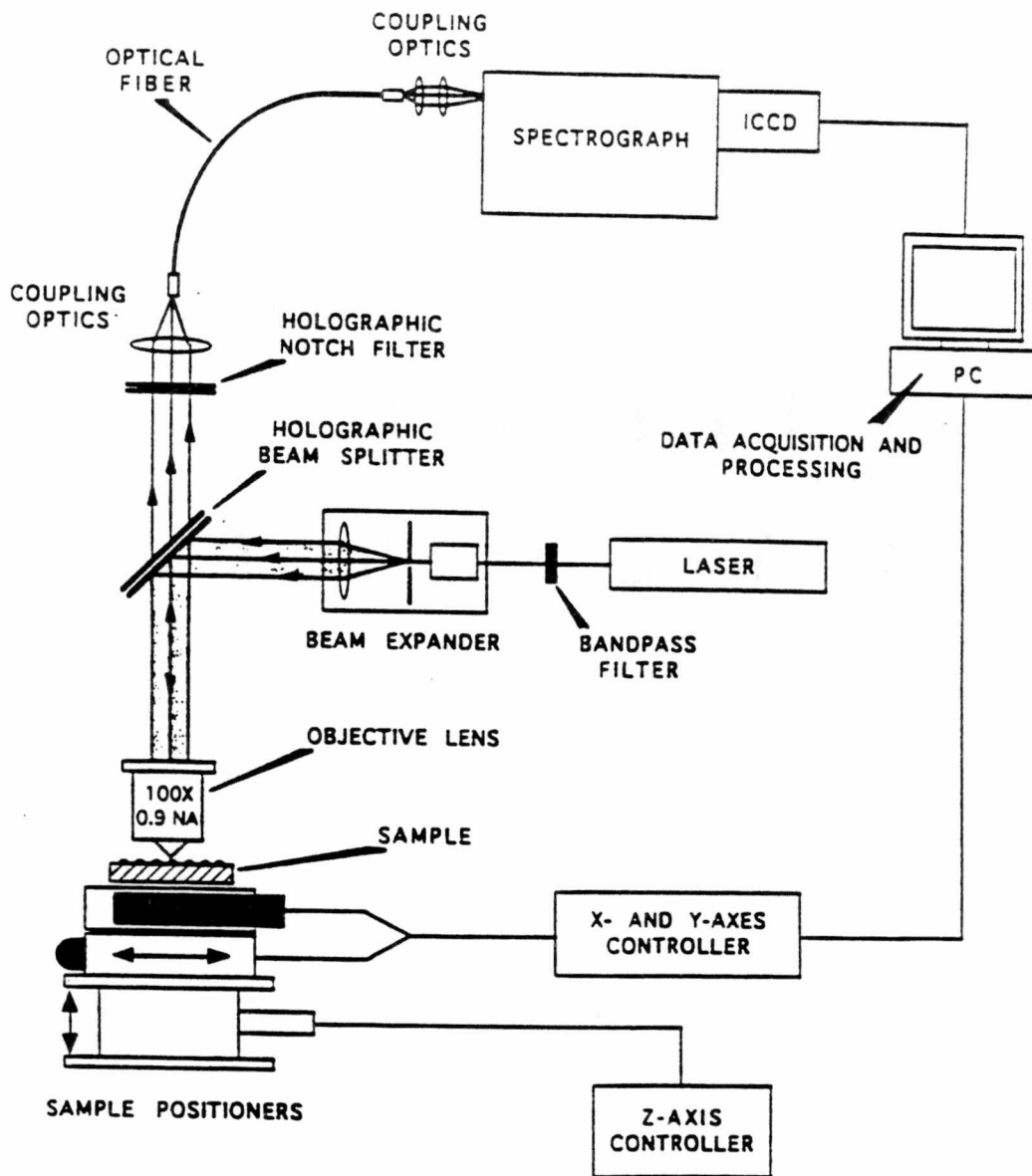
Figure 3.1. Schematic diagram of an optical system for SERS detection featuring an ICCD-based spectrograph and a high precision sample positioning system.

118

An additional holographic notch filter (Kaiser, Model HNPF-633-1.0) was placed in the isolated analytical signal beam to further reject any unfiltered Rayleigh scatter. A 1" silica lens was used to focus the analytical signal beam unto a 600-μm optical fiber (Fiberguide Industries, Model APC600/750Z). The f/2 lens was nearly optically matched with the 0.22-NA optical fiber. The optical fiber transmitted the signal to the spectrometer (ISA, Model HR-320), which was equipped with a red-enhanced intensified CCD (RE-ICCD) (Princeton Instruments, Inc. Model RE/ICCD 576S). Appropriate fiber-to-spectrometer coupling optics were mounted directly to the entrance port of the spectrometer. The RE-ICCD detector was thermoelectrically cooled to -34°C. Signal acquisition and processing was performed with the CSMA software which was supplied by Princeton Instruments.

Procedure

1-μl aliquots of the standard samples were dispensed onto the SERS substrate with a 2-μl total volume Gilsen Pipetman automatic dispenser. The sample-loaded substrate was placed on a high precision x-, y-, and z-positioning system. The z-axis coincided with the focus of the 100X objective lens, which was manipulated with a micrometer-driven translation stage (<1.5 μm resolution) (Melles-Griot, Model 07-TAC-004). The x- and y-axes were manipulated with Inchworm™-driven translation stages (Burleigh, Model TSE-75) for precise probing of the SERS substrate surface. Operation of the Inchworm-driven translation stages was enabled with a Burleigh Model 6000 control unit.

RESULTS AND DISCUSSION

For this study, we have selected a silver islands film substrate which is simply composed of a glass support medium over which a silver layer is deposited thin enough to result in a discontinuous surface of aggregate silver particles. In comparison to some other multilayered SERS substrates (e.g., metal-coated microspheres), work in our laboratory has demonstrated that this substrate yields a relatively low background spectrum and competitive detectivity. These advantages are imperative to single molecule detection. Another unique advantage of the silver island-based substrate in comparison to other solid surface-based substrates is its relative transparency. We have exploited this feature to enhance detectivity by using a mirror to direct the SERS signal scattered from the back side of the substrate back through the substrate and into the collection optics covering the front side of the substrate. Signal enhancements of up to 50% have been observed with this configuration. A disadvantage of the silver islands substrate is a short shelf life when not coated with a protective overlayer or stored in an inert atmosphere. This disadvantage is, however, offset by the fact that daily manufacture is quick and simple.

Thin Film Optimizations

The grain of the substrate surface is a pivotal parameter in the SERS process. From the electromagnetic viewpoint, the size and density of the surface features affect the magnitude and density of localized intense fields. From a chemical viewpoint, the grain can affect the orientation, and thus the polarizability, of the adsorbed sample molecule. For multilayer substrates such as the microsphere or quartz post-based substrates,

the grain is determined by the size and distribution of the microparticles, which are deposited in one step, then coated with the conductive metal layer in a separate step. In a silver islands-based substrate, by contrast, control of surface morphology in the one-step manufacture is possible via control of both the silver thickness and the rate of silver deposition. In a recent study, Chen and coworkers deposited the silver layer in a 1.5 torr atmosphere of argon (Chen *et al.*, 1995). It was determined that collisions of the silver particles with argon atoms caused loss of the kinetic energy induced on the silver particles during the thermal evaporation step, resulting in the agglomeration of uniformly-sized silver particles prior to contact with the substrate surface, regardless of the deposition rate. The thickness determines the absolute number of the constantly sized particles deposited onto the substrate surface, while the rate of deposition determines the degree of agglomeration of the particles into larger microbodies. It was reported that a fast deposition rate of 5 Å/s yielded the most optimum SERS signal for the 0.05 - 5.0 Å/s range studied.

In the work described herein, deposition was performed in a 1.5×10^{-6} torr atmosphere. Midair heteroparticulate collisions were therefore rare. Agglomeration largely originates at the substrate surface, making the unit silver particle size dependent on both the deposition rate and thickness in our substrate preparation. An island optimization study, specifically for use with a 632.8-nm excitation source, was therefore performed. Using a constant deposition rate of approximately 0.5 Å/s, we determined the optimum silver thickness to be 85 Å, out of a set including thicknesses of 55, 70, 85, and 100 Å. The results are illustrated in Figure 3.2. The test compound was CFV, deposited from a 10^{-6} M solution, and monitored at 585 cm^{-1}. Subsequently, while keeping the thickness constant at 85 Å, the deposition rate was varied between 0.5 and 2.5 Å/s. The results are illustrated in Figure 3.3. In striking
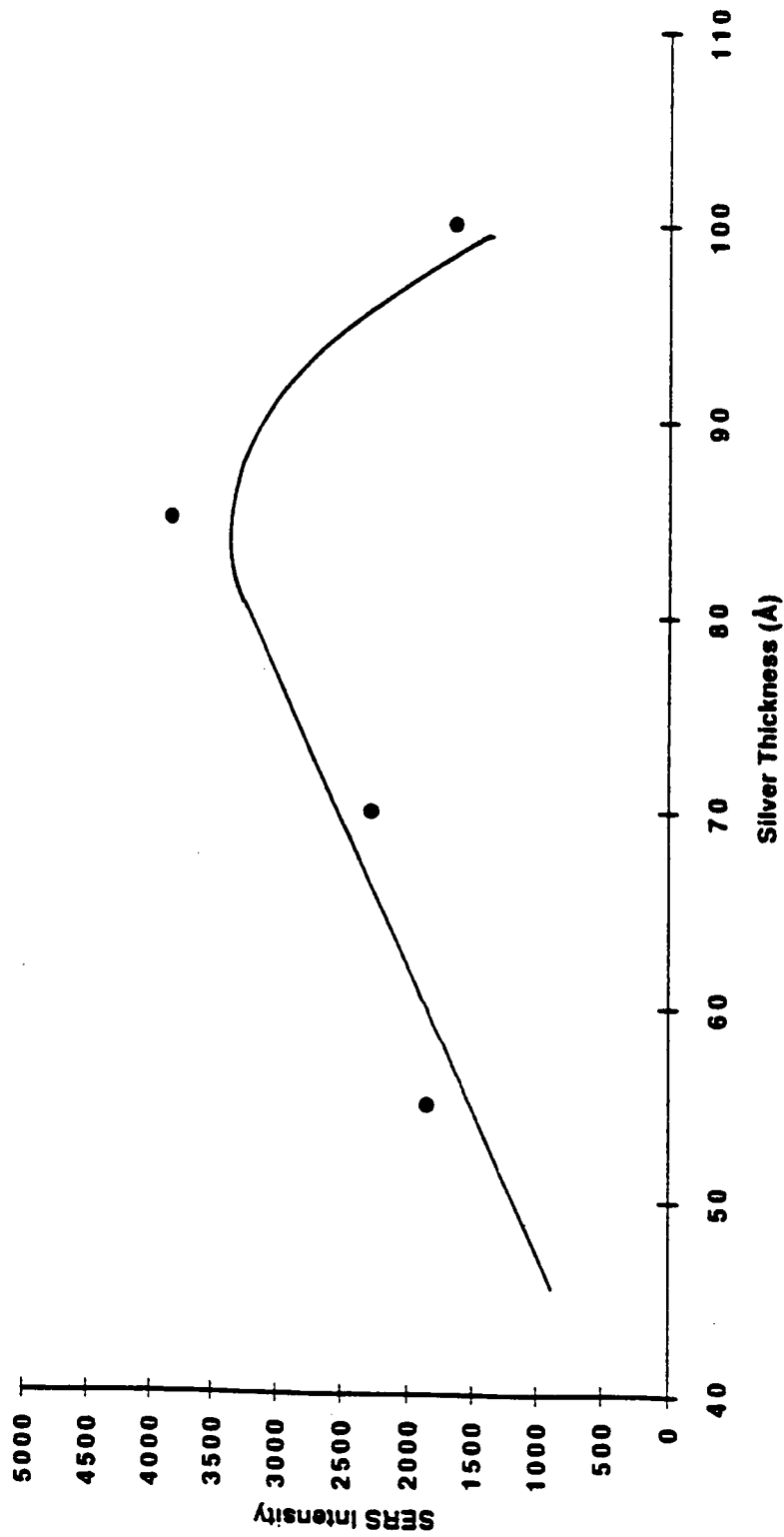
Figure 3.2. SERS intensity plot for the 585-cm^{-1} band of CFV (10^{-6} M) as a function of silver thickness used in island-based substrate preparation at a fixed deposition rate of 0.5 Å/s. Laser: HeNe, 632.8 nm, 5 mW.

122
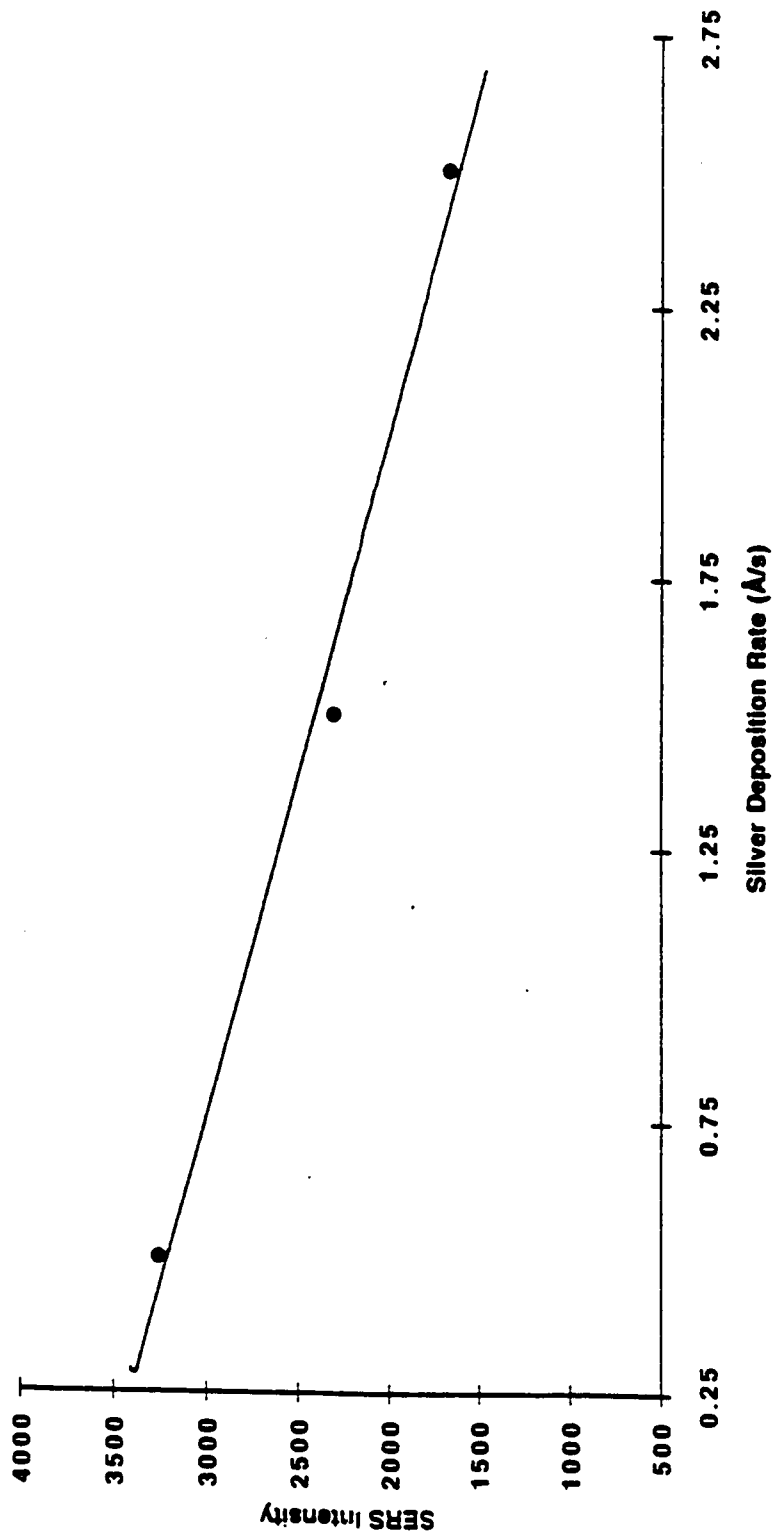
Figure 3.3. SERS intensity plot for the 585-cm^{-1} band of CFV (10^{-6} m) as a function of silver deposition rate used in island-based substrate preparation with a fixed silver thickness of 85 Å. Laser: HeNe, 632.8 nm, 5 mW.

contrast to the results reported by Chen *et al.* (Chen *et al.*, 1995), the optimum signal resulted from the slowest deposition rate studied, 0.5 Å/s. All subsequent silver island film SERS substrates were therefore prepared with 85 Å and a silver deposition rate of 0.5 Å/s.

UV-Vis spectra silver island-based substrates of varying silver thickness are illustrated in Figure 3.4. As demonstrated, the absorbance maxima become broader and more red-shifted as the thickness is increased. This result illustrates that the optimized substrate is suitable for use with the 632.8-nm excitation source, and may also be suitable for farther red-shifted excitation wavelengths. It is interesting to note that the broad nature of the absorption band indicates that the silver islands substrate optimized in this study could be effectively used with several other excitation sources in the visible region. For this particular study, the 632.8 nm radiation was selected due to an added preresonance enhancement effect offered for CFV and BCB detection (see below).

Ultra Sensitive Detection of CFV and BCB Molecules

We have evaluated the newly-optimized silver island-based SERS substrates with two model compounds, CFV and BCB. These compounds have shown unparalleled SERS activity in our laboratory when using red laser sources. As such, they have been successfully applied towards innovative technologies such as the surface-enhanced Raman gene (SERGen) probe DNA screening technique (Vo-Dinh *et al.*, 1994; Isola *et al.*, 1998). Figure 3.5 illustrates the SERS spectra of BCB and CFV, which were both deposited on the silver islands-based substrate as 1-μl aliquots from 10^{-5} M solutions. The prominent bands at 585 and 575 cm^{-1} for CFV and BCB, respectively,
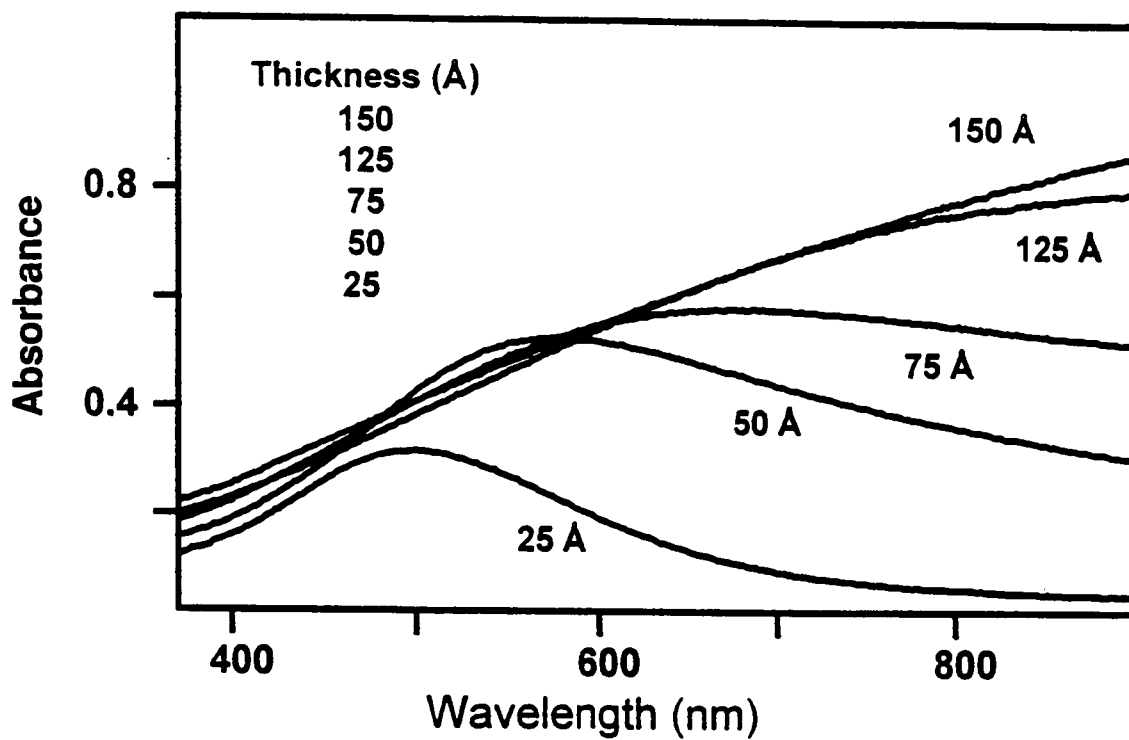
Figure 3.4. Uv-vis spectra of a silver island-based SERS substrates with silver thicknesses ranging from 25-150 Å deposited at a rate of 0.5 Å/s.
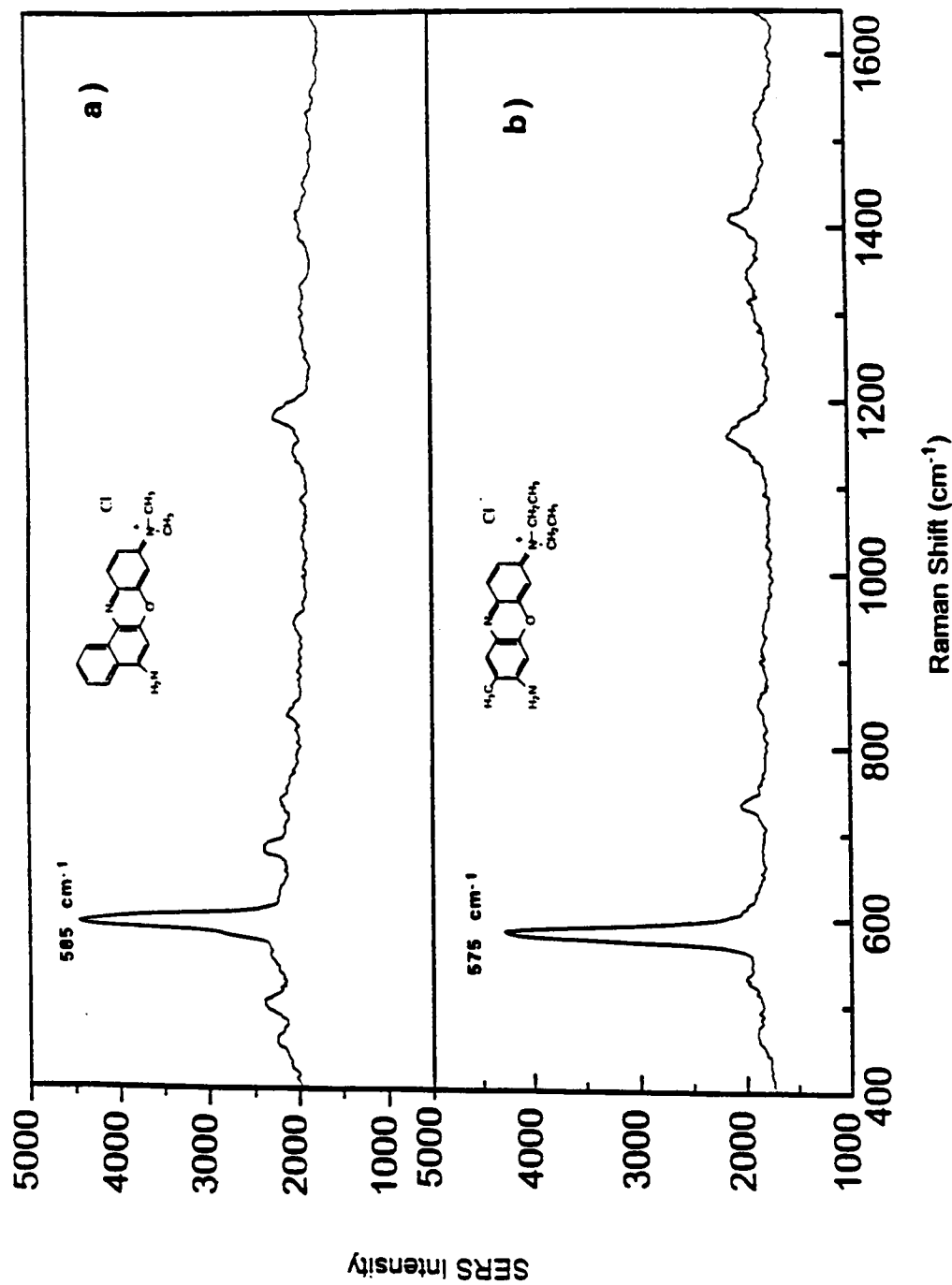
Figure 3.5. SERS spectra of 10^{-5} M samples (1-μl spots) of a) CFV, and b) BCB, acquired with optimized silver island- based substrates and 632.8-nm excitation radiation (5 mW).

126

can be attributed to benzene ring deformation modes of these structurally similar compounds. As is demonstrated by the figure, very comparable SERS intensity levels were observed for the two compounds.

The large Raman enhancement can, in part, be attributed to a preresonance enhancement. Figure 3.6 illustrates the visible absorption spectra of these two compounds, with the absorption maxima occurring at approximately 595 nm and 610 nm for BCB and CFV, respectively. These spectra demonstrate the possibility of a preresonance enhancement when exciting these compounds with red excitation radiation, such as the 632.8-nm line of a HeNe laser. While the emission line of the HeNe laser used in these studies matches these absorption profiles most closely (in comparison to the other laser sources available in our laboratory), it unfortunately places a 5-mW limit on the incident radiation intensity. Regardless of this fact, the HeNe laser has yielded the highest SERS signals witnessed to date in our laboratory for these two compounds. This observation can in part be attributed to the possibility of low photo-stability manifested by these compounds, thus offsetting the advantage of using high-power laser sources.

Comparison of photo-stability of CFV and BCB. A challenging factor needed to be considered for the detection of dye molecules at low concentrations is photo-stability. Even at the 5-mW laser intensity level, the SERS signals from CFV and BCB have been observed to decay very rapidly. Figure 3.7 illustrates the observed SERS signals at the respective characteristic peaks of CFV and BCB as a function of time. In both cases, a 1-μl aliquot of 10^{-5} M solution was deposited on a silver islands substrate. The sharp increase in signal for both profiles marks the initiation of fresh sample excitation. Both profiles illustrate two distinct decay trends. Initially, a very

127
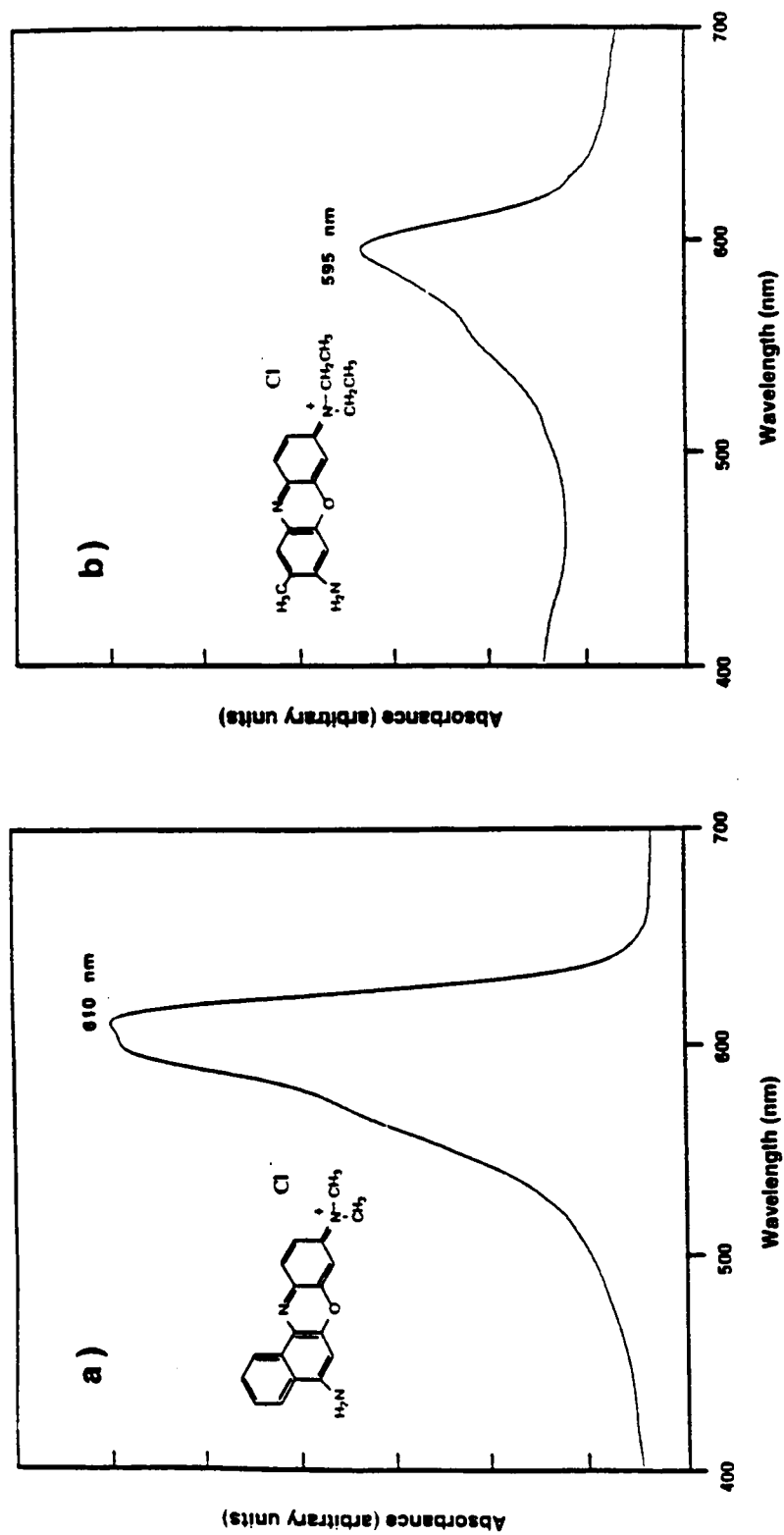
Figure 3.6. Visible absorption spectra 10^{-5} M solutions of a) CFV, and b) BCB. Pathlength = 1 cm.

128
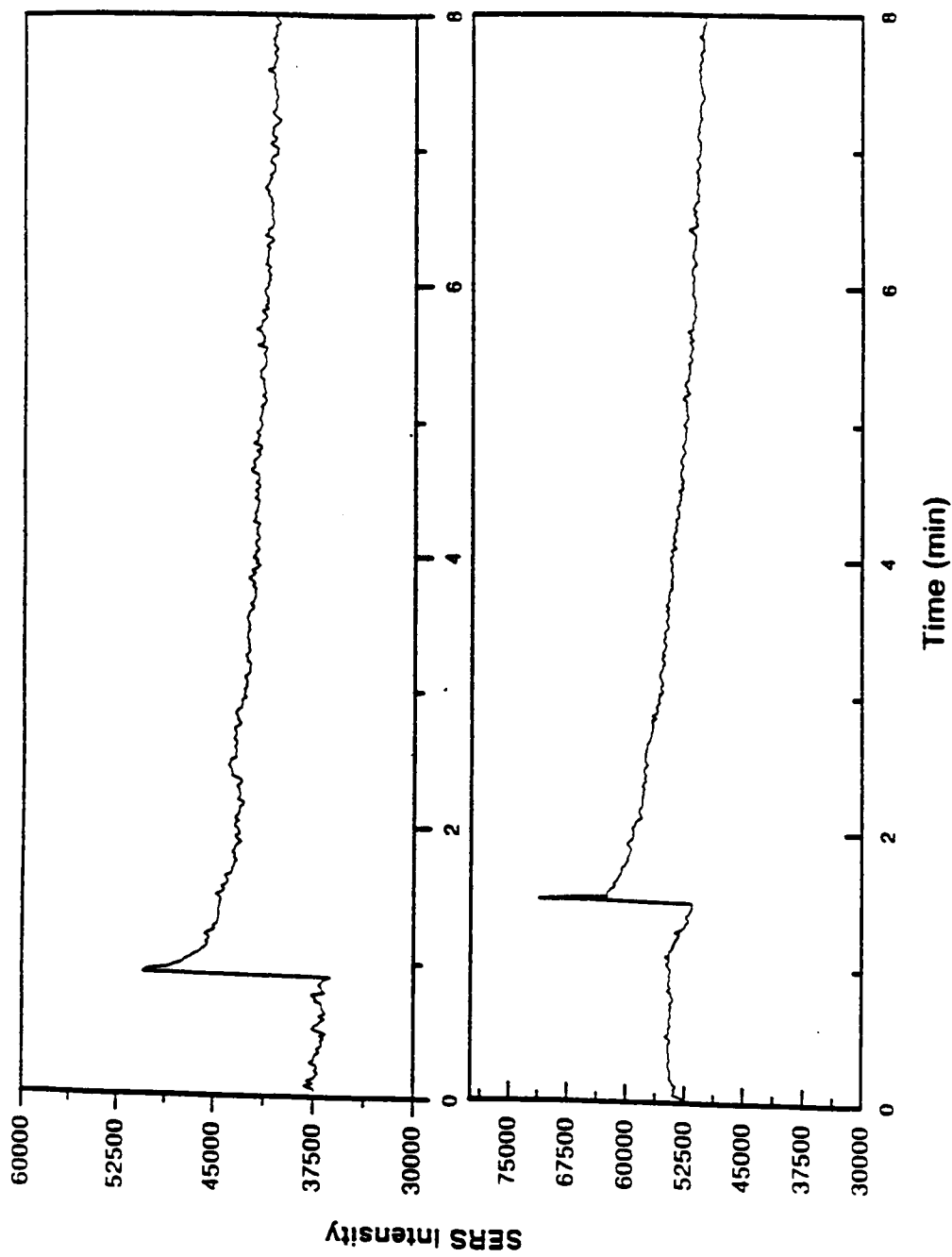
Figure 3.7. Decay curves for characteristic SERS signals of 10^{-5} M (1-µl spot) samples of a) CFV (585 cm^{-1}), and b) BCB (595 cm^{-1}) as a function of time with 632.8-nm excitation radiation (5 mW).

rapid 40-50% decay in signal is observed, followed by a more gradual decay towards the constant signal level. For the BCB, the initial 40-50% signal decay rate is greater than that for CFV, resulting in the spike-like appearance in the decay profile. As both of these profiles imply, the long integration times typically used for detection of low numbers of molecules is not applicable towards the detection of these compounds. The decay profiles indicate that the best chance for detection requires signal acquisition within 1 s of excitation.

LOD study of CFV using the silver island-based SERS substrate. Based on the photo-stability study discussed above, CFV was selected for further evaluations of the newly-optimized thin film substrate. Nevertheless, the detection of low levels of CFV has been a challenging feat in SERS, regardless of the intense signal that it yields. While calibration curves have been generated in our laboratory for the 10^{-3} to 10^{-7} M range, the behavior of CFV becomes unpredictable for solutions of much lower concentration levels when applied to the SERS substrate and dried. While signals have been observed down to the 10^{-10} M level, quantification has not been applicable. It seems that the surface covered by the applied sample becomes discontinuous, with the elusive signal being only occasionally observed as different points of the substrate surface are probed.

There are several possible explanations for this pattern. For example, Nie and Emory have reported the occurrence of sparsely observed agglomerates, among a field of particles with a wide size distribution, which have yielded exceptionally high Raman scattering enhancement (Nie and Emory, 1997). Similarly, the "hot" spots occurring with this silver island-based substrate probably arise from stochastic surface features which either provide further signal enhancement or cause localized

130

agglomeration of the sample molecules, such as fine cracks or microparticles. Unfortunately, such features are difficult to control in the production of delicate silver island substrates. The thinness of the silver layer makes surface features of the glass support medium or microparticulate impurities at the surface more significant in the observed SERS enhancement. As a result of the "hot" spot pattern and the transient nature of the CFV signal, detection at low molecular numbers becomes a matter of acquiring signal at the optimal place. Even when the CFV signal is observed, the intensity is variable.

Figure 3.8 illustrates the unpredictable nature of the CFV signal from a dried 1-μl spot deposited from a 5 x 10^{-9} M solution. The x-axis corresponds to a combination of time (in seconds) and substrate position. The y-axis corresponds to the SERS signal at the characteristic frequency of CFV (585 cm^{-1}). The integration time per data point was 1 second. Simply stated, the figure illustrates a series of decay curves, each profile yielded from a different point on the sample surface. The inchworm motor was used to instantaneously move the sample plate to a new position every 100 s, at which point the dramatic increase in the CFV SERS signal was observed. Figures 3.8a and b represent scans of the sample-spotted region of the substrate. Figure 3.8c represents scans of a unspotted region. As is demonstrated by the figure, the peak intensities for the various decay profiles are quite variable and short-lived. Results of similar scans from a dried spot sample from a 5 x 10^{-10} M solution is demonstrated in Figure 3.9. At this signal level, decay profiles from impurities in the blank become significant in comparison to the expected CFV decay profiles. In addition to peak intensity, the shapes of the decay profiles must be considered to distinguish CFV signal from blank signal. Very distinctive CFV profiles are much less frequently encountered at the 5 x 10^{-10} M concentration. Nevertheless, CFV spectra have been recorded from spots of
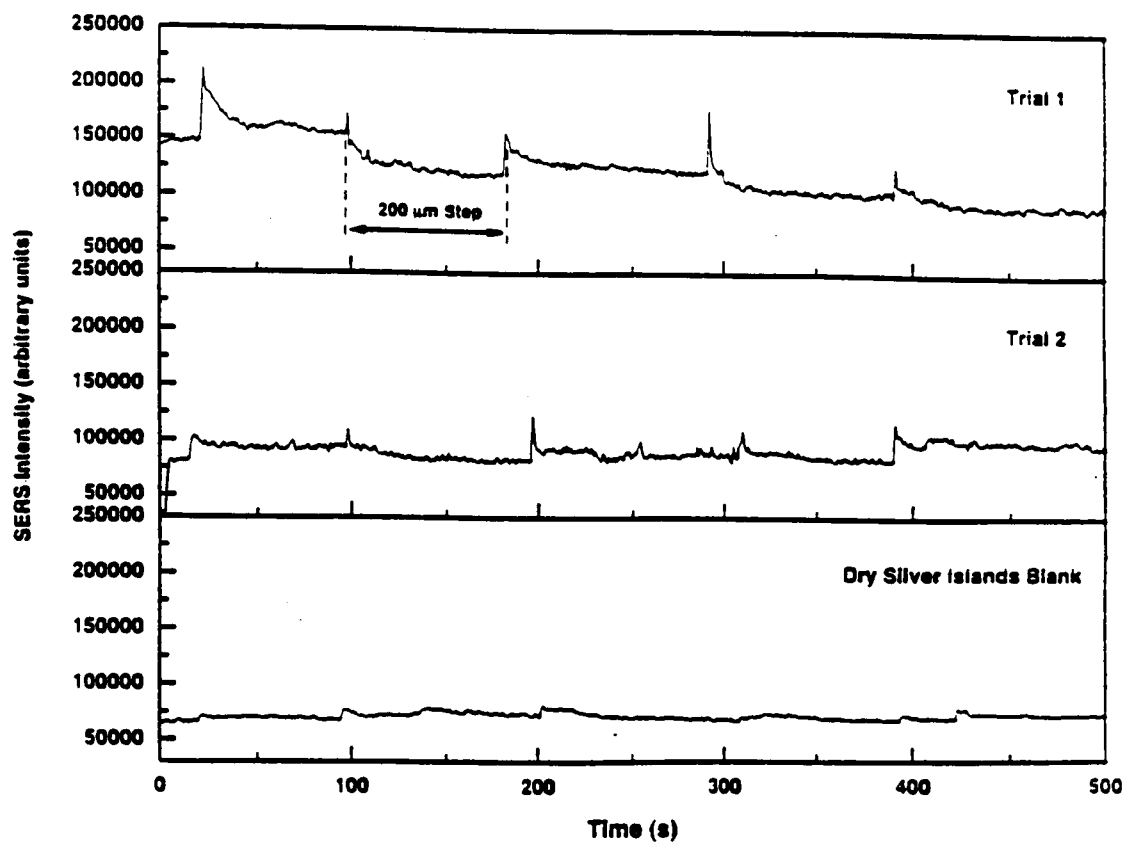
Figure 3.8. Decay profiles for the 585-cm^{-1} band of a 5 x 10^{-9} M (1-µl spot) CFV acquired from random positions on a silver island-based substrate, using 632.8-nm excitation radiation (5 mW).

132
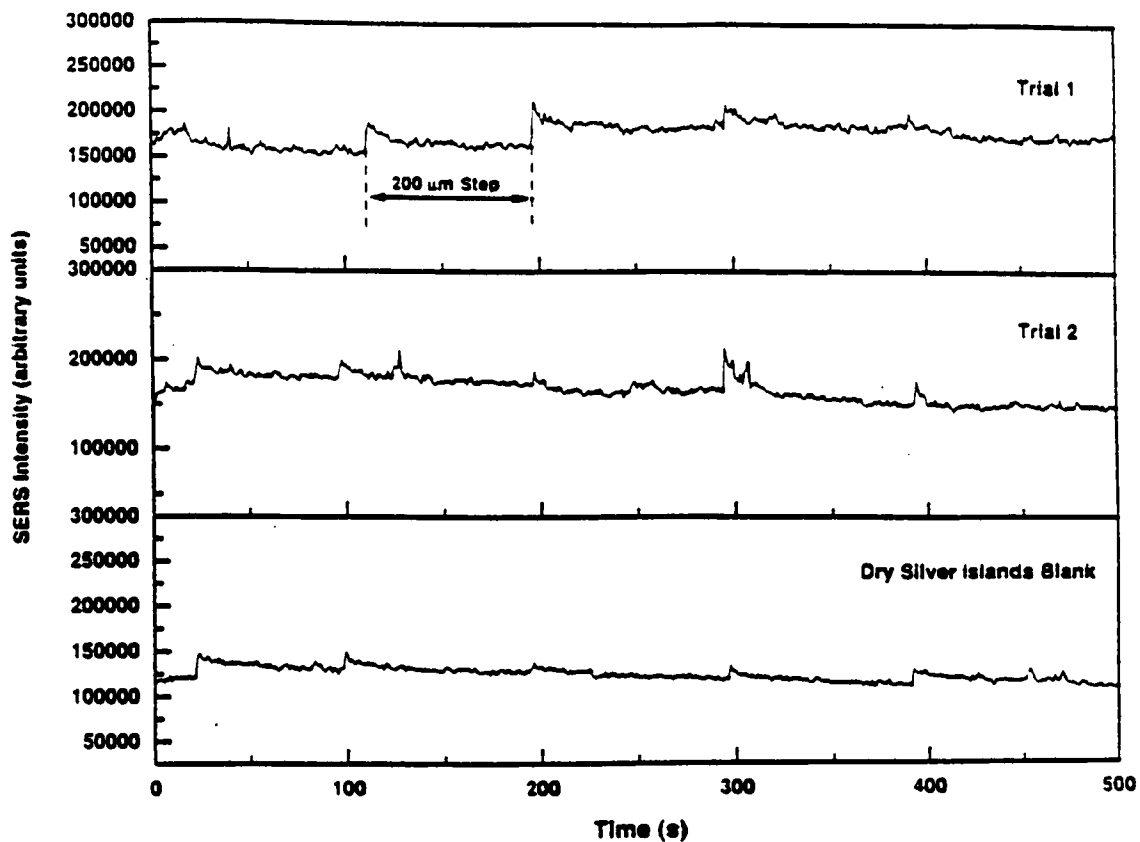
Figure 3.9. Decay profiles for the 585-cm^{-1} band of a 5 x 10^{-10} M (1-µl spot) CFV acquired from random positions on a silver island-based substrate, using 632.8-nm excitation radiation (5 mW).

133

even lower concentration. Figures 3.10a and b illustrate the CFV spectra acquired from 1-μl spots of 1 x 10^{-10} and 5 x 10^{-11} M solutions, respectively. Figure 3.10c is the blank. The broadness of the 595 cm^{-1} band in these spectra arises from the fact that the entrance slit of the spectrometer was set at 500 μm to improve signal collection. Spectra previously cited were acquired with a 30-μm slit width.

Estimation of detected molecules- towards single molecule detection. The extremely low LOD discussed above has provided an incentive to assess the feasibility of single-molecule detection with the silver-islands based substrate. Single molecule detection for liquid (Kneipp *et al.*, 1997,1998a, b) and solid (Nie and Emory, 1997) samples using SERS-active colloids has been previously reported. In a solid sample-based study similar to the work reported herein, Nie and Emory confirmed single molecule detection by analyzing polarized radiation from Rhodamine 6G adsorbed on immobilized silver colloids (Nie and Emory, 1997). In this work, the low photo-stability of the CFV did not allow such analysis. There are therefore several more critical parameters in evaluating the validity of the single molecule detection in this study. Aside from the obvious importance of the standard sample concentration, one must be highly confident in the volume deposited on the silver surface. Once confident of the total number of molecules deposited on the substrate, the surface area of the distributed sample spot and the relative homogeneity of the sample throughout the distributed spot must be noted. Finally, the number of molecules probed by the scanning laser is ultimately determined by the diameter of the focused laser spot.

When considering the probed surface area defined by the focused laser spot, one could estimate the dimensions of the spot by using a formula for the diffraction-limited spot
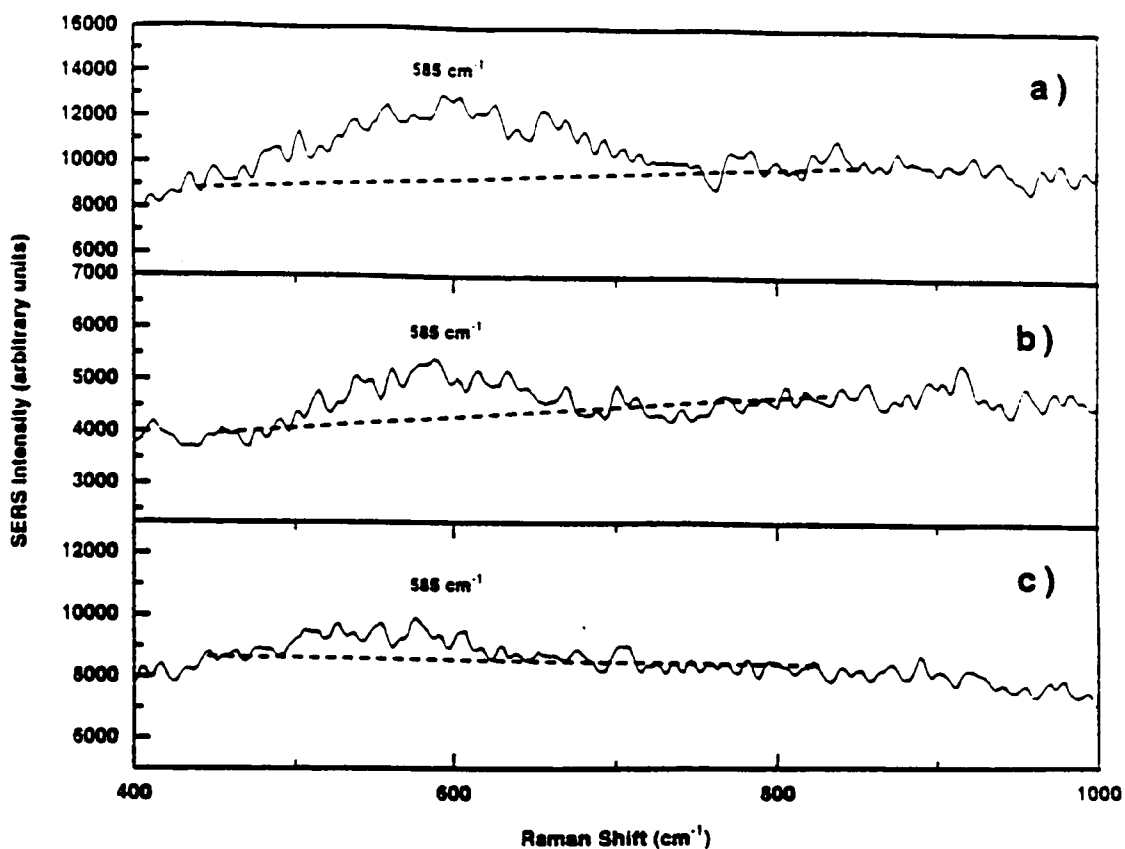
Figure 3.10. SERS spectra of 1-μl spot samples of a) 1 x 10^{-10} M and b) 5 x 10^{-11} M CFV, as well as c) a dry silver islands-based substrate blank, acquired with 632.8-nm excitation radiation and a 500-μm spectrograph entrance slit width. Laser power = 5 mW.

135

size. However, a theoretically-calculated diffraction-limited spot size assumes ideal optical configurations which are seldom met in actual measurements. For these studies, the sampling laser beam was considered optimally focused when yielding the highest SERS signal, as monitored in real time during the focusing step. While dependent on the incident number of photons, the SERS signal is directly proportional to the number of scattering molecules. Photodegradation is yet another factor which could affect the "apparent" optimum focus. Therefore, there may be some compromise in incident photon density to allow for a possibly more significant contribution from a greater number of undamaged molecules probed in the optimum observable SERS signal intensity. As a consequence, the optimum signal may not have coincided with the minimum possible focused laser spot size. Acknowledging this possibility, as well as the likelihood of optical aberrations, we opted to make a more direct determination of the laser spot size for the optimum observed SERS signal- measurement of a "hole" formed in the substrate surface by the focused probe beam after a relatively long period of irradiation.

The "hole" formed from the focused laser beam can result from either photochemical decomposition of the sample molecules, sample and/or surface ablation, or more subtle alterations in SERS-dependant interactions between the adsorbed sample molecules and the metal surface. For a surface on which SERS-active molecules have been evenly distributed, a "hole" is detected as an area of SERS-signal depression as the surface is scanned. This process has been exploited in the development of the surface-enhanced Raman optical data storage (SERODS) technology, in which "holes" as small as 0.5-μm in diameter have been observed (Vo-Dinh and Stokes, 1994).

136

Using high precision positioners, such as the Inchworm® motor-driven translation stages from Burleigh, it is possible to monitor hole dimensions by simply obtaining a profile of the SERS signal as a function of SERS substrate position in the laser probe beam. An example of such a profile is given in Figure 3.11. The "hole" is noticeable as a triangular-shaped depression in the otherwise relatively constant CFV SERS signal. The hole resulted from irradiation of the surface with a focused, 5-mW, HeNe laser beam for approximately 20 minutes. Without altering the focus, the substrate was then translationally moved to an unburned position, at which point the SERS signal profile was initiated. The plate was then scanned through the probe beam to analyze the burned region. While the SERS signal was monitored in real time, the points of signal depression and regeneration were recorded from the coordinates displayed on the translational stage control unit. The diameter of the hole, measured as the distance between the points of depression and regeneration of the base CFV SERS signal, was determined to be 20 μm.

It is worthy to note that this dimension is skewed due to a convolution effect analogous to the line-shape function of a scanning spectrometer, arising from the fact that the probe beam and the hole are of very similar diameter. In fact, the basis of this study is the assumption that the two entities are practically identical. With this fact in mind, one expects that the actual diameter of area sampled by the laser beam is approximately 1/3 the diameter illustrated in the figure, 6-7 μm. Embodied in this conclusion are the assumptions that the dimensions of the "hole" are identical to the dimensions of the area in which sample molecules contribute to the SERS signal, and that the incident photon flux density is constant across the diameter of the focused laser beam. Simply stated, detectable molecules must be equally burnable.

137
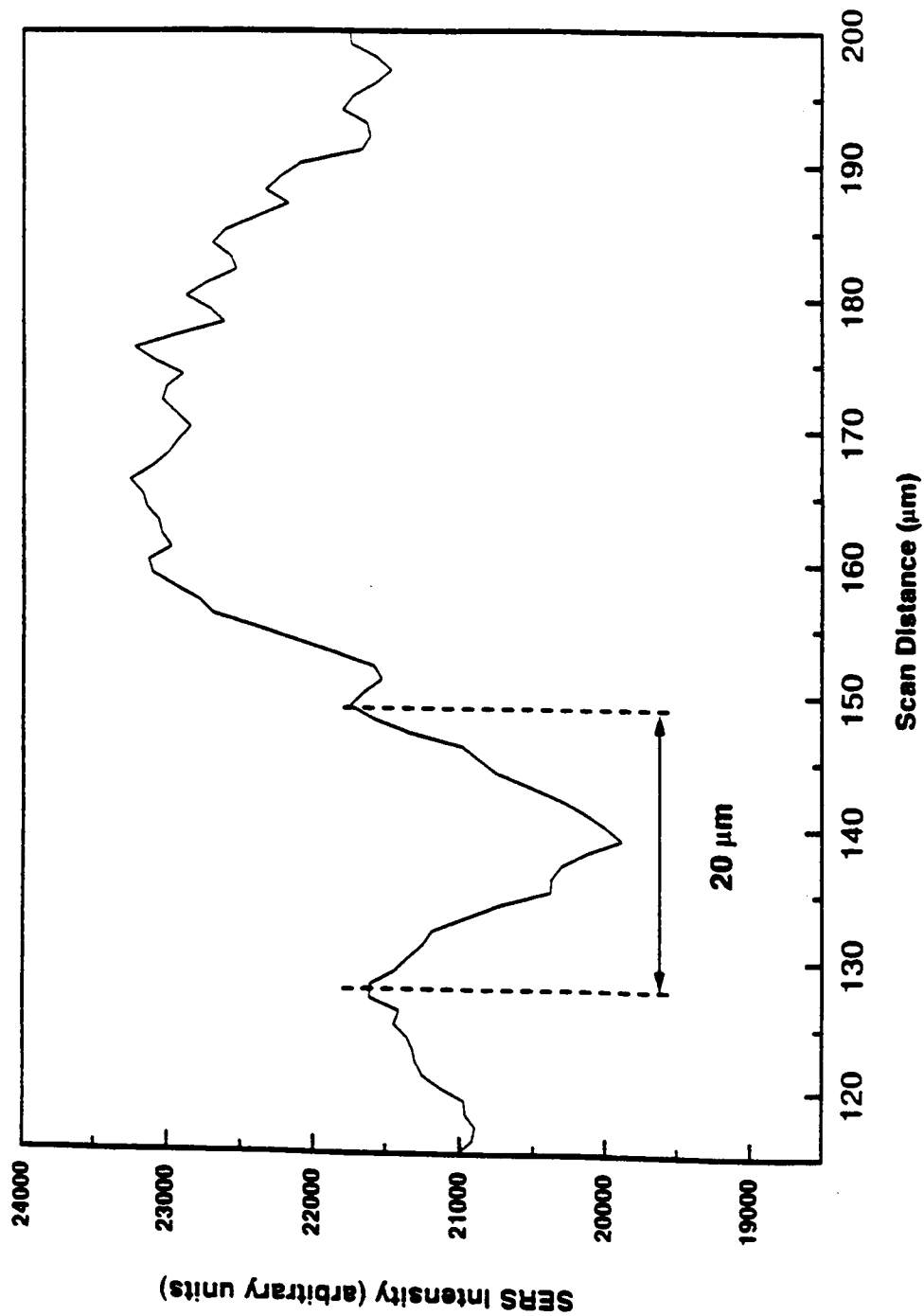
Figure 3.11. SERS signal profile of a 10^{-5} M spot sample (1 µl) of CFV as a function of substrate position, illustrating the burn "hole" used in estimating the 632.8-nm excitation laser beam diameter. CFV signal at 585 cm^{-1}. Laser power = 5 mW.

138

The distribution of molecules in terms of substrate area coverage and homogeneity is also a critical parameter in the determination of the number of sampled molecules. As was stated before, the deposition of the sample molecules on the SERS substrate surface involves the spotting of a 1-µl drop of an ethanolic solution of the sample molecules at the surface, followed by passive spreading and drying. The degree of spreading largely depends on the wettability of the substrate surface. This characteristic depends on relative surface hydrophobicity and surface roughness, both of which are dependent on the silver thickness of the silver-islands based substrate. Generally, solvent evaporation competes with spreading. The lower the wettability of the surface, the smaller the area of sample distribution.

In order to determine the nature of the coverage of the sample on the substrate surface, we acquired profiles of SERS signals as a function of substrate position. A typical profile is demonstrated in <u>Figure 3.12</u>. A 1-µl solution of 10^{-6} M CFV was deposited on the substrate. In order to get a profile truly representative of the spot diameter, the substrate was scanned through the probe beam with the inchworm driven translation stages while the SERS signal was recorded at 585 cm^{-1}. For a given scan, the center coordinate of the spot signal profile was noted from the translation stage control unit. An ensuing scan was performed with translation perpendicular to the previous scan and intersecting the center coordinate of the previous scan. Again, the center coordinate was noted and compared to that of the previous scan. These parallel scans were performed until agreement in the center coordinate for the perpendicular scans was made, after which a final scan, intersecting the established center coordinate, was performed to represent the spot diameter. For each spot tested, two perpendicular diameter scans were performed. After six trials, an average spot
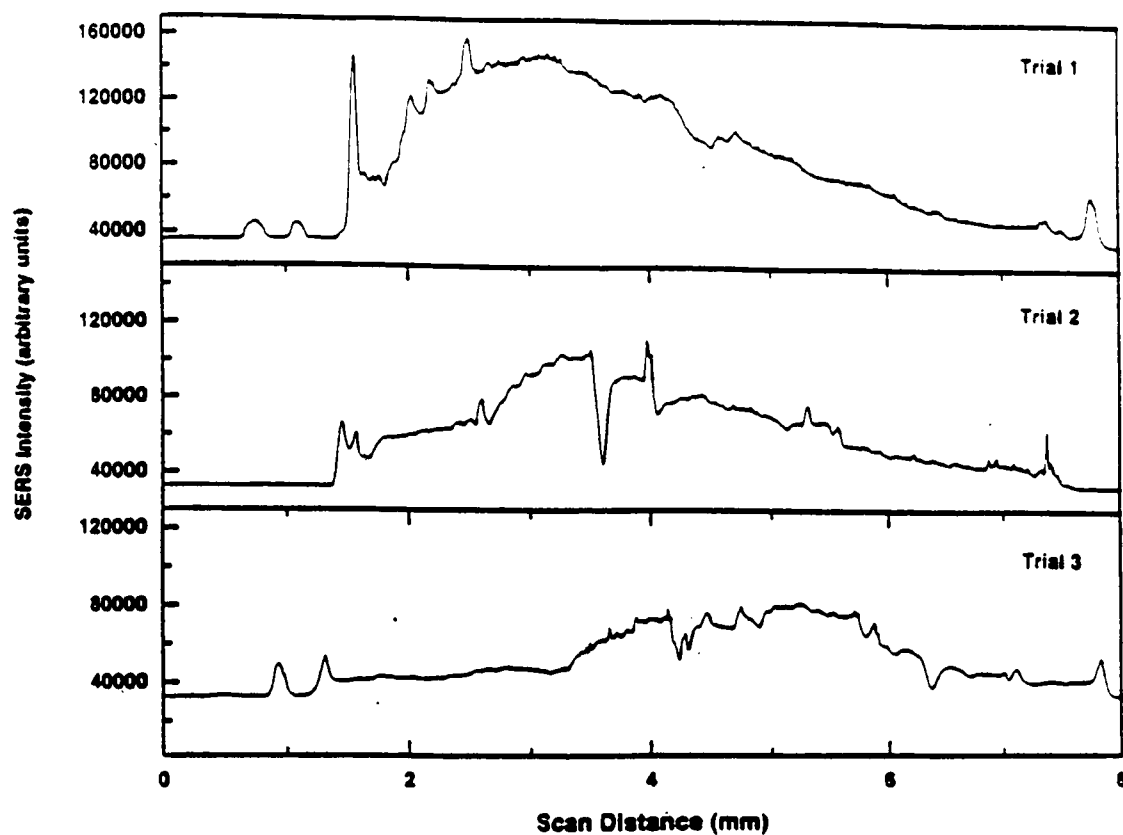
Figure 3.12. SERS signal profiles of a 10^{-5} M spot samples (1 µl) of CFV as a function of substrate position, illustrating the sample spot diameter. CFV signal at 585 cm^{-1}. Laser: HeNe, 632.8 nm, 5 mW.

140

diameter of 6.5 mm was established with a relative standard deviation of approximately 6%.

Figures 3.12a, b and c illustrate typical spot profiles. Common to each profile is a pair of intense spikes which define the rim of the spot. This effect is though the arise from a higher number of molecules which gather in a "ring" formed by the sample drop. Formation of the "ring" arises from the resistance to spreading due to surface tension, causing the laminar layers to pile up at the edge of the spot just prior to solvent evaporation. The resistance to spot spreading also explains the "bulge" typically observed in the inner region of the spot profile. Incomplete dissipation of the sample drop at the inner region of the spot while wet leads to the deposition of a larger number of molecules at the surface directly beneath the bulge when the solvent evaporates. In order to minimize this effect, the sample is typical deposited evenly on the substrate surface with the help of a photoresist spinner. Of course, loss of sample results. We bypassed this procedure so that we could be more confident of the total number of molecules distributed on the plate. Intense spikes in the inner regions of the spot profiles are also occasionally observed. As mentioned before, these "hot" spots probably arise from sporadic surface features which either provide further signal enhancement or cause localized agglomeration of the sample molecules, such as fine cracks or microparticles. Occasionally a sharp depression in the SERS signal is observed in a profile as well. This is thought to be simply a scratch in the delicate silver coating, probably resulting from the sample spotting step.

In closing, a conservative estimate of molecules detected was based on the CFV signal from the 5×10^{-11}M concentration deposited sample, which exhibited a S/N value of 2-3. The volume of the spot was 1-μl, corresponding to 5×10^{-17} moles or 3×10^{7}

141

molecules. These molecules were distributed over a spot of approximately 6.5 mm diameter. If we assume a focused laser excitation spot diameter to be 10 μm, the number of molecules probed was determined to be approximately 70, according to the following formula:

$$N_d = N_t * \left(\frac{D_p}{D_s}\right)^2$$

where N_d corresponds to the estimated number of molecules detected, N_t is the total number of molecules deposited, D_p represents the detection zone diameter (or laser spot diameter), and D_s denotes the total diameter of the distributed sample spot.

It is interesting to note that, for a laser spot diameter of 6-7 μm, as suggested above, the estimation is dramatically decreased to approximately 30 molecules. This calculation assumes an even distribution of the molecules with no agglomeration. It is also important to note that if the condition of "hot" spots applies to this silver-islands-based substrate, the actual number of detected molecules could be much less. For example, it would take on the order of 10^{12}-10^{15} CFV molecules to form a monolayer over a spot of 6.5 mm-diameter, depending on the preferred orientation of the compound on the substrate. This number is far greater than the estimated 3×10^7 molecules deposited. The scarceness of the deposited molecules coupled with the scarceness of the "hot" spots could explain why some probed areas ($\approx$10-μm diam.) of the spot sample yielded no signal. Moreover, if we assume an even distribution of the sample, such "hot" spots must be much more sparse than the sample molecules and/or must be nonuniformly distributed at the 10-μm scale. This condition would support

the claim for the detection of far less than the 70 molecules estimated for a homogeneously SERS-active 10-μm spot.

Finally, it is noteworthy to mention that the optical system used in this study was far less than ideal for the sole purpose of single molecule detection. The SERS substrate described herein could be expected to yield even more impressive LODs through elimination of the optical fiber and the associated coupling optics. Furthermore, judicious filter selection could replace the spectrograph for improved throughput at the expense of the spectral information offered by the spectrographic mode of detection.

CHAPTER 4

APPLICATION OF A POLYMER FILM TO SOLID SERS SUBSTRATES FOR ENHANCED SELECTIVITY AND STABILITY

INTRODUCTION

Since the SERS discovery, exhaustive efforts have been devoted towards the development of practical substrates that conform to the theoretical models mentioned above. A wide range of SERS-inducing media and applications has been discussed in previous chapters. Thus far, however, discussions of practical SERS substrates have been mostly limited to bare roughened metal surfaces. Application of these substrates to selective chemical detection in complex samples has been demonstrated, owing to the highly structured and narrow features common to the Raman scattering process. Nevertheless, additional measures have been taken to further enhance selectivity and detectivity of commonly-used SERS media. Electrochemical probes have been the basis for selective SERS sensors (Carrabba *et al.*, 1987; Angel and Archibald, 1989). The use of indicators for selective metal ion and pH detection has been reported (Carron *et al.*, 1990; Mullen *et al.*, 1992). Selective adsorption of metal ions and aromatic compounds by thiol-modified metal surfaces has also been demonstrated (Carron *et al.*, 1992; Heyns *et al.*, 1994). Other organic modifications of metallic surfaces has been reported as well (Thompson and Pemberton, 1994; Hill *et al.*, 1994; Hill *et al.*, 1995). A reversed phase liquid chromatography (HPLC) stationary phase applied to silver surfaces for the study of

144

nonpolar analyte interaction with the stationary phase via Raman spectroscopy has been reported (Thompson and Pemberton, 1994).

Despite the phenomenal successes demonstrated by these SERS-inducing media, limitations still exist. In the case of the solid surface-based substrate class of substrates described in Chapters 2 and 3, durability and longevity can be a limiting factor in practical applications. Among such limitations are the durability and longevity of bare SERS substrates. The typical SERS substrate active layer is vulnerable to mechanical disturbance as well as air oxidation (particularly in the case of silver island-based substrates). There has therefore been increased effort in developing protective coatings for the SERS substrate in the form of polymer layers. Such layers may hinder the interaction of the analyte with the metal surface which is imperative for the SERS effect. In this study the polymer, poly(vinylpyrrolidone)(PVPL), was investigated as a potential protective coating for the solid substrates described in Chapters 2 and 3. Previous studies have demonstrated the permeability of PVPL to compounds having hydrogen-bonding properties (Mourey *et al.*, 1976). Because of this permeability, the coating may be applied in relatively thick layers while still enabling the detection of monocyclic aromatic compounds including alcohol, carboxylic acid, and various nitrogen-based functional groups, with varying signal enhancement. This work demonstrates the potential for a long lasting, durable, and selective SERS detection probe using PVPL.

EXPERIMENTAL

Apparatus

SERS spectra were acquired with an Instruments SA, Inc., HR-320 spectrograph equipped with a Princeton Instruments RE-ICCD (Model RE/ICCD-576S). The spectrograph was equipped with a 600 groove/mm grating, yielding a reciprocal linear dispersion of 50 nm/mm. All measurements were performed with a 30-μm entrance slit; the resolution was approximately 3.3 cm^{-1} at 657 nm. After calibration, the spectral accuracy of the spectrograph was ± 1.5 cm^{-1}. The RE-ICCD was thermoelectrically cooled to -34° C. All data acquisition and processing steps were carried out with a software package developed by Princeton Instruments (CSMA, v.2.0).

The auxiliary optical system used for this work is illustrated in <u>Figure 4.1</u>. The 632.8-nm line of a helium-neon laser (Spectra Physics, Model 106-1) was the excitation source. A narrow bandpass filter (Corion, Model P3-633-A-X516) was placed in the laser beam to reject laser plasma lines before being focused onto the sample. The filter bandpass was 3.0±0.5 nm (FWHM), and the resulting beam power was approximately 3 mW at the sample. The laser beam was focused to a diameter of approximately 100 μm at the SERS substrate surface. A backside (glass side) excitation geometry was used with the laser beam normal to the substrate plane, and the Raman-scattered radiation was collected at 180° with respect to the laser beam using a two-lens system. A Raman holographic notch filter (Physical Optics Corporation) was placed in the collected beam to reject Rayleigh scattering. The Raman scattering was focused onto a 600-μm core, 0.22-NA optical fiber (General Fiber Optics).

146
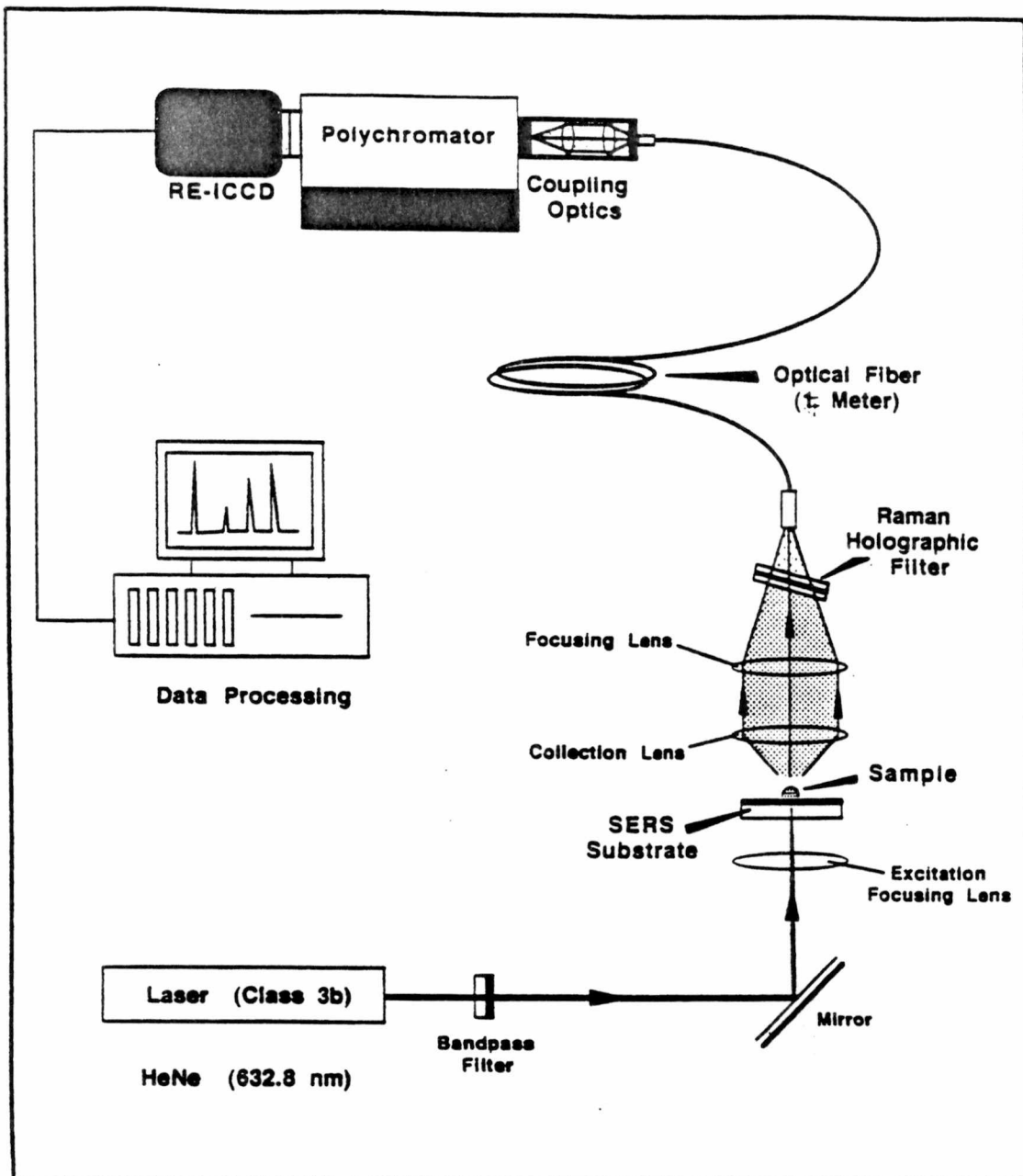
Figure 4.1. Schematic diagram of an optical system for SERS detection featuring an ICCD-based spectrograph and a backside/frontside geometry for excitation/collection.

147

For liquid sample measurements, a 5-mm path length quartz cell was used to contain the aqueous sample solutions. The SERS substrates were cut to fit the cell (0.6 cm x 1 cm) and placed in the bottom of the cell with the SERS-active (silver) side up. Sample solutions were then added to the cell, completely submerging the substrate.

SERS Substrates

Alumina-based substrates and silver island film-based substrates were prepared for maximum SERS enhancement as described in Chapters 2 and 3, respectively. For polymer-coated substrates, a simple dipping procedure was employed. A 5% (wt/vol) solution of PVPL (Aldrich) was first prepared in reagent-grade methanol (J.T. Baker). The 5 - 10 ml PVPL solution was prepared daily in a 20-ml glass scintillation vial. The bare alumina-based or silver island-based substrates were individually dipped in the solution with forceps and immediately laid on a level surface and allowed to cure for at least thirty minutes at room temperature (300 K) prior to use. The angle of dipping was varied for evaluation, as described in later discussions.

Chemicals

All sample chemicals were purchased with the highest purity and used without further treatment. Test compounds included PABA (99% pure, Aldrich), 4-aminopyrimidine (98% pure, Aldrich), benzoic acid (reagent grade, Mallinckrodt), 2,4-dinitrophenol (90-95% pure, Sigma), isonicotinamide (99% pure, Aldrich), isonicotinic acid (99% pure, Aldrich), and 4-picoline (98% pure, Aldrich). All samples were prepared in water which was purified with a Waters Milli-Q+ filtration system, at concentrations cited in the discussions.

RESULTS AND DISCUSSION

Evaluation of Polymer Coating Procedures

Parameters that could affect the thickness and density of the polymer layer were investigated to optimize the enhancement in SERS signal yielded by PVPL-coated SERS substrates. Such parameters included polymer solution concentration, dipping time, and the angle of dipping. Using the report of previous a study as a reference (Mourey *et al.*, 1976), a 5% methanolic solution of PVPL was selected for this study. Furthermore, the dipping time was kept constant at 1 s for these optimization studies. Measurements were performed to determine the effect of the angle of dipping on the observed SERS signal. Benzoic acid SERS spectra acquired with alumina-based SERS substrates which were coated via horizontal dipping (0° with respect to the polymer solution surface) and vertical dipping are illustrated in Figures 4.2a and b, respectively. These spectra were acquired *in situ* at 3.4 x 10^{-3} M analyte concentration. For these two extremes, the horizontal dipping procedure appeared to be the most effective, yielding a SERS signal at 1010 cm^{-1} which was approximately 13 times more intense than that yielded by the vertically-dipped substrate. The horizontal dipping procedure was thus used for all subsequent experiments. The thickness of the polymer coating for this optimized substrate was determined to be approximately 7 μm by confocal microscopy.

Signal Stabilization with Exposure Time Study

Directly related to the effect of polymer thickness on signal enhancement is the exposure time, *t*, required to obtain the optimum, stable SERS signal. One can assume that the
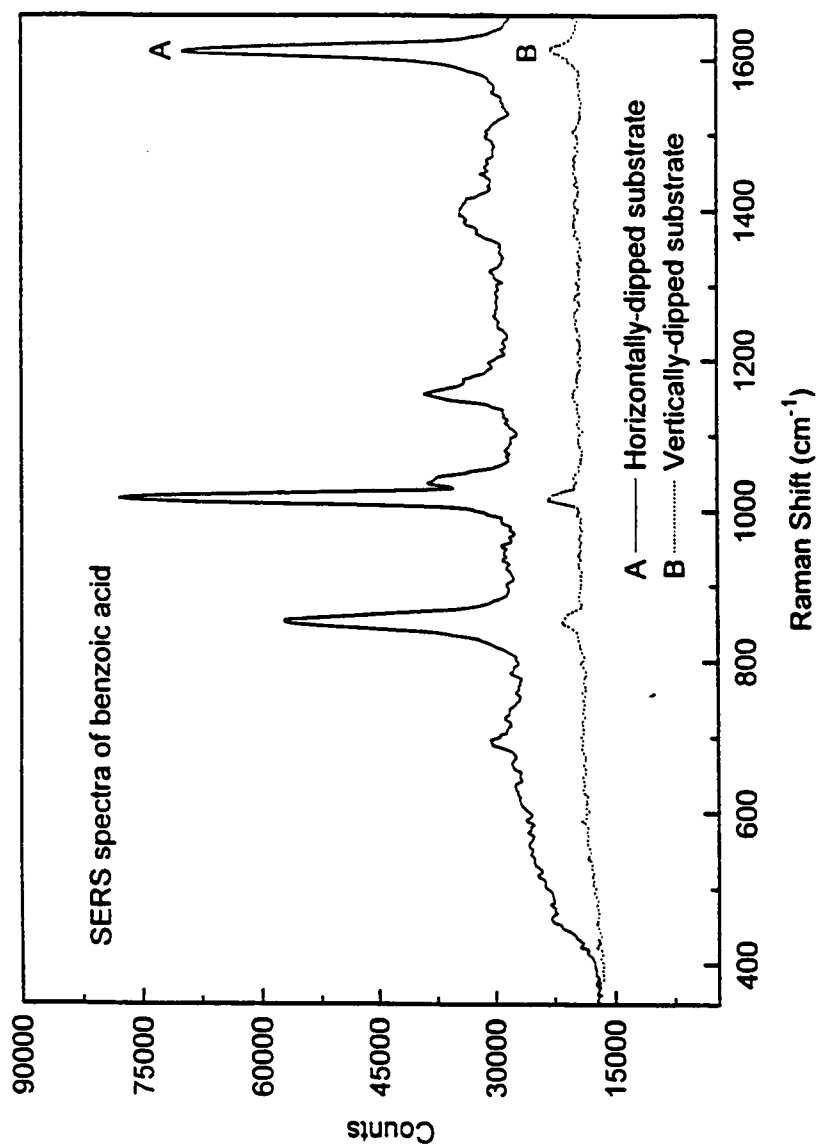
Figure 4.2. SERS spectra of 3.4 x 10^{-3} M solution samples of benzoic acid acquired *in situ* with PVPL-coated alumina-based substrates prepared with a) horizontal, and b) vertical polymer dipping procedures. Laser: HeNe, 632.8 nm, 5 mW.

Source: A. Pal, D. L. Stokes, J. P. Alarie, and T. Vo-Dinh, *Anal. Chem.* **67**, 3154 (1995).

signal enhancement is a time-dependent process which is a function of the permeability of the coating to an analyte compound as well as the film thickness. When taking into consideration the fact that at the initial exposure time the barrier polymer film produces a concentration gradient, dC/dx, between the bulk analyte solution and the active substrate surface, one can expect adherence to Fick's 2nd law:

$$\frac{dC}{dt} = D\left(\frac{d^2C}{dx^2}\right)$$

(4.1)

where D would represent the coefficient for analyte diffusion across the polymer film, x denotes the polymer film thickness, and dC corresponds to the difference in analyte concentration between the bulk solution and the interface with the metal substrate surface.

Figure 4.3 demonstrates that intensity of the SERS signal is indeed a time-dependent process, particularly when the polymer-coated substrate is used. In generating the data, a 3.4 x 10^{-3} M solution of benzoic acid was added to the sample cell. The polymer-coated, alumina-based SERS substrate was submerged in the cell at time zero. Once SERS signal growth tapered off, the procedure was repeated for an uncoated substrate for comparison. For this example, signal growth for the polymer-coated substrate was linear till approximately 30 minutes of exposure, at which point the enhancement factor was approximately 2.3 with respect to the SERS signal from the uncoated alumina-based SERS substrate. As would be expected, the analyte concentration between the SERS active surface of the substrate and the bulk solution came to equilibrium, thereby diminishing the driving force of the concentration gradient as is observed in the figure. The enhancement of the signal implies sample enrichment due to the matrix of the polymer

151
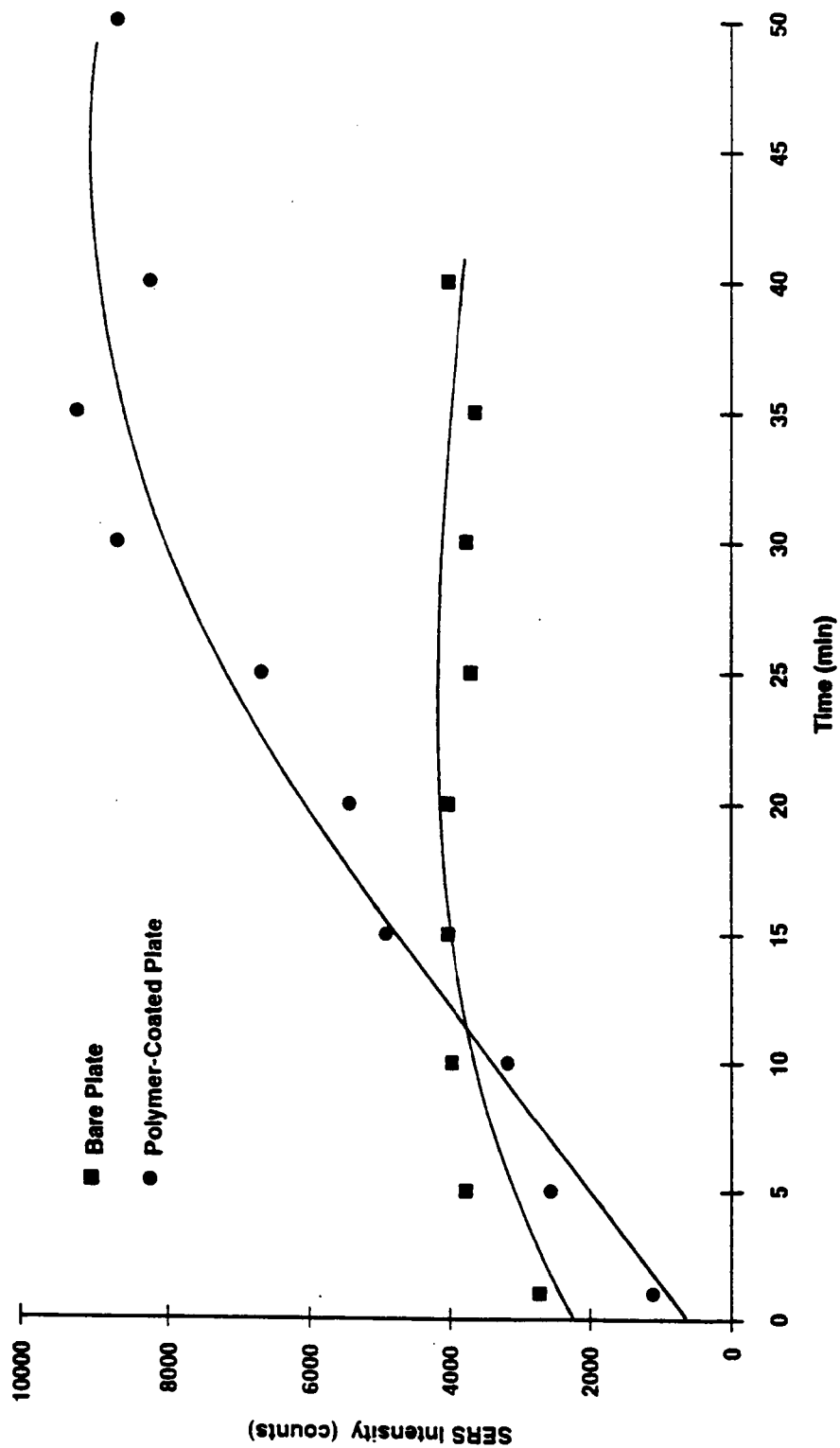
Figure 4.3. SERS intensity plots as a function of time for the 1010-cm^{-1} band of benzoic acid (3.4 × 10^{-3} M) acquired *in situ* with bare and polymer-coated, alumina-based substrates. Laser: HeNe, 632.8 nm, 5 mW.

film at the SERS active surface as well. It is also interesting to note that the uncoated substrate exhibited a time-dependent signal, but to a much lesser degree. While no barrier is present to set up a concentration gradient, the SERS effect is dependent upon the process of adsorption of the analyte to "active sites" on the substrate, which also requires time for equilibrium between the substrate surface and the bulk solution to be reached. Of course, the same effect occurs for the polymer-coated substrate, but its contribution is presumably insignificant in comparison to the diffusion across the polymer layer. This condition would also explain why the initial signal for the uncoated substrate is more intense than that for the coated substrate. The results of this study illustrate that exposure time to analyte solutions could be an important factor for the accuracy and precision of substrate evaluations or quantitative analyses. Because this parameter is likely dependent on the molecular structure of analyte compounds, all subsequent measurements in subsequent studies were performed upon observing time-stabilized SERS signals, regardless of the time interval required for a given analyte.

Reproducibility and Background Evaluations for the PVPL-Coated Substrate

A relatively high degree of substrate-to-substrate reproducibility was observed for the 1020-cm^{-1} SERS signal of an isonicotinic acid sample. In performing the study, a 2.2×10^{-3} M solution of the analyte was added to the sample cell. Upon submersion of a PVPL-coated alumina-based substrate in the solution, the SERS signal was observed to become stabilized after approximately 10 min. Five trials were performed, each with fresh PVPL-coated substrates and sample solutions. The relative standard deviation was determined to be approximately 20%. In light of all the experimental variables possible throughout the substrate preparation and measurement steps, this result is especially

encouraging since one can expect a 10-15% relative standard deviation in signals based on the performance of uncoated SERS substrates with *in situ* measurements.

A useful feature of the PVPL coating is its low background SERS signal. <u>Figure 4.4</u> illustrates a blank spectrum for the polymer substrate submerged in pure water. No significant SERS or normal Raman bands from the PVPL coating are observed for the spectral region of interest.

PVPL-Coated Substrate Durability Studies

The use of a polymer coating for SERS substrates is important because it can provide a protective coating for the otherwise delicate SERS-active surface. For example the polymer can make the SERS substrate more resistant to scratching, thereby making it more rugged for field work. This feature was illustrated when both polymer-coated and uncoated alumina-based substrates were scraped with a brush. While the uncoated substrate was severely damaged, no visible surface change was observed for the PVPL-coated substrate.

In addition, the coating can minimize air oxidation of the silver surface and thereby extend its useful shelf life. In an experiment designed to illustrate this advantage, 10-μl aliquots of a 10^{-3}M PABA solution were deposited evenly on clean glass strips and allowed to dry. The chemically-coated glass strips were then placed in a vacuum evaporation silver and coated with 10 nm silver. Subsequently, half of the PABA-based silver islands film substrates were coated with 5% PVPL as described above, while the other half were left uncoated. These substrates were periodically measured to compare SERS activity between the polymer-coated and uncoated substrates. Although a freshly-

154
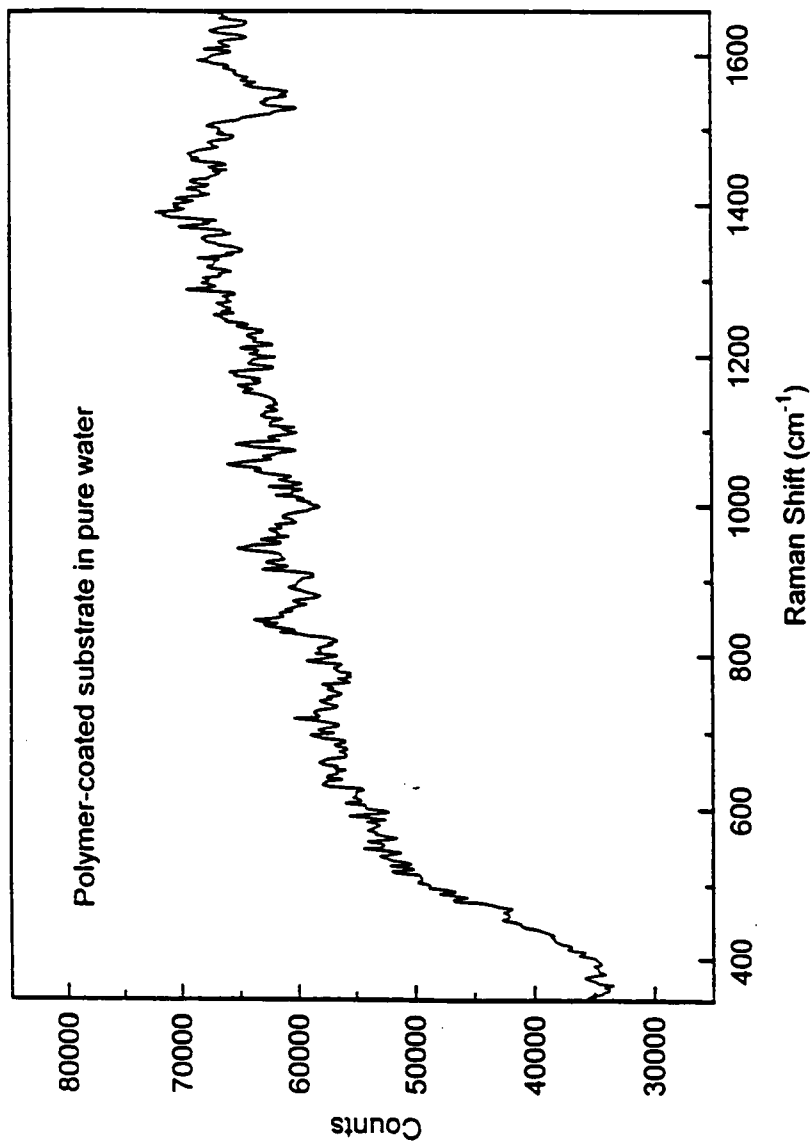
Figure 4.4. Blank spectrum of a PVPL-coated alumina-based substrate submerged in water. Laser: HeNe, 632.8 nm, 5 mW.

Source: A. Pal, D. L. Stokes, J. P. Alarie, and T. Vo-Dinh, *Anal. Chem.* **67**, 3154 (1995).

155

prepared silver islands-based substrate performs comparably to an alumina-based substrate, degradation of SERS activity with age is much more pronounced with the silver islands substrate. Figure 4.5 depicts the PABA SERS signal intensities at 1464 cm^{-1} measured from PVPL-coated and uncoated silver islands substrates over a 24 day period. The protective capability of the PVPL coating is clearly demonstrated. By the 24th day, the PABA signal from the uncoated substrate is reduced to zero while the corresponding signal remains at maximum intensity for the polymer-coated substrate. The increase in signal over the first few days is probably due to improved adsorption of the PABA to the silver islands as the polymer layer cures. Subsequent measurements were performed for the polymer-coated substrate for up to 116 days, when the PABA signal was observed to decrease to approximately 30% of the maximum value. The decreasing signal trend over the extended period was gradual and consistent enough to justify ruling out abrupt changes in experimental conditions (e.g. optical alignment) as the source of the decreased signal. Detector response drift, another possible factor in the trend of decreasing signal, was not monitored.

SERS Spectra of Selected Compounds Using PVPL-Coated SERS Substrates

In general, the SERS effect is strong for analyte molecules adsorbed on or close to the metal surface. A discussed above, the polymer coating thickness was determined to be approximately 7 μm. A distance of 7 μm is large even for the long-range electromagnetic contribution to the SERS effect, which decreases proportionally with the cube of the distance from the surface. For this reason, it is believed that the analyte molecules need to permeate through the polymer coating and get close to the silver coating to experience significant Raman scattering enhancement. The relatively thick layers of PVPL have permitted the detection of various compounds for which the polymer

156
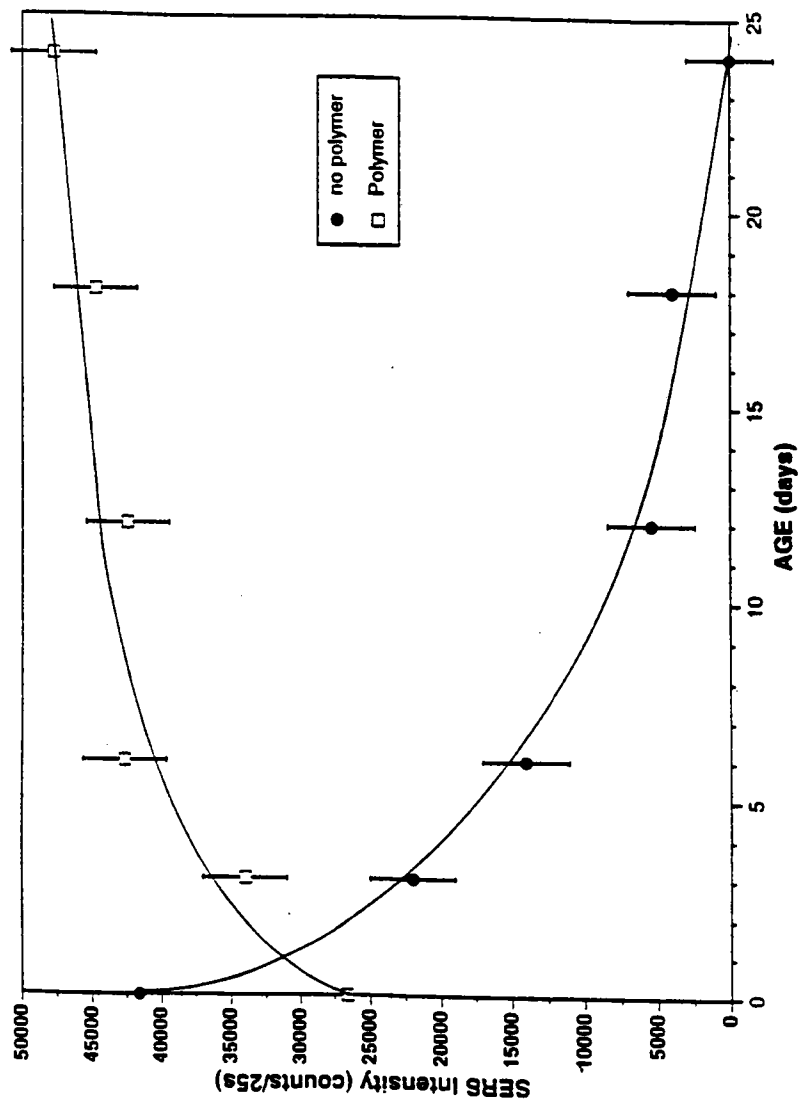
Figure 4.5. SERS intensity plots of the 1464-cm^{-1} band of PABA acquired from bare and polymer-coated, alumina-based substrates monitored over a 24-day period, illustrating the shelf life-prolonging capability of the PVPL coating. Laser: HeNe, 632.8 nm, 5 mW.
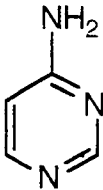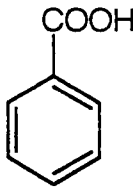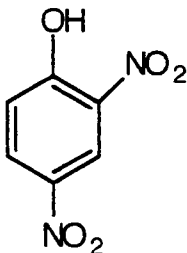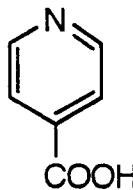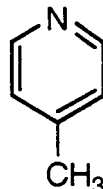
Source: D. L. Stokes, M. J. Sepaniak, and T. Vo-Dinh, *Anal. Chim. Acta.* (1999) in press.

coating exhibits permeability. Some of the compounds that we have investigated are listed in Table 4.1, along with their chemical structures. Generally, we have been able to detect monocyclic aromatic compounds with carboxylic acid or alcohol functional groups, as would be expected from permeability data reported in the literature (Mourey, 1976). Our results have also included detection of monocyclic compounds with nitrogen-based functional groups, including amino, amide, nitro, and azo groups. The PVPL coating has produced a signal enhancement in addition to the SERS effect for several compounds. This feature is herein referred to as the additional enhancement (AE). Figures 4.6-4.8 illustrate SERS spectra for several compounds measured, *in situ*, from solutions using a)polymer-coated, and b) uncoated alumina-based SERS substrates. Figure 4.6 illustrates the comparison of the SERS spectra for a 3.4 x 10^{-4} M benzoic acid solution. In this case, an AE factor of approximately 6.7 (using the 1010-cm^{-1} peak as reference) is observed for the PVPL-coated substrate. Figure 4.7 illustrates a similar comparison for a 2.2 x 10^{-3} M solution of isonicotinic acid. Based on the peak at 1020 cm^{-1}, an AE factor of approximately 9.6 is demonstrated. Figure 4.8 shows the spectra of a 2.5 x 10^{-3} M solution of 2.4-dinitrophenol. In this case, the AE factor is approximately 1.3, based of the peak at 1346 cm^{-1}. The differences in the AE factor for different compounds may be used as a selectivity parameter for the analysis of mixtures.

Selectivity Study with Binary Mixtures

As demonstrated in the above discussion, the PVPL coating exhibits different AE factors for different compounds. We further investigated this selectivity feature through analyses of binary mixtures having varying affinities for the PVPL-coated substrate. In the first test, a mixture of 4-picoline and benzoic acid was tested with the anticipation

158

Table 4.1. Compounds selected for evaluation of PVPL-coated SERS substrates

Compound	Structure	AE Factor
4-aminopyrimidine		
Benzoic acid		6.7
2,4-dinitrophenol		1.3
Isonicotinic acid		9.6
4-picoline		

159
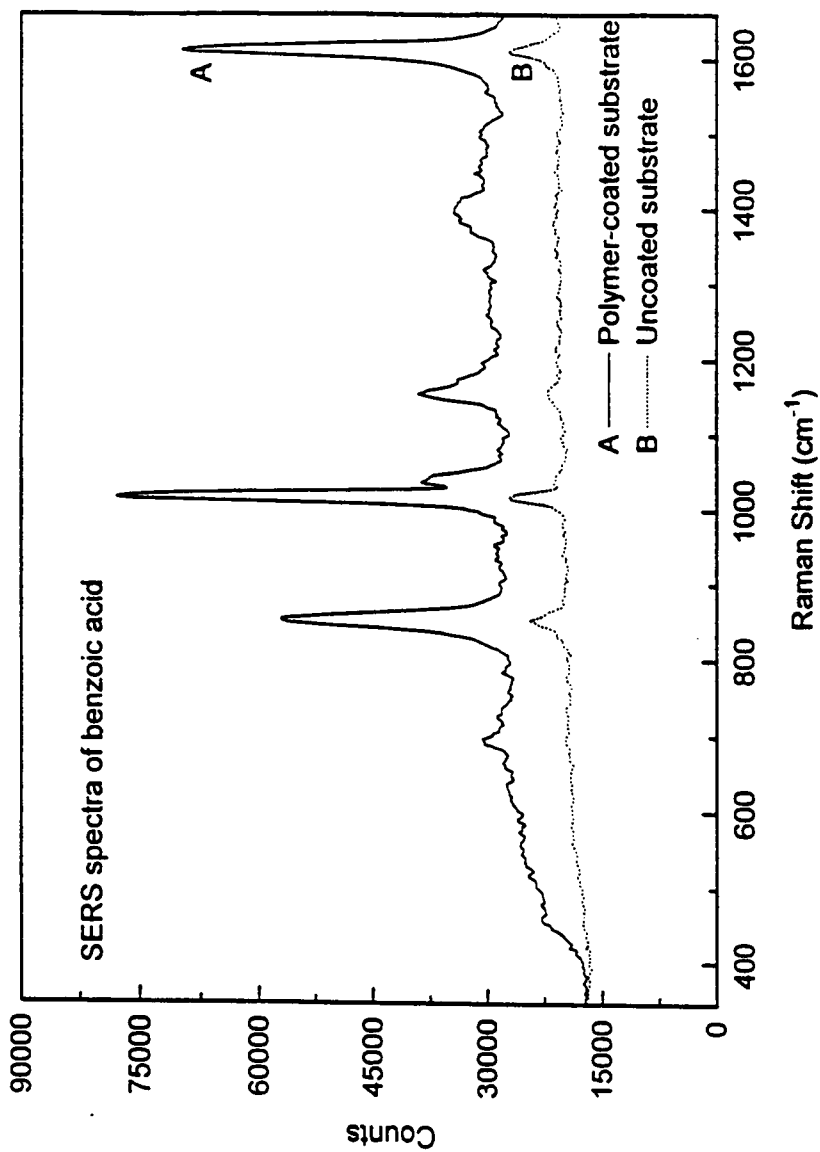
Figure 4.6. SERS spectra of a 3.4 x 10^{-4} M solution sample of benzoic acid acquired *in situ* with a)PVPL-coated, and b) bare alumina-based substrates. Laser: HeNe, 632.8 nm, 5 mW.

Source: A. Pal, D. L. Stokes, J. P. Alarie, and T. Vo-Dinh, *Anal. Chem.* **67**, 3154 (1995).
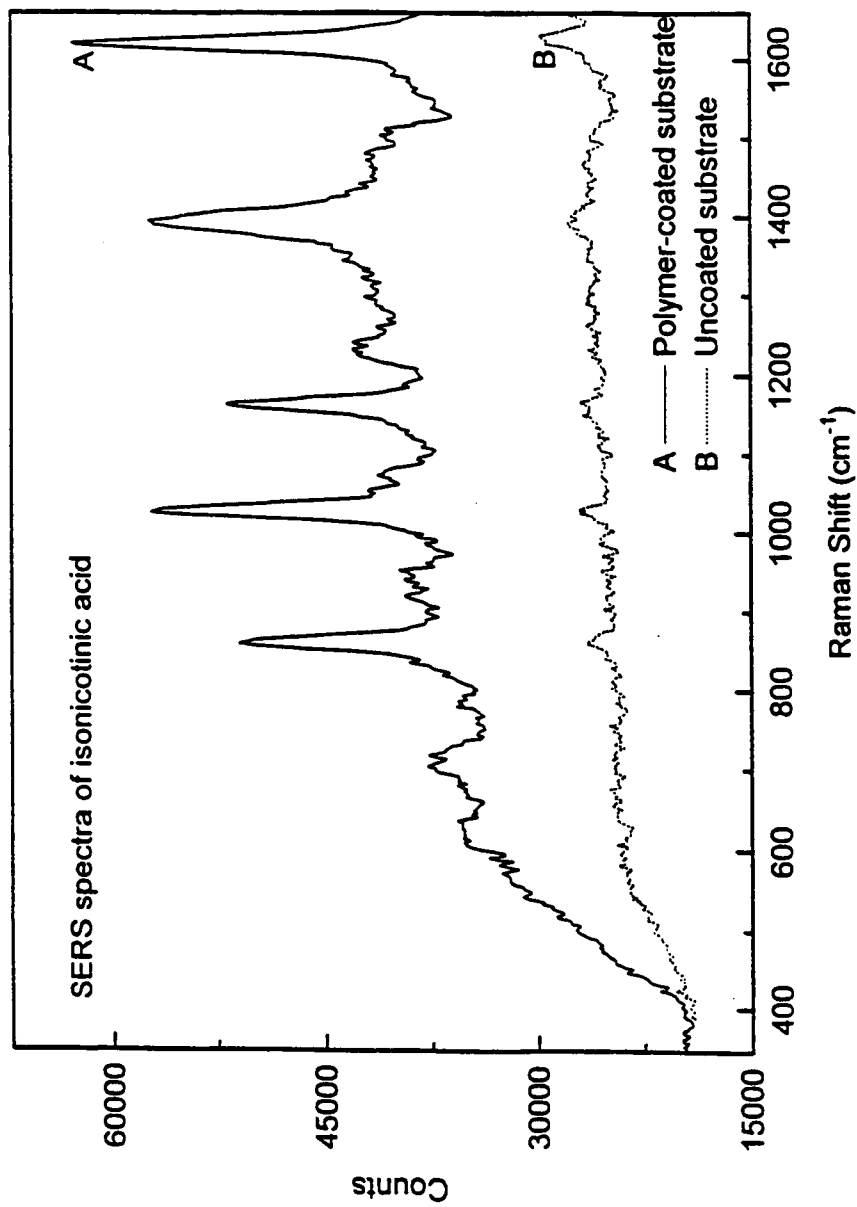
Figure 4.7. SERS spectra of a 2.2 x 10^{-3} M solution sample of isonicotinic acid acquired *in situ* with a)PVPL-coated, and b) bare alumina-based substrates. Laser: HeNe, 632.8 nm, 5 mW.

Source: A. Pal, D. L. Stokes, J. P. Alarie, and T. Vo-Dinh, *Anal. Chem.* **67**, 3154 (1995).
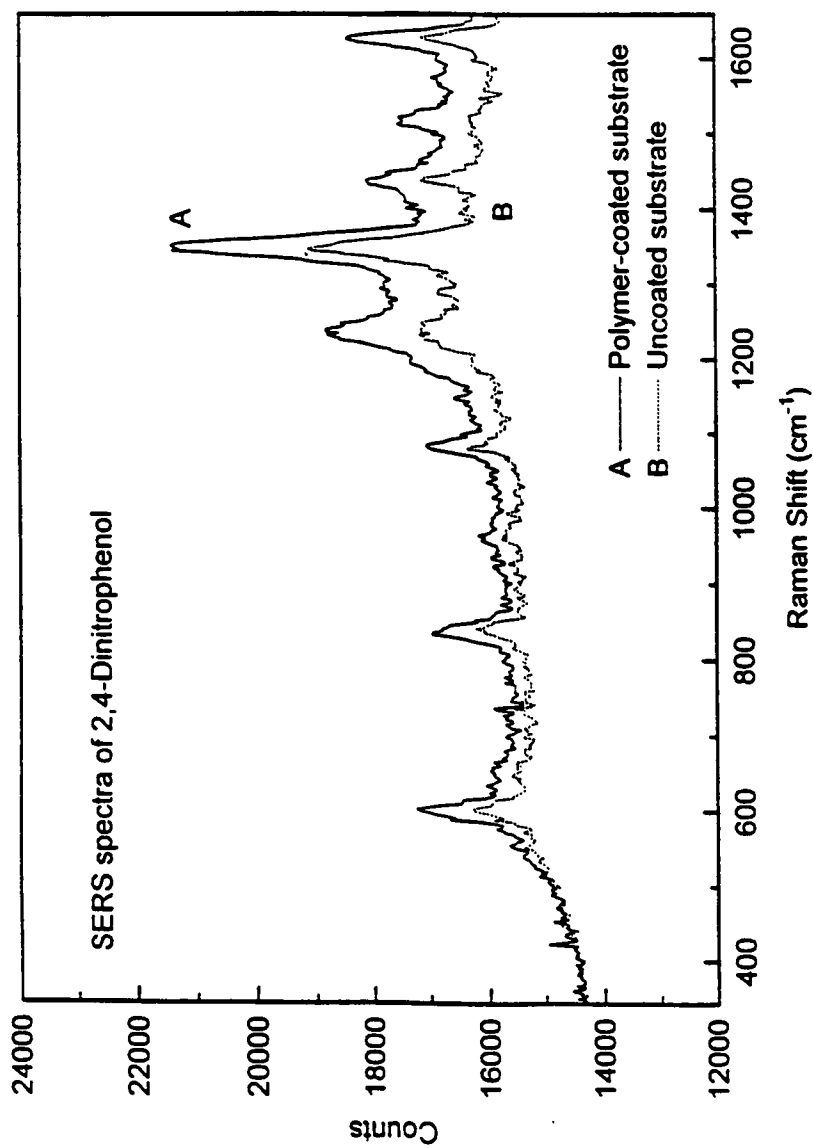
Figure 4.8. SERS spectra of a 2.5 x 10⁻³ M solution sample of 2,4-dinitrophenol acquired *in situ* with a)PVPL-coated, and b) bare alumina-based substrates. Laser: HeNe, 632.8 nm, 5 mW.

Source: A. Pal, D. L. Stokes, J. P. Alarie, and T. Vo-Dinh, *Anal. Chem.* **67**, 3154 (1995).

that the benzoic acid detection would be favored due to the carboxylic acid functional group (see Table 4.1). The concentration of benzoic acid was 1.73×10^{-3} M while the concentration of 4-picoline was 2.55×10^{-3} M. Parts A and B of Figure 4.9 show the SERS spectra obtained with the use of a polymer-coated and uncoated alumina-based SERS substrate, respectively. A summary of assignments of the bands observed for the benzoic acid/4-picoline mixture using the coated and uncoated substrates is compiled in Table 4.2. The results of this study indicate that the dominant compound detected with uncoated substrate was 4-picoline, with two bands (1248 and 1472 cm^{-1}) uniquely attributable to 4-picoline. Unfortunately, the bands at 1026, 1405, and 1626 cm^{-1} are common to both compounds, so their assignments was uncertain. Further review of Figure 4.9a reveals the presence of bands uniquely characteristic for benzoic acid (864 and 1174 cm^{-1}). This observation demonstrated the permeability of the polymer layer to both compounds. However, the relative enhancement of the unique benzoic acid bands in Figure 4.9a indicates that the PVPL favors the detection of benzoic acid in this binary mixture, as expected.

A second test was performed for a mixture of 4-aminopyrimidine (1.73×10^{-3} M) and isonicotinic acid (1.1×10^{-3} M), with the anticipation that the isonicotinic acid detection would be favored with the polymer-coated substrate due to its carboxylic acid functional group (see Table 4.1). Figures 4.10a and b represent SERS spectra of the mixture acquired with coated and uncoated alumina-based SERS substrates, respectively. A summary of assignments of the bands observed for the isonicotinic acid/4-aminopyrimidine mixture using the coated and uncoated substrates is compiled in Table 4.3. For the uncoated SERS substrate submerged in the sample mixture (Figure 4.10b), the bands characteristic of isonicotinic acid (868, 1036, 1402, and 1630 cm^{-1}) and of 4-aminopyrimidine (898, 1216, 1330, and 1504 cm^{-1}) were present. In addition,

163
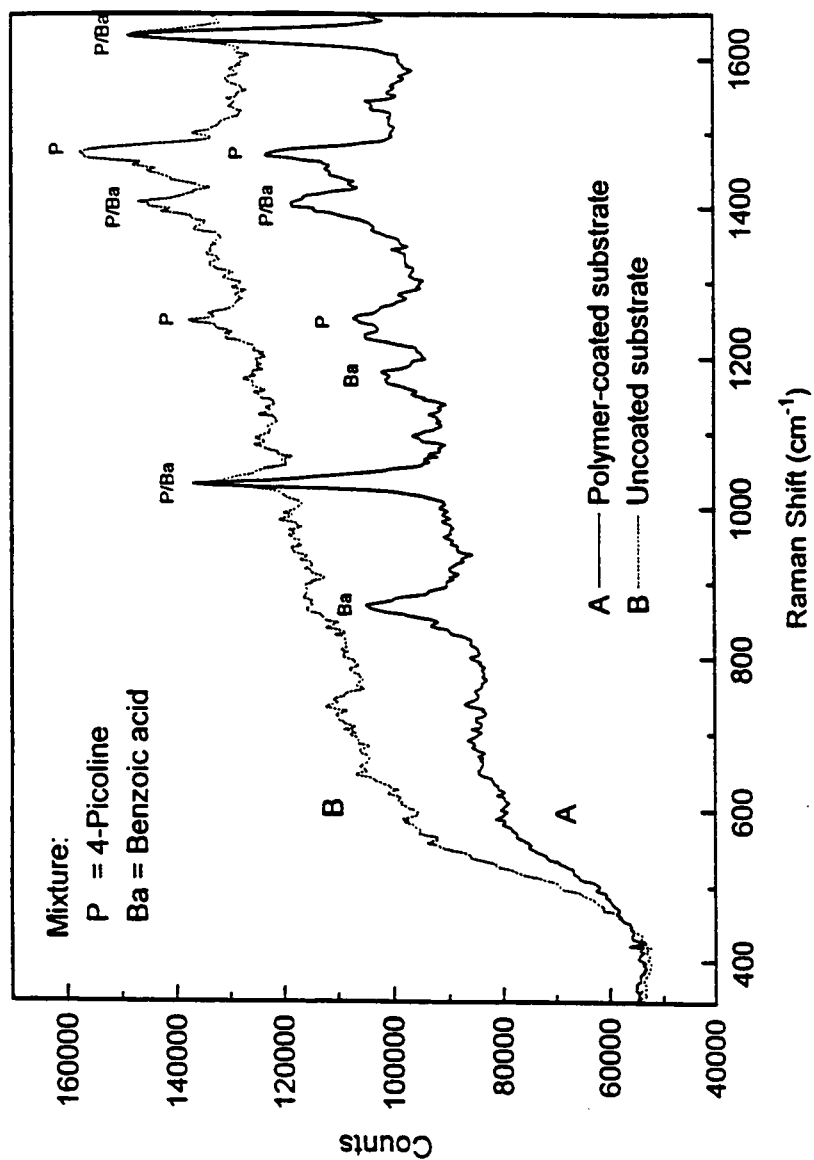
Figure 4.9. SERS spectra of a binary mixture solution of benzoic acid (1.73×10^{-3} M) and 4-picoline (2.55×10^{-3} M) acquired *in situ* with a)PVPL-coated and b) bare alumina-based substrates. Laser: HeNe, 632.8 nm, 5 mW.

Source: A. Pal, D. L. Stokes, J. P. Alarie, and T. Vo-Dinh, *Anal. Chem.* **67**, 3154 (1995).

Table 4.2. Analysis of binary mixture of 4-picoline and benzoic acid: uncoated vs. PVPL-coated SERS substrates

No coating			Polymer coating		
Band position (cm⁻¹)	Band intensity (counts/100 s)	Chemical assignment	Band position (cm⁻¹)	Band intensity (counts/100 s)	Chemical assignment
			858	18400	benzoic acid
1024	13900	4-picoline/benzoic acid	1020	48700	4-picoline/benzoic acid
			1160	9210	benzoic acid
1235	11400	4-picoline	1237	11800	4-picoline
1388	15200	4-picoline/benzoic acid	1388	19700	4-picoline/benzoic acid
1457	26600	4-picoline	1455	23700	4-picoline/benzoic acid
1614	17700	4-picoline/benzoic acid	1612	47400	4-picoline/benzoic acid

165
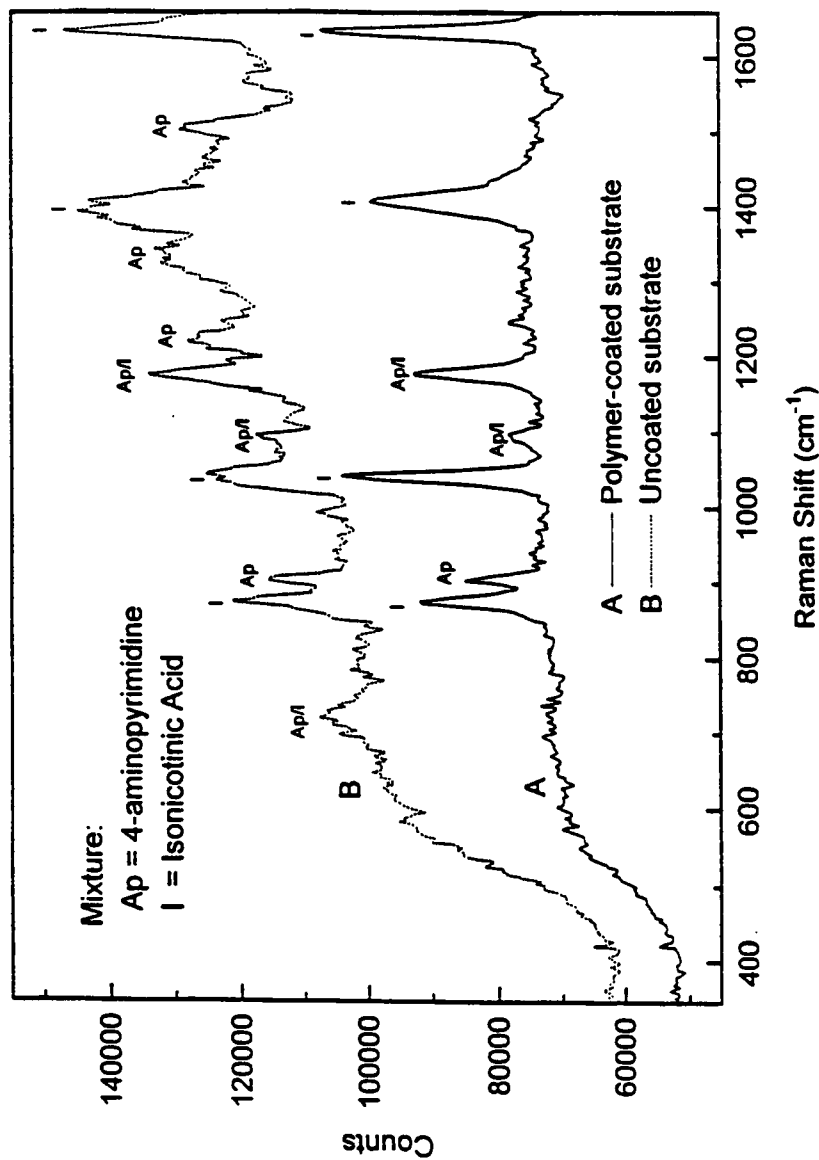
Figure 4.10. SERS spectra of a binary mixture solution of 4-aminopyrimidine (1.73 x 10⁻³ M) and isonicotinic acid (1.1 x 10⁻³ M) acquired *in situ* with a)PVPL-coated and b) bare alumina-based substrates. Laser: HeNe, 632.8 nm, 5 mW.

Source: A. Pal, D. L. Stokes, J. P. Alarie, and T. Vo-Dinh, *Anal. Chem.* **67**, 3154 (1995).

Table 4.3. Analysis of binary mixture of isonicotinic acid and 4-aminopyrimidine: uncoated vs. PVPL-coated SERS substrates

No coating			Polymer coating		
Band position (cm^{-1})	Band intensity (counts/100 s)	Chemical assignment *	Band position (cm^{-1})	Band intensity (counts/100 s)	Chemical assignment *
715	8110	Blank			
865	8780	INA	863	20300	INA
893	8780	AMP	893	12800	AMP
1031	10800	INA	1029	29100	INA
1083	10100	AMP/INA	1083	6080	AMP/INA
1163	5410	AMP/INA	1165	20300	AMP/INA
1207	6760	AMP			
1320	12200	AMP			
1390	6760	INA	1390	26400	INA
1488	10800	AMP			
1616	10800	INA	1614	33800	INA

*INA = isonicotinic acid; AMP = 4-aminopyrimidine

the Raman bands occurring at 1090 and 1170 cm^{-1} can be attributed to either compound. In this case, both compounds are practically equally represented by the spectrum obtained with the uncoated SERS substrate. On the other hand, the spectrum in Figure 4.10b, obtained with the PVPL-coated substrate, is clearly dominated by the SERS bands representative of isonicotinic acid. One major peak and one minor peak at 1172 and 1090 cm^{-1}, respectively, can be attributed to either compound. However, the change in intensity of these bands relative to the major bands unique to isonicotinic acid between the spectra of Figures 4.10a and b suggests that isonicotinic acid is the major contributor to these common bands in the spectrum obtained with the polymer-coated substrate. For this example, the results illustrate that the PVPL-coated substrate favored the detection of isonicotinic acid, as anticipated. In fact the spectrum in Figure 4.10a is almost entirely composed of bands that can be assigned to isonicotinic acid, with one exception- the medium band occurring at 897 cm^{-1}.

In conclusion, this chapter has demonstrated the SERS detection of various compounds using a polymer-coated substrate. A useful feature of the PVPL coating is that it can provide a protective barrier to mechanical disturbance and air oxidation of the SERS-active, roughened metal surface layer. As a result, the PVPL-coated substrate may be better suited for field work than uncoated SERS substrates. The commendable reproducibility and the absence of background structure exhibited by this coated substrate are also very useful characteristics. The fact that the coating is insoluble in water and exhibits variable permeability to different compounds further demonstrates its potential for use as a selective chemical probe.

CHAPTER 5

DEVELOPMENT OF SERS FIBEROPTIC PROBES USING THE MICROPARTICLE-BASED SUBSTRATE TECHNOLOGY

INTRODUCTION

The development of optical fibers has had a significant impact on the field of analytical chemistry. The high transmission efficiency of these devices has enabled their effective coupling to various spectroscopic instruments, thereby promoting new applications of spectroscopic methods. An obvious example is the analysis of samples in remote locations from often heavy and bulky spectrometers. Aside from the convenience and flexibility of remote sensing, sampling of hostile environments without subjecting personnel or instruments to harsh conditions is clearly an advantage. Optical fibers also facilitate multiplexing monitors to a single detection system, thus offering an economical approach towards applications requiring, for example, high sample throughput or multipoint process monitoring. It is therefore no surprise that extensive efforts have been devoted towards the development of fiberoptic sensors in recent years, as is demonstrated by several review articles (Angel *et al.*, 1989; Norris, 1989; Kersey and Dandridge, 1990; Boisde *et al.*, 1991; Lambeck, 1991; Miller and Mettler, 1991). The earliest fiberoptic probes were based on UV-Vis absorption and fluorescence spectroscopies; however, the broad spectral features of these techniques limited the selectivity offered by these probes. While additional measures can be taken to impart

169

chemical selectivity in such devices, such as various selective coatings (Sepaniak *et al.*, 1988; Vo-Dinh *et al.*, 1991; De Olivera and Narayanaswamy, 1992; Lerchi *et al.*, 1992; Kriz *et al.*, 1995; Piletsky, 1997), vibrational spectroscopies such as IR absorption (Saito and Kikiuchi, 1997) and Raman scattering have been recognized as the potential bases of more simple, spectrally selective fiberoptic probes.

Raman scattering offers several advantages in remote detection with fiberoptic sensors. The narrow and highly-resolved bands of typical Raman spectra can help elucidate chemical structure of analyte molecules and thus enable chemical identification based on unique spectral features. In fact, libraries of Raman spectra and algorithms have been developed for automatic identification of chemical samples (McCreery *et al.*, 1998). The sharp spectral features may also permit the simultaneous multicomponent analysis of sample mixtures or selective detection and quantitative analysis of analyte compounds in complex media. An obvious limitation of Raman scattering process, however, is low efficiency and thus low detectability. This drawback is compounded by the fact that fiber optics themselves exhibit large background signals due to silica Raman bands and fluorescence from impurities. This background is induced by laser excitation and is frequently a limiting factor in the length of optical fibers that can be used in remote detection. Nevertheless, many Raman scattering-based fiberoptic sensors have been reported (Schwab and McCreery, 1984; Schwab and McCreery, 1986; Hendra *et al.*, 1988; Archibald *et al.*, 1988; Lewis *et al.*, 1988; Soper and Kuwana, 1989; Allred and McCreery, 1990; Bello and Vo-Dinh, 1990; Bello *et al.*, 1990; Ganter and Steinhart, 1990; Myrick *et al.*, 1990; Myrick and Angel, 1990; Mullen and Carron, 1991; Sqalli *et al.*, 1991; Zimba and Rabolt, 1991; Alarie *et al.*, 1992; Ma and Li, 1994; de Bakker and Fredericks, 1995; Cooney *et al.*, 1996a,b; Cooper *et al.*, 1997; Heaton, 1997; Sprunt and Jayasooriya, 1997) For example, it has been demonstrated that, with

proper fiber geometries and optical filters, Raman spectra can be acquired with optical fibers as long as 250 m (Myrick and Angel, 1990). Furthermore, multichannel detection has been successfully coupled to fiberoptic probes in recent years. CCDs have been used for both visible (Alarie *et al.*, 1992) and near IR Raman studies with fiberoptic sensors (Allred and McCreery, 1990). Taking advantage of the reduced fluorescence background associated with the near IR region, many authors have also reported FT-Raman detection-based systems for remote analysis (Archibald *et al.*, 1988; Zimba and Rabolt, 1991; de Bakker and Fredericks, 1995; Heaton, 1997; Sprunt and Jayasooriya, 1997). Modulated FT-Raman fiberoptic spectroscopy has been reported for even further background reduction (Cooper *et al.*, 1997).

In light of all the above mentioned normal Raman-based remote detection technologies, the low Raman scattering efficiency is still a limiting factor, particularly for trace analysis. Even so, SERS-based fiberoptic sensors have not been widely reported (Soper and Kuwana, 1989; Bello and Vo-Dinh, 1990; Bello *et al.*, 1990; Myrick and Angel, 1990; Mullen and Carron, 1991; Alarie *et al.*, 1992; Ma and Li, 1994). The scarceness of SERS-based fiberoptic sensors may be due to a general lack of practical solid-based SERS substrate technologies. As reported in Chapter 2, the microparticle-based SERS substrates developed in this laboratory are easy to prepare, are economical, and exhibit a high degree of reproducibility (typically 10-15% RSD for substrate-to-substrate Raman enhancement). Furthermore, the microparticle-based substrates have been proven to be effective in the detection of various chemicals of environmental interest, such as polycyclic aromatic compounds (Vo-Dinh *et al.*, 1984), organophosphorus chemical agents (Alak and Vo-Dinh, 1987), chlorinated pesticides (Alak and Vo-Dinh, 1988), and fungicides (Narayanan *et al.*, 1992).

In acknowledgment of these attributes, the microparticle-based SERS substrate technology was applied to the development of fiberoptic SERS sensors. This chapter describes various steps taken in this effort. There are three sections. In the first section, remote SERS detection is described using a microparticle-based planar SERS substrate, which was coupled to a dual, 2-m fiberoptic system. A large, single-channel scanning spectrometer and a powerful class-IV laser were also used with this first setup. In the second section, dramatic improvements in both instrumentation dimensions and data acquisition times are reported by using an RE-ICCD-based spectrograph. Again, the planar microparticle-based substrate was coupled to a dual-fiber system, but the fibers were 20 m long for this study. Furthermore, a small, low-power, helium-neon laser was used to generate spectra of comparable quality to a conventional laboratory-based detection system. In the third section, an integrated sensor is described in which the microparticle-based roughening technique was applied directly to a single fiber, which carried both laser excitation and SERS signal radiation. This new single-fiber design is simple and very compact, thus potentially allowing *in situ* measurements at microscale environments.

FIBEROPTIC REMOTE SENSOR FOR *IN SITU* SERS ANALYSIS USING A SINGLE-CHANNEL SCANNING INSTRUMENT

Experimental

Instrumentation. All SERS measurements were performed with a SPEX Model 1403 double grating spectrometer (SPEX Industries), equipped with a thermoelectrically-cooled gallium arsenide PMT (Burle Industries, Model C31034), operating in the

photon-counting mode. Data storage and processing was performed with SPEX Datamate-3000 software. The bandpass of the spectrometer was 3 cm^{-1}. The detection integration time was 0.4 s. The excitation source was a krypton ion laser (Coherent, Innova 70), operated in the single-line mode and tuned to 647.1 nm. A laser power of 50 mW was used for all measurements.

Auxiliary optical system for remote detection. A schematic diagram of this first SERS dual-fiberoptic system is illustrated in <u>Figure 5.1</u>. Silica optical fibers of 400-μm- and 600-μm- core diameters were purchased from General Fiber Optics, Inc. The NA of both fibers was 0.26. A 2-m section of the 400-μm optical fiber was used for excitation, while a 2-m section of the 600-μm optical fiber was used for signal collection. A head-on configuration of the fibers on opposite sides of the substrate was used, with an angle of 180° between the excitation and collection fibers. By use of a smaller diameter fiber for excitation, the cone of excitation radiation was smaller than the acceptance cone of the collection fiber. As demonstrated by the figure, after passing through a bandpass filter, the laser beam was focused into the excitation fiber with a 10x (0.25 NA) objective lens. A fiberoptic holder with x-y-z positioning capability (Newport) was used to optimize the coupling. The distal end of the excitation fiber was then placed against the bottom of a small beaker that would contain the analyte solution and the SERS substrate. The SERS substrate (see below) was placed in the beaker with the silver side up, thus implementing the back-side excitation geometry which was proven to be effective in previous work (see Chapter 2). In order to collect as much SERS signal as possible, the tip of the collection fiber was submerged in the analyte solution and placed very close (< 1 mm) to the metallic surface of the SERS substrate. Furthermore, the detection end of the collection fiber was mounted on an x-y-z positioning stage (Oriel) to facilitate optimization of signal collection. The terminus end

Figure 5.1. Schematic diagram of an optical system for remote *in situ* SERS detection featuring a dual-fiber SERS sensor and a single-channel scanning instrument.

Source: J. M. Bello, V. A. Narayanan, D. L. Stokes, and T. Vo-Dinh, *Anal. Chem.* **62**, 2437 (1990).

174

of the collection fiber was mated to a two-lens focusing assembly whose f/ number (7.8) matched that of the spectrometer. The sample cell was also mounted on a translation stage (Oriel) to enable scanning of the SERS substrate.

SERS substrates. Alumina-based substrates, produced on glass supports, were prepared as described in Chapter 2 for maximum Raman scattering enhancement.

Chemicals. Benzoic acid (Mallinckrodt), PABA (Aldrich), fluorescein isothiocyanante (FITC) (Molecular probes Co.), o-chlorophenol (Aldrich), o-bromophenol (Eastman Organic Chemicals), TPA (Pfaltz and Bauer) and 2,4-dinitrotoluene (Aldrich) were all purchased at the highest available purity and used as received. Ethanol-based and aqueous samples were prepared in spectroscopic-grade ethanol (Warner-Graham Co.) and high performance liquid chromatography-grade water (Burdick and Jackson), respectively.

Results and Discussion

In situ **SERS spectra and background evaluations.** Figure 5.2a illustrates a solution spectrum of 1 ppm PABA in ethanol acquired with the *in situ* SERS fiberoptic system. As evidenced by comparison to the ethanol blank spectrum of Figure 5.2b, a major drawback of this mode of detection is a dominant background from the optical fiber. For example, the strong continuous bands in the 200-700-cm^{-1} region can be attributed to silica Raman scattering in both optical fibers. On the other hand, the bands at 778 and 1590 cm^{-1} in the blank spectrum are due to background signals from the SERS substrate. Nevertheless, several Raman bands attributable to PABA are observed in Figure 5.2a. For example, the dominant band at 1590 cm^{-1} (superimposed on a

175
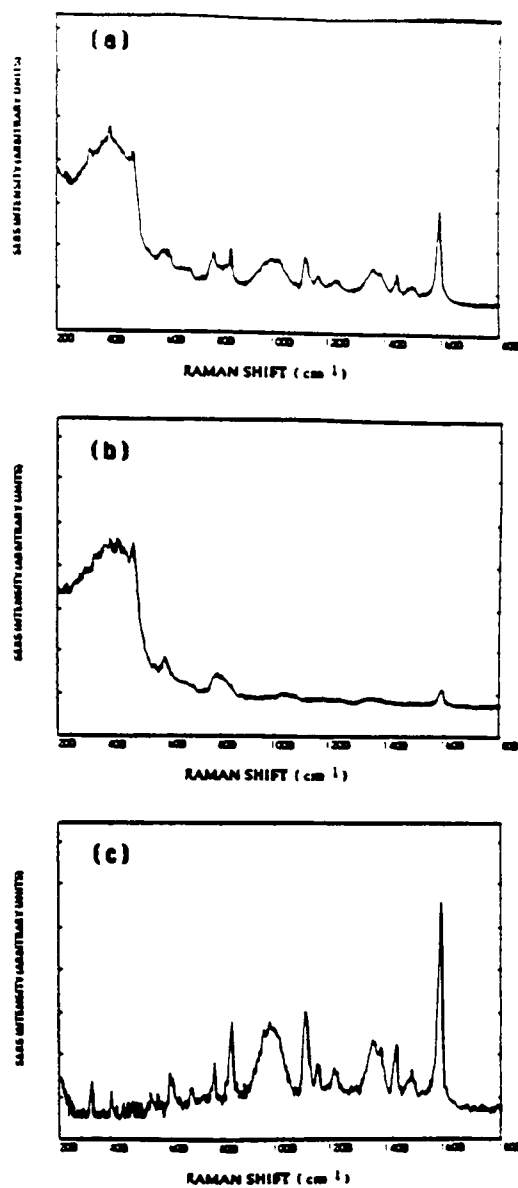
Figure 5.2. SERS spectra of a)1-ppm PABA solution, b) ethanol blank, and c) blank-subtracted background spectrum of the PABA sample, acquired *in situ* with the alumina-based substrate incorporated in the dual-fiber sensor design and the single-channel instrument.

Source: J. M. Bello, V. A. Narayanan, D. L. Stokes, and T. Vo-Dinh, *Anal. Chem.* **62**, 2437 (1990).

substrate background peak) is, in part, due to a C-C stretching mode of the benzene ring. Other useful bands demonstrated by the figure occur at 314, 392, 1132, 1180, 1374, 1390, 1452 and 1498 cm^{-1}. Vibrational mode assignments of these bands have been discussed in Chapter 2.

Generally, the SERS bands of PABA are very sharp and narrow in comparison to the background features of the optical fiber. It is also noteworthy that even the weak PABA bands at 314 and 392 cm^{-1}, also attributable to benzene ring modes, are discernible as sharp features superimposed on the strong broad background exhibited by the optical fibers in this region. Subtraction of the ethanol solution spectrum from the PABA solution spectrum was also performed and the resulting spectrum is illustrated in Figure 5.2c. As demonstrated by the figure, the background bands were efficiently removed from the SERS spectrum of PABA, and as a result, the solution SERS bands of PABA are more pronounced throughout the entire spectrum.

Similar subtractions were performed for the presentation of SERS spectra illustrated in Figure 5.3, acquired from solutions of a) 3 ppm fluorescein isothiocyanate (FITC), b) 3 ppm o-chlorophenol and c) 800 ppb TPA. One important observation of the blank-subtracted spectra, in general, is that the noise level of the 200-700-cm^{-1} region is somewhat higher than that of rest of the spectrum. This effect could compromise the detection and quantitative potential of this system at trace analyte levels. When possible, spectral features in other regions should be used for reference in quantitative analysis. Nevertheless, the solution SERS spectra of FITC, o-chlorophenol, and TPA show a large number of well-resolved bands, even in the 200-700-cm^{-1} region.
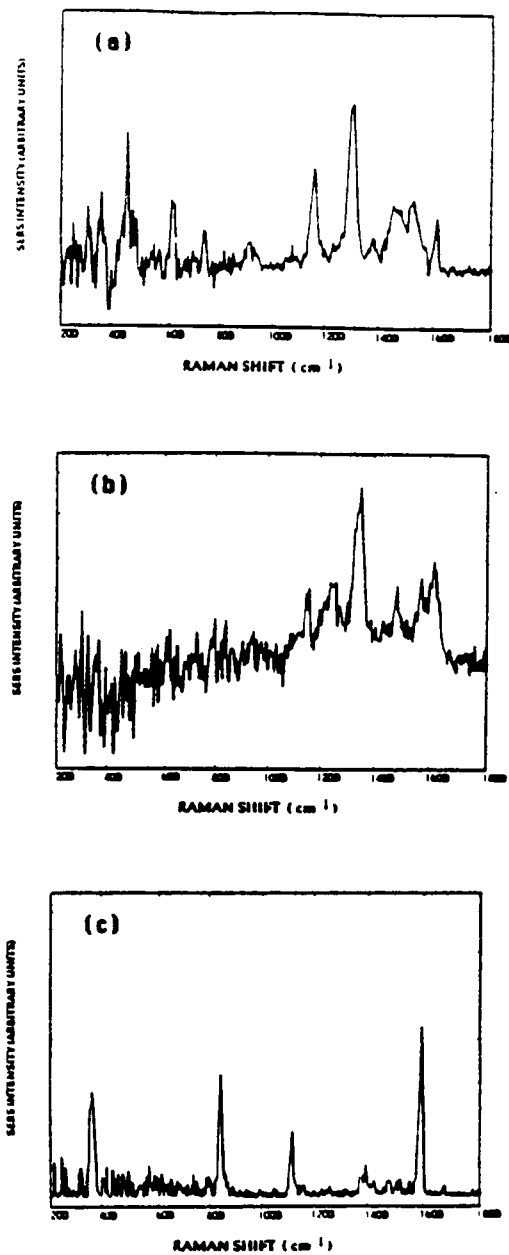
Figure 5.3. Blank-subtracted SERS spectra of a)3-ppm FITC, b) 3 ppm o-chlorophenol, and c) 800 ppb TPA solutions (in ethanol), acquired *in situ* with alumina-based substrates incorporated in the dual-fiber sensor design and the single-channel instrument.

Source: J. M. Bello, V. A. Narayanan, D. L. Stokes, and T. Vo-Dinh, *Anal. Chem.* **62**, 2437 (1990).

178

SERS signal stabilization study. It has been demonstrated in previous studies that a SERS signal stabilization period may be required for quantitative analyses via *in situ* solution measurements (Chapter 2). The stabilization of signal with time is reflective of attainment of a time-dependent state of equilibrium between analyte molecules in the bulk solution and those adsorbed at the substrate surface. Because the rate of adsorption can be influenced by chemical structure and functional groups, response time studies were performed for two different compounds of widely differing size and functionality, PABA and FITC. Figure 5.4 illustrates the response curves for these two compounds. The abscissa of this figure corresponds to the time after which the analyte was added to the ethanol solvent. The final concentrations of the PABA and FITC were 2 ppm and 3 ppm, respectively. The measurements were performed without stirring the solution during the course of the experiments. Both curves exhibit two distinct regions: one region of almost linear increase in SERS intensity with time, and a second region where a plateau of maximum SERS intensity was observed. For PABA, the rising portion of the curve extended from 0 to 40 min. On the other hand, only 20 min was required for observance of maximum signal from the FITC sample.

The temporal behavior of the signal observed for both samples could be due to increasing adsorption of the analyte molecules on the substrate surface with time and/or dispersion of the analyte spike throughout the relatively large volume of the solvent matrix. The faster attainment of the equilibrium state exhibited by the FITC sample could have been due to its higher concentration relative to the PABA sample. The adsorption rate could have been greater for FITC, as well. Photodegradation rates could have been another factor. Further fundamental studies are required.
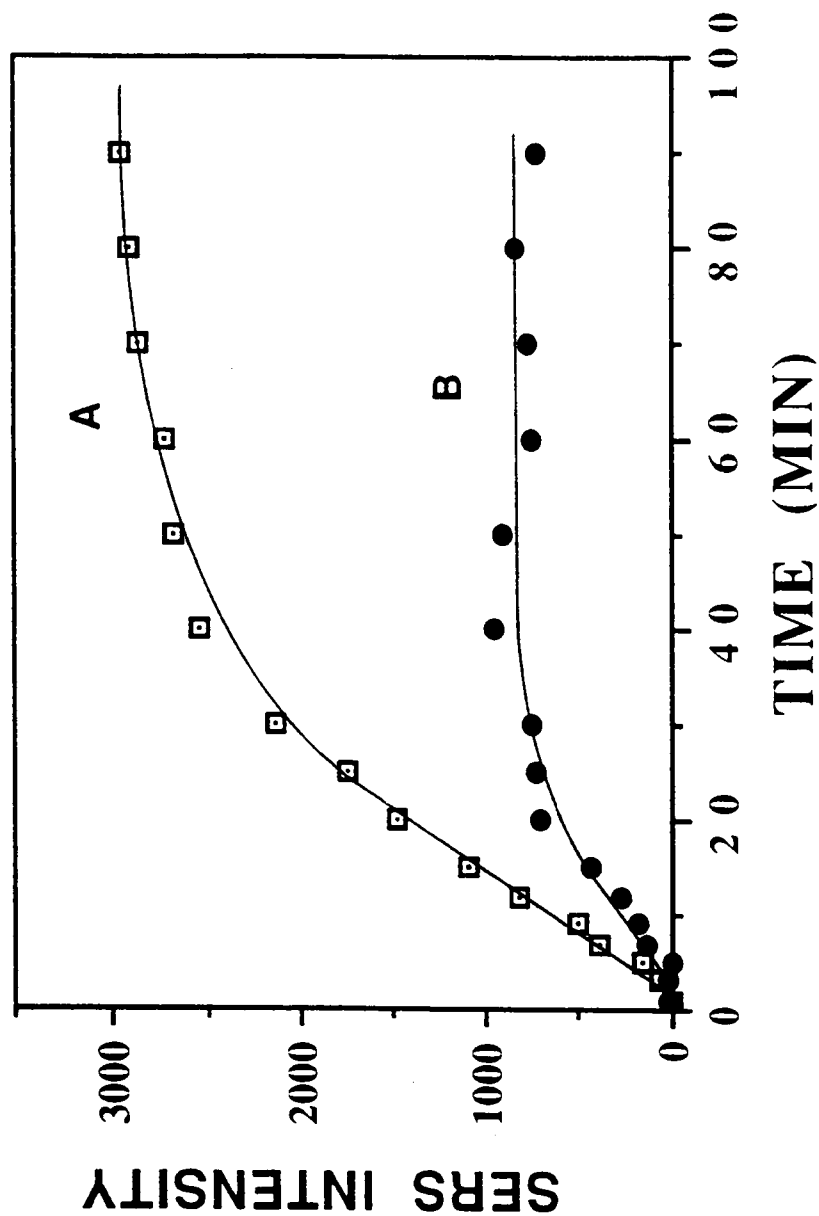
Figure 5.4. SERS intensity plots illustrating signal stabilization times for a) 1-ppm PABA, and b) 3-ppm FITC solutions (in ethanol), acquired *in situ* with alumina-based substrates incorporated in the dual-fiber sensor design and the single-channel instrument.

Source: J. M. Bello, V. A. Narayanan, D. L. Stokes, and T. Vo-Dinh, *Anal. Chem.* **62**, 2437 (1990).

From a practical standpoint, this study implies that stabilization studies should always be performed for different analytes at a wide range of concentrations before performing their respective quantitative analyses. Finally, it is noteworthy that the SERS substrates were continuously irradiated during the course of these studies. Neither of the stability curves manifests a decrease in SERS intensity with time. This result indicates that for the plateau region, any photodegradation of the adsorbed molecules by the 50-mW laser beam was either insignificant or offset with the replacement of photodegraded chemicals by fresh molecules from the bulk solution.

Analytical figures of merit. LODs of several compounds obtained with the *in situ* SERS optical fiber system were determined and are listed in Table 5.1. As suggested in the previous discussion, all results were based on the maximum signals observed after appropriate stabilization periods. The LOD range of the compounds investigated ranged from 34 ppb (2.05×10^{-7} M) for TPA to 11 ppm (6.04×10^{-5} M) for 2,4-dinitrotoluene. The LODs assume a minimum detectable signal level to be 3 times the standard deviation of the noise. The wide range of LODs is likely due to the varying degrees of adsorption experienced by each compound. The relative standard deviation in SERS signal intensity using this system was determined to be approximately 10%- comparable to all previous studies utilizing the microparticle-based SERS substrates.

Matrix effects. For a better demonstration of the practicality of this remote *in situ* detection system, measurements of aqueous samples were also performed. Figure 5.5 shows the aqueous solution SERS spectra of a)PABA (2 ppm) and b) TPA (2 ppm). Blank subtractions were not performed for these spectra. A comparison of these spectra with those obtained from ethanol-based samples (Figures 5.2 and 5.3) demonstrates little difference in spectra for these two solvent matrices.

181

Table 5.1. LODs of various compounds obtained from *in situ* ethanolic solution measurements with alumina-based SERS substrates and the dual-fiber, single-channel scanning instrument

Compound	LOD,[a] ppb	LOD,[a] M
TPA	34	2.1×10^{-7}
o-chlorophenol	240	1.8×10^{-6}
FITC	110	3.3×10^{-7}
Benzoic acid	220	1.8×10^{-6}
o-bromophenol	620	3.6×10^{-6}
2,4-dinitrotoluene	11,000	6.0×10^{-5}
PABA	38	2.8×10^{-7}

[a]Relative standard deviation $\approx 10\%$

Source: J. M. Bello, V. A. Narayanan, D. L. Stokes, and T. Vo-Dinh, *Anal. Chem.* **62**, 2437 (1990).
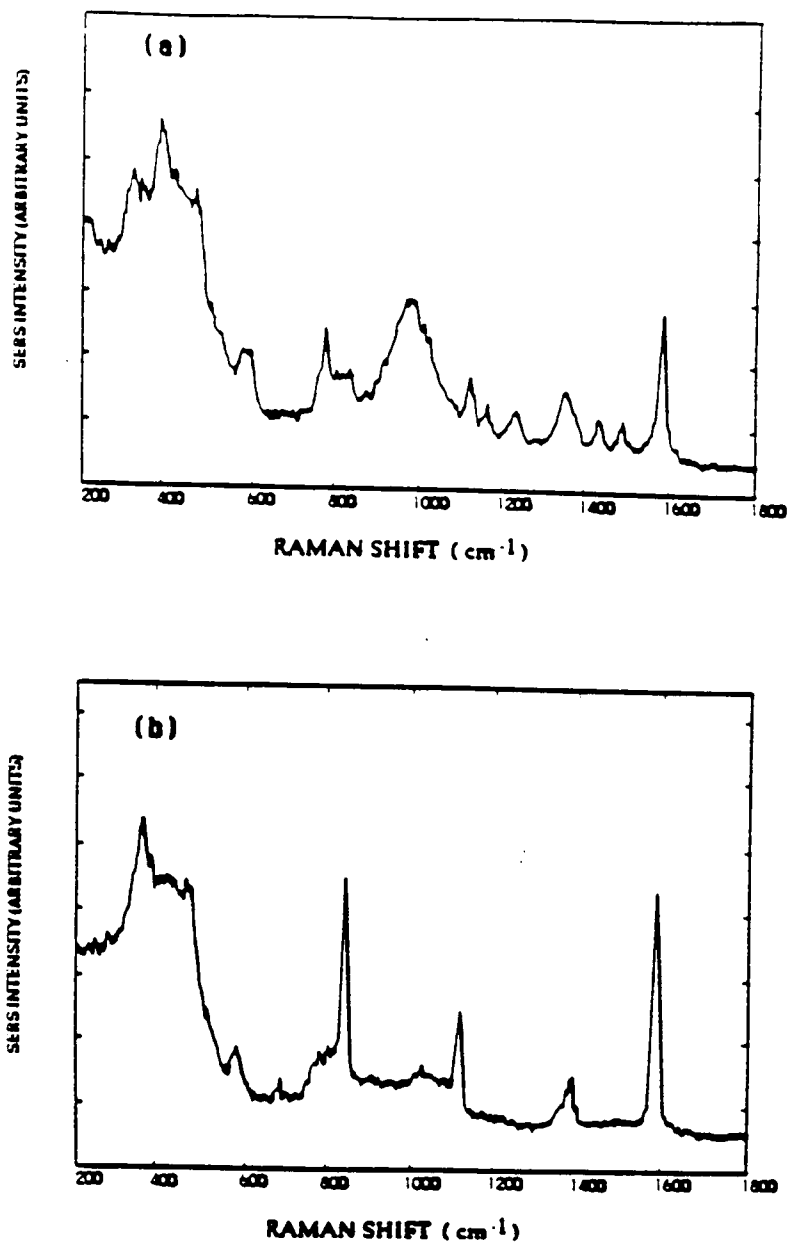
Figure 5.5. SERS spectra of aqueous solutions of a) 2ppm PABA, and b) 2 ppm TPA, acquired *in situ* with alumina-based substrates incorporated in the dual-fiber sensor design and the single-channel instrument.

Source: J. M. Bello, V. A. Narayanan, D. L. Stokes, and T. Vo-Dinh, *Anal. Chem.* **62**, 2437 (1990).

183

In conclusion, this study demonstrated the feasibility of remote *in situ* solution SERS detection with optical fibers and the microparticle-based SERS technology. However, the study also demonstrated that optical fiber background may be a limiting factor in trace analysis, even for 2-m fiber lengths. Additional focusing and collection optics between the optical fibers and the sample could have improved observed SERS intensity while enabling better placement of optical filters for the reduction of the fiber background. Such factors were considered in subsequent developments.

FIBEROPTIC REMOTE SENSOR FOR *IN SITU* SERS ANALYSIS USING A RED-ENHANCED INTENSIFIED CHARGE-COUPLED DEVICE (RE-ICCD)-BASED SPECTROGRAPH

Experimental

Instrumentation. This study involved the use of two detection systems. In addition to the newly introduced spectrographic-based system, a single-channel scanning detection-based system similar to those described in previous chapters was used. In this study, the single-channel scanning system was not intended for remote detection, but was instead used as a reference for evaluation of the new spectrographic system.

Spectrographic-based detection system. The spectrographic measurements were performed with an ISA Model HR-320 spectrograph equipped with an RE/ICCD (Princeton Instruments, Model RE/ICCD-576S). The detector was thermoelectrically cooled to -34° C. All data acquisition and processing steps were carried out with software provided by Princeton Instruments (CSMA, v2.0). The spectrograph was also

equipped with a 600 gr/mm holographic grating, yielding a reciprocal linear dispersion of 50 nm/mm. The entrance slit was set to 30 μm for all measurements; the resolution was approximately 3 cm^{-1} at 675 nm. After calibration, the spectral accuracy of the spectrograph was ±1.5 cm^{-1}.

Figure 5.6 is a schematic diagram of the auxiliary optical system that was used with the spectrograph for remote detection using the microparticle-based SERS technology. It was a dual-fiber system, with both excitation and collection fibers (Fiberguide Industries) being 20-m long. Both fibers had a 600–μm core diameter and a numerical aperture of 0.26. The 632.8-nm laser line from a helium-neon laser (SpectraPhysics, Model 106-1) was focused onto the excitation fiber with a 10X, 0.25-NA objective lens. A more detailed schematic diagram of the sample probing optical system is illustrated in Figure 5.7, and is referred to as the remote SERS detection module.

Within the detection module, the excitation fiber was coupled to a beam focusing probe (General Fiber Optics) with an SMA connector. This probe focused the laser beam unto the sample through the back side of the SERS substrate. A bandpass filter (Corion, Model P3-633-A-X516) was placed between the probe and the sample to remove plasma lines as well as any interfering silica Raman bands or fluorescence generated in the excitation fiber. The excitation intensity at the sample was approximately 3 mW. A small beaker could have easily been installed for solution measurements. The scattered radiation was collected at 180° with respect to the excitation beam with a two-lens collection system, which refocused the collected light onto the collection optical fiber. The two lens system was composed of a collection lens (1", f/1) and a focusing lens (1", f/2). A Raman holographic notch filter (Physical Optics Corporation) was placed within the collection lens system to drastically attenuate the collected Rayleigh scatter and thus prevent
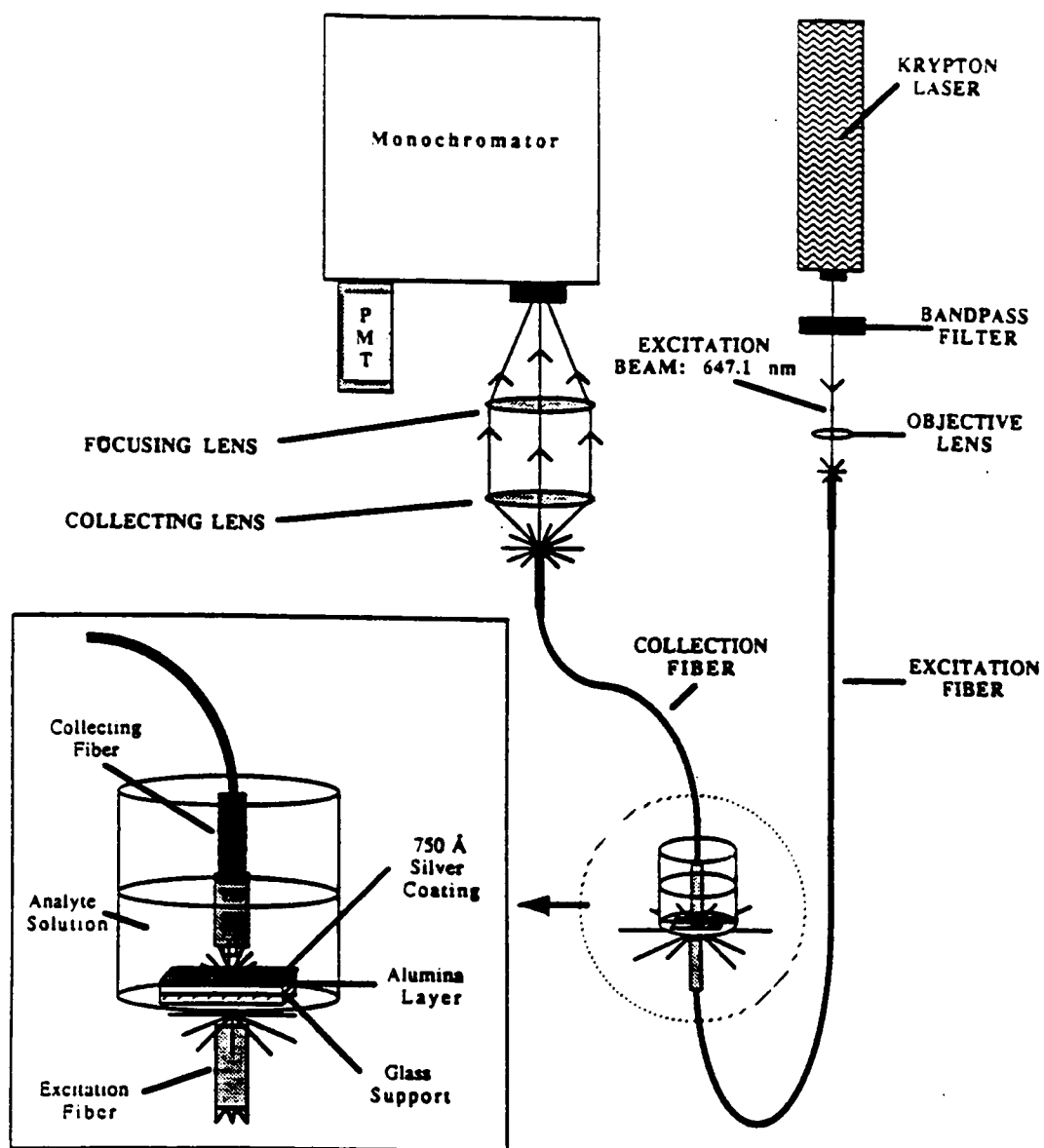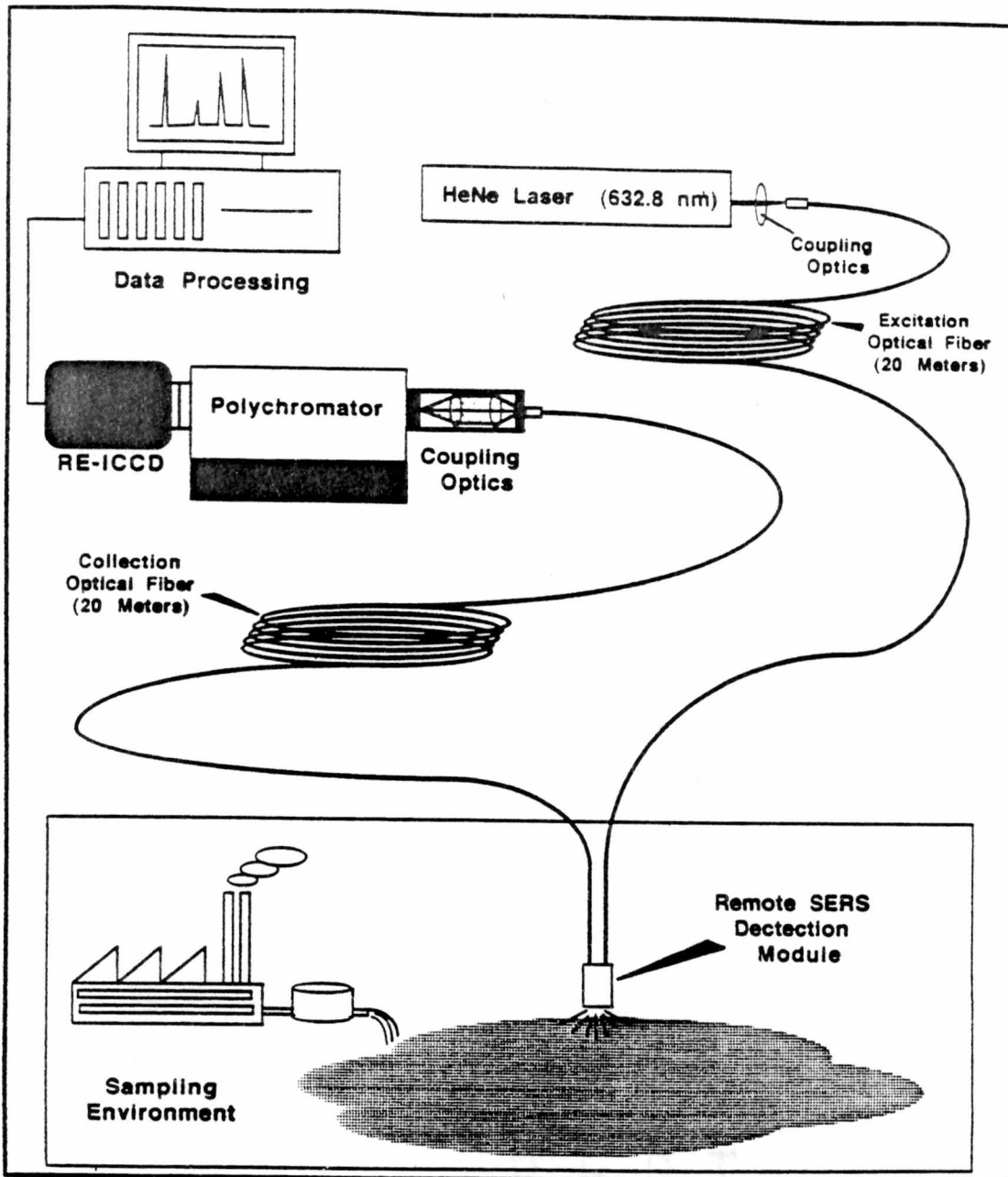
Figure 5.6. Schematic diagram of an optical system for remote *in situ* SERS detection featuring a dual-fiber SERS sensor and an RE-ICCD-based spectrograph.

186
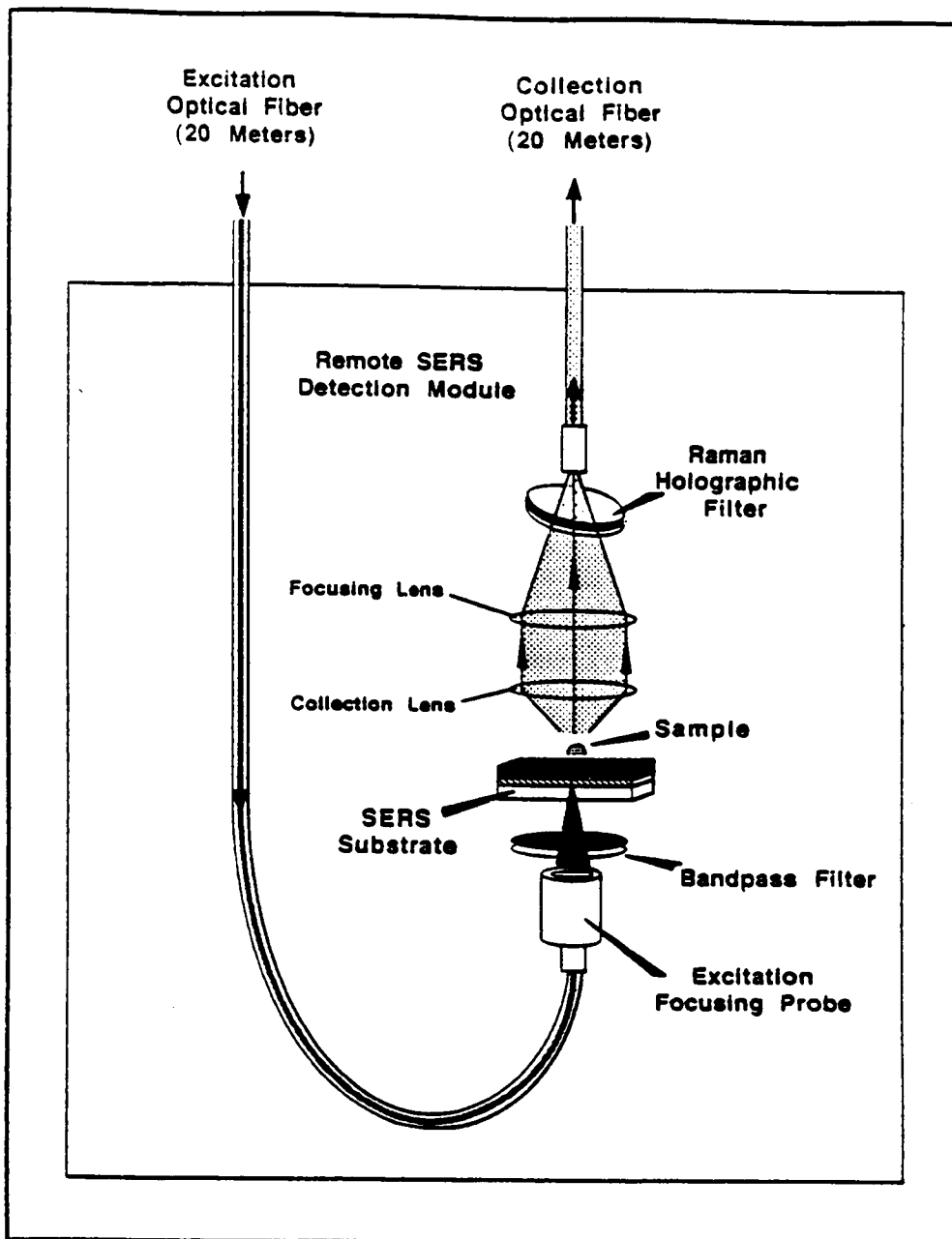
Figure 5.7. Detailed schematic diagram of the remote SERS detection module.

further generation of silica Raman bands and fluorescence in the collection fiber. The output end of the collection fiber was coupled to the spectrograph with another two-lens system: an f/2 collimating lens and an f/4 focusing lens to nearly match the speed of the spectrometer.

Single-channel scanning-based detection system. The single-channel scanning measurements were performed with the SPEX, Model 1403, double grating spectrometer system described in the preceding section. The spectral bandpass was 2 cm^{-1}. The auxiliary optical detection system is illustrated in Figure 5.8. The excitation source was a krypton ion laser (Coherent, Innova 70), operated in the single-line mode and tuned to 647.1 nm. A laser power of 50 mW was used for all measurements. A bandpass filter was used to reject plasma lines from laser beam before being focused onto the sample through the back side of the SERS substrate with an f/2.5 lens. The scattered radiation was collected from the front side of the SERS substrate at 180° with respect to the excitation beam. Signal collection was performed with a 1-m section of 600–μm core diameter optical fiber (Fiberguide Industries, NA=0.26). The optical fiber was placed very close to, but not touching, the substrate surface (< 1mm). The terminus end of the collection fiber was mated with a two-lens coupling probe that matched the speed of the spectrometer (f/7.8).

Chemicals. 1-aminopyrene, 4-aminopyrimidine and 2,4-dinitrophenol and pyridine were purchased from Aldrich. Benzene was purchased from E. M. Scientific. All chemicals were used as received. Sample solutions were prepared in spectroscopic-grade ethanol (Warner-Graham Co.).
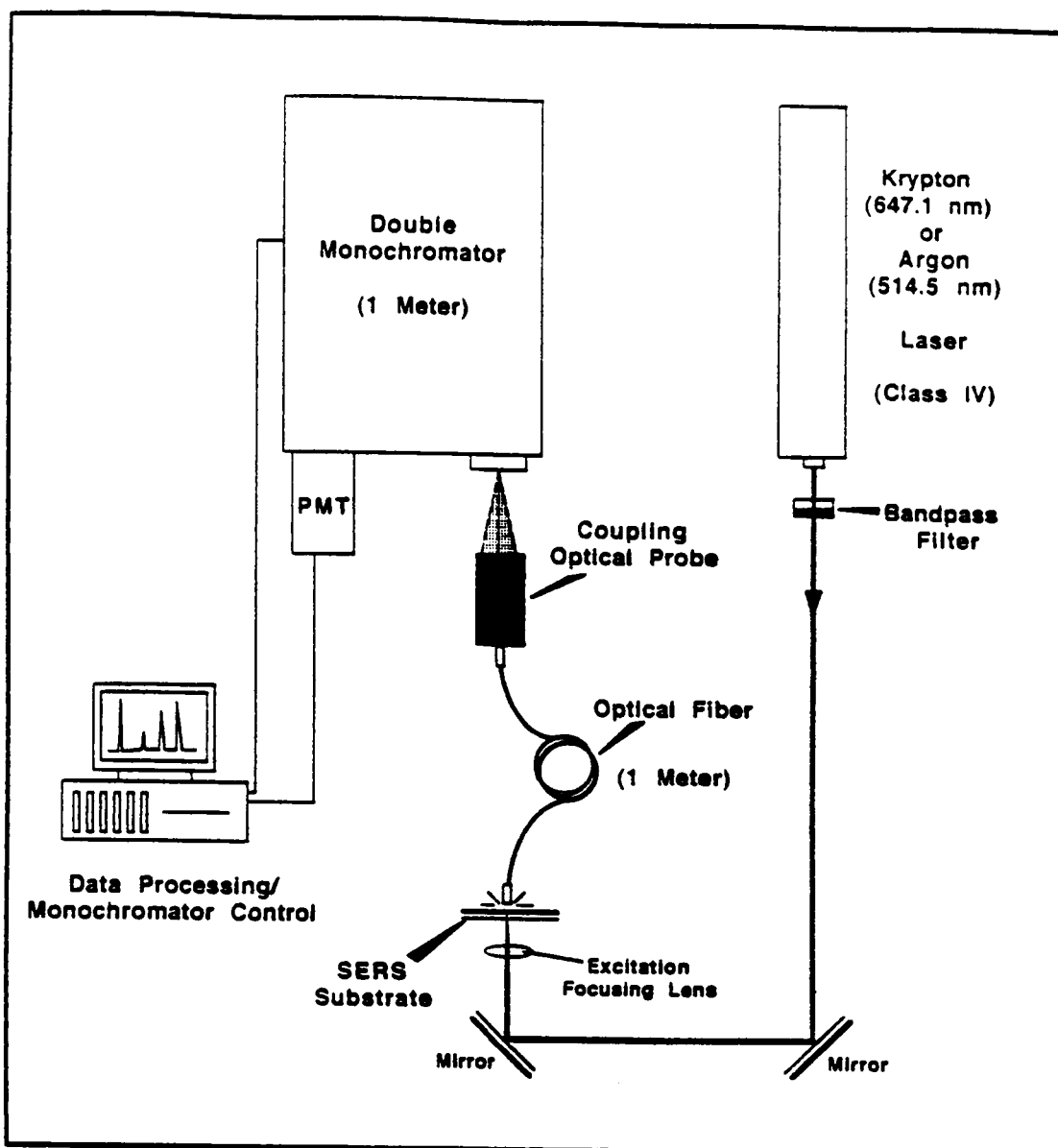
Figure 5.8. Schematic diagram of a conventional Raman detection system for laboratory-based research.

SERS substrates. Alumina-based and TiO$_2$-based SERS substrates, produced on glass supports, were prepared as described in Chapter 2 for maximum Raman scattering enhancement.

Results and Discussion

The previous section described a dual-fiber SERS sensor for use with a single-channel scanning detection system. Although the system yielded respectable LODs for several compounds, the system was large. It featured a double-stage, 1-m focal length spectrometer, and a Class IV laser. While remote detection capability eases the inconvenience of large, nonportable detection systems, compact instrumentation is nevertheless an attractive feature in any venue, provided that the performance is acceptable. Another drawback of the single-channel scanning system was the relatively long periods required for acquisition of spectra. The potential for real-time analysis with spectral characterization was therefore quite limited.

In this work, the potential advantages of the holographic notch filter and CCD technologies were combined in the development of a compact instrument for remote Raman detection via fiberoptics and the microparticle-based SERS technology. The holographic notch filter enabled the use of a 320-mm focal-length, single-stage spectrometer in comparison to the 1-m, multiple-stage spectrometer used in the previous fiberoptic SERS study. Furthermore, the high-quantum efficiency of the RE-ICCD, coupled with the array detection configuration, enabled the use of a low-power, compact and inexpensive helium-neon laser for generation of spectra in a fraction of the time required with the scanning instrument. Furthermore, this study utilized 20-m

excitation and collection optical fibers, in comparison to the 2-m fibers used previously.

Comparison of SERS spectra acquired with spectrographic and single-channel-based detection systems. A dramatic illustration of the enhanced performance of the RE-ICCD-based fiberoptic SERS detection system, relative to the conventional single-channel scanning instrument, is evidenced by the comparison of spectra acquired with these two systems. Figures 5.9, 5.10, 5.11, and 5.12 demonstrate spectra of 4-aminopyrimidine, 1-aminopyrene, Dichloran, and Thiram, respectively, acquired with a) the conventional scanning detection system, and b) the RE-ICCD-based fiberoptic detection system. In each case, a 1-μL aliquot of a 1000 ppm analyte solution was applied to an alumina-based substrate and allowed to dry before measurement. It is noteworthy that the scanning system used a 50-mW excitation source and required 12 min for acquisition of the 200-1800-cm^{-1} spectra. Furthermore, a 1-m optical fiber was used to transmit the Raman signal to the spectrometer. No excitation fiber was used is this system. In sharp contrast, the RE-ICCD-based detection system utilized a 3-mW excitation intensity at the sample, and 20-m optical fibers for both excitation and collection. Even so, the 345-1645-cm^{-1} spectra were acquired with 25-s detector duty times.

It is immediately apparent in each example that the performance of the RE-ICCD-based system is comparable to that of the scanning system. For example the S/N observed with the RE-ICCD-based system was comparable and sometimes better than that of the scanning instrument. The multichannel advantage was clearly demonstrated; although a 12-min scanning time was required for full spectrum acquisition with the scanning instrument, the integration time used for each step in the scan was only 0.5 s. By
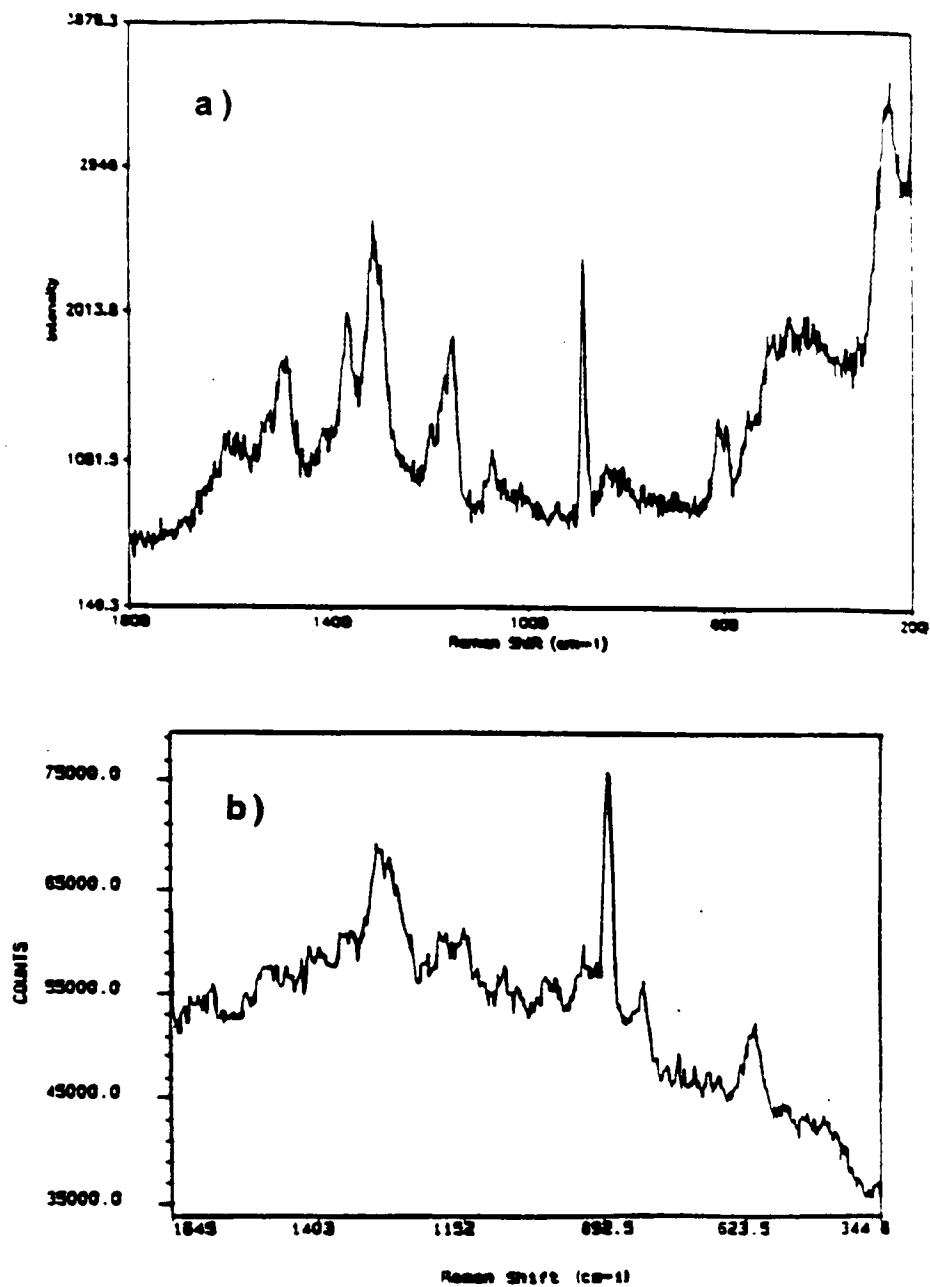
Figure 5.9. SERS spectra of a 10-ng sample of 4-aminopyrimidine acquired with a) a conventional laboratory-based Raman detection system, and b) the spectrograph-based fiberoptic system for remote detection. Alumina-based substrates. Conventional Raman system: Kr laser, 647.1 nm, 50 mW; 12-min scan time. Spectrographic system: HeNe laser, 632.8 nm, 3 mW; 20-m fiberoptics; 25-s acquisition time.

192
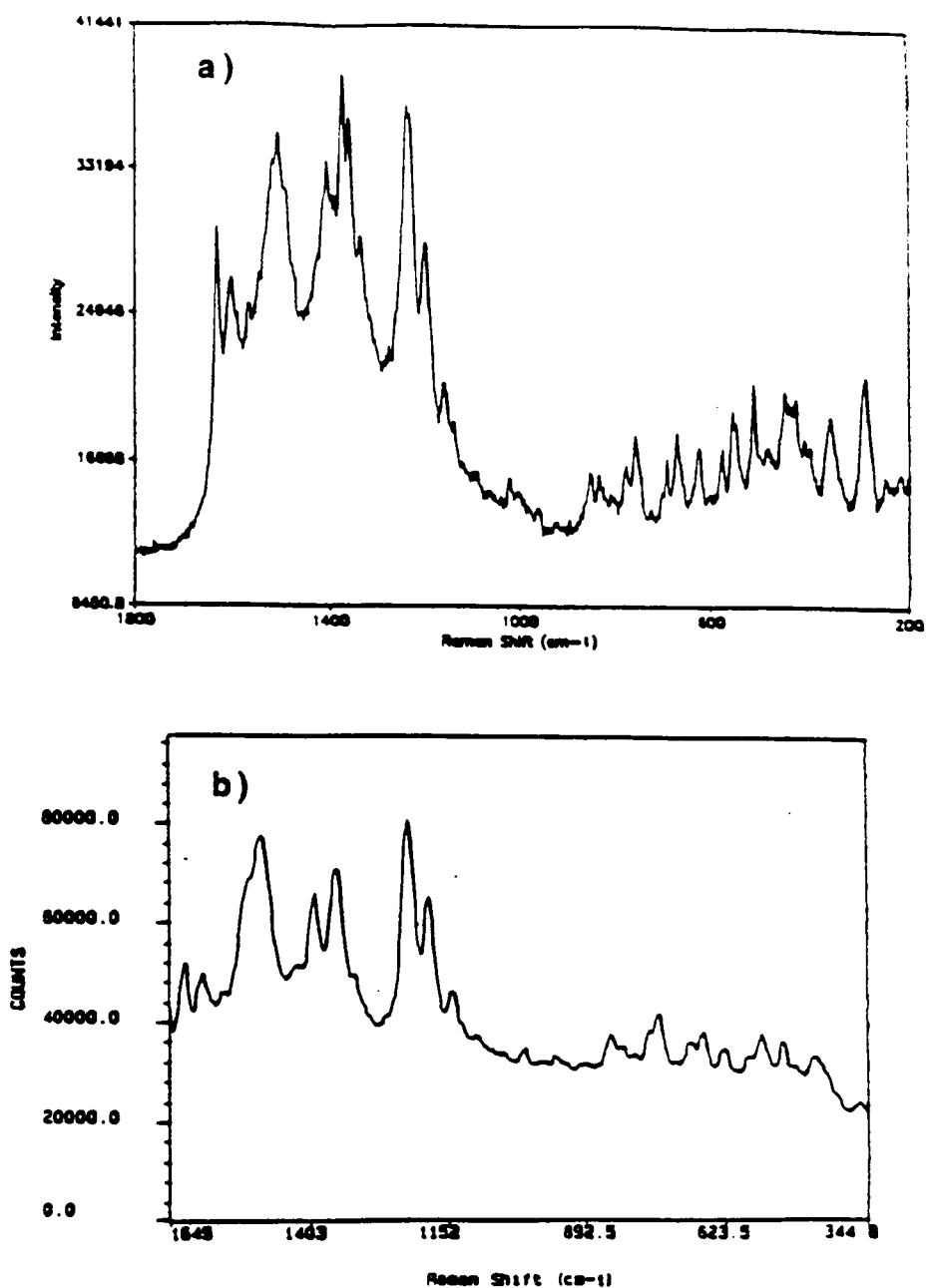
Figure 5.10. SERS spectra of a 10-ng sample of 1-aminopyrene acquired with a) a conventional laboratory-based Raman detection system, and b) the spectrograph-based fiberoptic system for remote detection. Alumina-based substrates. Conventional Raman system: Kr laser, 647.1 nm, 50 mW; 12-min scan time. Spectrographic system: HeNe laser, 632.8 nm, 3 mW; 20-m fiberoptics; 25-s acquisition time.

193
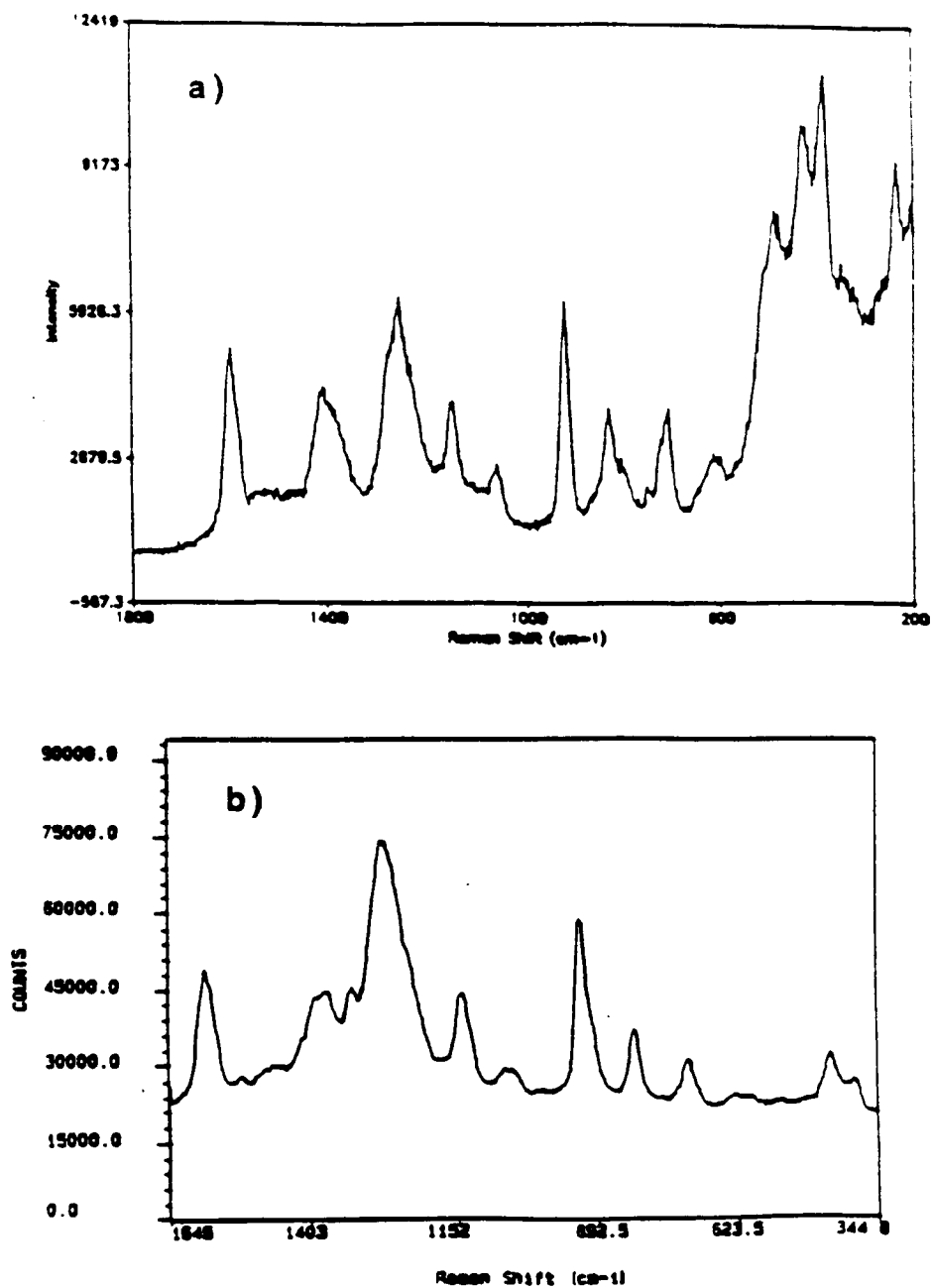
Figure 5.11. SERS spectra of a 10-ng sample of Dichloran acquired with a) a conventional laboratory-based Raman detection system, and b) the spectrograph-based fiberoptic system for remote detection. Alumina-based substrates. Conventional Raman system: Kr laser, 647.1 nm, 50 mW; 12-min scan time. Spectrographic system: HeNe laser, 632.8 nm, 3 mW; 20-m fiberoptics; 25-s acquisition time.

194
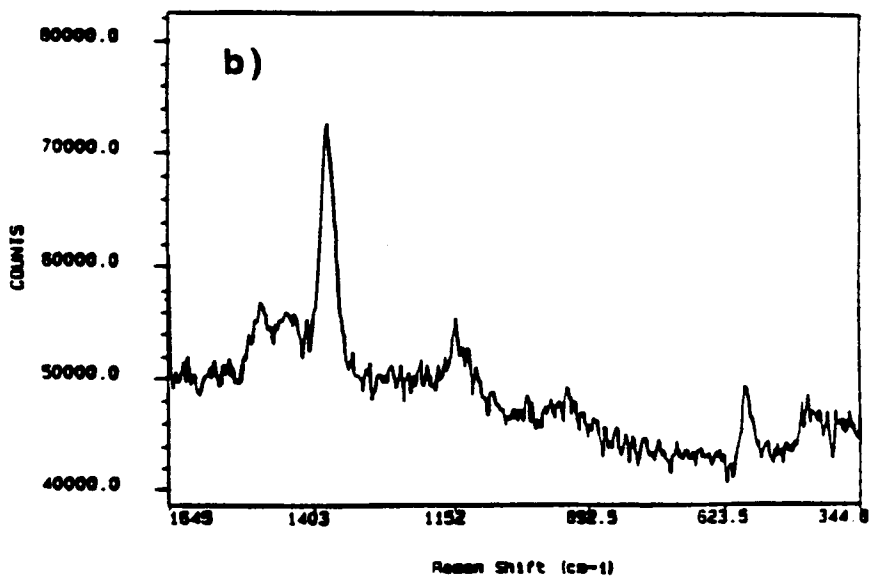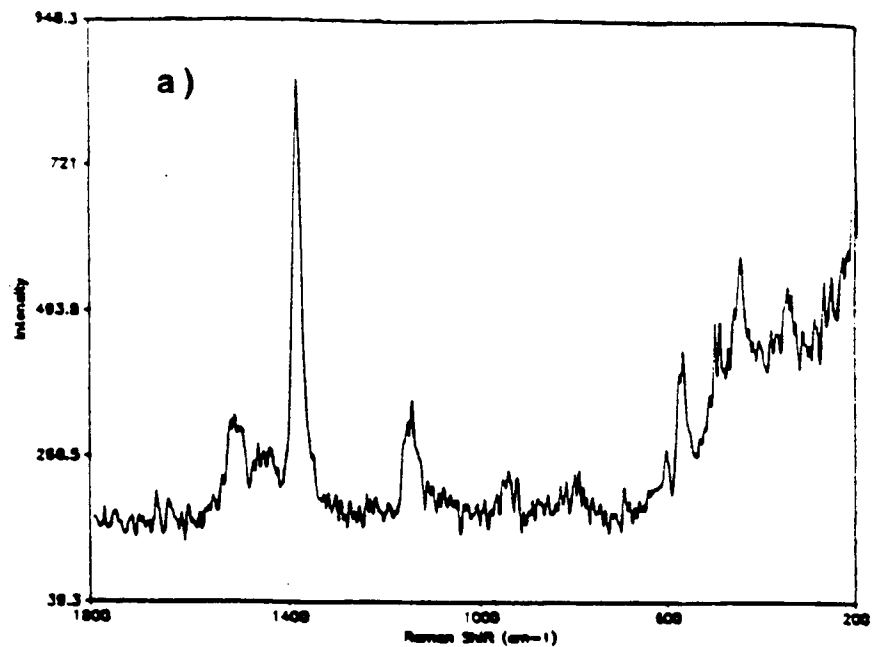
Figure 5.12. SERS spectra of a 10-ng sample of thiram acquired with a) a conventional laboratory-based Raman detection system, and b) the spectrograph-based fiberoptic system for remote detection. Alumina-based substrates. Conventional Raman system: Kr laser, 647.1 nm, 50 mW; 12-min scan time. Spectrographic system: HeNe laser, 632.8 nm, 3 mW; 20-m fiberoptics; 25-s acquisition time.

195

contrast, longer 25-s duty times were implemented simultaneously for each detection element of the RE-ICCD. For both Dichloran and 1-aminopyrene, superior S/N values were observed for the RE-ICCD-based system. This observation could have in part been due to photodegradation or ablation of the sample over the relatively long data acquisition period required with the scanning system. The wider bandpass could have been another factor in the apparent enhanced S/N values observed with the RE-ICCD-based system. Nevertheless, the resulting resolution was adequate for high spectral selectivity. For example, Figure 5.10 illustrates that most of the fine spectral features of the 350-900-cm^{-1} region of the 1-aminopyrene spectrum, fully resolved by the scanning instrument, were at least partially resolved and identifiable in the spectrum yielded by the spectrographic instrument.

Another improvement, demonstrated especially by the 4-aminopyrimidine, Dichloran and Thiram spectra, was the drastic reduction of fiberoptic background signal exhibited by the RE-ICCD-based detection system. Note the intense, broad fiberoptic background manifested in the 200-700-cm^{-1} region of spectra yielded by the scanning system. This background is virtually absent from the spectra produced with the spectrographic system, even though a 40-m total length of optical fiber was used in this system. This length is in striking contrast to the 1-m fiber used in the scanning system. Also note that no background subtraction was performed for these spectra. Strategic placement of filters accounts for this dramatic improvement. As is demonstrated by the schematic diagram of the remote SERS detection module in Figure 5.7a bandpass filter was placed between the excitation fiber and the sample. This placement rejected any fiber background outside the bandpass. In addition, the holographic notch filter rejected the intense Rayleigh scatter, thus preventing generation of further intense silica Raman scatter in the collection fiber. As a result, the otherwise obscured spectral features of

4-aminopyrimidine, Thiram and Dichloran were clearly discernible in the 350-700-cm^{-1} range of spectra acquired with the spectrographic-detection-based system. While a notch filter could have likewise been installed in the scanning instrument, its omission in this example serves as a reference to emphasize its effectiveness in preventing fiber background in the spectrographic-based system. Unfortunately, use of the filters necessitated the use of additional lenses which added bulk to the remote SERS detection module. It is noteworthy, however, that both bandpass and notch filters have been applied to fiberoptic tips (Gazer Raman Bioprobe). This technology, coupled with the use of grin lenses, could significantly reduce the dimensions of the remote SERS detection module.

As has been demonstrated in the preceding discussion, the spectrographic-based system allowed short data acquisition times in comparison to single-channel scanning instruments. As a further demonstration of the rapid sampling capability, Figure 5.13 illustrates SERS spectra acquired for 1-aminopyrene using various detector duty times. For each case, a 1-μL aliquot of 1000 ppm 1-aminopyrene solution was deposited on the alumina-based SERS substrate and allowed to dry. It is demonstrated that all major spectral features in the 1100-1645-cm^{-1} region were fully discernible even for the 50-ms detector duty time. Some of the minor features of the 345-1000-cm^{-1} were observed, as well. This rapid detection capability with full spectral characterization could be particularly valuable in monitoring dynamic chemical or physical processes. Furthermore, it may enable better detection and characterization of photosensitive or volatile compounds, especially in the dry state.
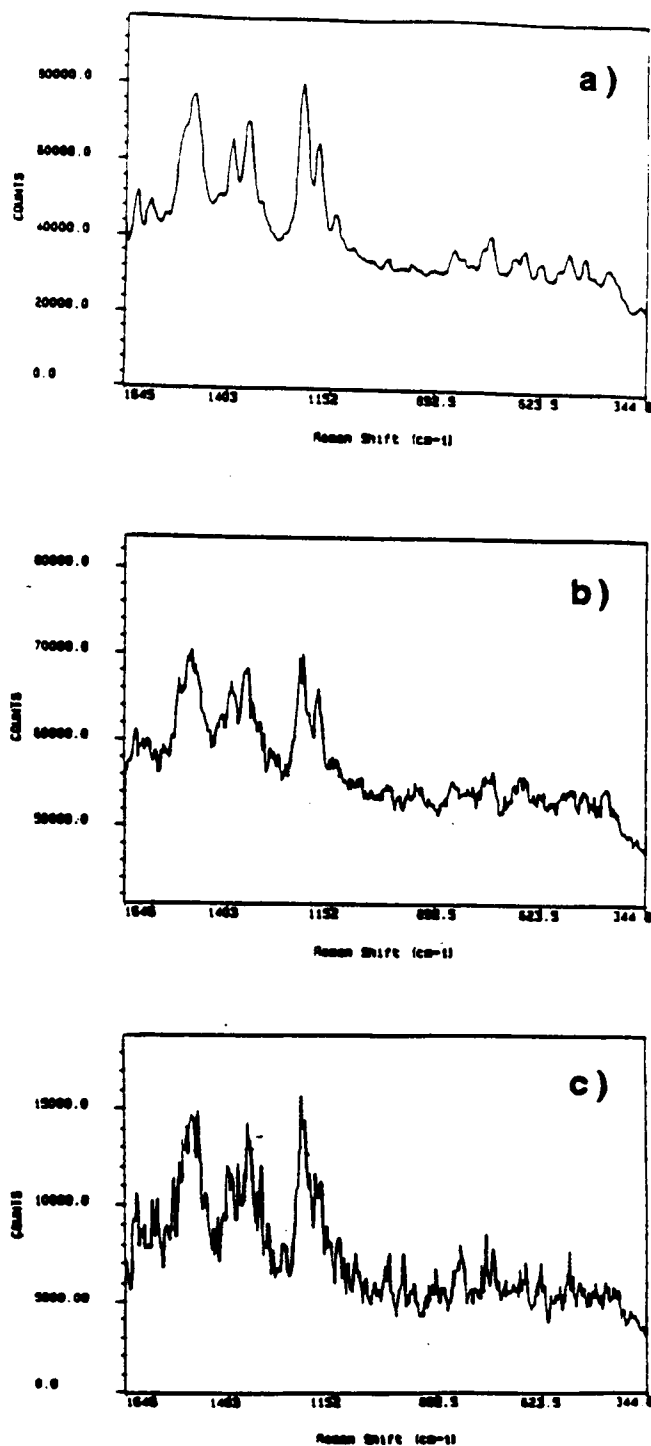
Figure 5.13. SERS spectra of a 10-ng sample of 1-aminopyrene generated with a) 25-s, b)150-ms, and c) 50-ms detector duty times, acquired with the spectrograph-based fiberoptic system for remote detection. Alumina-based substrate. HeNe laser, 632.8 nm, 3 mW; 20-m fiberoptics.

198

Comparison of SERS substrates for use with the remote SERS detection module. Exhaustive optimization studies were performed for alumina- and TiO_2-based substrates, as discussed in Chapter 2. Both substrates were installed in the remote SERS detection module for comparison and selection for future studies. Figure 5.14 illustrates spectra of 1-aminopyrene acquired with a) the TiO_2-based SERS substrate, and b) the alumina-based SERS substrate. In both cases, a 1-µL spot of a 1000 ppm analyte solution was deposited on the substrate and allowed to dry prior to measurement. As is demonstrated by the figure, the S/N value exhibited by the alumina-based substrate exceeded that of the TiO_2-based substrate by a factor of approximately 10. Alumina substrates were therefore used in all subsequent studies involving the spectrographic-based fiberoptic SERS detection system. It is interesting to also note that both substrates were equally stable in aqueous solutions (with respect to maintaining the microparticle layer required for the SERS effect).

Analytical figures of merit. Figure 5.15 illustrates a calibration curve for the selective fungicide, Dichloran, generated with the spectrographic fiberoptic SERS detection system. Each point represents detection of a dry sample and was acquired after stabilization of the SERS signal. Detector duty times were 25 s. It is noteworthy that two distinct regions of linearity appear to have been observed for the studied range: one for the 0.5-10 ng range, and another for the 0.01-0.5 ng range. The steeper slope observed for the 0.01-0.5-ng range probably corresponds to the distributed mass range leading up to the completion of a molecular monolayer on the SERS substrate surface, for which the SERS effect would have been most dramatic. Likewise, the 0.5-10-ng range corresponds to the distribution of molecules atop the monolayer. Such molecules could have experienced reduced SERS enhancement, and also could have attenuated the Raman signal from the underlying molecules, thus accounting for the decreased slope.
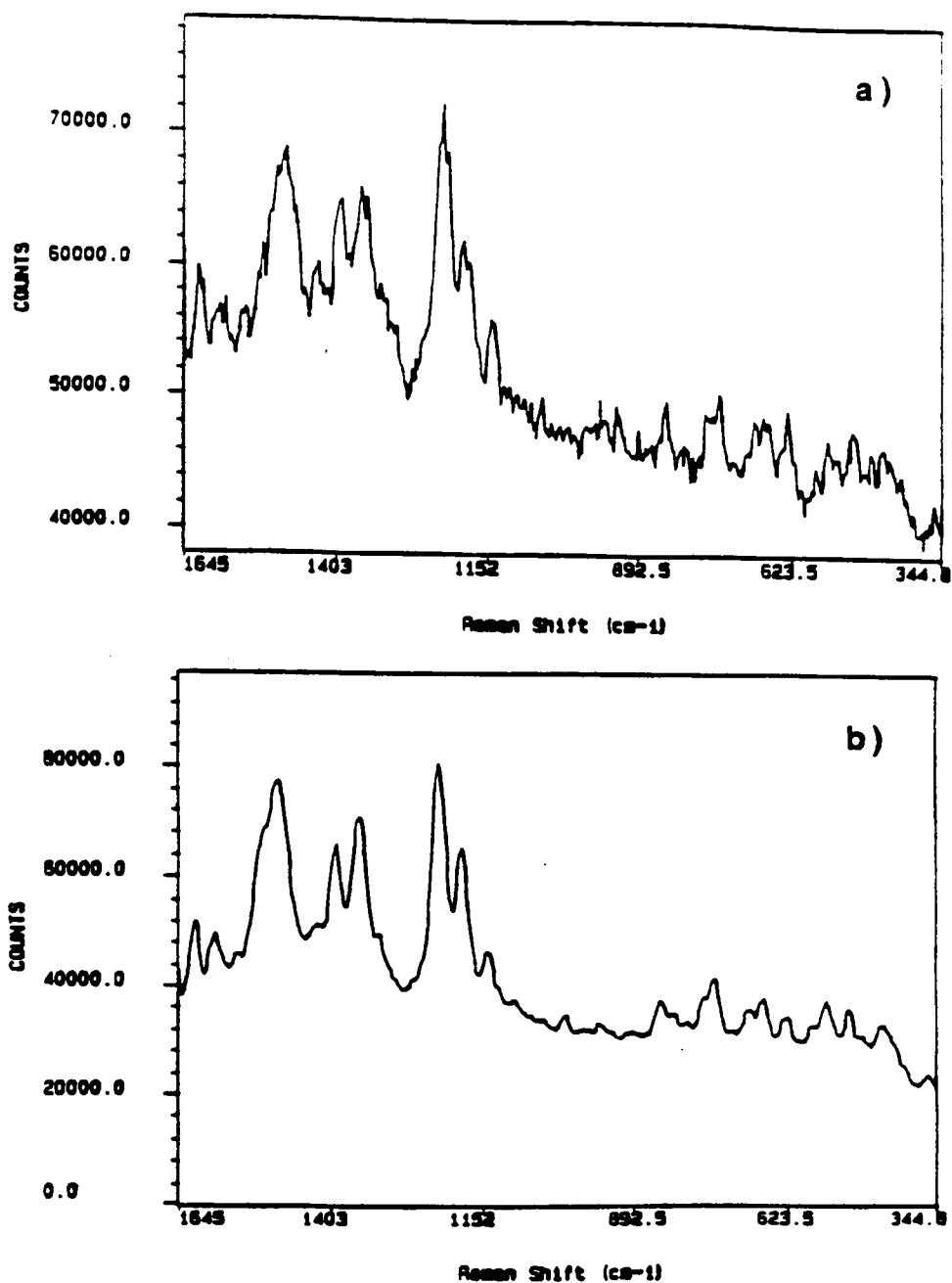
Figure 5.14. SERS spectra of a 10-ng sample of 1-aminopyrene acquired with a) the TiO_2-based, and b)alumina-based substrates installed in the spectrograph-based fiberoptic system for remote detection. HeNe laser, 632.8 nm, 3 mW; 20-m fiberoptics; 25-s acquisition time.

200
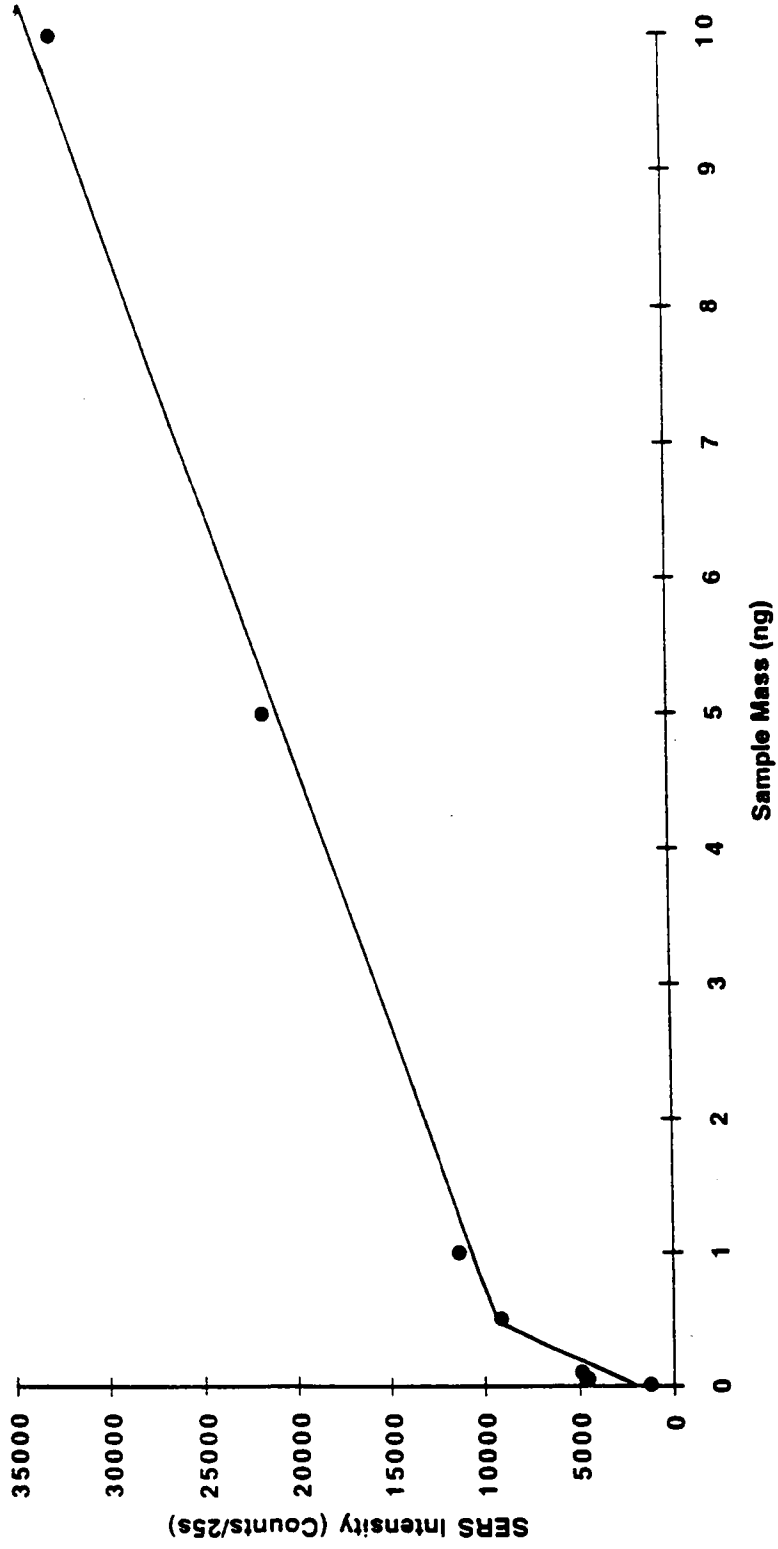
Figure 5.15. Calibration curve for SERS detection of Dichloran using the spectrograph-based fiberoptic system for remote detection. Dichloran signal at 1250 cm^{-1}. Alumina-based substrate.

Nevertheless, quantitative analyses may be possible for both regions. Least squares analyses have indicated absolute standard deviations of 1500 and 850 in y values comprising the best straight lines for the 0.01-0.5-ng and 0.5-10-ng ranges, respectively. The LOD for Dichloran was determined to be approximately 0.06 ng, assuming a minimum detectable level to be 3 times the standard deviation of the noise.

Analysis of a mixture solution. As a final demonstration, the spectrographic-based fiberoptic SERS detection system was applied to the analysis of a complex mixture of both volatile and nonvolatile compounds in both the liquid and dry states. A mixture of 55% benzene, 14% pyridine, 30 ppm Dichloran, and 300 ppm 2,4-dinitrophenol was prepared in ethanol. An alumina-based substrate was place in a beaker and covered with thin layer of the mixture solution. The beaker was then placed in the remote SERS detection module, and a spectrum was immediately acquired for the solution, which rapidly evaporated (within minutes) to leave a dry SERS substrate. A spectrum was then acquired for the dry SERS substrate. Figure 5.16 illustrates the two spectra, which have dramatically different appearances. For the solution state, the spectrum is dominated by doublet bands at 975 and 1005 cm^{-1}, which are attributed to the pyridine component of the mixture. No benzene bands were observed. After evaporation, the characteristic bands of the volatile pyridine disappeared, and bands characteristic of both Dichloran and 2,4-dinitrophenol emerged. The dominant band at 1310 cm^{-1} is due to 2,4-dinitrophenol. Another discernible band uniquely attributable to 2,4-dinitrophenol occurs at 606 cm^{-1}. Otherwise, the band at 814 cm^{-1} can be assigned to both Dichloran and 2,4-dinitrophenol. Nevertheless, clear evidence of Dichloran detection is the distinct band at 900 cm^{-1}. Other, not-so-obvious bands unique to Dichloran include a shoulder at 1250 cm^{-1}, and weak bands at 1110, 700 and 440 cm^{-1}. This study thus demonstrates the value of the spectrographic-based detection of
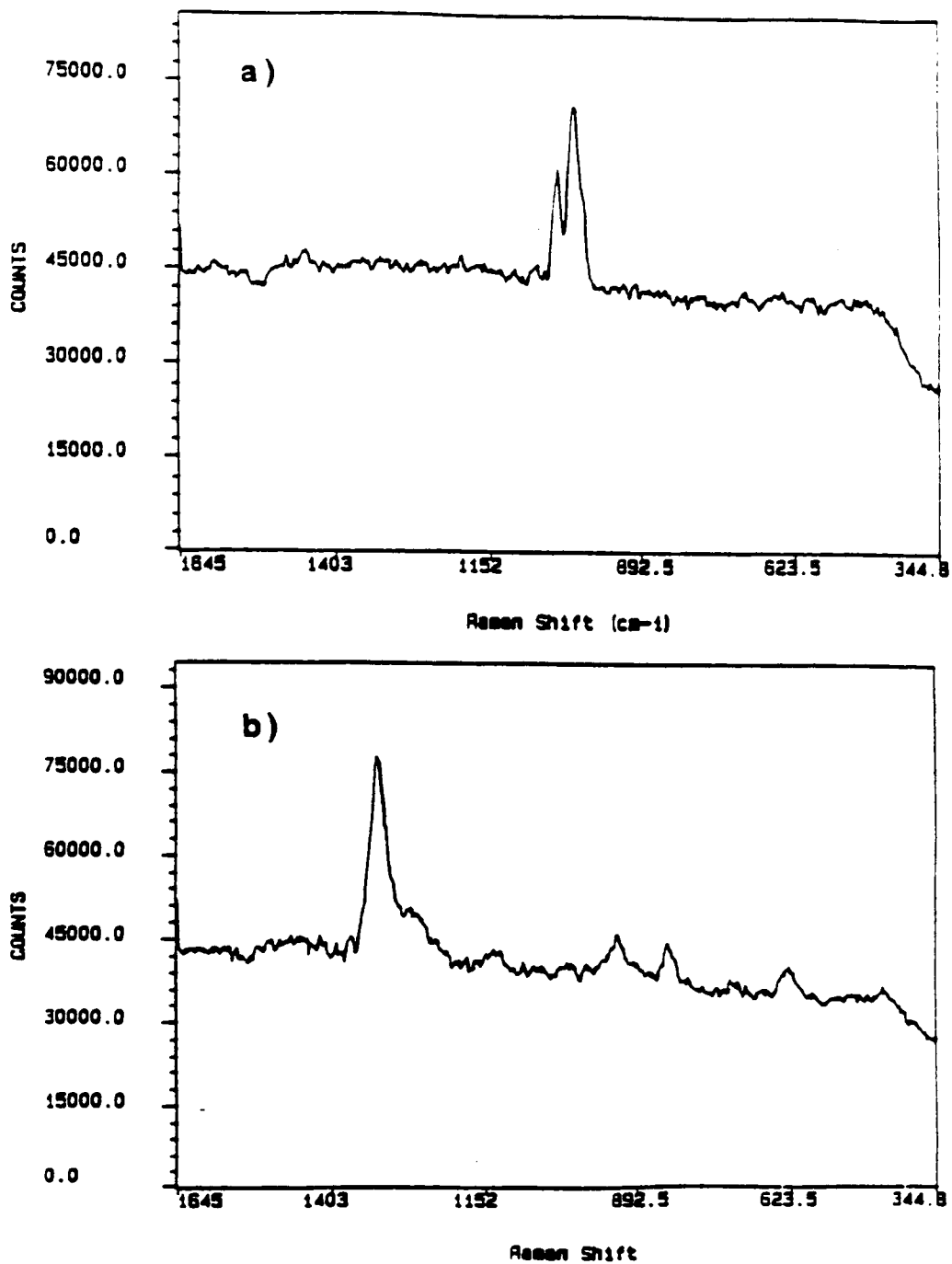
Figure 5.16. SERS spectra of a mixture of benzene (55%), pyridine (14%), Dichloran (30 ppm), and 2,4-dinitropheol (300 ppm) generated from a) solution, and b) dry -state samples, as measured with the spectrograph-based fiberoptic system for remote detection. Alumina-based substrate

volatile compounds, while also illustrating the ability for multicomponent analysis with the remote SERS detection module.

In conclusion, two emergent technologies, the holographic notch filter and the RE-ICCD, were combined in the development of a compact spectrographic detection system which was used for remote SERS detection by coupling to a 20-m, dual-element, fiberoptic system. Using several compounds of health and environmental interest, several advantages relative to a conventional single-channel detection instrument were demonstrated, including speed, detectivity, and compactness. For example, it was demonstrated that with the spectrographic system, SERS spectra could be acquired in approximately 1/30 of the time required when using the scanning instrument for comparable S/N values and spectral resolution. Furthermore, the high detectivity and multichannel advantage offered by the RE-ICCD enabled the use of a low-power helium-neon laser (1/10 of the power used for the scanning instrument). The resulting spectrographic system, including the laser and optical components, measured 1,260 cubic inches. This volume was in striking contrast to the 20,850 cubic inches occupied by the laser and optical components comprising the scanning system.

DEVELOPMENT OF AN INTEGRATED SINGLE-FIBER SERS SENSOR

Experimental

Single-fiber SERS sensor fabrication. A schematic diagram of the SERS sensor is illustrated in <u>Figure 5.17</u>. An 8-cm section of 600-μm core diameter optical fiber
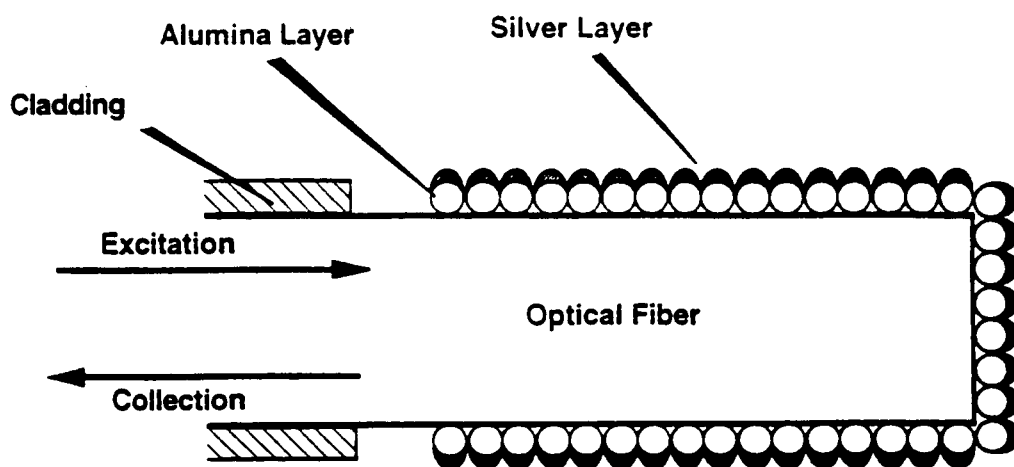
Figure 5.17. Schematic diagram of an integrated single-fiber SERS sensor.

Source: D. L. Stokes, and T. Vo-Dinh, *Sensor Actuat. B-Chem.* (1999) in press.

(Fiberguide Industries, NA=0.26) was cleaved and the jacket and cladding was stripped to a length of approximately 1 cm from each end. The ends were then polished with alumina polishing sheets (0.5-μm grain), after which they were cleaned with dilute nitric acid, then rinsed with water and ethanol. Once the fiber was polished and cleaned, one end was dipped in a 5% (wt/vol) aqueous alumina suspension for about five seconds. The alumina-coated tip was then allowed to dry for at least ten minutes, after which the fiber was mounted in a vacuum evaporation system (Cooke Vacuum Products, Model CV-301) for deposition of 100 nm silver. The fiber was situated so that the entire diameter of the alumina-coated tip was exposed directly to the metal source. Silver deposition was performed at 2×10^{-6} torr, with a rate of 1-1.5 Å/s.

Planar SERS substrates. As a standard for evaluating the performance of the new SERS optical fiber sensor, conventional alumina-based planar SERS substrates were prepared as described in Chapter 2 for maximum enhancement.

Instrumentation. All SERS measurements were performed with the 320-mm spectrograph described in the previous section (ISA, Model HR-320). All spectrometer parameters were the same as described in the previous section. In addition, the RE-ICCD (Princeton Instruments, Model RE/ICCD 576S) was operated as described in the previous section.

The auxiliary optical system used for this study is illustrated in <u>Figure 5.18</u>. A helium-neon laser (SpectraPhysics, Model 106-1) was used to provide the 632.8-nm radiation which was spectrally purified with a bandpass filter (Corion, Model P3-633-A). Once past the filter, the laser beam power was approximately 5 mW. A 632.8-nm holographic beam splitter (Kaiser, Model HB-633-1.0) was used to direct nearly
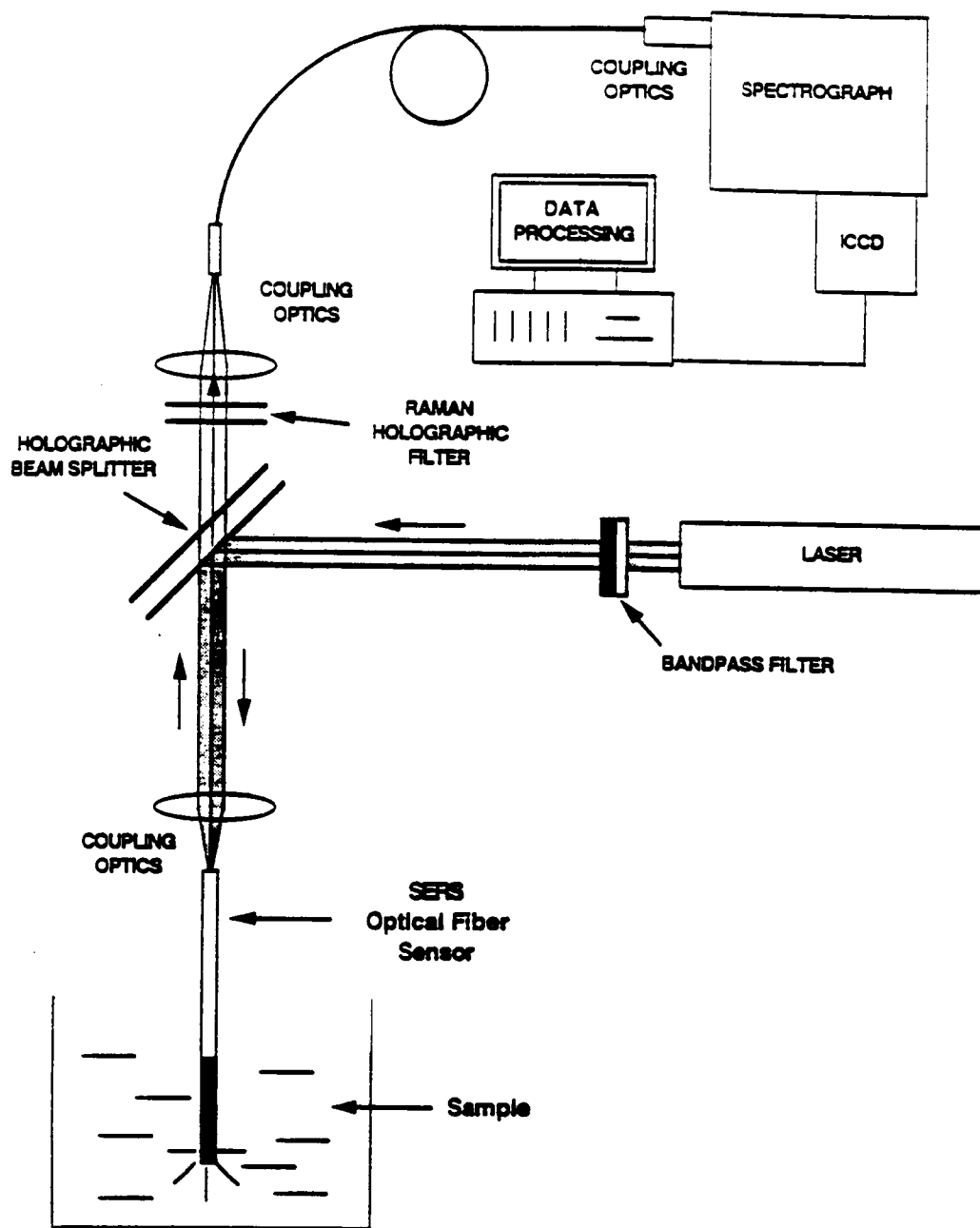
Figure 5.18. Schematic diagram of the auxiliary optical system used with the integrated single-fiber SERS sensor.

Source: D. L. Stokes, and T. Vo-Dinh, *Sensor Actuat. B-Chem.* (1999) in press.

207

100% of the beam into an objective lens (10X) which then focused the beam into the SERS sensor for sample excitation. The signal returning from the SERS-active tip was collected and collimated by the objective lens. The signal beam was then nearly 100% transmitted through the holographic beam splitter to a 1", f/2 lens which focused the signal beam onto a second 600-μm optical fiber (Fiberguide Industries, NA=0.26). A Raman holographic notch filter (Physical Optics Corporation) was also used to reject any unwanted reflected or Rayleigh scattered radiation from the expanded signal beam prior to focusing onto the second optical fiber, which transmitted the signal to the spectrograph for detection. A two-lens system was used to provide efficient coupling between the optical fiber and the f/4 spectrometer. For cases when the planar SERS substrates were used for comparison, the substrate was simply placed at the focus of the objective lens, thereby replacing the fiberoptic sensor.

Chemicals and reagents. PABA (Aldrich, 99% pure), 3-aminopyrene (Pfaltz and Bauer, technical grade), Brilliant Cresyl Blue (BCB) (Allied Chemical and Dye Corp., 68% pure) and Cresyl Fast Violet (CFV) (Fluka, standard purity for microscopy) were all used as purchased. A stock solution of PABA (1.0×10^{-3}M) was prepared in water. Stock solutions were prepared in ethanol for BCB (1.0×10^{-4}M) and CFV (9.9×10^{-5}M). All ethanol solutions were prepared with reagent-grade ethanol (J. T. Baker), while all aqueous solutions and cited dilutions were prepared with water which had been filtered with a Waters Milli-Q+ filtration system.

Results and Discussion

In previous sections describing developments of SERS-based fiberoptic sensors, a dual-fiber approach was taken for remote detection. The microparticle-based substrate

208

technology was incorporated into the sensors as a planar substrate which was a detachable entity, independent from the fiberoptic system itself. In this section, the development of a single-fiber sensor is described for *in situ* remote detection at the microscale level. The fiber, used for both sample excitation and signal collection, was modified by applying the microparticle layer required for the SERS effect directly to the optical fiber and coating the fiber with the silver layer. The relative merits of single-fiber detection of luminescence and Raman scattering have been discussed in the literature (Cooney *et al.*, 1996a,b). Furthermore, abrasively-roughened optical fibers coated with silver have been reported for possible use in single-fiber SERS detection (Mullen and Carron, 1991). Our approach to single-fiber SERS sensor development merits reporting because it utilizes the microparticle-based SERS substrate technology which has been proven successful in a variety of applications, as discussed in Chapter 2. Furthermore, the microparticle-based SERS technology exhibits commendable reproducibility and is simple to fabricate.

Comparison study of the fiberoptic SERS sensor probes and planar substrates. The silver-coated alumina design of the SERS-active fiberoptic is analogous to the planar SERS substrates previously discussed (Chapter 2). We therefore used the standard planar alumina-based substrate as a reference for evaluation of the fiberoptic sensor. Figures 5.19a and b show the SERS spectra of BCB using a conventional planar SERS substrate and the fiberoptic sensor, respectively. The laser power, detector duty time (25 s) and the detector gain level were constant for the two measurements. In the case of the planar substrate, a 50-ng sample (1-µL aliquot of a 50 ppm solution) of BCB was deposited onto the substrate and allowed to dry. In a manner analogous to this spotting and drying technique, the fiberoptic SERS sensor was
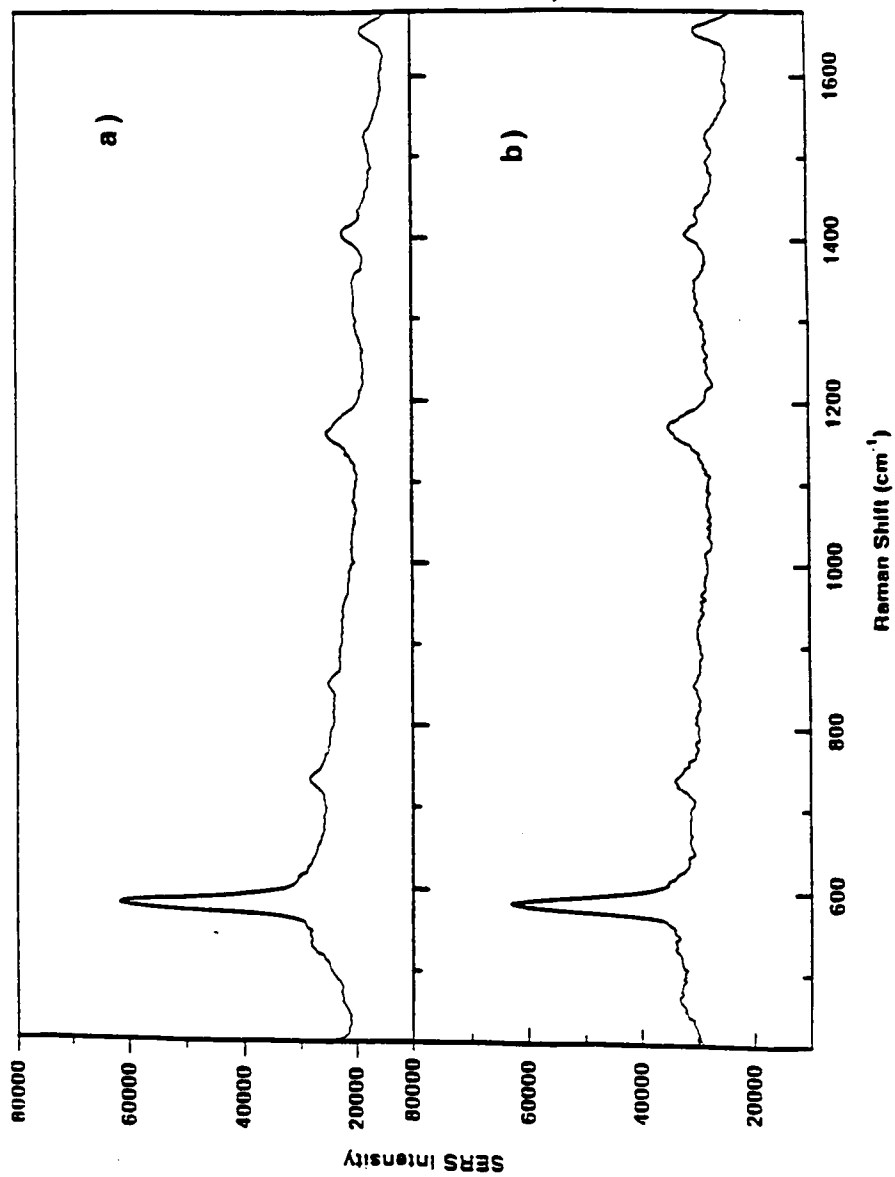
Figure 5.19. SERS spectra of 50-ppm BCB acquired with a) a conventional planar alumina-based substrate, and b) the integrated single-fiber SERS sensor. HeNe laser, 632.8 nm, 5 mW.

Source: D. L. Stokes, and T. Vo-Dinh, *Sensor Actuat. B-Chem.* (1999) in press.

dipped into the 50 ppm solution and quickly removed and allowed to dry prior to measurement.

The results depicted by Figure 5.19 illustrate that the optical fiber sensor is capable of yielding signals comparable to those obtained with the conventional planar SERS substrate. It is noteworthy that an exact comparison of the two different probe systems is not possible. While the concentration of the analyte solution is the same in both cases, several differences exist in the two optical systems. For example, the planar substrate measurement involved tightly focusing the laser beam directly onto the substrate with a 10X objective lens. For the fiberoptic sensor example, the divergent laser radiation excited the 0.28 mm^2 area corresponding to the tip of the SERS sensor, defined by the 600-μm core diameter. This area is likely more than thirty times the area probed with the objective lens. Excitation of the molecules adsorbed to the SERS-active sides of the optical fiber was also possible, but this contribution to the total observed signal has not yet been fully evaluated. Although the laser power was constant at 5 mW for both experiments, attenuation of the excitation beam as well as the collected SERS signal would have been more significant in the fiberoptic sensor measurement due to the additional optical coupling losses and attenuation by the fiberoptic probe. Some attenuation of the laser excitation beam and SERS signal by the alumina and silver layers on the probe tips may also occur in the single fiber sensor design. In order to take into account and simulate this attenuation condition with the planar substrate measurements, excitation was performed from the back side of the substrate. However, regardless of these variable conditions, the S/N values of the reported spectra obtained with both probe systems are similar.

"Dip-and-dry" mode of detection. The sensor was tested for a variety of compounds in the "dip-and-dry" mode of detection described above. Figures 5.20a and b illustrate spectra of PABA and 3-aminopyrene (3AP) taken with two separate probes. Their respective ethanolic solution concentrations were both 1.0×10^{-3} M (137 ppm PABA; 217 ppm 3AP). High quality spectra were observed in each case with total acquisition times of less than two minutes. A typical blank spectrum of a sensor prior to dipping in an analyte solution is given in Figure 5.20c. As demonstrated, background from the sensor was minimal, with the most prominent feature being a broad band in the 370-700-cm^{-1} region. As mentioned in previous sections, this band can be attributed to silica Raman scattering in the SERS sensor fiber rising from the intense laser beam and Rayleigh scatter. Corrective filters can often be used to offset this effect, as discussed in the previous section. For example, the schematic diagram of the optical system illustrated in Figure 5.18 demonstrates that a Raman holographic filter was used to reject the intense Rayleigh scatter from the system, but was on the spectrograph side of the beam splitter which separated the signal from the excitation beam. As a result, Raman scattering in the long fiber that transmitted the signal to the spectrograph was minimized. This corrective measure could not be implemented on the single-fiber sensor side of the beam splitter because both excitation and the collected SERS signal are transmitted through the fiber simultaneously. Nevertheless, use of the fiber in the "dip-and-dry" mode of detection has some distinct advantages over the use of the planar substrate. For example, it permits sampling of microenvironments with minimal sample handling (no transfer steps are required) and data acquisition times are typically less than two minutes.

In situ detection scheme. In addition to the "dip-and-dry" mode of detection cited above, the single-fiber SERS sensor offers the possibility of *in situ* analysis of
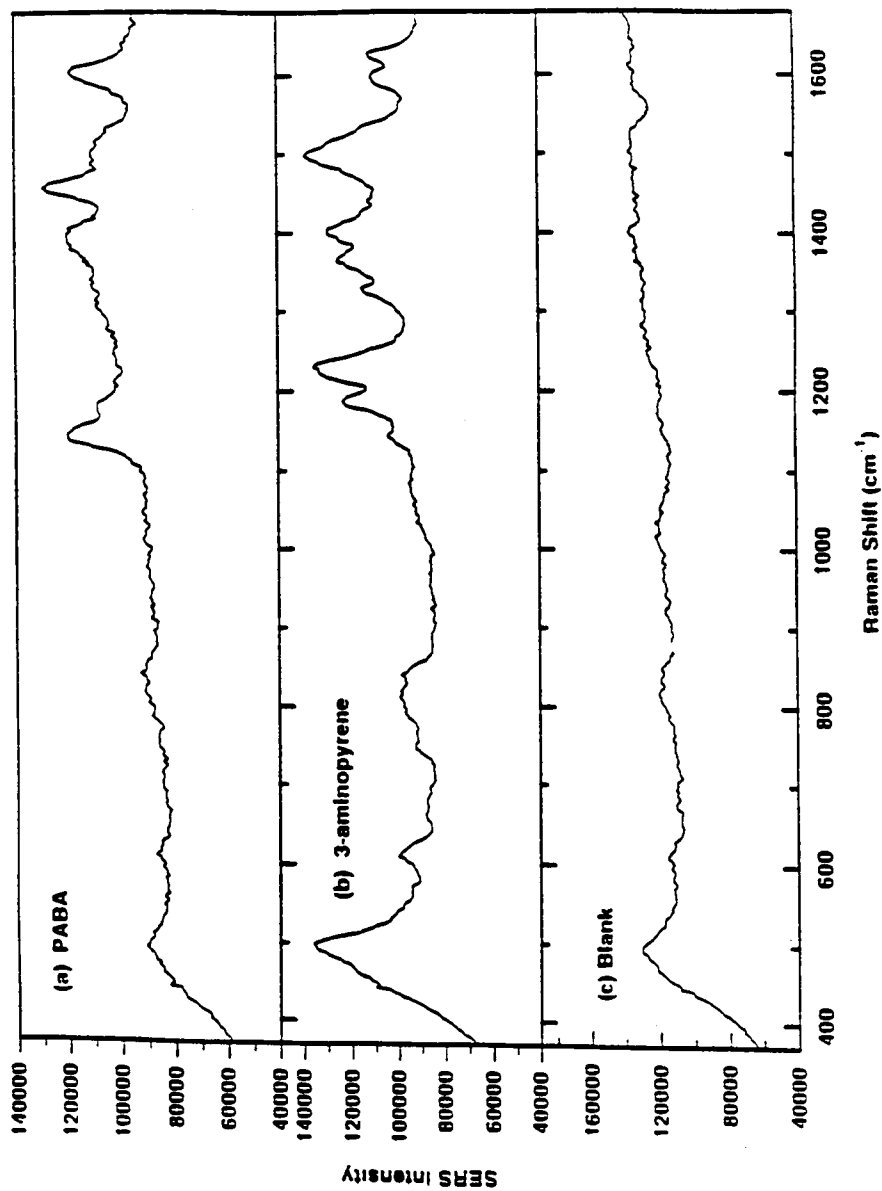
Figure 5.20. SERS spectra of a) PABA (137 ppm), b) 3-aminopyrene (217 ppm), and c) a dry blank, all acquired with the integrated single-fiber SERS sensor. HeNe laser, 632.8 nm, 5 mW.

Source: D. L. Stokes, and T. Vo-Dinh, *Sensor Actuat. B-Chem.* (1999) in press.

microenvironments. Real-time measurements of dynamic processes may be feasible. Figure 5.21 demonstrates the SERS spectra of 30 ppm CFV in the a)"dip-and-dry" and b) *in situ* modes of detection. Both spectra were acquired with the same sensor, which was dipped in the aqueous CFV solution. The *in situ* spectrum was acquired before removing the sensor and allowing it to dry for the "dip-and-dry" spectrum acquisition. Detection parameters were constant for both spectra (5 accumulated spectra of 5 s each). The 595 cm^{-1} band intensity for the *in situ* measurement was approximately 40% lower than that shown for the "dip-and-dry" mode. The higher intensity observed with the "dip-and-dry" measurement could have been due to a higher fiberoptic numerical aperture (light gathering capability) in air resulting from the lower refractive index of air relative to water. It is also possible that the number of analyte molecules excited by the dry measurement may have been enhanced due to the concentrating effect via solvent evaporation from the residual volume of the sample solution which adhered to the sensor tip when it is removed from the analyte solution.

Figure 5.22 illustrates a similar comparison using a 0.77 ppm solution of BCB. Although the concentration level is far removed from that of the previous example, the signal attenuation due to submersion in water was very similar, approximately 45%. Another point of interest for the spectra in Figures 5.21 and 5.22 is the apparent lack of the fiberoptic background which is observed in the "dip-and-dry" spectra of Figure 5.20. The reason for the absence is the sheer intensity of the CFV and BCB spectra arising from some resonance or preresonance enhancement. As a result, lower detection gains were used which did not bring out the background structure. On the other hand, the "dip-and-dry" spectra of Figure 5.20 appear much less noisy even though detector gain levels were much higher. This observation is due to the longer integration time (10 s)
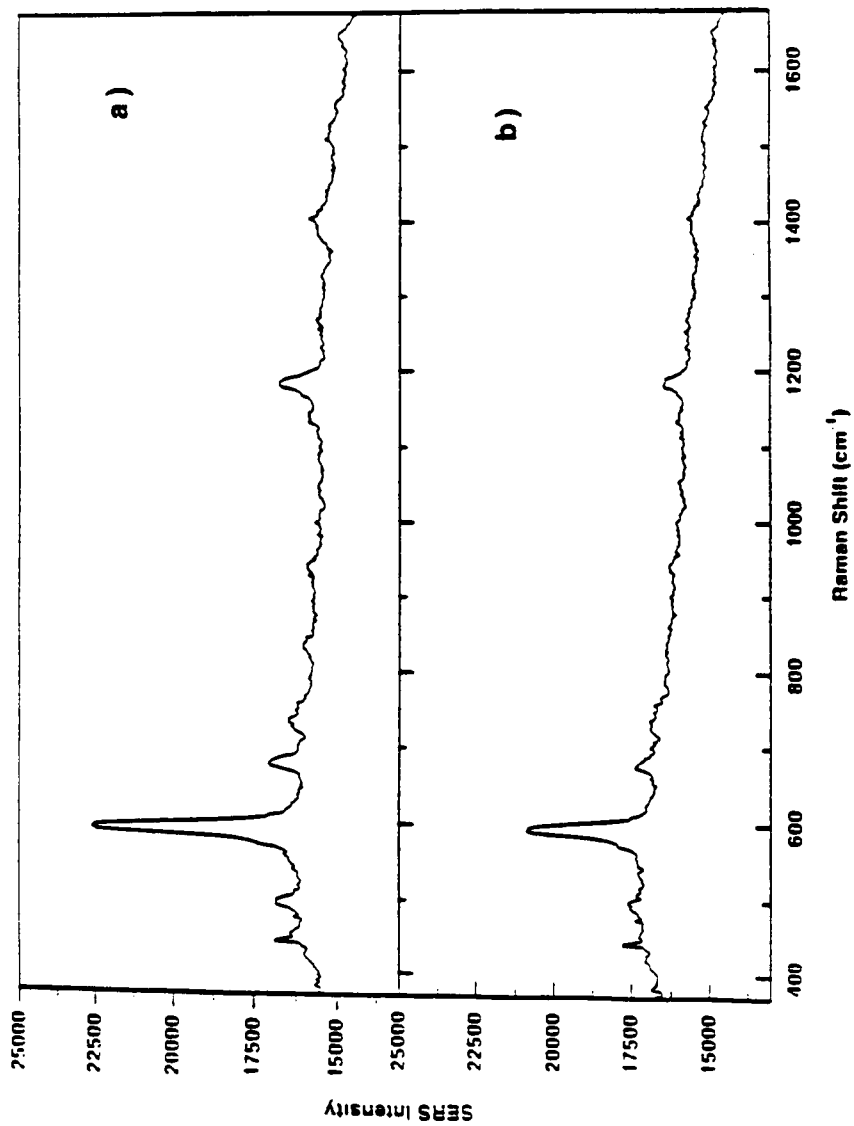
Figure 5.21. SERS spectra of 50 ppm CFV (aqueous sample) acquired with the integrated single-fiber SERS sensor in the a) "dip-and-dry", and b) *in situ* modes of detection. HeNe laser, 632.8 nm, 5 mW.

Source: D. L. Stokes, and T. Vo-Dinh, *Sensor Actuat. B-Chem.* (1999) in press.
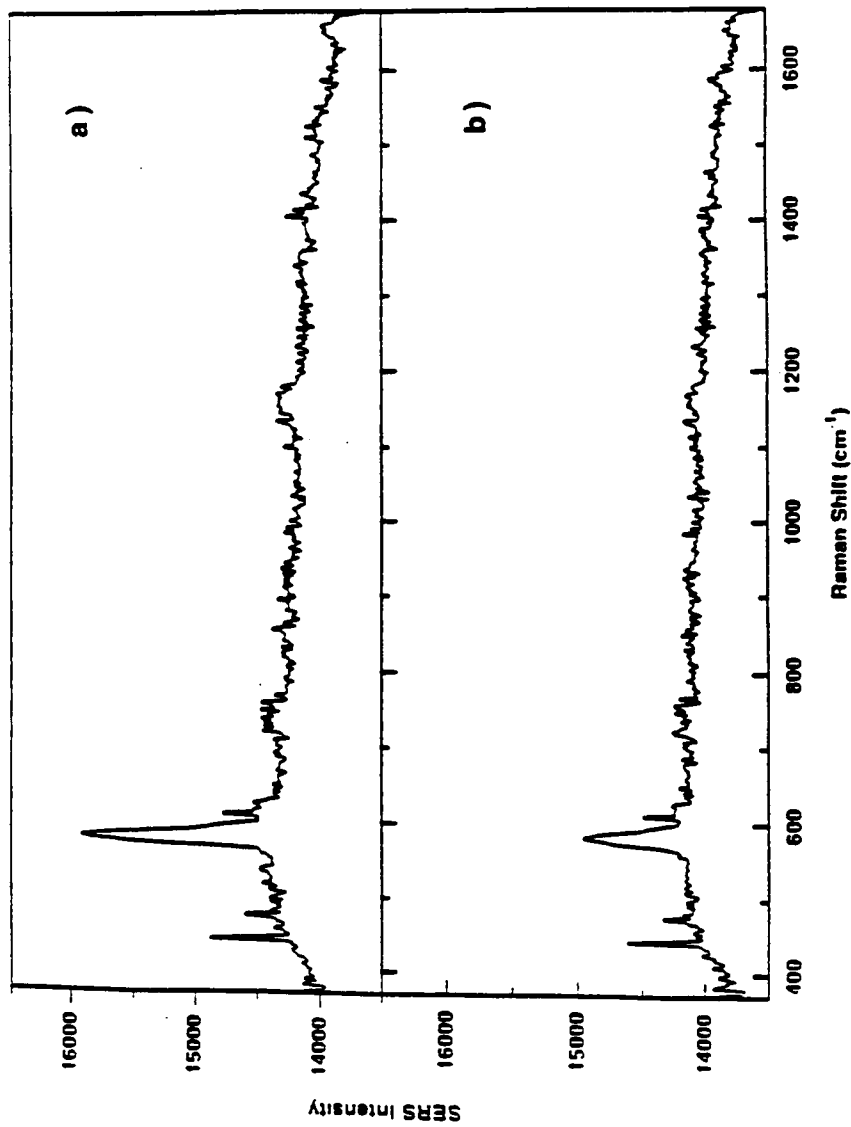
Figure 5.22. SERS spectra of 0.77 ppm BCB (aqueous sample) acquired with the integrated single-fiber SERS sensor in the a) "dip-and-dry", and b) *in situ* modes of detection. HeNe laser, 632.8 nm, 5 mW.

Source: D. L. Stokes, and T. Vo-Dinh, *Sensor Actuat. B-Chem.* (1999) in press.

and larger accumulation number (ten) relative to those used for the spectra in Figures 5.21 and 5.22 (5 s and 5 accumulations, respectively).

Figure 5.23 shows *in situ* spectra of groundwater acquired from an industrial waste site. The groundwater blank yielded no significant Raman structure at the selected detector gain level, yet there appears to be some fluorescence background in the 1000-1700-cm^{-1} range. When spiking the sample with 500 ppb CFV, the broadband interference became insignificant, as shown by Figure 5.23a, thus demonstrating the selectivity of analysis. The feasibility of monitoring groundwater migration with CFV dye using the SERS sensor is demonstrated by these results.

SERS signal stabilization study for *in situ* measurement with the single-fiber SERS sensor. It has been demonstrated in previous studies that a SERS signal stabilization period may be required for quantitative analyses via *in situ* solution measurements (Chapter 2). As was previously discussed, the stabilization of signal with time is reflective of the attainment of a time-dependent state of equilibrium between analyte molecules in the bulk solution and those adsorbed at the substrate surface. Because the rate of adsorption could be influenced by the analyte concentration in the bulk solution, signal stabilization studies were performed for CFV at two concentrations, 82 and 600 ppm.

Figure 5.24 illustrates the resulting stabilization curves for peak intensities measured at 595 cm^{-1}. The abscissa of this figure corresponds to the time after which the SERS sensor was dipped in the premixed, aqueous sample. The sample was continuously irradiated. Consistent with previous studies, both curves appear to exhibit two distinct
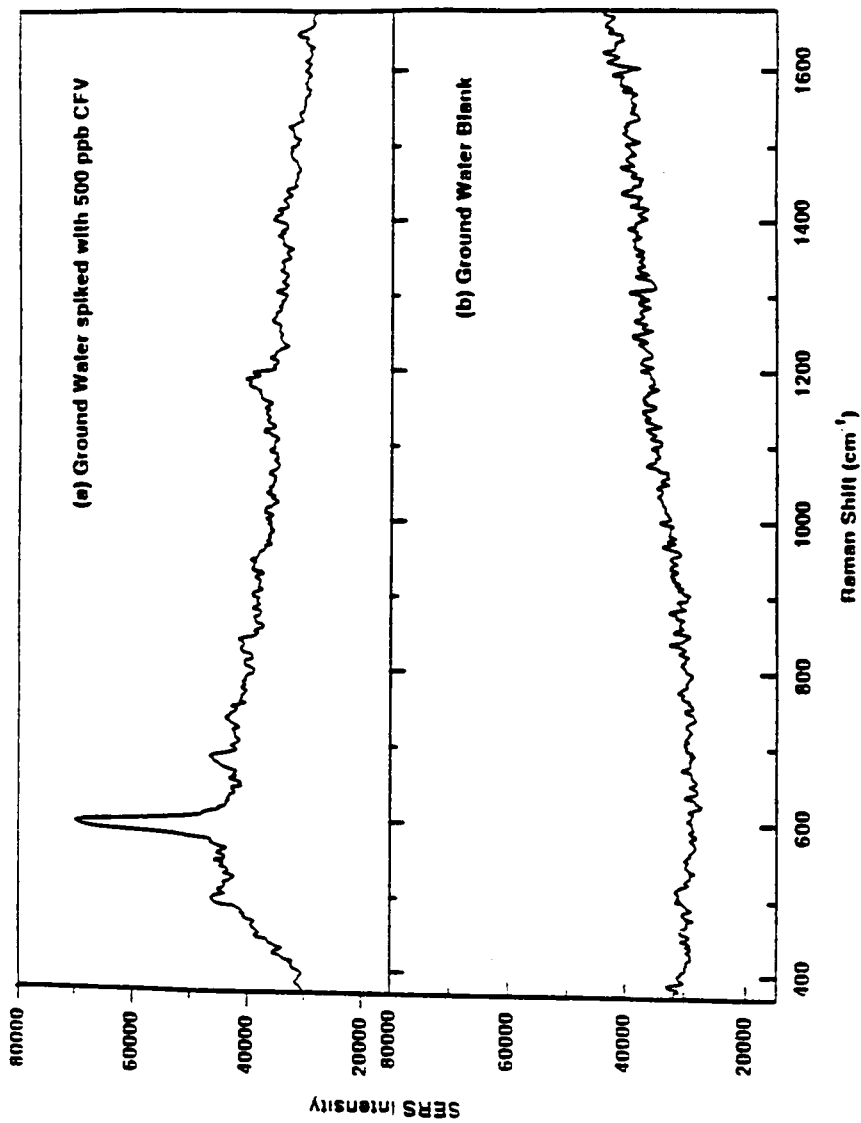
Figure 5.23. SERS spectra of a) groundwater spiked with 500 ppb CFV, and b) unspiked groundwater, acquired *in situ* with the integrated single-fiber SERS sensor. HeNe laser, 632.8 nm, 5 mW.

Source: D. L. Stokes, and T. Vo-Dinh, *Sensor Actuat. B-Chem.* (1999) in press.
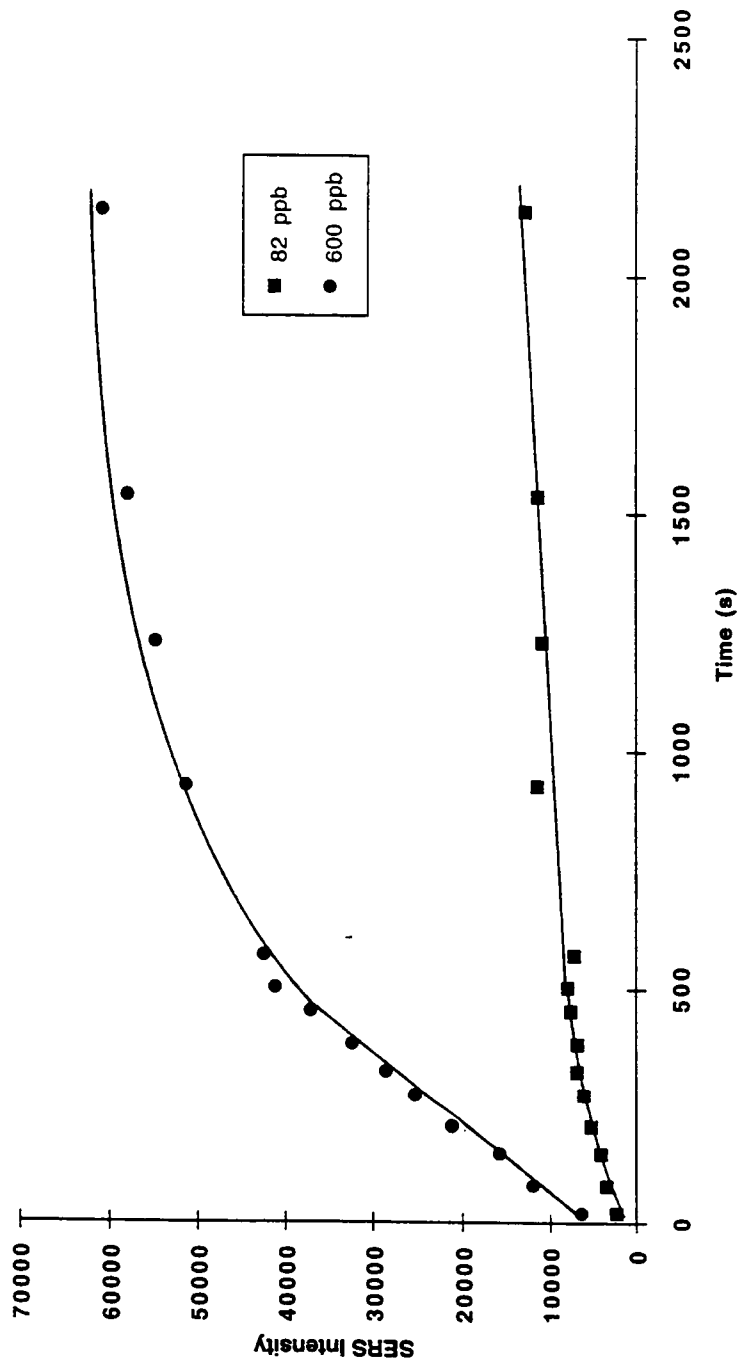
Figure 5.24. SERS intensity plots illustrating signal stabilization times for 82-ppb and 600-ppb CFV solutions, acquired *in situ* with the integrated single-fiber SERS sensor. CFV signal at 585 cm^{-1}. HeNe laser, 632.8 nm, 5 mW.

regions: one region of almost linear increase in SERS intensity with time, and a second linear region of much more gradual signal increase with time.

For both concentrations, the most rapid rate of signal growth tapers off by 10 min of exposure to the analyte solution. This result indicates that for 80-600 ppb concentration range, the stabilization process is not dramatically dependent on the concentration of the analyte in the bulk solution. Furthermore, the result implies that the variation of stabilization observed for different analytes studied in previous studies (e.g., PABA and FITC) could have been more dependent on chemical structure and functional groups in the analyte adsorption process than the bulk analyte concentrations. While a plateau region was never attained in these studies, Figure 5.24 illustrates that enhanced precision in quantitative analyses could be achieved upon allowing 10-min signal stabilization periods.

Analytical figures of merit. Several quantitative figures of merit were evaluated for sensor performance with groundwater samples. Figure 5.25 illustrates a calibration curve for CFV, measured *in situ*. All data points are related to the peak intensity at 585 cm^{-1}. The entire curve was generated using the same single-fiber SERS sensor. The tip was simply dipped into the initially unspiked groundwater sample. Appropriate amounts of concentrated aqueous CFV spiking solution were added between measurements. Solutions were stirred after each stock addition, and the spectra were then acquired after a 10-min signal stabilization period, as suggested by the previous study. The sample was continuously irradiated during the stabilization period. As demonstrated by the figure, linearity of the analytical curve is observed for the range spanning from the LOD up to 560 ppb. The correlation coefficient for this range was 0.9949. At higher concentrations, the negative deviation from linearity could indicate
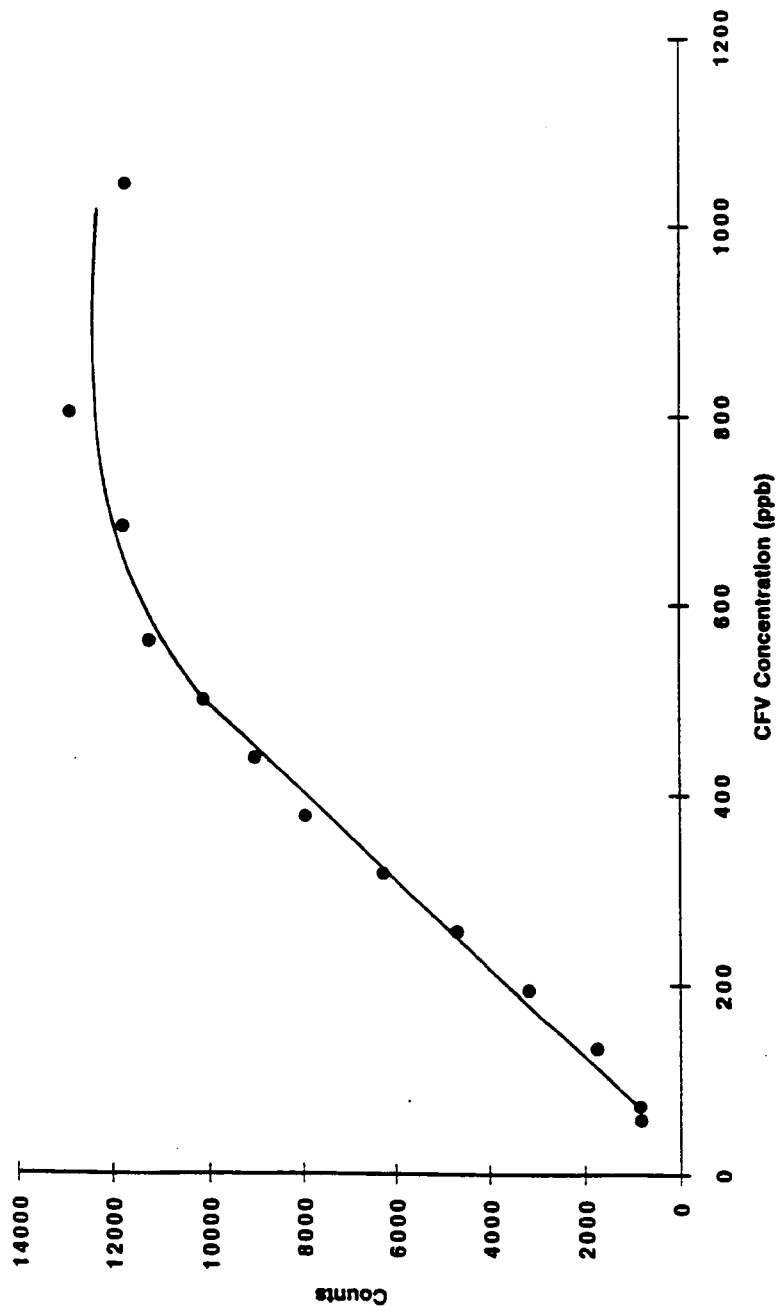
Figure 5.25. Calibration curve for SERS detection of CFV (585 cm^{-1}) in groundwater using the integrated single-fiber SERS sensor. HeNe laser, 632.8 nm, 5 mW

Source: D. L. Stokes, and T. Vo-Dinh, *Sensor Actuat. B-Chem.* (1999) in press.

saturated analyte coverage of the SERS sensor tip. In general, the sensor has a limited capacity for adsorption of molecules in a molecule. Once this capacity is exceeded, any additional molecules attracted to the sensor do not exhibit an optimal SERS effect, which decreases with distance between the analyte molecule and the metal surface. Using the sensitivity of the linear region cited above, the LOD of CFV in groundwater for this particular sensor was determined to be 50 ppb, assuming a minimum detectable signal level to be 3 times the standard deviation of the noise.

The use of indicator dyes is common in monitoring underground water flow patterns in environmental remediation applications. The detection of fluorescence of various dyes (e.g., fluorescein) has been used for this purpose. SERS can provide a sensible alternative for environmental monitoring of underground waters due to the spectral selectivity it offers. Indeed, multiple dyes could be used for multiple underground sources and monitored simultaneously at a given site due to the multicomponent analysis capability offered by SERS, as demonstrated in previous studies.

In conclusion, a new single-fiber sensor has been developed which uses a microparticle-based metallic coating for SERS detection. The design, based on a single-fiber for both excitation and SERS signal collection, allows the development of in situ sensors for sampling microscale environments. This microparticle-based SERS substrate technology may prove to be valuable in the use of single-fiber SERS sensors due to the ease of fabrication and high degree of reproducibility. Furthermore, the microparticle-based substrate technology has been successfully demonstrated in a wide variety of environmental applications, as demonstrated in by previous studies (Chapter 2). This study involved both "dip-and-dry" and in situ modes of detection. In situ measurement potentially offers the advantage of real-time remote data acquisition. Nevertheless, the

"dip-and-dry" mode of detection with this new sensor has advantages over the use of planar SERS substrates. For example, the small diameter of a typical fiber may allow direct entry into very small sample environments, thus potentially minimizing sample handling. Moreover, the sensor may have bioanalytical applications. The simplicity of the design may enable microscale and nanoscale fabrication for sampling such small venues as intracellular environments.

CHAPTER 6

APPLICATION OF SOLID-BASED SERS SUBSTRATES TO THE DETECTION OF AIRBORNE CHEMICALS/ DEVELOPMENT OF A SERS VAPOR DOSIMETER

INTRODUCTION

Previous works with the SERS technology have primarily involved the analysis of solid and liquid samples. In this study, the solid-based SERS substrate technology is applied to the detection of airborne chemicals and the development of a SERS vapor dosimeter. While radiation dosimetry has a long history of development and successful implementation in some hazardous work environments, there has also been much recent interest in the development of dosimeters for the detection of harmful airborne chemicals. The interest can in part be due to the emergence of Gulf War Syndrome and the suspected use of chemical warfare agents. As is reported in the literature, vapor dosimeters have been developed in a variety of fashions (Wallace and Ott, 1982; Palmes, 1979). However, many of these devices employ a sorbing medium to adsorb the pollutant vapors. Subsequent analyses typically require multiple steps, such as sample extraction from the sorbing medium, sample concentration, sample shipping and handling, and the analytical measurement (which is often a form of chromatography). Needless to say, the process can be very time-consuming and complicated.

The SERS technology therefore offers many potential advantages in the detection of airborne pollutants. For example, the solid SERS substrate discussed in previous chapters can act as the sorbing medium. Because the SERS substrate acts as a signal amplification medium, there is no need for sample extraction and concentration steps prior to analysis. Furthermore, because of the spectral selectivity of SERS and the potential for simultaneous multicomponent analysis, there may be no need for complicated separation procedures. As a demonstration of these potentials, the solid SERS substrate technology has been incorporated into a passive dosimeter previously developed in this laboratory for luminescence-based analysis (Vo-Dinh, 1985). This dosimeter is a compact and lightweight device (30 g). Furthermore, the principle of operation is very simple. The analyte is simply collected via molecular diffusion towards and subsequent adsorption onto the metallic SERS substrate surface. The dosimeter is then inserted into a SERS detection system for analysis. As has been demonstrated in previous spectrograph-based studies (Chapter 5), the SERS detection system can be compact and relatively economical.

For a more detailed description of the principles of sample collection, the reader is first referred to the schematic diagram of the SERS dosimeter in Figure 6.1. The device, measuring 4.0 cm x 1.0 cm, consists of a badge-size dosimeter holder, a SERS substrate (the heart of the dosimeter), and diffusion tubes. There is a retaining plate with 0.5-cm diameter air sample holes to both house the diffusion tubes and secure the SERS substrate to the dosimeter holder. A variety of SERS substrates can be easily installed in this design. In this study, alumina-based substrates and polymer-coated silver islands substrates described in Chapters 2 and 3 were evaluated for potential use. The diffusion tube is a honeycomb tube of parallel cylindrical holes of 0.001-m diameter and 0.004-
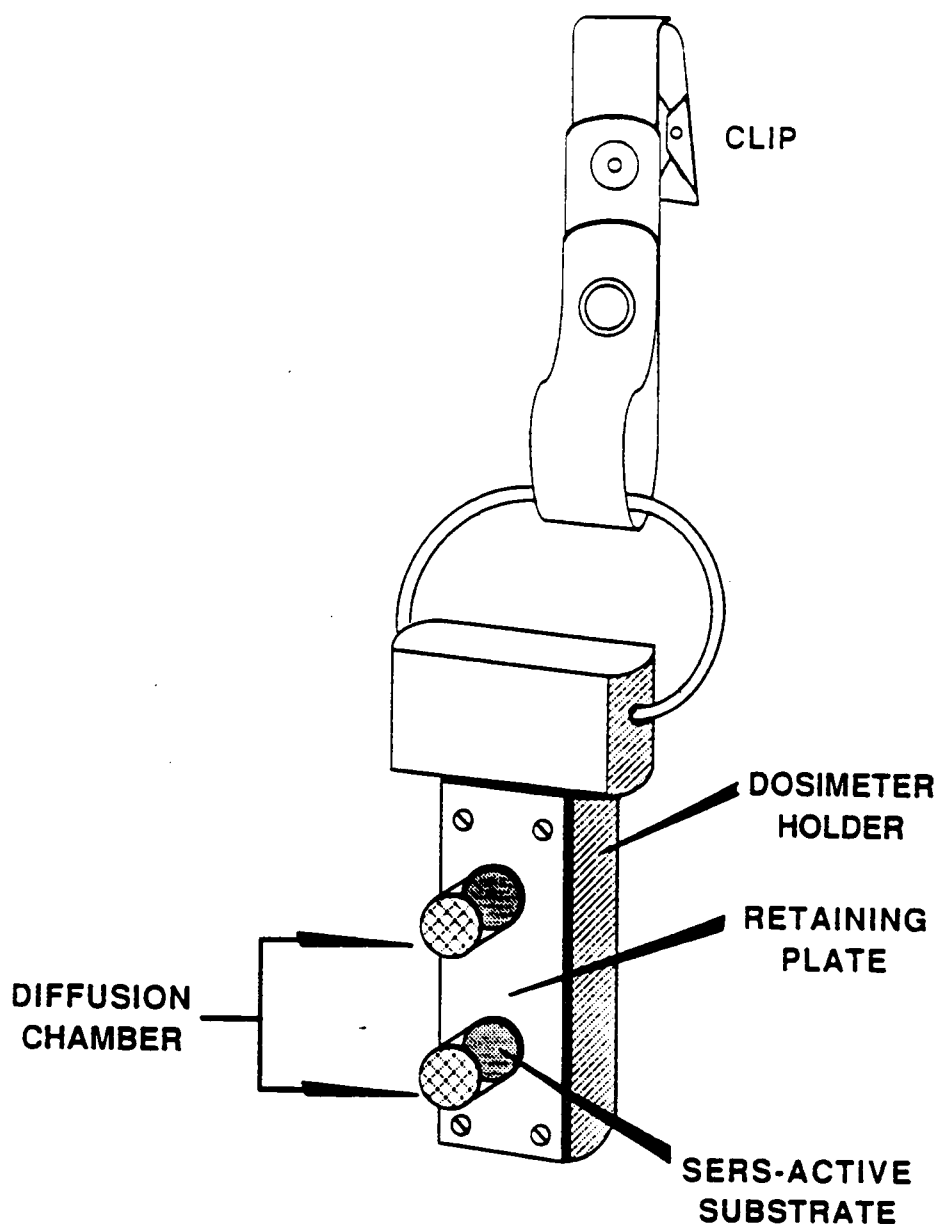
Figure 6.1. Schematic diagram of the SERS dosimeter.

Source: T. Vo-Dinh, and D. L. Stokes, *Appl. Spectrosc.* **47**, 1728 (1993).

m length. The honeycomb array prevents turbulence in windy environments, thus preventing artifacts from sporadic mass transfer and preserving reproducibility.

Vapor collection of the dosimeter is based on molecular diffusion across the diffusion tube, driven by a concentration gradient (dC/dx)(kg $\cdot$ m^4) established between the inlet end of the tube $(x = L)$ and the SERS substrate surface $(x = 0)$. The higher concentration is defined by the ambient analyte vapor molecules at the open end of the tube (C_0), while the lower concentration corresponds to the concentration of analyte molecules very near, but not adsorbed to, the SERS substrate surface C_s (kg $\cdot$ m^{-3}). Assuming the adsorption process maintains an analyte concentration near the surface at a steady state, the concentration gradient is maintained as long as the substrate remains unsaturated. The concentration gradient deteriorates once the adsorbing surface becomes saturated with the analyte molecules. The diffusion process is approximated by Fick's first law:

$$J = -D\frac{dC}{dx}$$
(6.1)

where J is the molecular flux (kg $\cdot$ m^{-2} $\cdot$ s^{-1}) across the diffusion tube, and D corresponds to the diffusion coefficient (m^2 $\cdot$ s^{-1}), $dC = C_0 - C_s$, and dx is the length of the diffusion path defined by the length of the diffusion tube. The resulting mass collected at the substrate surface is given by:

$$M = D\frac{S}{L}C_0 t$$
(6.2)

where M is the adsorbed mass (kg) at the substrate surface, S is the effective cross-sectional area (m^2) defined by the honeycomb channels of the diffusion tube, and t is the exposure time (s).

It is important to note that the dosimeter described in this work is intended for long-term exposures. It is not suitable for monitoring rapidly fluctuating atmospheres. For example, the time required to establish the concentration gradient across the diffusion tube can be defined as:

$$T = k\frac{L^2}{D}$$

(6.3)

where k is a constant between 0.5 and 1.5 (Heard and Manning, 1980; Fowler, 1982). Assuming the typical diffusion coefficient to be 1 x 10^{-5} m^2 $\cdot$ s^{-1}, the response time is approximately 2 s for the 6-mm long diffusion tube of this dosimeter.

In this work, the feasibility of a SERS dosimeter is demonstrated by installing an alumina-based SERS substrate in the passive dosimeter design described above and exposing it to a well-controlled chemical vapor environment. Furthermore, the feasibility of using a silver islands SERS substrate which is coated with the polymer, poly(vinylpyrrolidone) (PVPL), is investigated. The application of polymer coatings or other organic modification of metallic SERS substrate surfaces has been a focus of recent studies (Chapter 4, Pal *et al.*, 1995; Thompson and Pemberton, 1994; Hill *et al.*, 1994; Hill *et al.*, 1995; Deschaines and Carron, 1997). As was illustrated in Chapter 4, the polymer coating offers many potential advantages for the SERS dosimeter. Used as a protective layer it may prevent deterioration of the silver surface by air oxidation and

exposure to chemically harsh environments, thus increasing the dosimeter's life span. It can also make the substrate surface more scratch-resistant and thus amenable as a rugged, practical dosimeter. Finally, a polymer coating can impart some chemical selectivity. For example, PVPL is permeable to compounds having hydrogen-bonding properties (Mourey *et al.*, 1976). This chemical selectivity not only simplifies spectral analysis, but also may increase the loading capacity of the dosimeter for the analyte molecules of interest, thus increasing the dynamic range of the dosimeter.

EXPERIMENTAL

Instrumentation

Two instruments were used for these studies: 1) a single-channel scanning spectrometer-based system for the initial dosimeter evaluations and the generation of the calibration curve, and 2) a spectrographic system employed for the evaluation of polymer-coated silver island substrates. The single-channel scanning system included a SPEX 1403 double grating spectrometer equipped with a thermoelectrically-cooled gallium arsenide PMT (Burle Industries, Model C31034) and operated with a 2 cm^{-1} bandpass. A right-angle excitation/collection geometry was employed, as described in Chapter 2. The excitation source was the 514.5-nm line of an argon ion laser (Coherent, Innova 70). The laser beam was spectrally purified by a laser line bandpass filter. Laser powers of 40-50 mW were employed with this detection system. Sample excitation and signal collection was performed from the front (silver) side of the SERS substrate. The second detection system included a 320-mm spectrograph (ISA, Model HR320) equipped with a 600-gr/mm holographic grating and an RE-ICCD detector

(Princeton Instruments, RE-ICCD576S). The entrance slit to the monochromator was set at 30 μm for all measurements, and the resulting resolution was approximately 3.3 cm^{-1}. The detector was cooled to -34° C. Detector control and data acquisition was enabled with the CSMA software provided by Princeton Instruments. A confocal excitation/collection geometry from the front side of the SERS substrate was used, enabled by the beam splitting optical system described earlier. A schematic diagram of the auxiliary optical system is illustrated in Chapter 3 (Figure 3.1). As before, the 632.8-nm line of a helium-neon laser (SpectraPhysics, Model 106-1) was used for sample excitation. A 3.0 ± 0.5-nm FWHM bandpass filter was used to remove laser plasma lines. The laser intensity at the sample was approximately 5 mW. A 43X objective lens was used for sample excitation/collection. Otherwise, the optical components, including the 600-μm signal transmission fiber, were the same as described in Chapter 3.

Vapor Exposure System

A simple system was set up for the dosimeter exposure studies utilizing the alumina-based substrates and is illustrated in Figure 6.2. Ethanol-based solutions were injected via syringe into a rapid air stream directed though a network of 0.5-cm i.d. Teflon tubing which delivered the analyte-laden air to an exposure chamber. The injection point was a plumbing Tee joint which had been modified with a rubber septum, through which the analyte was applied via syringe. Injections were performed constantly during each exposure study with a an automated syringe pump. Air was passed through a charcoal filter to remove impurities and through a calcium sulfate filter for drying before entering the analyte carrier flow system. The air flow rate was carefully monitored with flow meters installed prior to the sample injection point and prior to the

230
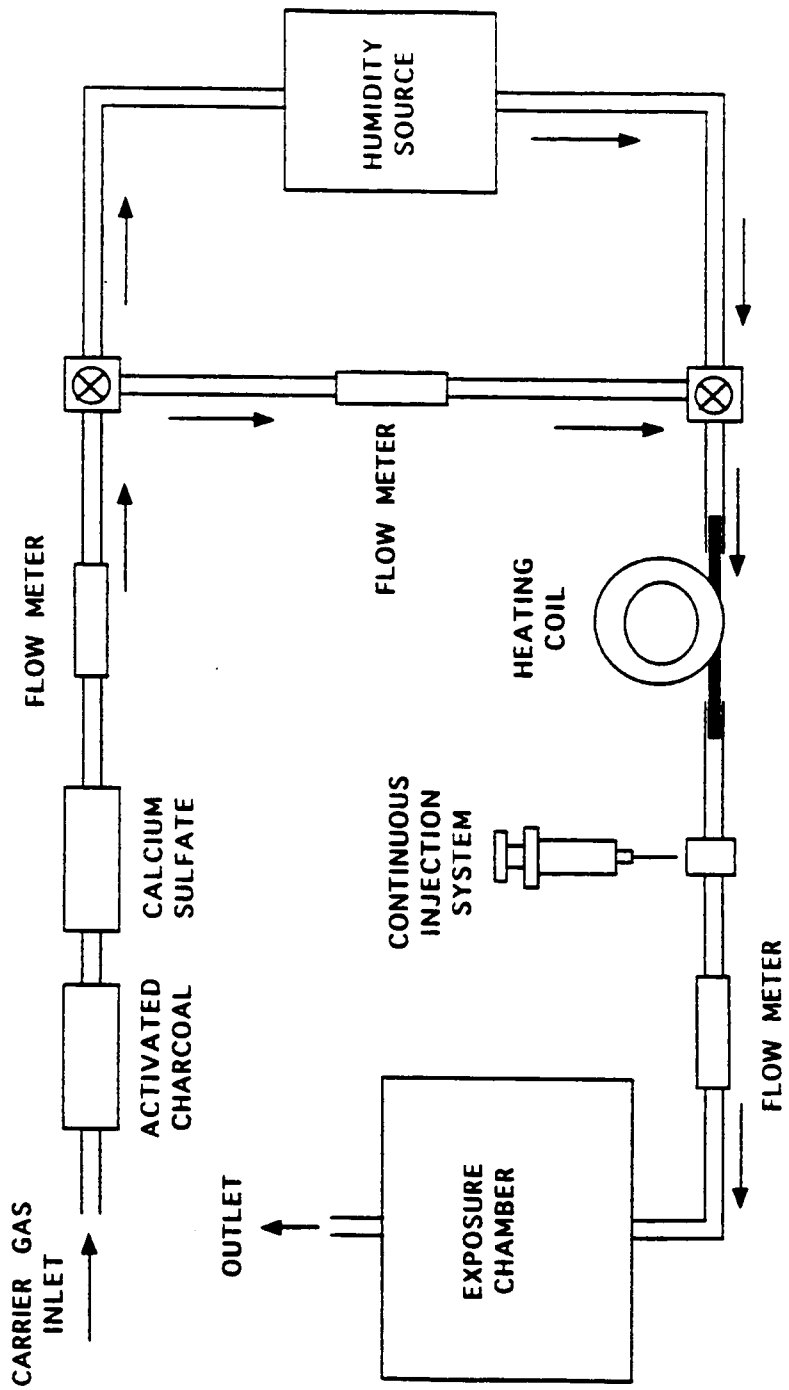
Figure 6.2. Vapor exposure system.

231

exposure chamber. Air temperature was controlled with a heating coil placed in the air flow path just prior to the sample injection point. A simple equation was used to determine the air vapor concentration of the analyte within the chamber. The following equation was used to estimate the vapor concentration of the analyte within the air vapor exposure chamber, C_{AVC} (ppm):

$$C_{AVC} = \frac{C_{inj} \bullet R_{inj} \bullet V}{F_{AVC} \bullet mw} \qquad (6.4)$$

where C_{inj} is the analyte concentration for the injected test solution (mg/ml), R_{inj} is the analyte solution injection rate (ml/hr), V is the molar volume assumed from the ideal gas law (24.45 L at room temperature), F_{AVC} is the air flow rate through the air vapor chamber (L/hr), and mw is the molecular weight of the analyte (g). A typical rate for F_{AVC} is 900 L/hr.

SERS Substrates

Alumina-based substrates were prepared as described in Chapter 2 for maximum performance. For the polymer-coated substrate studies, a 10-nm silver layer was deposited directly on a set of clean glass slides, via thermal evaporation at approximately 2 x 10^{-6} torr, as described in Chapter 3. Immediately following the silver deposition step, half of the silver islands substrates were individually, horizontally dipped into a fresh solution of 5% PVPL (Aldrich), prepared in reagent grade methanol (J. T. Baker). The polymer-coated substrates were then placed on a level surface and allowed to cure for at least 30 min at room temperature. Half of the silver islands substrates were left uncoated for comparison studies. A more detailed

discussion of the polymer-coating technique, including optimization studies, is found in Chapter 4.

Chemicals

Test compounds included benzoic acid (reagent grade, Mallinckrodt), TPA (95%, Pfaltz and Bauer), 2-aminopyrimidine (97%, Aldrich), and 2,4-dinitrophenol (90-95%, Sigma). All chemicals were used as received. Sample solutions were all prepared in reagent-grade ethanol (Warner-Graham Co.).

RESULTS AND DISCUSSION

Comparison of Spectral Response of Vapor and Spot Samples

Measurements were conducted to evaluate the sensitivity of the SERS vapor dosimeter to benzoic acid (BA) vapor. An alumina-based substrate was installed in the passive dosimeter and placed in the vapor chamber for a 5-h exposure to 1.0 ppm BA vapor. The resulting SERS spectrum is illustrated in <u>Figure 6.3b</u>. For a comparison to a conventional spot sample, a SERS spectrum of 10 ng BA is likewise illustrated in <u>Figure 6.3a</u>. The spot sample was applied from an ethanol solution and allowed to dry prior to measurement.

As is demonstrated by the figure, the two spectra are virtually identical with respect to relative peak intensities and peak positions. The SERS spectrum of the BA vapor manifests the sharp characteristic peaks at 848, 1014 and 1610 cm^{-1}, which are
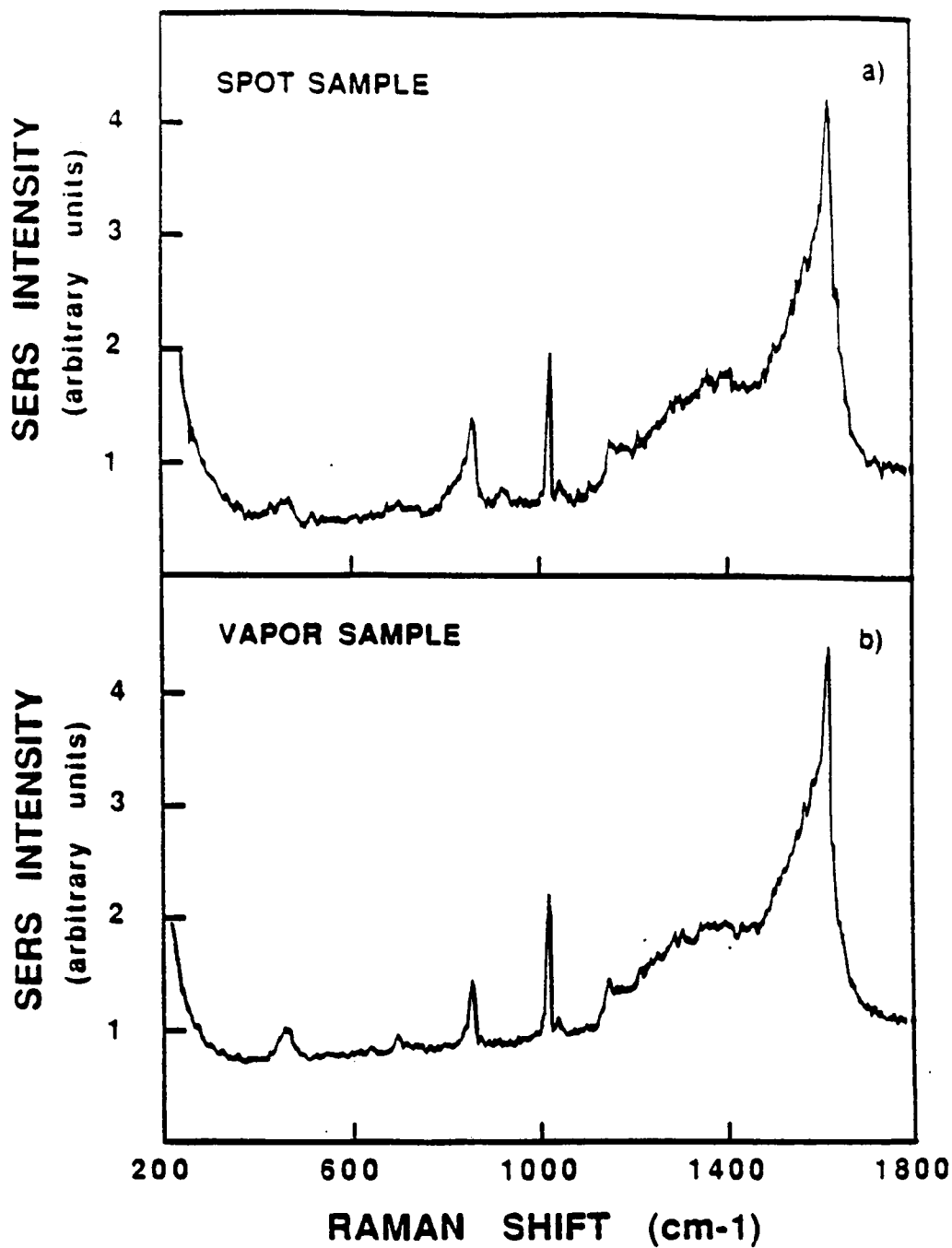
Figure 6.3. SERS spectra of benzoic acid on alumina-based substrates as a) 15 ng spot sample, and b) vapor sample resulting from a 5-hour exposure of the substrate to 1.0 ppm vapor. Laser: Ar, 514.5, a) 40 mW, b) 50 mW.

Source: T. Vo-Dinh, and D. L. Stokes, *Appl. Spectrosc.* **47**, 1728 (1993).

attributable to the skeletal stretch, ring breathing, and ring stretching vibrations, respectively. Also common to both spectra is a broad background in the 1200-1600-cm^{-1} region, probably due to Raman scattering from a graphitic carbon monolayer created by the laser decomposition of the benzoic acid (Tsang *et al.*, 1980; Otto, 1978). This effect has been observed in previous studies using 514.5-nm excitation radiation (Chapter 2).

The S/N exhibited by the vapor dosimeter compares favorably to the spot sample, as well. For example, the collected mass of BA on the 2×10^{-5} m^2 sampling area of the dosimeter, from a 1 ppm atmosphere and after a 5 h exposure period, is estimated to be approximately 1 ng. By comparison, the spot sample involves a 15 ng distribution over an area of approximately 8×10^{-5} m^2, or approximately 3.8 ng for a similar 2×10^{-5} m^2 area. Nevertheless, the S/N for the vapor sample spectrum is slightly better than that observed for the spot sample. This observation may in part be due to the increased laser excitation intensity used for acquisition of the vapor sample spectrum.

Analytical Figures of Merit

Calibration measurements were performed for the observed BA SERS signal with respect to exposure time. The vapor exposure chamber was prepared with a 100 ppb BA concentration at room temperature. A set of six SERS dosimeters equipped with the alumina-based substrates was placed in the chamber at the start of the experiment. Substrates were periodically removed from the chamber and immediately measured, one-by-one, until all dosimeters were removed. Figure 6.4 demonstrates the result of an 8-h exposure study. Each point represents the average SERS intensity observed at the characteristic 1010-cm^{-1} benzoic acid peak. Four measurements were acquired for
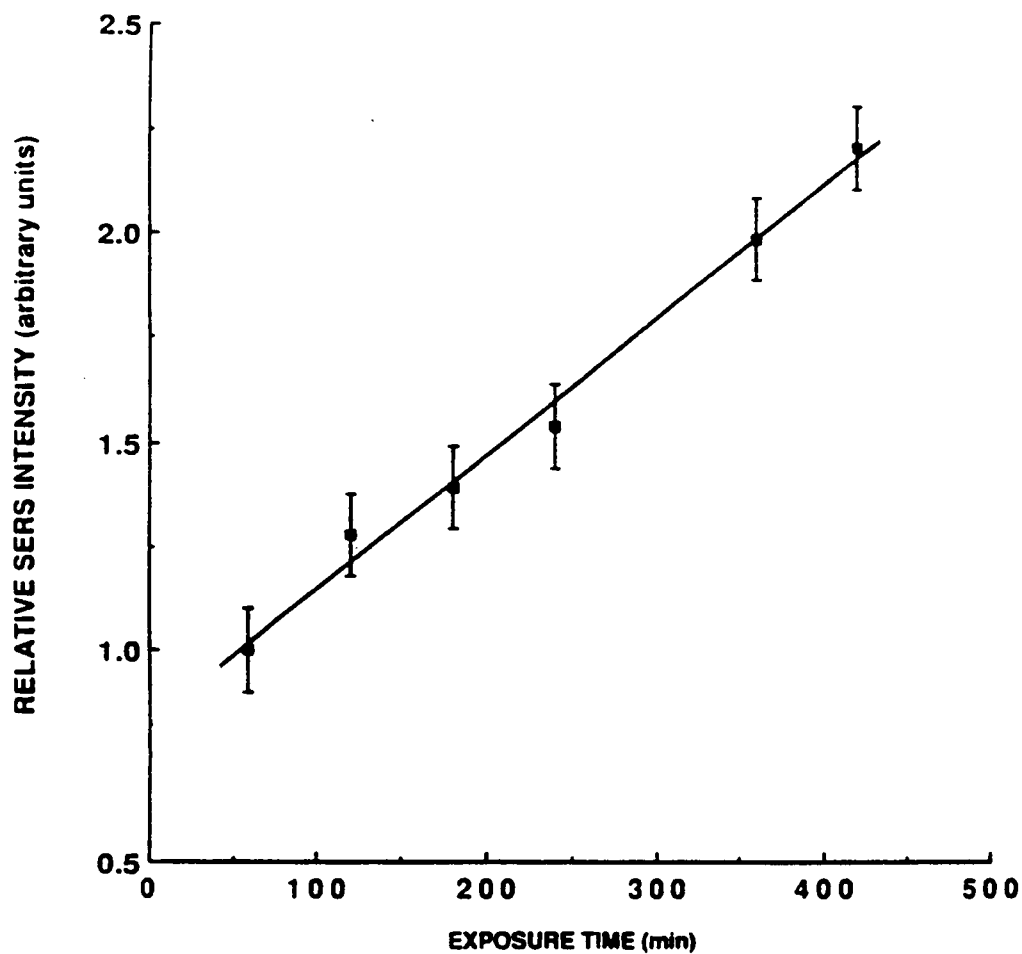
Figure 6.4. SERS intensity plot for the detection of 100 ppb benzoic acid vapor as a function of exposure period. Benzoic acid signal at 1010 cm^{-1}. Laser: Ar, 514.5 , 50 mW.

Source: T. Vo-Dinh, and D. L. Stokes, *Appl. Spectrosc.* **47**, 1728 (1993).

each dosimeter. The data appear to be linear over the entire time period with no evidence of SERS substrate saturation. This study demonstrates that a SERS vapor dosimeter may be designed for daily monitoring of occupational exposure to potentially hazardous vapors over 8-h workshifts.

It is also important to note that dosimeter design does offer some flexibility in the observed temporal dynamic range. For example, the diffusion tube can be simply lengthened or shortened to decrease or increase the sample collection rate, respectively. For a case where a compound has a high vapor pressure, thus producing a relatively high ambient vapor concentration, saturation of the dosimeter may occur rapidly, causing a negative deviation from linearity. As the SERS substrate becomes saturated, it can lose its adsorbing ability and thus allow the airborne molecules to amass in the diffusion tube and reach concentration equilibrium with the ambient vapor molecules at the diffusion tube inlet. The higher concentration gradient, the faster the saturation of the SERS substrate surface is attained. Increasing the length of the diffusion tube decreases the concentration gradient driving the diffusion process and thus can extend the temporal dynamic range of the dosimeter. Nevertheless, this corrective measure also increases the response time of the dosimeter, as the response time is directly proportional to L^2.

In addition to the 8-h temporal linear dynamic range, the dosimeter exhibited a high degree of reproducibility. Figure 6.5 illustrates the SERS spectra acquired for four different dosimeters exposed to 100 ppb terephthalaldehyde vapor for 2 h. The observed band at 1610 cm^{-1} is attributed to symmetric CC stretching vibrational modes. The relative standard deviation of the dosimeter responses was typically 15-20%. This result is comparable to the reproducibility of the alumina-based substrate when used for solid or liquid measurements.

237
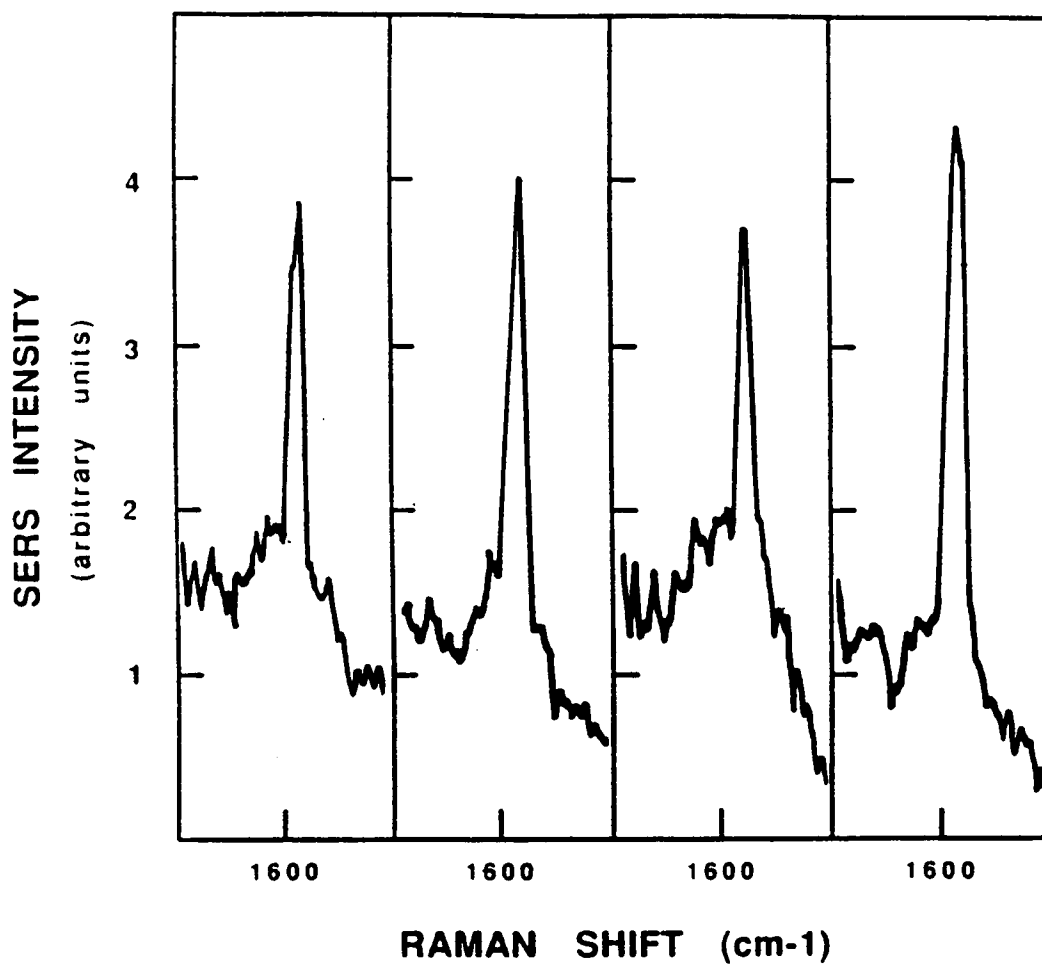
Figure 6.5. SERS spectra of terephthalaldehyde following 2-hour exposure of four different dosimeters to 100 ppb analyte vapor, illustrating reproducibility of the technique. Laser: Kr, 647.1 nm.

Source: T. Vo-Dinh, and D. L. Stokes, *Appl. Spectrosc.* **47**, 1728 (1993).

Evaluation of Polymer-Coated Substrate for Vapor Detection

It has been demonstrated previously that the application of the polymer, PVPL, can extend the shelf life of a SERS substrate by protecting it from air oxidation as well as making the otherwise delicate SERS substrate surface more scratch-resistant in a rugged SERS dosimeter. As a preliminary evaluation of vapor detection feasibility with PVPL-coated SERS substrates, polymer-coated silver island SERS substrates were exposed to various chemical vapors. In this case however, static environments in 20-ml scintillation vials were used for the vapor exposures. 10-20 mg of the solid chemicals (benzoic acid, 2,4-dinitrophenol, and 2-aminopyrimidine) were placed in individual glass vials. A pair of silver island substrates, one with and one without the polymer coating, was placed in each vial. The vials were equipped with spacers which elevated the substrates from the bottom of the vials, thus preventing direct contact with the pure chemicals. The vials were sealed. Substrates were removed for measurement after two days and twenty days of exposure.

Figure 6.6 illustrates SERS spectra acquired from polymer-coated and uncoated substrates exposed to BA vapor for 2 days. The PVPL-coated silver islands yields a well-resolved SERS spectrum for BA, consisting of the characteristic sharp peaks at 848, 1012 and 1610 cm^{-1}. However, the intensities of these bands are approximately 50% of those observed with the untreated bare substrate. As shown by Figure 6.7, the BA spectra acquired with the coated and uncoated substrates after 20 days exposure are of comparable intensity. Permeability of the PVPL film to BA vapor is therefore demonstrated. It is also noteworthy that the broad band observed from 1200 cm^{-1} to 1400 cm^{-1} with the bare substrate is absent in the polymer-coated substrate spectrum
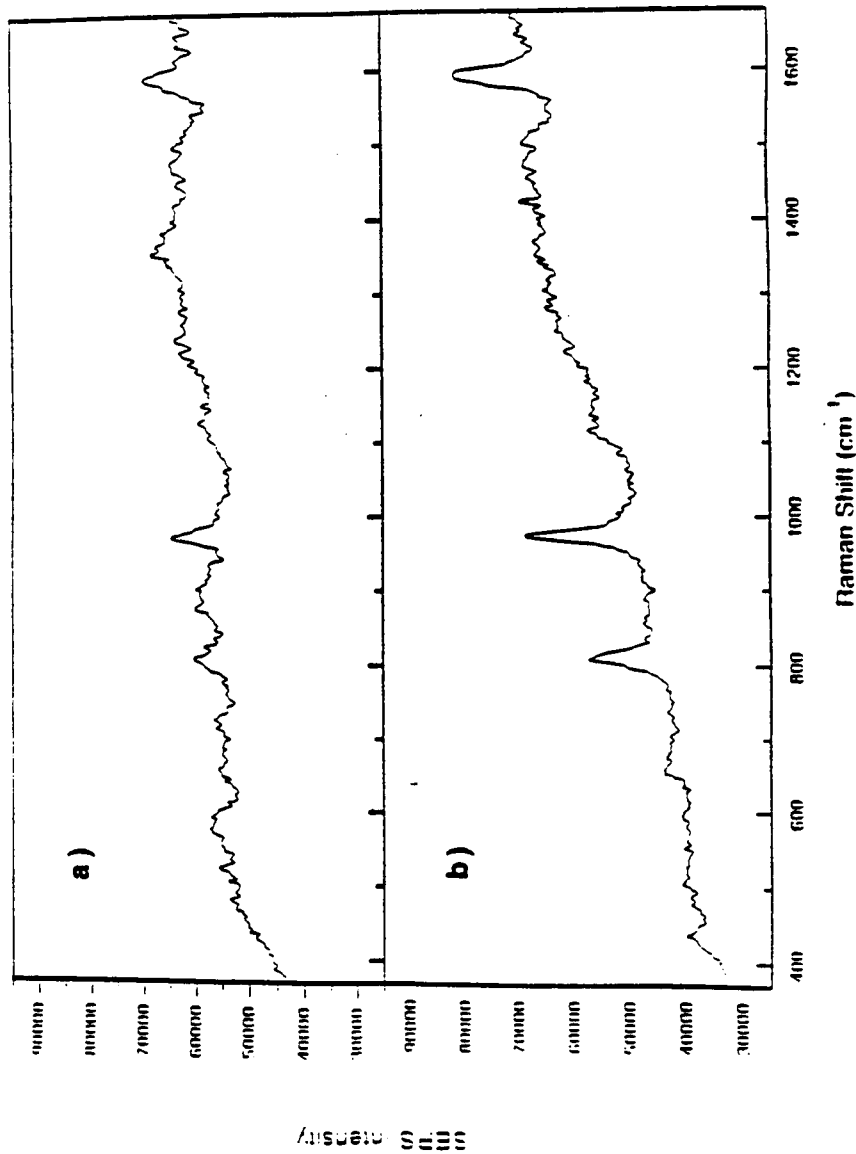
Figure 6.6. SERS spectra of a) PVPL-coated, and b) uncoated silver island-based substrates exposed in static benzoic acid vapor chamber for 2 days. Laser: HeNe, 632.8 nm, 5 mW.

Source: D. L. Stokes, V. A. Narayanan, and T. Vo-Dinh, *Anal. Chim. Acta.* (1999) in press.
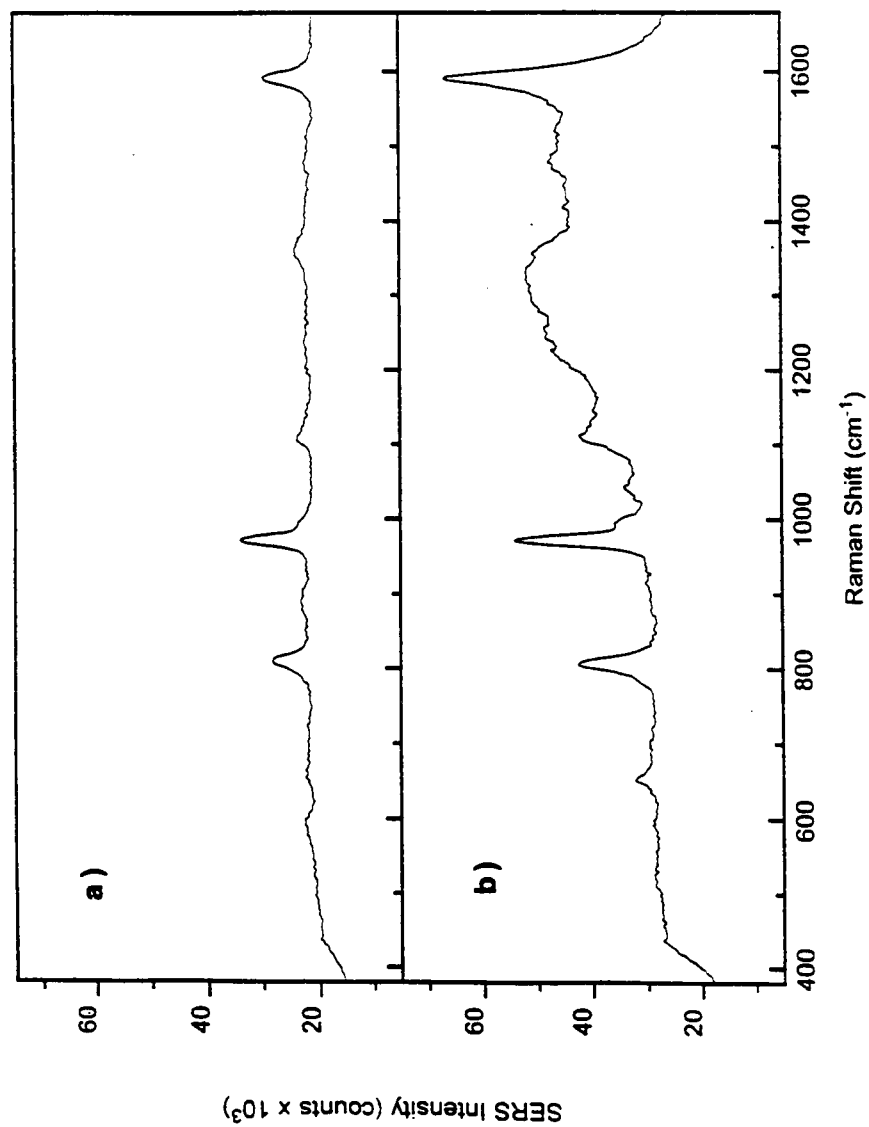
Figure 6.7. SERS spectra of a) PVPL-coated, and b) uncoated silver island-based substrates exposed in static benzoic acid vapor chamber for 20 days. Laser: HeNe, 632.8 nm, 5 mW.

Source: D. L. Stokes, V. A. Narayanan, and T. Vo-Dinh, *Anal. Chim. Acta.* (1999) in press.

of the BA exposures. This observation may be due to discrimination against an impurity imparted by the polymer layer.

Another compound studied was 2-aminopyrimidine (2-AP). Figure 6.8 illustrates that, after just two days of exposure, the intensity of the SERS spectrum acquired with the PVPL-coated substrate exceeds the barely perceptible 2-AP spectrum obtained with the uncoated substrate. The SERS spectrum of 2-AP on the PVPL-coated silver substrate exhibits bands at 622 cm^{-1}, which is a substitution insensitive in plane vibration; and the pyrimidine quadrant stretch vibration at 1590 cm^{-1}. In this case, the polymer layer apparently not only permits diffusion of the 2-AP, but also yields enhanced detection. This observation is probably the result of analyte enrichment at the metal surface enabled by the polymer coating, which could have facilitated the adsorption process or trapped the 2-AP molecules in the vicinity of the metal surface. After 20 days of exposure, the 2-AP spectrum from the polymer-coated substrate still exhibited a 2-fold higher intensity relative to that yielded by the uncoated substrate, as illustrated by Figure 6.9.

Enhanced detection with the PVPL-coated substrate was also observed with the 2,4-dinitrophenol (DNP) vapor study. Figure 6.10 illustrates SERS spectra acquired after 20 days of exposure. Virtually no DNP bands were detected with the uncoated substrate. The polymer-coated substrate, by contrast, yielded a very intense spectrum for the collected DNP vapor. The prominent SERS bands have been measured and are tabulated in Table 6.1. The normal Raman (NR) bands are also tabulated as reported in the literature (Singh *et al.*, 1986). The SERS effect is prominent in vibrations involving CC stretching (1624 cm^{-1}), and CCC bending (594 cm^{-1}), and ring breathing (834 cm^{-1}) modes. The symmetrical NO$_2$ stretching mode is also strongly evident at 1348
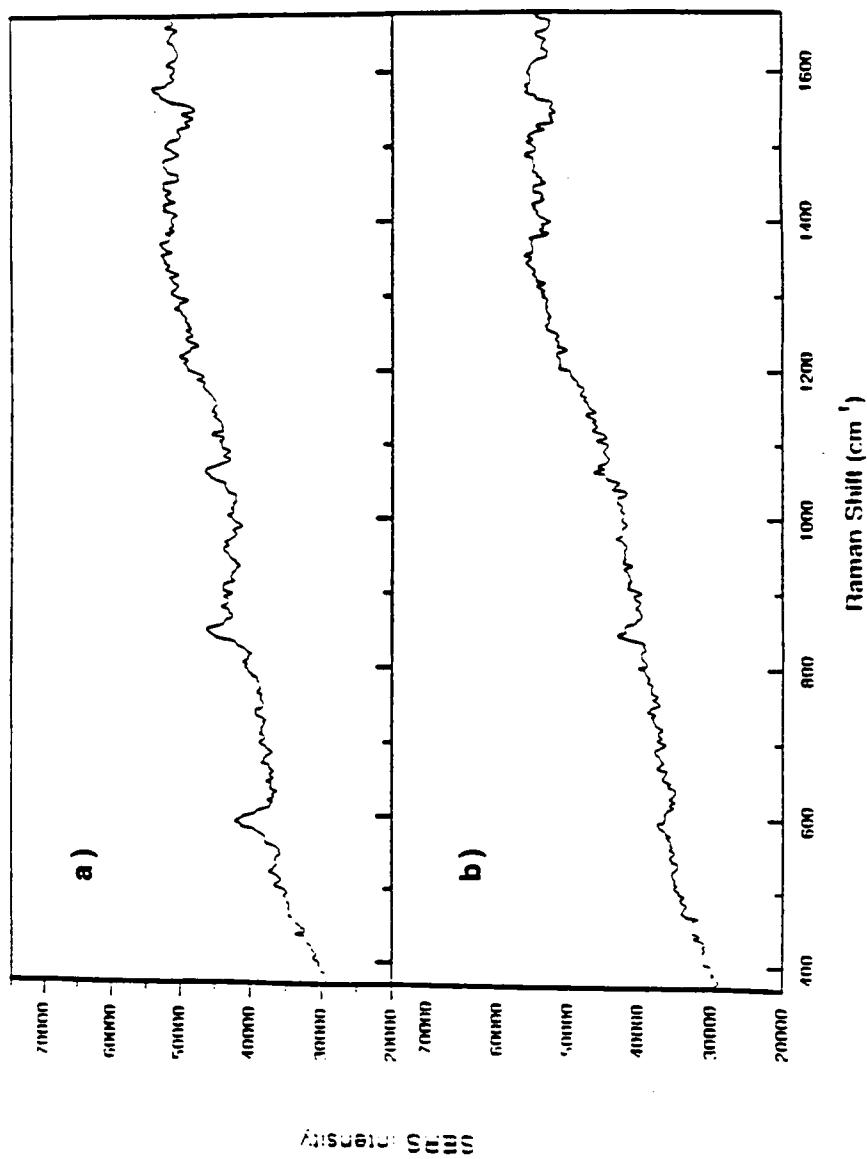
Figure 6.8. SERS spectra of a) PVPL-coated, and b) uncoated silver island-based substrates exposed in static 2-aminopyrimidine vapor chamber for 2 days. Laser: HeNe, 632.8 nm, 5 mW.

Source: D. L. Stokes, V. A. Narayanan, and T. Vo-Dinh, *Anal. Chim. Acta.* (1999) in press.
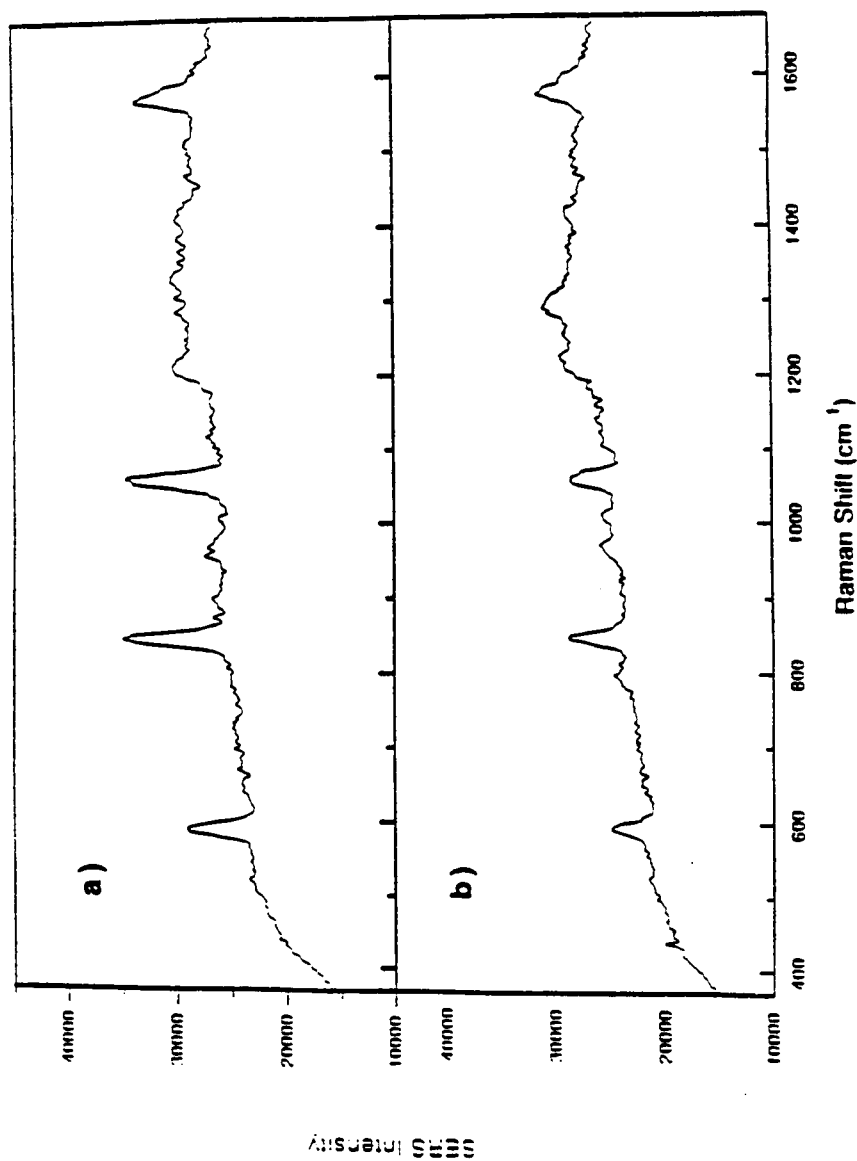
Figure 6.9. SERS spectra of a) PVPL-coated, and b) uncoated silver island-based substrates exposed in static 2-aminopyrimidine vapor chamber for 20 days. Laser: HeNe, 632.8 nm, 5 mW.

Source: D. L. Stokes, V. A. Narayanan, and T. Vo-Dinh, *Anal. Chim. Acta.* (1999) in press.
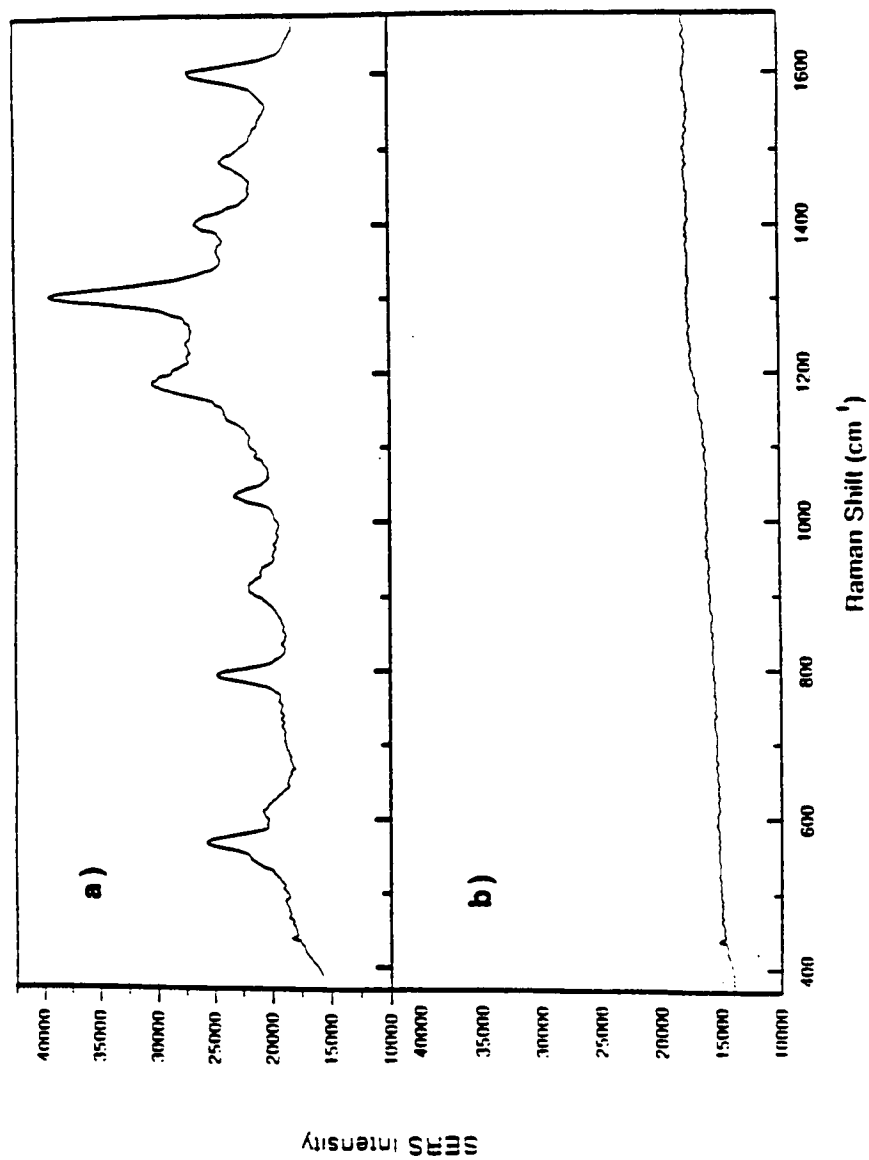
Figure 6.10. SERS spectra of a) PVPL-coated, and b) uncoated silver island-based substrates exposed in static 2,4-dinitrophenol vapor chamber for 20 days. Laser: HeNe, 632.8 nm, 5 mW.

Source: D. L. Stokes, V. A. Narayanan, and T. Vo-Dinh, *Anal. Chim. Acta.* (1999) in press.

Table 6.1. Comparison of SERS (PVPL-coated silver islands) and normal Raman spectra of 2,4-dinitrophenol

SERS (cm^{-1})	Normal Raman (cm^{-1})	INormal Raman -SERSI (cm^{-1})	Vibrational Mode Assignment
1624 (m)	1628 (s)	4	(C-C) stretching
	1590 (m)		(C-C) stretching
	1544 (s)		Asym. NO_2 stretching
1524 (w)	1513 (w)	11	(C-C) stretching
1348 (vs)	1352 (vvs)	4	Sym. NO_2 stretching
	1275 (s)		(C-H) i.p. bending
1250 (w)			
1228 (w)			
	1190 (w)		(C-H) i.p. bending
	1145 (s)		(C-NO_2) stretching
	1122 (w)		(C-NO_2) stretching
1080 (vw)	1080 (w)	0	(C-H) o.p. bending
944 (w)			
	845 (s)		Sym. NO_2 bending
834 (m)	830 (s)	4	Ring breathing
642 (vw)	654 (m)	12	(C-C-C) i.p. ring bending
594 (m)	592 (w)	2	(C-C-C) o.p bending

v = very; s = strong; m = medium; w = weak

Source: Singh, R. B.; Mukul, M.; Sharma, S. K. *Indian J. Phys.*, **62B**, 556 (1988).

cm^{-1} in the SERS spectrum acquired with the PVPL-coated substrate. In this case the large difference between the polymer-coated and uncoated substrates can be attributed to the protection against DNP provided by the polymer coating. The uncoated substrate was apparently destroyed by the DNP vapor over the 20-day exposure. In view of the facts that DNP is a by-product in some explosives and the vapors are hazardous, the SERS detection of this vapor in such an unequivocal way assumes great significance.

In conclusion, an important factor in health effects assessments is the knowledge of exposure to pollutants. The passive vapor dosimeter reported herein marks the first development of a practical device suitable for large-scale monitoring of airborne chemicals. Because of the signal amplifying ability of the collection medium, a solid-based SERS substrate, the dosimeter can be directly measured in post-exposure analysis. The many complicated, expensive, and time-consuming steps associated with conventional vapor monitoring procedures are thus bypassed. The spectral selectivity of Raman may further simplify analyte identification and permit simultaneous multicomponent analysis. Nevertheless, additional selectivity can be imparted by the use of protective, selectively-permeable polymer coatings. For example, a PVPL-coated silver island-based substrate has been used for vapor phase detection over a 20-day period. Variable permeability has been demonstrated for several chemical vapors, including BA, 2-AP, and DNP. These results indicate that the new substrate could be installed into the passive dosimeter for additional chemical selectivity and simplification of the spectral analysis. The coating may help extend the temporal dynamic range of the dosimeter, as well. In addition to protection against air oxidation, the feasibility of protection of the metallic SERS surface from harsh chemical environments (e.g., DNP) has been demonstrated with the PVPL coating.

PART II

SEPARATIONS-BASED FIBEROPTIC SENSING

PREFACE

The second part of this dissertation introduces a different approach to remote fiberoptic sensing of complex samples with selectivity being enabled by remote separations. In part I, the spectral selectivity offered by Raman scattering was emphasized for the analysis of complex samples. In Part II, a sensor is described for which laser-induced fluorescence (LIF) is the mode of detection. While offering exceptional detectability, the broadband nature of this luminescence process offers limited spectral selectivity. To compensate for this inadequacy in the analysis of complex samples, this new sensor is designed to perform separations at the remote end of a fiberoptic via capillary electrophoresis (CE). The high efficiency common to CE permits a compact sensor design. Furthermore, the facile regeneration of the CE column and modification of the separation medium fortifies this sensor with the unique advantage of combined reusability and flexibility. The materialization of this far-reaching concept of a separations-based fiberoptic sensor (SBFOS) was achieved after overcoming several challenges. The following sections describe the various inherent complications, the approaches taken to confront these challenges, and detailed performance evaluations which address issues of reproducibility and detectability. The versatility of the SBFOS is demonstrated with separations of metal ions, neutral organic compounds of environmental significance, and large biomolecules. In addition to remote environmental monitoring in the field, the potential for automation and high sample throughput offered by the SBFOS technology may prove valuable in more controlled environments which are common to process monitoring and bioanalysis.

CHAPTER 7

THE CONCEPT OF SEPARATIONS-BASED FIBEROPTIC SENSING: PRINCIPLES OF CAPILLARY ELECTROPHORESIS, FIBEROPTICS AND LASER-INDUCED FLUORESCENCE

INTRODUCTION

The purpose of this chapter is to introduce and justify the concept of a separations-based fiberoptic sensor (SBFOS) technology for selective, remote, *in situ* analysis based on the strengths of its components and mode of detection. Simply stated, the SBFOS introduced herein combines the exceptional detectability of laser-induced fluorescence (LIF), the potential selectivity enabled by capillary electrophoresis (CE), and the ability for remote optical detection via optical fiber.

The concept of using fiberoptics for remote chemical sensing is rapidly becoming a mature subject. In fact, the implementation of fiberoptics in chemical sensors for remote optical detection has been the subject of intense research and development for decades, as is demonstrated by several excellent reviews (Angel *et al.*, 1989; Norris, 1989; Kersey and Dandridge, 1990; Boisde *et al.*, 1991; Lambeck, 1991; Miller *et al.*, 1991). In spite of these efforts, there has rarely been the development of a sensor which collectively manifests the attributes which would comprise a versatile, long-lived, and economical sensor. Such attributes include adequate detectability, selectivity

250

(ideally tunable selectivity), flexibility, reusability, diminutive size, a minimal analysis time requirement, and automation capability.

Often, certain of these attributes are realized with the sacrifice of others. For example, spectral selectivity has been demonstrated with IR (Saito and Kikiuchi, 1997) and Raman-based (Cooney et al., 1996a,b) remote sensors, but at the expense of competitive detectability. As demonstrated in previous sections, signal enhancement techniques such as SERS have been used in remote sensors to combine spectral selectivity with commendable detectability (Vo-Dinh, 1995b). Unfortunately, SERS-based sensors are rarely regeneratable. Alternatively, luminescence-based sensors have been among the most competitive in terms of detectability, but spectral selectivity has been limited. Nevertheless, means for achieving additional dimensions of chemical or physical selectivity, such as immobilized immunological reagents (Sepaniak et al., 1988; Vo-Dinh et al., 1995), polymer films (De Olivera and Narayanaswamy, 1992) or molecularly imprinted matrices (Lerchi et al., 1992; Kriz et al., 1995) have been combined with highly sensitive (yet otherwise nonselective) modes of detection. However, such technologies tend to be inflexible and not easily regenerated for multiple measurements. Considering these shortcomings, the SBFOS technology described in the following sections provides a potentially valuable contribution to the large and maturing field of fiberoptic chemical sensor development. It uniquely provides the combined advantages of selectivity, competitive detectability, flexibility, and reusability- all in a compact design which may be amenable to automation.

The potential combined strengths of selectivity, flexibility and reusability enabled with the SBFOS technology parallel the attributes of modern CE, which have been extensively exploited since its introduction in 1981 (Jorgenson and Lukacs, 1981). The potential

251

selectivity that CE can provide a remote sensor arises, in part, from the extremely high efficiency. Due to the "plug-like" profile of the electroosmotic flow (EOF), the primary driving force for flow in CE (see below), efficiencies of 10^3-10^4 plates/cm are routinely observed. Such efficiency permits separations with a relatively small-scale system. CE also provides the potential for a highly versatile sensor. Based on the differential migration of charged molecules, it is readily applicable to the separations of charged solutes ranging from small inorganic ions to large proteins and nucleotides. CE has even been applied to the more challenging separation of neutral compounds with the aid of micelles and cyclodextrins (Terabe *et al.*, 1984; Sepaniak *et al.*, 1992a,b; Holland and Sepaniak, 1993; Otsuka and Terabe, 1996; Matsubara and Terabe, 1996; Nishi and Terabe, 1996). Furthermore, a multitude of running buffer additives have been investigated to impart various retention properties, including organic modifiers, metal ions, linear hydrophobic polymers, complexing ligands, crown ethers, and various zwitterionic substances (Grossman and Colburn, 1992).

As a result, by incorporating CE in the SBFOS technology, a single sensor may be used with a wide range of selectivities by simply flushing the capillary with appropriately modified running buffer systems. Indeed, a single SBFOS could be applied to a host of applications. In addition, the capillary is highly regeneratable with minimum system treatment times required between trials. Finally, analyses require relatively short separation times and low nl sample volumes. In summary, the many advantages of CE make it especially useful in the development of a selective sensor for *in situ* analysis. In fact, it has previously been coupled with electrochemical detection to probe low-volume, biological samples (Ewing *et al.*, 1989; Chien *et al.*, 1990). Conversely, the sensor described herein is based on LIF detection for exceptional detectability and ease of

discrimination against background signals which are generally exacerbated by remote detection, regardless of the detection mode.

With the intent of further demonstrating the justification of the SBFOS approach to remote sensing with CE and LIF, the following sections describe a modular approach to the description of the proposed sensor. Detailed descriptions are provided for the major components and their individual merits. A brief review of the history, theory, modes of detection, and far reaching applications of CE is included. The basic principles of fiberoptics and LIF are also discussed. The actual inclusion of these components in the fabrication of a true sensor and the inherent challenges associated with their union will be described in great detail in later chapters.

CAPILLARY ELECTROPHORESIS

The separation of charged molecules in solution with electrophoresis arises primarily from the differential migration rates of molecules of different charges, sizes and shapes when subjected to an electric field. Under the influence of the electric field, a charged molecule moves towards the oppositely charged electrode at a constant rate (at steady-state conditions) for which the electromotive force is balanced by frictional drag. Under this steady-state condition, the migration velocity (v_e) of the molecule is linearly proportional to the applied electric field strength (E) (V/cm):

$$v_e = \mu_e E \qquad\qquad (7.1)$$

253

where μ_e is a proportionality constant termed the electrophoritic mobility ($cm^2 \cdot V^{-1} \cdot s^{-1}$) and

$$E = \frac{V}{L_T} \qquad (7.2)$$

where V is the total applied voltage, and L_T is the total length of the separation medium (cm). μ_e can be expressed in terms of more fundamental solute parameters as follows:

$$\mu_e = \frac{q}{6\pi\eta r} \qquad (7.3)$$

where q is the ionic charge of the solute, η is the solvent viscosity, and r is the ionic radius of the solute.

This separation mechanism was first exploited in the 1930's (Tiselius, 1937), and has since been the premier method for the separation of large biomolecules (Bier, 1959; Bier, 1967; Deyl, 1979; Allen et al., 1984). However, early methods of electrophoresis were performed in relatively large vessels and were complicated by the Joule heating which was generated at the typically large applied fields (100-900 V/cm), especially for free solutions. Because of the poor heat dissipation from the large separation vessels, this current-induced heating formed temperature gradients which in turn produced convection in the separation media. In order to overcome this disruptive effect, stabilizers were added to the separation media in order to both improve heat dissipation and physically retard any residual convection. Such stabilizers, which have included paper, starch gel, agarose, cellulose acetate, and polyacrylamide gel, had made

large-scale electrophoresis a labor-intensive technique. This unattractive feature limited the early use of electrophoresis as a practical analytical tool.

The role of electrophoresis in analytical chemistry took a dramatic turn in the 1970's, when electrophoretic separations in 200-500-µm i.d. tubes were pioneered by Virtanen (Virtanen, 1974) as well as Mikkers and coworkers (Mikkers *et al.*, 1979). Nevertheless, the widespread popularity of CE can be largely attributed to the later contributions of Jorgenson and Lukacs, whose work involved the use of even smaller bore capillaries and on-column fluorescence detection (Jorgenson and Lukacs, 1981, 1983; Jorgenson, 1986). The enhanced interest in this small-scale electrophoresis technique is a consequence of the efficient heat dissipation through capillary walls, as enabled by the inherent high interior surface-to-volume ratios of capillaries. Heat-induced convection is virtually eliminated, resulting in efficiencies limited only by diffusion, even for free-solution separation media. Because of the relaxed requirement for stabilizers, the implementation of electrophoresis has been greatly simplified with capillaries.

An additional factor for the efficiency of free-solution separations by CE is the induced EOF when voltage is applied to relatively high pH media (see below). Simply stated, EOF is an electromotive pumping action which originates at the wall of the capillary and results in a "plug-like" flow profile. In contrast to the parabolic laminar profile common to pressure driven modes of mobility, the "plug-like" profile of EOF causes minimal band dispersion. An additional factor for solute mobility is produced with minimal sacrifice of the separation efficiency. As with electromigration, EOF is proportional to the applied voltage. When present in conjunction with migration, EOF can reduce the applied voltage requirement and/or separation time, thus minimizing the

corresponding joule heating and/or axial diffusion. The combination of these factors has led to the observance of plate heights (a measure of separation efficiency) approaching theoretical limits.

CE Theory

EOF. As was previously discussed, the total velocity of a solute in free-solution CE can be a consequence of both the electrophoretic migration rate of the solute and the magnitude of EOF in the separation medium. While the following discussion takes both factors into consideration, it is prudent to mention that there are certain applications for which EOF is purposely eliminated. Nevertheless, the following principles can be applied to such applications with minimal, simple modifications. Otherwise, the major propulsion force in the flow of free-solution CE is EOF (Rice and Whitehead, 1965) which when properly adjusted causes all solutes, regardless of charge, to travel in the same direction.

The source of EOF is the net negative charge formed on the interior surface of silica capillaries in the presence of water or alkaline buffer systems, and can be accounted for using the Gouy-Chapman-Stern model of the electrical double layer formed at a charged interface (Gouy, 1910a; Gouy, 1910b; Chapman, 1913; Stern, 1924; Myseis, 1976). In the presence of aqueous buffer solutions, a fraction of the surface silanol groups of the capillary wall become ionized resulting in the excess negative charge at the wall surface. This net negative charge is balanced by positive ions in the buffer solution which are drawn to the wall/solution interface. These cations become arranged in two regions: 1) a compact region of ions next to the capillary wall, and 2) a diffuse region of ions extended into the bulk solution. The cations of the compact region are generally immobilized due

256

to strong electrostatic forces exerted by the negative capillary wall. Nevertheless, thermal motion permits some of these ions to diffuse further out into the bulk solution, forming the diffuse layer.

The separation of charges results in the development of electric potential which propagates from the wall through the diffuse region of the double layer. Figure 7.1 illustrates the potential as a function of the distance from the capillary wall (Heftmann, 1976; Myseis, 1976). The maximum potential, ψ_0, is observed at the surface/solution interface. This potential decreases linearly across the compact region until reaching the interface with the diffuse region, after which point the potential (ψ_d) decays exponentially across the diffuse region. The distance from the compact/diffuse region interface to the point at which the potential decays to 0.37 ψ_d corresponds to the double layer thickness, δ. At some point in the diffuse region, the hydronium counterions are free to move towards the cathode when subjected to an electric field. This point is illustrated as the "plane of shear" in Figure 7.1, and the corresponding potential at this point is the zeta potential $\left(\zeta\right)$:

$$\zeta = \frac{4\pi\eta\mu_{eo}}{\varepsilon} \qquad (7.4)$$

where ε and η are the dielectric constant and viscosity of the buffer solution, respectively, while μ_e is the electroosmotic mobility. The Helmholtz-von Smoluchowski equation (Equation 7.5) illustrates a direct proportionality between ζ and the linear velocity of EOF (v_{eo})(Heftmann, 1976; Pretorius et al., 1974; Jorgenson and Lukacs, 1981; Myseis, 1976):
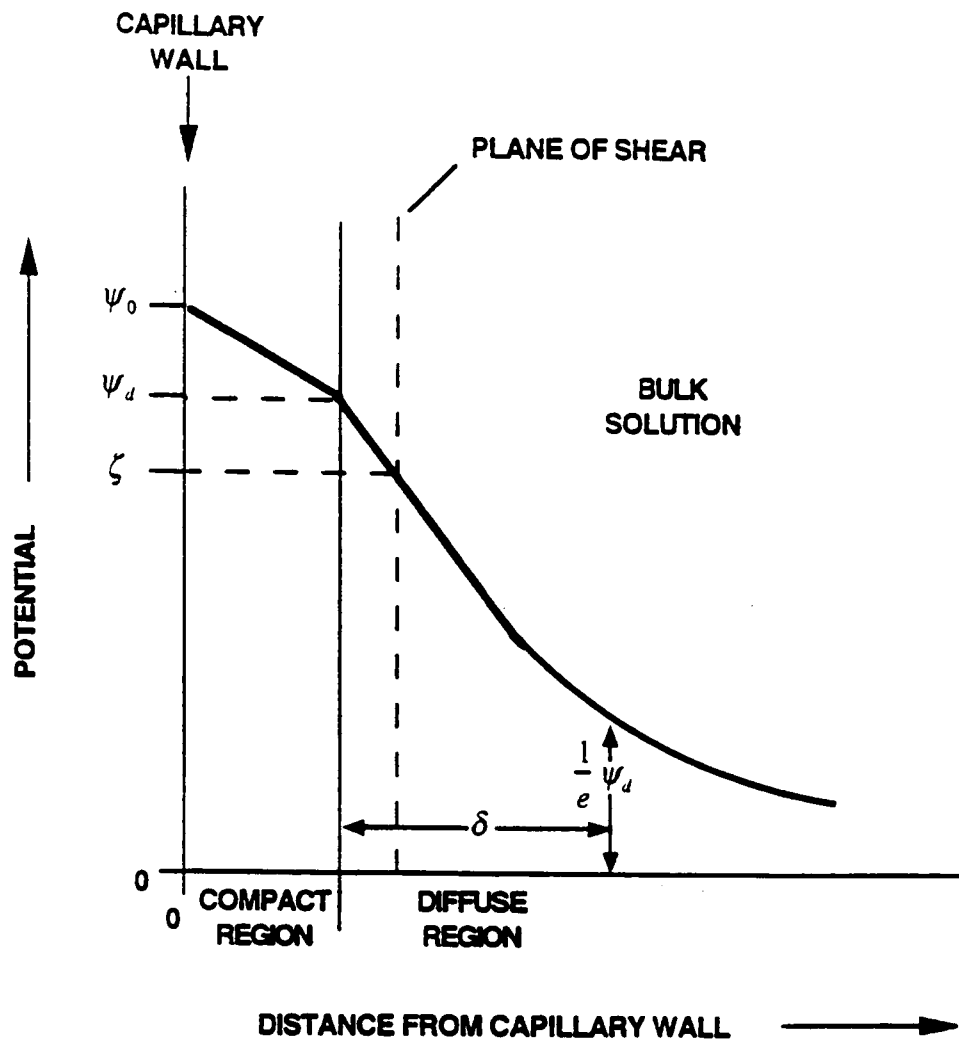
Figure 7.1. Conceptual illustration of the electric potential in the double layer as a function of the distance from the capillary wall.

$$v_{eo} = \left(\frac{\varepsilon}{4\pi\eta} \right) E\zeta \qquad\qquad (7.5)$$

From the above expressions, it is clear that EOF rate is readily adjustable not only through variation of the applied field strength, E, but also through adjustment of the ionic strength and viscosity of the buffer medium.

A simple explanation for the "plug-like" flow profile observed with EOF would be that counter cations at and beyond the shear plane are solvated and thus drag the solvent with them, generating a flow that essentially originates at the wall of the capillary. In the absence of opposing forces towards the middle of the capillary, the resulting flow profile is flat. A typical representation of the EOF profile is illustrated in Figure 7.2. A more accurate description for the EOF profile takes into account greater detail regarding the effects of the double layer. For example, two factors which influence the profile include 1) the resistance to flow experienced by counterions, and 2) the concentration of counterions, both as a function of the distance from the plane of shear. The resistance to flow results from the electrostatic attraction between the counterions and the capillary wall, and varies inversely with the square of the distance between the two. As a result, a trend of increasing flow magnitude is observed as a function of the distance from the plane of shear towards the center of the capillary bore. However, the trend is short-lived because the concentration of electroosmotic counterions decreases exponentially over the diffuse region of the double layer. For example, the probability, P, of finding a counterion at a given distance from the inner boundary of the diffuse region is described as a Boltzmann distribution (Myseis, 1976):
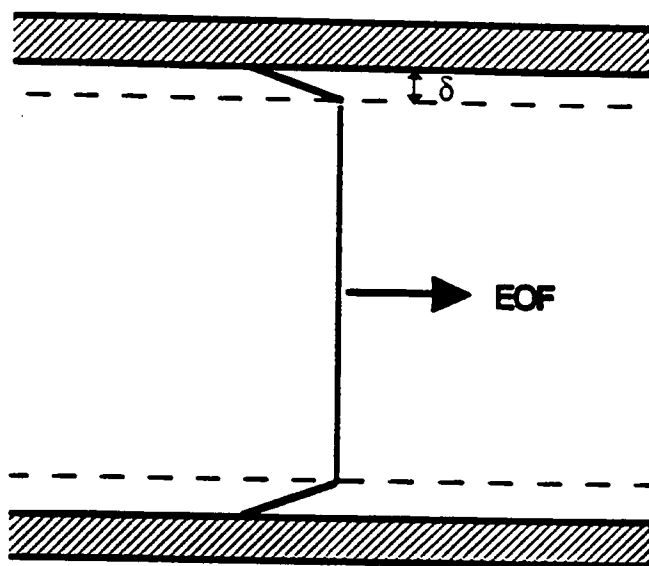
Figure 7.2. A commonly used depiction of the electroosmostic flow profile.

$$P = P_0 e^{\frac{-C(\psi - \psi_d)}{kT}}$$
(7.6)

where P_0 is the probability of finding a counterion at the inner boundary of the diffuse region, C is the electronic charge of the counterion, ψ is the potential at the given distance from the inner boundary, K is the Boltzmann constant, and T is the temperature (K). Because EOF requires electroosmotically-active counterions, their concentration gradient is the dominant factor for the observed flow profile. Once the concentration becomes insignificant, the resulting profile flattens.

The question remains as to how far from the inner boundary of the diffuse layer that such concentration remains significant. It is noteworthy that, because the highly dense distribution of counterions near the inner boundary of the diffuse layer can shield the more distant counterions from the attractive force of the capillary wall, a significant concentration of counterions may extend to farther distances than might be inferred from Equation 7.6. For example, Rice and Whitehead have determined that electroosmotic flow will take on the parabolic laminar profile which is characteristic of pressure-driven flow when generated in capillaries of bore radii less than 7δ (Rice and Whitehead, 1965). A more accurate depiction of the EOF profile is therefore represented by Figure 7.3. For this reason, δ could be a significant factor in the observed efficiency. δ is readily adjusted by varying the ionic strength of the buffer solution. For example, the typical range of δ varies from 3 to 300 nm for a binary electrolyte concentration range of 10 to 0.001 mM. Therefore, for typical capillaries used in CE (i.d.'s ranging from 25-150 µm), δ may cause minimal band dispersion at normal operating conditions.
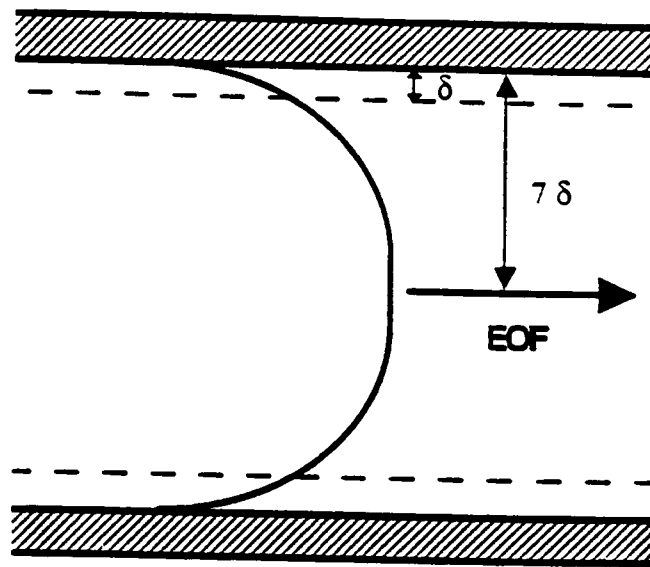
Figure 7.3. A more realistic depiction of the electroosmotic flow profile taking into account more details regarding the electrical double layer.

Efficiency and resolution. Ultimately, the selectivity of the SBFOS will depend on the ability of the sensor to resolve components of interest from a complex mixture in a given task. Resolution is a general chromatographic term which describes the amount of overlap between adjacent eluting bands and depends on not only the degree of separation between the bands (a thermodynamic factor), but also the width of the bands (a kinetic factor). For resolution values > 1, baseline resolution of the bands is observed.

The efficiency (N) of a separation is the kinetic factor for resolution and is reflected by the widths of the eluting bands. In free-solution CE at ideal conditions, axial diffusion is the major contribution to band broadening. As discussed above, the flow profile of EOF contributes minimally to band broadening. Furthermore, the lack of a stationary phase eliminates the associated resistance-to-mass-transfer component to band broadening which is common to most other chromatographic methods of separation. It is noteworthy, however, that some hybrid variations of CE do involve mass transfer during separation, which can lead to band broadening.

For symmetric bands, Gaussian statistics can be used to describe efficiency in terms of variance (σ^2) and standard deviation (σ) of the elution time or volume. In terms of retention time,

$$N = \frac{t_r^2}{\sigma_t^2} \qquad\qquad (7.7)$$

where N is the plate number, t_r is the peak retention time, and σ_t^2 is the variance of the band profile in time units. For Gaussian peaks, the baseline width corresponds to

approximately 4σ. The efficiency can thus be expressed in terms in the experimentally observed bandwidth:

$$N = 16\frac{t_r^2}{W_b^2} \qquad (7.8)$$

where W_b^2 is the baseline width of the eluting band.

Because axial diffusion is the theoretically dominant contribution to band broadening in CE, Einstein's Law of Diffusion can be used to express the efficiency in terms of the diffusion constant for a solute in the mobile phase (D_M).

$$\sigma_L^2 = 2D_M t \qquad (7.9)$$

where σ_L^2 is the variance in the distance traveled by the solute in a given time period, t. Another general expression for the efficiency is as follows:

$$N = \frac{L}{H} \qquad (7.10)$$

where L is the length of the separation medium, and H is the height equivalent of a theoretical plate. H is also related to the peak variance (in terms of solute travel distance at the peak retention time) as follows:

$$H = \frac{\sigma_L^2}{L} \qquad (7.11)$$

Substitution of Equation 7.11 into Equation 7.10 yields Equation 7.12:

$$N = \frac{L^2}{\sigma^2} \qquad (7.12)$$

Using Einstein's Law, the efficiency can now be expressed in terms of the diffusion coefficient of for the solute in the mobile phase (D_M) :

$$N = \frac{L^2}{2D_M t} \qquad (7.13)$$

where t is peak elution time (s). Recalling that the solute velocity is the sum of EOF and solute migration, the following expression is derived:

$$v = \frac{(\mu_e + \mu_{eo})V}{L} \qquad (7.14)$$

After substitution of the velocity expression $(v = L/t)$, rearrangement of Equation 7.14 yields the following expression:

$$L^2 = (\mu_e + \mu_{eo})Vt \qquad (7.15)$$

where μ_e and μ_{eo} are the solute and EOF mobilities, respectively. Finally, after substituting Equation 7.15 in Equation 7.13, the efficiency can be expressed in terms of more fundamental theoretical parameters:

$$N = \frac{(\mu_e + \mu_{eo})V}{2D} \qquad (7.16)$$

The efficiency can then be combined with the band separation parameters to determine the resolution:

$$Rs = \frac{\sqrt{N}}{4}\left(\frac{\Delta t_r}{\bar{t}_r}\right)$$
(7.17)

or

$$Rs = \frac{\sqrt{N}}{4}\left(\frac{\Delta v_r}{\bar{v}_r}\right)$$
(7.17)

where Δt_r and Δv_r are the differences in the solute zone retention times and velocities, respectively, for two adjacent bands; while $\bar{t}_r$ and $\bar{v}_r$ correspond to the average of the adjacent band retention times and velocities. Substitution of Equations 7.14 and 7.16 into Equation 7.18 yields the corresponding expression based on the more fundamental theoretical terms:

$$Rs = \frac{\left(\mu_{e,1}-\mu_{e,2}\right)\sqrt{\dfrac{V}{D_M\left(\bar{\mu}_e+\mu_{eo}\right)}}}{4\sqrt{2}}$$
(7.19)

where $\mu_{e,1}$ and $\mu_{e,2}$ are the electrophoretic mobilities of the solutes and $\bar{\mu}_e$ is the average electrophoretic mobility for the two solutes.

It is interesting to note that the resolution can be enhanced in CE by increasing the column length, while maintaining a constant field strength. Nevertheless, the extremely high efficiency exhibited by CE may produce a resolution rivaling those of other

chromatographic separation techniques over a comparatively small length of separation medium. Furthermore, as inferred from Equation 7.19, the resolution produced by short columns can be further enhanced by simply adjusting $\bar{\mu}_e$ or $\bar{v}_r$ to oppose, with nearly matching magnitude, μ_{eo} or v_{eo}, respectively. This enhancement will occur at the expense of separation time. In summary, the high separation power of CE may permit the development of an SBFOS with a compact separation medium. Furthermore, the "internal" pumping mechanism of EOF and/or solute electromigration can easily be remotely generated and regulated through wire leads which add minimal bulkiness to the sensor. These factors were crucial in the selection of CE as the basis for this SBFOS technology.

General Modes of Electrophoresis

Another advantage of CE is the ease in applying various modes of separation. The most common modes of free-solution CE include capillary zone electrophoresis (CZE) and frontal-mode electrophoresis. Other hybrid modes involving size-selective media and complexation with organic additives will be discussed in detail in later chapters.

CZE. The previous theoretical discussion was based on CZE. In this mode of operation, a small plug of sample (low nl volume) is injected into the column where it is surrounded by the buffer medium. Under the force of the applied electric field, each component of the sample migrates at a characteristic velocity which is dependent on its size and charge (see Equation 7.3). Under proper conditions, the components separate into individual pure zones which are detected as peaks as they elute past the point of detection. Ideally, the lengths of the individual sample zones are minimally broadened relative to the original injected mixture plug. In order to improve detectability, solute stacking can be

267

accomplished when the sample medium is of lower conductivity than the running buffer and is thus controlled through adjustment of the electrolyte concentration of either the sample or the running buffer. Sample stacking has recently been applied to samples ranging from small anions (Albert, 1997a, b) and cations (Zhang and Thormann, 1996) to DNA molecules (Figeys *et al.*, 1996) and peptides (Shihabi, 1996). Unfortunately, CZE would complicate the design of the SBFOS in remote analysis because it would require an extravagant gated injection scheme. Nevertheless, an SBFOS design has been described which involves electrokinetic switching between an internal buffer reservoir and the sample inlet channel (Dickens and Sepaniak, 1999).

Frontal-mode CE. The frontal mode of operation is more amenable to the SBFOS technology. During the separation, the sample is continuously fed into the column. As with CZE, the sample components migrate at independent velocities. However, since the sample is continuously fed onto the column, complete separation of individual solute bands is never attained. Coelution of increasing numbers of solutes as the separation proceeds results in an electropherogram resembling a staircase function. Only the fastest migrating component of a sample mixture can be isolated in this mode of CE. Nevertheless, each bandfront of the staircase corresponds to the retention time of an individual sample component. Therefore, the frontal mode of CE can be used to identify sample components based on known retention characteristics. Since sample identification, rather than purification, may be of primary importance in remote sensing, the frontal-mode CE may be adequate for SBFOS applications. Furthermore, frontal-mode CE promotes a simple, compact SBFOS design. For example, in the case of continuous sample injection the sample medium serves as the inlet buffer reservoir, thus precluding the need for a complicated and cumbersome dual buffer reservoir design. However, this is not accomplished without complications, as described later. Several

examples of frontal-mode separations are demonstrated with the SBFOS described herein.

Modes of Detection

Detection is a particularly challenging aspect of CE. Because sample injection volumes are typically 5-50 nl, the band broadening effect of dead volume detectors can be severe, leading to drastically reduced peak heights (hence reduced detectability) and/or loss of band resolution. In order to preserve the unparalleled separation power which makes CE such an attractive method, on-column detection is commonly used. Even so, the low volume of solute bands places a stringent demand on detection sensitivity in the analysis of trace analytes, particularly for optical detection modes where signal is proportional to the optical pathlength through the sample. Spectrophotometric methods of detection that have been successfully applied to on-column detection in CE include UV-visible absorption, fluorescence, thermal lens and Raman scattering (Ewing et al., 1989). Radiometric methods can also be performed on-column.

Electrochemical methods, including conductometric, potentiometric and amperometric detection, are feasible for on-column detection with fiber and other microelectrodes. However, such measurements are complicated by signal interference caused by the high electric fields used to drive the CE process. As a result, various designs for efficient off-column electrochemical detection have been reported (Wallingford and Ewing, 1987; Wallingford and Ewing, 1988). Other successful methods of detection necessitate off-column detection and have required extensive efforts towards designing efficient coupling schemes. For example, mass spectrometric detection has been achieved through various forms of electrospray ionization (Smith et al., 1988; Olivares et al., 1987;

Ramsey and McLuckey, 1995; Wachs *et al.*, 1996; Mazereeuw at al., 1997; Cao and Moini, 1997). Otherwise, a flurry of activity has been devoted to postcolumn derivatization schemes to expand the range of applications of various modes of detection. The SBFOS technology described herein encompasses designs for both on- and off-column detection with LIF. Along with a detailed description of LIF, this section includes brief descriptions of some common methods of detection in CE (including relative merits and drawbacks) in order to support the selection of LIF-based detection for the SBFOS.

Fluorescence. On-column fluorescence is among the most popular modes of detection in CE. Its prevalence is probably due the superior sensitivity, especially for LIF. Detection limits in the 10^{-16} to 10^{-20} mole range have been reported (Jorgenson and Lukacs, 1981; Cheng and Dovichi, 1988; Pentoney *et al.*, 1988; Rose and Jorgenson, 1988). Lasers are very well-suited for fluorescence detection with CE due to the directionality, collimation and high photon flux of a laser beam. For example, the directionality and collimation facilitate focusing a laser beam into a low volume detection zone through the capillary wall. The intense photon flux is an additional advantage since the fluorescence signal is linearly proportional to the incident excitation intensity.

A major drawback of fluorescence detection is its limited applicability. As an illustration, a Jablonski diagram demonstrating the fluorescence process is illustrated in Figure 7.4. An incident photon promotes an electronic transition from the ground state (S_0) to some vibrational energy level of the first excited state energy level (S_1). The energy of the incident photon must match the energy of the electronic transition. Because of the various vibrational energy levels of the excited state, hence the possibility for several electronic transitions of varying energy, the absorption band may be relatively wide. In general, absorption occurs for π-π^* or n-π^* transitions

270
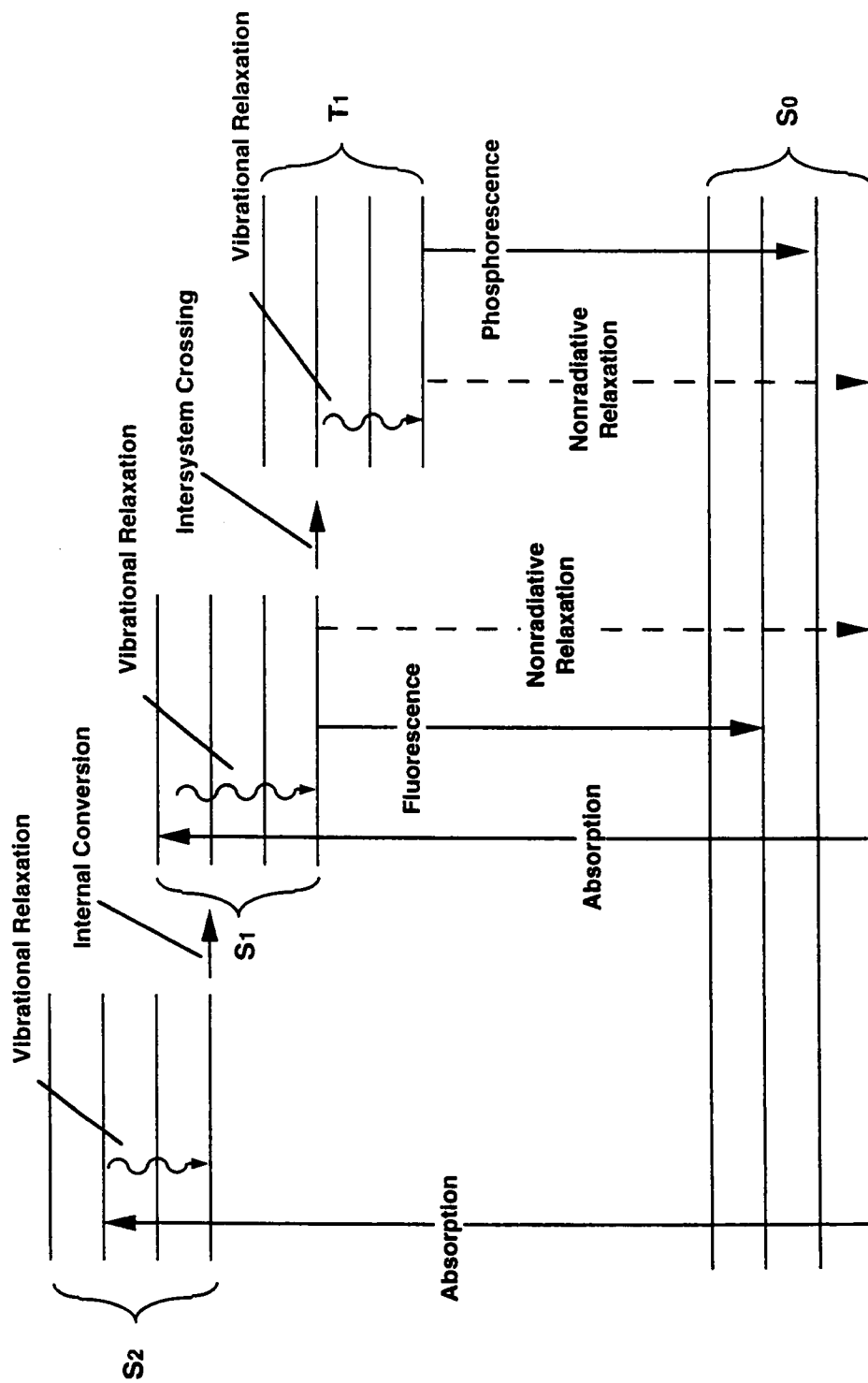
Figure 7.4. Jablonski diagram illustrating various deactivation processes for an excited molecule.

271

between S_0 and some elevated singlet state. Of the two, the π-π^* transition probability is much higher. Aromatic hydrocarbons are generally intensely fluorescent due to an inherent low-energy π-π^* transition. Nonaromatic hydrocarbons with a high degree of conjugation can also exhibit substantial fluorescence, but nonaromatic compounds with few double bonds rarely exhibit appreciable fluorescence. Furthermore, fluorescence from metal ions typically requires organometallic complexation (an effect which will be demonstrated with the SBFOS).

Even for molecules that meet the criteria for absorption, the probability for the ensuing fluorescence emission can be relatively small. Indeed, many molecules that absorb radiation do not fluoresce. As illustrated by the Jablonski diagram, after the molecule is promoted to a vibrational energy level of S_1, it immediately ($\approx 10^{-12}$ s) relaxes to the ground vibrational energy level of the excited electronic state. From this point, fluorescence can occur as the molecule relaxes to some vibrational energy level of the ground electronic state (S_0) with the emission of a photon. However, the competing processes of intersystem crossing to the triplet state (T_1), or the radiationless relaxation to the ground electronic state by internal conversion can dramatically reduce the probability of fluorescence. The probability for internal conversion is largely influenced by environmental conditions (e.g., temperature, viscosity and pH). Environmental factors can therefore have a dramatic effect on the quantum efficiency. Otherwise, functional groups of the excited molecule, itself, can influence the probability for fluorescence. Generally, while electron-donating groups enhance quantum efficiency, electron-withdrawing groups, some of which may promote intersystem crossing, decrease the quantum efficiency.

As a result of these criteria, relatively few molecules are fluorescent under normal conditions, thus severely limiting the range of applications involving direct LIF detection. Furthermore, in spite of the advantages of a laser source described above, the applicability of LIF is further limited by the tunability of the laser. Only molecules with an absorption band energy range overlapping the energy of the laser emission will be detectable. For nontunable, single-line lasers, this limitation is extreme.

One method of overcoming the limited applicability of LIF is to derivatize sample components with fluorescent tags. Precolumn (Jorgenson and Lukacs, 1981; Cheng and Dovichi, 1988; Beijersten and Westerlund, 1995; Orwar *et al.*, 1995; Wang and Giese, 1995; Lada and Kennedy, 1996; Rassi *et al.*, 1997), on-column (Pentoney *et al.*, 1988; Swaile and Sepaniak, 1991a,b; Clark and Sepaniak, 1993), and post column (Rose and Jorgenson, 1988; Gilman and Ewing, 1995; Staller and Sepaniak, 1995; Zhang and Yeung, 1996a; Abler *et al.*, 1997; Zhu and Kok, 1997) derivatization schemes have all been reported for LIF detection with CE. Common to all derivatization modes is the limitation in the selection of the fluorescent tag imposed by the required absorption compatibility with the excitation source emission. Otherwise, the restrictions for precolumn derivatization are minimal.

With precolumn derivatization being performed prior to injection of the sample, there is no time constraint. Derivatization reaction kinetics are therefore an insignificant factor in the outcome of the separation at normal sample concentrations. Furthermore, detection limits achieved with precolumn derivatization are among the lowest reported (10^{-17}-10^{-20} moles) (Jorgenson and Lukacs, 1981; Cheng and Dovichi, 1988). However, derivatization reagents can complicate the electropherogram and even obscure analyte peaks.

273

At the other extreme, postcolumn derivatization requires fast reaction kinetics. This additional limitation can drastically minimize the number of acceptable fluorescent tags to choose from. However, the separation complications associated with the introduction of derivatization reagents into the column are eliminated. Detection limits are comparable to those achieved with precolumn derivatization (2×10^{-17} moles)(Rose and Jorgenson, 1988). On the other hand, postcolumn derivatization necessitates a reaction vessel which introduces dead volume.

On-column derivatization precludes this dead volume, yet the derivatization kinetics limitation is comparable to that of post-column derivatization. In addition, unless regents are continuously fed from a buffer reservoir, on-column reagent depletion occurs. This complication (inherent with *in situ* analysis) generally limits the elution window (the span of time or range of separated eluents included in a single separation), especially with free-solution CE. Detection limits as low as 8×10^{-16} moles have been reported for on-column derivatization (Pentoney *et al.*, 1988). Both on-column and postcolumn derivatization methods are amenable to remote *in situ* analysis, but reagent depletion can be a problem. Both precolumn and on-column modes of derivatization have been pursued with this SBFOS technology, as will be demonstrated in Chapters 8 and 9.

Yet another means of detecting nonfluorescent compounds is indirect fluorescence (Kuhr and Yeung, 1988a; Kuhr and Yeung, 1988b; Desbene and Morin, 1996; Lee and Whang, 1996). In this strategy, a fluorophore is added to the running buffer that produces a continuous background signal. The fluorophore is selected with similar charge to the analyte molecules of interest. As a result, the migrating analyte zones displace the fluorophore and disrupt the background signal as they elute past the detection window. The zones are detected as decreases in the background fluorescence. Despite the potential

noise associated with the fluorescent baseline, detection limits as low as 5×10^{-17} moles have been reported (Kuhr and Yeung, 1988a; Kuhr and Yeung, 1988b). Because of the charge of the fluorophore, a continuous supply is imperative. Reagent depletion could be an insurmountable challenge in remote *in situ* analysis. This strategy was not implemented with the single-reservoir SBFOS design reported in later chapters.

UV-visible absorption. The criteria for molecular absorption have been described above. In light of the criteria for ensuing luminescence, it is clear that molecular absorption is applicable to the direct detection of a wider range of compounds than fluorescence. Furthermore, because the absorption signal is not proportional to incident radiation power, low power, continuous lamps are attractive excitation sources. Tunable wavelength selection from a continuous lamp source enables the excitation of a wider variety of compounds. Because of these advantages, UV-visible absorption is the most common and straightforward method of on-column detection with CE. Nevertheless, the short pathlength of the detection zone in CE (defined by the bore diameter of the capillary) severely limits the sensitivity. The most impressive detection limits for conventional detection systems have been in the 10^{-13}-10^{-15} mole range (Mikker *et al.*, 1979; Terabe *et al.*, 1984; Walbroehl and Jorgenson, 1984). Addressing the issue of sensitivity, recent efforts have been devoted towards increasing the pathlength in the capillary (Djordjevic *et al.*, 1997; Delonge and Fouckhardt, 1995; Djordjevic and Ryan, 1996). In addition, an unconventional technique, forward-scattering four-wave mixing, has enabled the detection in the 10^{-16}-10^{-17} mole range (Wu and Tong, 1997).

While applicable to a wider variety of compounds than fluorescence, UV-visible absorption is not a universal detector. A chromophoric group is required for detection.

275

Analogous to the strategies discussed for fluorescence detection, indirect UV-absorption detection schemes have been reported (Shamsi and Danielson, 1996; Lu and Westerlund, 1996; Nussberger et al., 1996). Derivatization (Plocek and Novotny, 1997; Lin et al., 1997; Oguri et al, 1996) and selective complexation schemes (Schaeffer et al., 1996; Xu and Ma, 1996; Baraj et al., 1996; Haumann and Baechmann, 1995) have also been described and are commonly performed on-column. Detection limits as low as 10^{-6} M (Oguri et al, 1996) and 5 x 10^{-9} M (Baraj et al., 1996) have been reported for derivatization and selective complexation methods in CE, respectively. The complications associated with these methods are generally consistent with those described for fluorescence detection as described above.

Raman scattering. Raman scattering is a topic that has been discussed in great detail in Part I of this dissertation. Fundamentals are included in Chapter 1. Simply stated, Raman scattering spectroscopy is a powerful tool in structural elucidation. Very sharp spectral features offer the potential for spectral selectivity in the analysis of complex mixtures. It is generally applicable to highly symmetric molecules (polarizable molecules). Because Raman scattering does not involve absorption of a photon to promote the molecule to an excited electronic energy state, a single high photon source (e.g., single-line laser) can be applied to the detection of a wide range of molecules. When coupled to CE, it can facilitate the identification of eluting bands. Unfortunately, the cross section for the Raman scattering process is extremely low in comparison to luminescence. The resulting low sensitivity of Raman scattering has therefore limited its acceptance as a practical analytical tool. A detection limit of merely 2 x 10^{-15} molecules has been reported when coupled with CE (Chen and Morris, 1988). While progress in surface-enhanced Raman scattering (SERS) technologies (Part I) have

spurred recent interest in Raman scattering for trace analysis, coupling of SERS with CE has yet to be demonstrated.

Thermal lens. The thermal lens technique can be applied to the detection of organic molecules which absorb incident radiation and have a high heat capacity relative to the running buffer system in CE (Yu and Dovichi, 1989; Waldron and Li, 1996; Seidel *et al.*, 1996). Detection limits as low as 10^{-17} moles (10^{-8} M) have been reported (Yu and Dovichi, 1989). An indirect mode of thermal lens detection has been reported in which a background absorber was added to the running buffer system. This has enabled an LOD of 10^{-6} M even when using a relatively low-power (20-mW) heating beam (Ren *et al.*, 1995).

Electrochemical. Electrical signal-based detection modes include conductometric, amperometric, and potentiometric detection. Among these, the conductometric mode is by far the most versatile, as electrical conductivity is a bulk property. It is among the most universal modes of detection in CE (Foret *et al.*, 1986; Everaerts *et al.*, 1976; Huang *et al.*, 1987; Huang *et al.*, 1988; Buchberger, 1996; Jones *et al.*, 1996). Unfortunately, as is generally the case with bulk property detection, detection sensitivity is limited. While typical LODs are on the order of 10^{-7} M (Huang *et al.*, 1987), an LOD in the nanomolar range has recently been demonstrated (Mueller *et al.*, 1996). On the contrary, amperometry and potentiometry are routinely extremely sensitive modes of detection (Virtanen, 1974; Wallingford and Ewing, 1988; Wallingford and Ewing, 1987); however, versatility of these detection modes is limited owing to the fact that relatively few analyte compounds are electroactive. Nevertheless, this inherent condition often results in very low background interference in CE. As result, detection limits as low as 10 fmol have recently been reported (amperometric

mode) (Lin *et al.*, 1997). Unfortunately, on-column electrical detection modes are vulnerable to interference induced by the high voltage required to drive the electrophoresis.

Applications

A unique advantage of CE is the inherent ability to use a single system for the analysis of a host of classes of both charged and neutral compounds, ranging from small inorganic ions and organic molecules to large proteins and nucleotides. Amazingly, this flexibility is often achievable by the simple modification of the running buffer solution with such additives as micelles, cyclodextrins, zwitterionic substances, crown ethers, linear hydrophilic polymers, organic modifiers, metal ions, and complexing ligands (Sepaniak *et al.*, 1992a,b; Grossman and Colburn, 1992). Several recent reviews give detailed accounts of the effects of some of these additives. For example, the role of organic modifiers in selectivity for the analysis of inorganic ions, small organic ions, pharmaceutical compounds, illicit drugs, amino acids, peptides, and proteins has been described (Sarmini and Kenndler, 1997). The general analysis of negatively charged carbohydrates by CE has been reviewed (Linhardt and Pervin, 1996). Pharmaceutical applications via micellar electrokinetic capillary chromatography (MECC) has been reviewed, including the determination of active ingredients in cold medicines as well as separation analyses of narcotics, amino acids, peptides, vitamins, antibiotics, corticosteroids, and estrogens (Nishi, 1997). Methods of CE have hence been validated and are in routine use in the pharmaceutical industry.

FIBEROPTICS

Fiberoptics are cylindrical dielectric waveguides which can efficiently transmit light over long distances. Since their development, their most significant application has been in the telecommunications industry. Nevertheless, they have also contributed notably to the development of chemical sensors in recent years, as demonstrated by some extensive reviews (Boisde *et al.*, 1991; Angel *et al.*, 1989; Lambeck, 1991; Norris, 1989; Kersey and Dandrige, 1990; Miller *et al.*, 1991).

Development of an effective fiberoptic-based chemical sensor would require a basic understanding of fiberoptic properties and methods of efficient coupling to signal transducers and/or excitation sources. As illustrated in Figure 7.5, optical fibers are composed of a central core surrounded by a concentric cladding, followed by an outer protective coating or jacket. While the jacket contributes robustness to the otherwise fragile fiberoptic, the characteristic optical properties of the optical fiber are determined by the core and cladding. The cladding is generally of $\approx$ 1% lower refractive index than the core. The relative indices of the core and cladding (both typically silica) are generally produced with index-modifying dopants (e.g., GeO_2). The lower refractive index of the cladding promotes internal reflections within the core for incident light over a wide angular range relative to the normal of the core/cladding interface. As a consequence of this waveguide effect, light can be propagated over tortuous paths by way of fiberoptics, provided bends in the fiber do not cause propagating light rays to hit the core wall at less than the critical angle, as defined by the relative indices of the core and cladding. Implementing Snell's Law, $n_1 \sin \theta_1 = n_2 \sin \theta_2$, the critical angle can be expressed solely in terms of the core and cladding refractive indices:
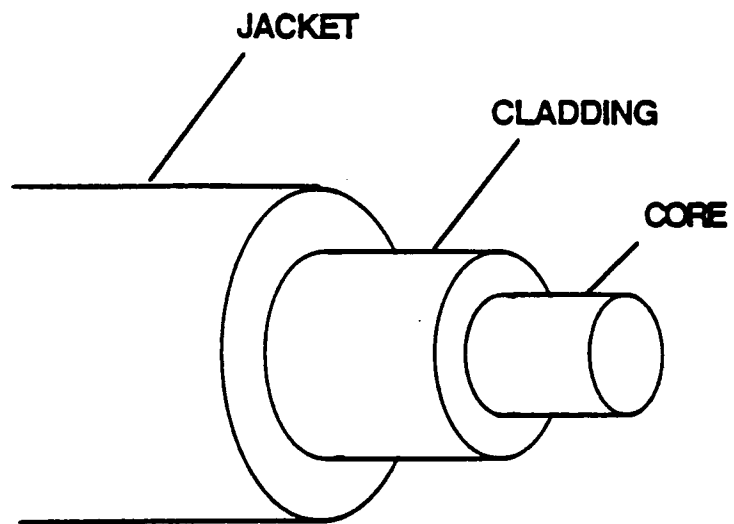
Figure 7.5. Illustration of a typical optical fiber illustrating its concentric layer structure.

$$\sin \theta_1 = \frac{n_2}{n_1} \qquad (7.20)$$

where θ_1 is the critical angle with respect to the normal of the core/cladding interface, above which incident light is internally reflected in the medium of n_1. For an optical fiber, n_1 and n_2 represent the refractive indices of the core and cladding, respectively.

Optical fibers are generally characterized by the core diameter, jacket width, numerical aperture and attenuation. The attenuation is commonly expressed in dB (decibels)/km, where $dB = 20 \log \left(\frac{E_{out}}{E_{in}} \right)$. This parameter is wavelength-dependent and therefore an important factor in fiber selection, particularly in spectroscopy-based applications. The numerical aperture (NA) is another critical parameter in sensor fabrication because it determines the light gathering capability of the sensor and defines the proper optical parameters for auxiliary optics used in any coupling scheme (e.g., air-to-fiber radiation propagation, etc.) required of the sensor. The numerical aperture, a measure of the acceptance angle of the fiber, is also dependent on the refractive indices of the core and cladding, as demonstrated by the following expression:

$$NA = n_0 \sin \theta_0 = \sqrt{\left(n_1^2 - n_2^2 \right)} \qquad (7.21)$$

where θ_0 is the acceptance angle of the optical fiber (see _Figure 7.6_), and n_0 corresponds to the refractive index of the ambient medium.

An alternative expression of light gathering power, generally used to describe conventional lenses, is the f-number (F/n). For conventional lenses, F/n corresponds
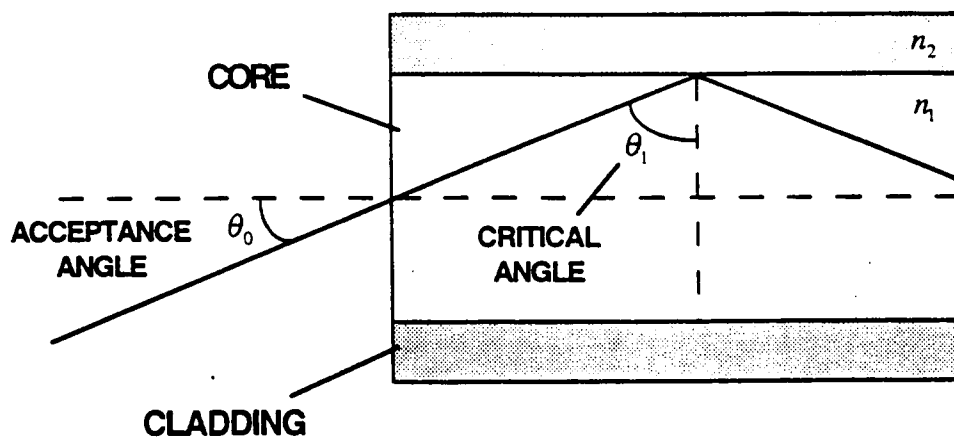
Figure 7.6. Ray diagram illustrating the acceptance angle of an optical fiber of core and cladding refractive indices, n_1 and n_2.

to the ratio of the focal length to the aperture diameter (usually defined by the lens diameter). F/n is related to NA by $F/n = \dfrac{1}{2 \tan \theta_0}$. For efficient coupling, the numerical aperture or F/n of the optical fiber should match that of the coupling optic.

In summary, when selecting an optical fiber for use in a sensor, the designer must confirm that the fiber exhibits adequate transmission at the analytical signal wavelength, that the fiber has adequate light gathering capability, and that adequate coupling optics (e.g., matching the NA of the fiber) can be installed for any coupling scheme required of the sensor design. Other, not-so-obvious complications associated with the use of optical fibers are inherent background signals, such as fluorescence and Raman scattering, particularly for laser-based applications. The significance of these factors obviously depends on the excitation source and the analytical signal sought (e.g., fluorescence vs. Raman scattering). For effective sensing with fiberoptics, sensors must generally be designed with a means of discriminating against background.

CHAPTER 8

MATERIALIZATION OF THE SBFOS TECHNOLOGY FOR ENVIRONMENTAL APPLICATIONS

INTRODUCTION

The concept of the SBFOS technology was introduced in Chapter 7. Simply stated, the SBFOS couples capillary electrophoresis (CE) with optical detection through an optical fiber for remote analysis. In the studies reported herein, laser-induced fluorescence (LIF) is the mode of detection. As a result, the high sensitivity of LIF is combined with the high separation efficiency and far reaching applications of CE for the development of a versatile, yet selective, sensor which exhibits competitive sensitivity. The design is compact. Furthermore, the SBFOS is reusable, requires minimal sample volume and analysis time, and may be amenable to remote control and automation. Rarely does a chemical sensor exhibit all of these virtues. However, these advantages have not been realized without overcoming some significant challenges. While the previous chapter emphasized the potential advantages offered by the selected sensor components and mode of detection in great detail, this chapter describes the actual materialization of the SBFOS technology. General challenges of the SBFOS sensor development are presented. Subsequently several designs are described and evaluated in terms of overcoming such challenges.

General Complications

With the intent of fully demonstrating the challenges associated with the development of the SBFOS technology, comparisons will be made with a conventional laboratory CE system for which optimum experimental conditions are possible. Figure 8.1 illustrates a typical laboratory apparatus for CE with LIF detection. It is composed of a 25-70 cm capillary in an arched geometry with two buffer reservoirs positioned at equal heights. This configuration virtually eliminates hydrostatic flow, which can severely disrupt the "plug-like" profile of EOF. Any distortion of the EOF profile can compromise the unparalleled efficiency of CE which enables competitive separations over relatively short columns with short trial times. Another feature of the typical laboratory setup is on-column excitation and signal collection with extra-column lenses or fiberoptics. Owing to the small volumes associated with the use of CE, on-column detection is generally required to preserve the integrity of the separation.

In order to make CE amenable to *in situ* optical sensing, the proposed configuration is in striking contrast to a typical laboratory setup. Figure 8.2 depicts the general SBFOS concept design. It utilizes a relatively short segment of separation capillary ($\approx$10 cm), configured in a linear geometry, with a single optical fiber probing the elution end of the capillary. The optical fiber is coupled to the separation capillary with a tee joint which also serves as a conduit for flushing the sensor with capillary conditioning reagents and running buffer systems. This linear geometry precludes the use of the two, equal-height reservoirs common to the laboratory-based arrangement. Instead, the sample acts as one of the reservoirs. As a result, a significant amount of gravity-driven hydrostatic flow may be introduced. As described above, the downward hydrostatic flow (away from the optical fiber) is expected to cause band dispersion due to the disruption of the EOF
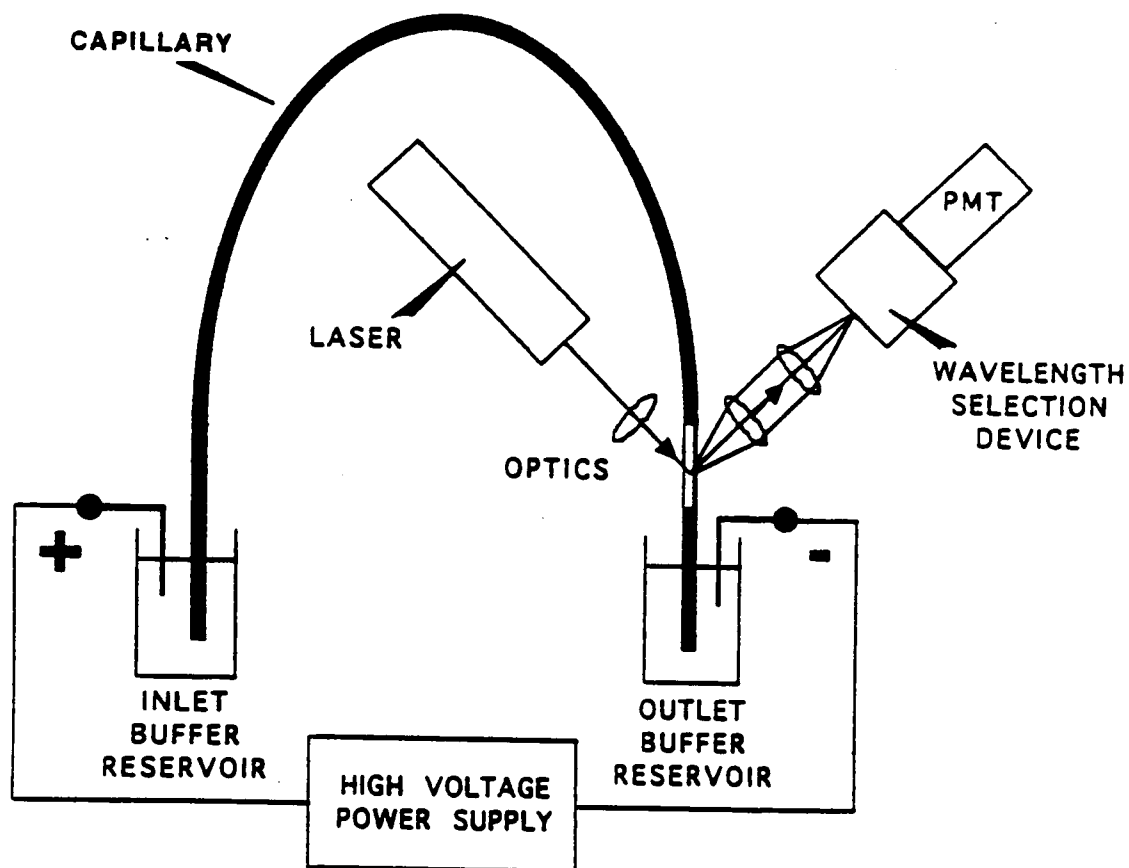
Figure 8.1. Schematic diagram of a typical laboratory-based apparatus for CE with LIF detection.
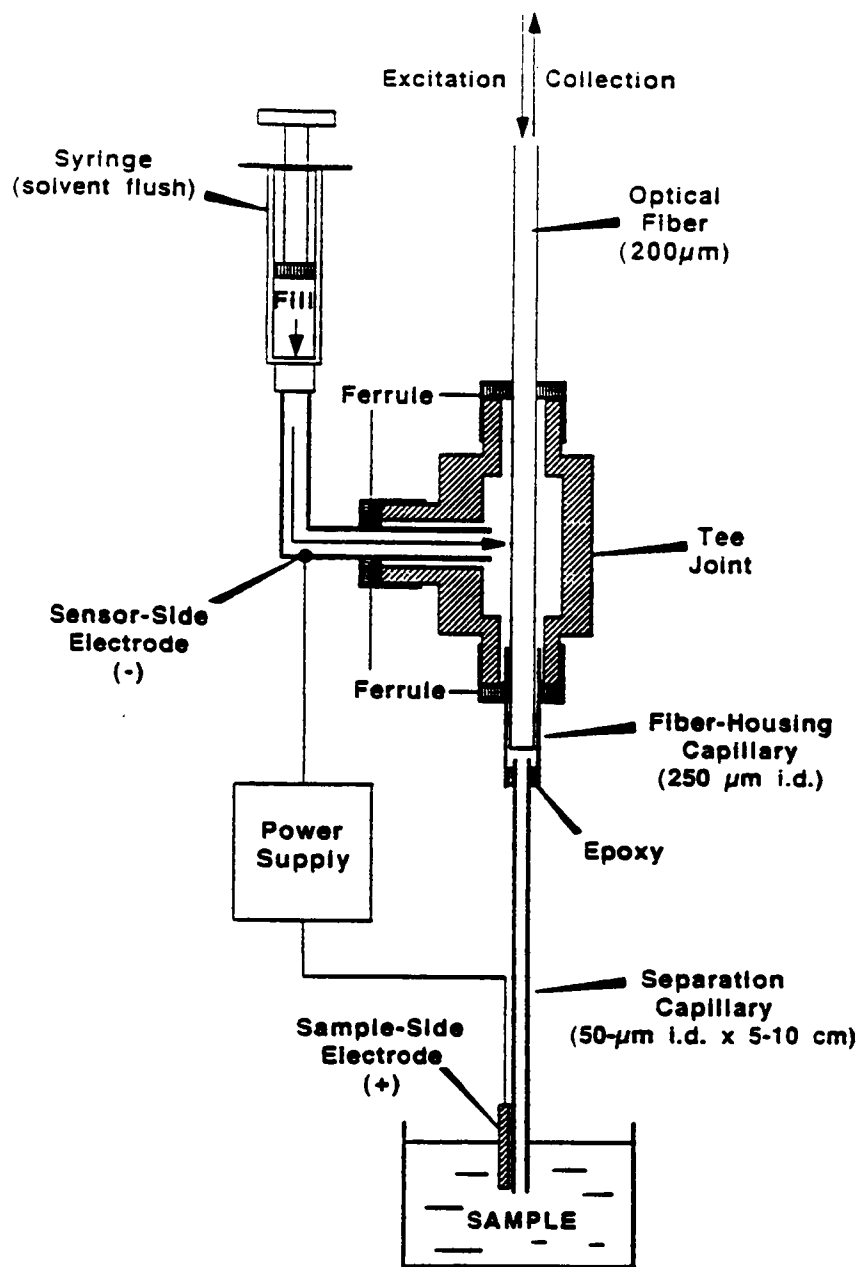
Figure 8.2. Schematic diagram of SBFOS Design A (the general SBFOS concept).

Source: D. L. Stokes, M. J. Sepaniak, and T. Vo-Dinh, *Biomed. Chromatogr.* 11, 187 (1997).

profile. While elevated fields may be applied to provide sufficient EOF to overcome the opposing hydrostatic flow, such measures can further disrupt the EOF profile due to thermal dispersion (joule heating).

Also note from Figure 8.2, the detection end of the capillary is isolated from the atmosphere. Electrolysis gases formed at the detection-side electrode can therefore become trapped within the sensor and thus introduce additional EOF-opposing pressure.

Finally, the general SBFOS design features a single optical fiber which transmits both excitation radiation to the sensor and LIF signal from the sensor. It is configured to probe the outlet of the capillary in an axial geometry which streamlines the design. Although the distance between the optical fiber and the separation capillary is minimal, separation-defeating dead volume is introduced. In summary, three major challenges are implied by the above discussion: 1) elimination (or acceptable reduction) of hydrostatic flow, 2) expulsion or elimination of electrolysis gases, and 3) establishment of a suitable compromise between detectability and separation performance. This chapter describes approaches to overcome these challenges which entail minor modifications of the general design depicted in Figure 8.2. Among these modifications are hydrostatic flow-restriction devices, tee joints of varying internal volumes and materials to ease the effects of dead volume and trapped electrolysis gases, and varying positions of the detection-end electrode to further reduce generation of electrolysis gases within the sensor.

EXPERIMENTAL

Fabrication of Sensors

SBFOS Design A fabrication. Design A is illustrated in <u>Figure 8.2</u>. A 1/16" brass tee joint (Alltech: Deerfield, IL) was used to combine the elements of the sensor. The separation element was a 5-cm segment of 50-μm i.d., 365-μm o.d. fused silica capillary (Polymicro Technologies, Inc.: Phoenix, AZ). The detection element was a 200-μm core diameter optical fiber (General Fiber Optics: Cedar Grove, NJ, Cat. No. 14-200). The separation capillary was fixed within the bore of a 250-μm i.d. fused silica capillary with epoxy. As demonstrated by the figure, the 250-μm i.d. capillary served as a sleeve into which the fiberoptic could be placed, thereby providing a relatively low-volume, stable junction between the optical fiber and the 50-μm i.d. separation capillary. The relatively large inner volume of the brass tee joint was excluded from the junction. The ends of a 1-m segment of the optical fiber were polished with alumina lapping paper (down to 0.3-μm grain). In addition, the end of the fiber to be inserted into the SBFOS was stripped of its jacket (by flame) to a length suitable for insertion into the 250-μm sleeve until touching the separation capillary.

The separation/sleeve capillary assembly was immobilized in the lower arm of the tee joint with a 1/16" Vespel® reducing ferrule (Alltech), while the optical fiber was immobilized in the opposite arm with a Teflon® reducing ferrule (Alltech). A 16-gauge syringe needle was affixed to the side arm of the tee with a Teflon reducing ferrule (Alltech) to allow flushing or filling of the sensor with column pretreatment or buffer solutions. In order to limit gravity-driven hydrostatic flow (GHF) during

electrophoresis, the rinsing needle (shown in the figure) was replaced by a similar 16-gauge needle that housed a 1-cm segment of 25-μm i.d. capillary which was cemented within its bore. The metallic tee joint served as the detection-side electrode and was set at ground potential. Likewise, the sample-side electrode (a platinum wire submerged in the sample) was electrically isolated from the CE sensor assembly and set at positive bias voltages for all experiments. The source of potential for the separations was a Hipotronics (Brewster, NY) high voltage power supply.

SBFOS Design B fabrication. A schematic diagram of SBFOS Design B is illustrated in Figure 8.3. Similar to Design A, Design B was composed of the following five essential parts: 1) the separation capillary; 2) the optical fiber; 3) a gravity-driven hydrostatic flow (GHF)-restricting capillary; 4) a low-volume, nonmetallic PEEK tee joint; and 5) the sample-side/detection-side electrode pair. The salient feature of this design was the PEEK tee joint (Upchurch Scientific: Oak Harbor, WA; Model P712), which eliminated much of the interior void volume of Design A. Furthermore, the nonconductive PEEK material prevented electrolysis from occurring at interior surfaces of the tee joint. The PEEK tee featured three ports with finger-adjustable threaded fittings. Seated in each fitting was a flangeless ferrule for 1/16" tubing. Channels extending from each port socket to the central union of the tee joint were of 0.020" diameter and 0.19" length. The two opposing ports of the PEEK tee joint were used to position the optical fiber on-axis with, and very close to, the elution end of the separation capillary. Sensor condition reagents and buffer solutions were flushed through the third port (perpendicular to the separation/optical axis). This third port also housed the GHF-restricting capillary as well as the detection-side electrode.
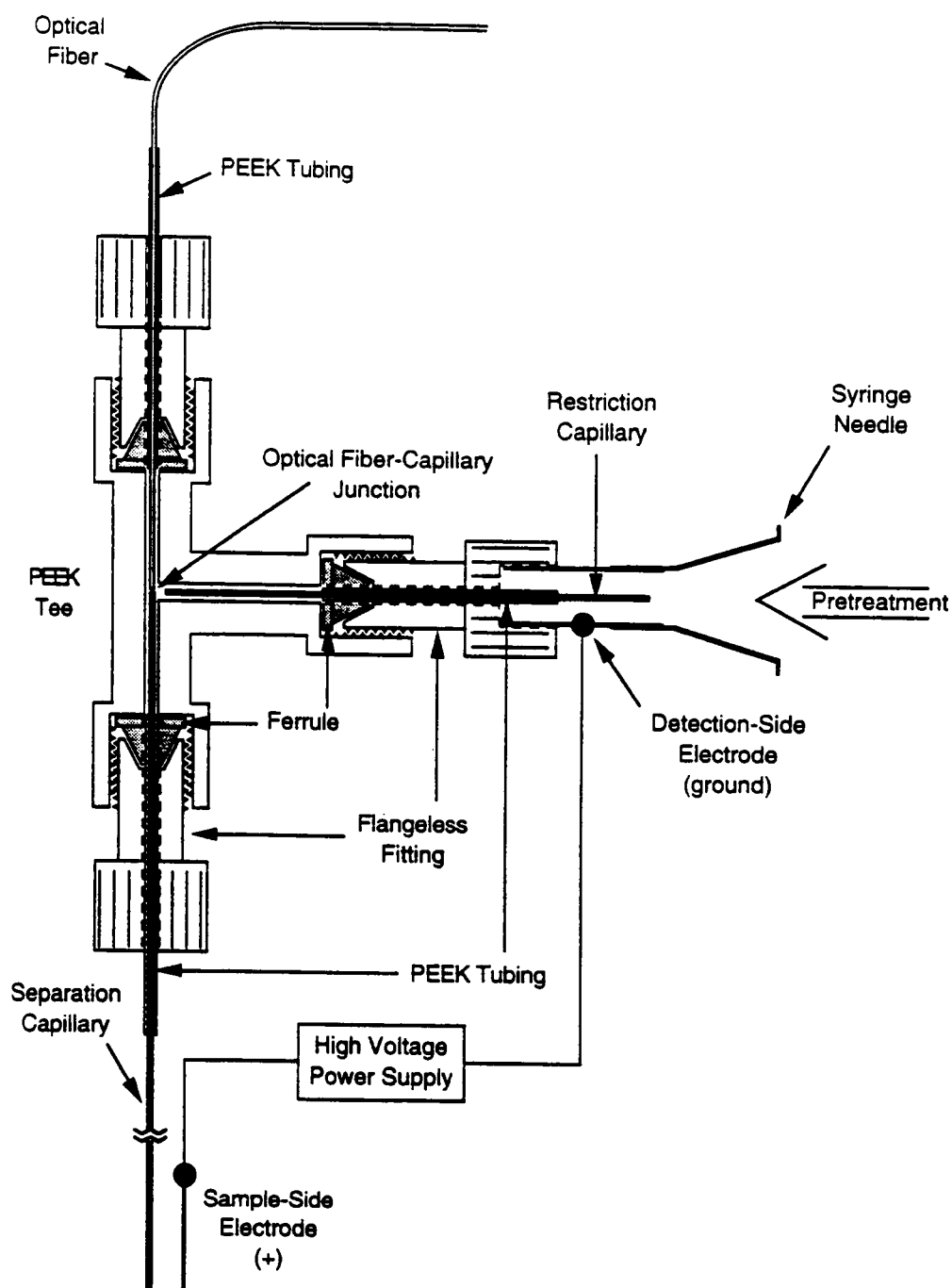
Figure 8.3. Schematic diagram of SBFOS Design B.

Source: M. J. Sepaniak, T. Vo-Dinh, V. Tropina, and D. L. Stokes, *Anal. Chem.* **69**, 3806 (1997).

The separation element was a 50-μm i.d. fused silica capillary (Polymicro Technologies: Phoenix, AZ) of 5.0 or 8.0-cm length as stated in discussions. This capillary was affixed (5 min epoxy, Devcon) within the 0.020" bore of a 3-cm segment of 1/16" o.d. PEEK tubing (Upchurch Scientific). The PEEK tubing provided an air-tight coupling to a flangeless ferrule which was seated in a finger-adjustable threaded fitting, thus enabling stable positioning within the tee joint. The capillary itself extended from the fitting into the channel, towards the center of the tee joint.

Various optical fibers were used in this design for compatibility with the various excitation sources used for the different studies involving this design. The following types of fiberoptic were used: 1) 200-μm core diameter; 0.22-NA (General Fiber Optics: Cedar Grove, NJ, Cat. No. 14-200); 2) 100-μm core diameter; 0.22-NA (Polymicro Technologies: Phoenix, AZ; Cat. No. FVP100110125); and 3) 100-μm core diameter; 0.66-NA (Polymicro Technologies; Cat. No. FSU100120). For each type of fiber, a 1-m segment was cleaved and polished with alumina lapping paper down to 0.3-μm grain. In the case of the 200-μm optical fiber, the fiber was simply epoxied within a 3-cm section of 0.02" (500-μm) i.d. PEEK tubing and connected to the tee in a manner similar to that used for capillary placement. In the case of the 100-μm core diameter, the fiber was first cemented within the bore of a 10-cm segment of 180-μm i.d /400-μm o.d. capillary. The fiber tip, cement and encasing capillary were then collectively polished to a flush surface with lapping paper. This assembly, intended to center the fiberoptic in the PEEK tee channel, was then cemented within the 3-cm section of 0.02" PEEK tubing as described above.

As with the previous design (Design A), the side port was used for flushing or filling the sensor with pretreatment or buffer solutions. This was accomplished through a syringe

292

needle which was cemented within the bore of the threaded fitting, as shown in the figure. The side port was further modified to house a GHF-restricting capillary. In doing so, the restriction capillary was cemented within a 4-5 mm segment of 1/16" o.d. PEEK tubing, which provided an air-tight seal with the ferrule. This restrictor capillary-housing ferrule was seated in another threaded fitting which also housed a syringe needle. Two GHF-restricting capillaries were used: 1) 3 mm x 15 µm, and 2) 5 mm x 25 µm. The metal shaft of the needle served as the detection-side electrode, and was hence a potential source of electrolytic gases during electrophoresis. Nevertheless, the restrictor capillary served the additional purpose of blocking gas bubbles from entering the tee joint. Exposure of the active surface of the electrode to the atmosphere was possible in this design because residual liquid in the syringe needle engulfed the outside end of the restrictor capillary, thus completing the electrical circuit required for electrophoresis. As with the previous design, the sample-side electrode was set at positive bias voltages, supplied by the Hipotronics high-voltage power supply.

SBFOS Design C fabrication. A schematic diagram of Design C is illustrated in Figure 8.4. It was mainly used for fundamental studies including fluorescent dyes. Design C is similar to Designs A and B, in that it features the axial geometry of the optical fiber positioned against the elution end of a separation capillary. The union was formed within a tee joint, with which the side arm housed both the GHF-restricting capillary and the detection-side electrode. Again, the key salient feature was the tee joint, a "zero-volume" quartz tee (Microquartz: Pheonix, AZ). By using this tee, the interior void volume of the SBFOS was even further reduced relative to Design B. Another attractive feature of this tee was its transparency, thereby facilitating positioning of the sensor components within the sensor during fabrication. The tee also permitted visual observation of the bandfront behavior (for highly fluorescent test

293

Optical Fiber
(100-μm Core)

Excitation

Emission

Capillary
Liner
(150-μm i.d.)

Restriction Capillary
(25-μm i.d. x 3 cm)

PEEK Tubing
(0.01" i.d.; 1/16" o.d.)

Quartz
Tee

Syringe Needle
(Detection-Side Electrode)

Heat-Shrink
Tubing

PEEK Tubing
(1/16" i.d.; 1/8" o.d.)

Separation
Capillary
(50-μm i.d. x 365-μm o.d. x 8 cm)

High Voltage
Power Supply

Sample-Side
Electrode
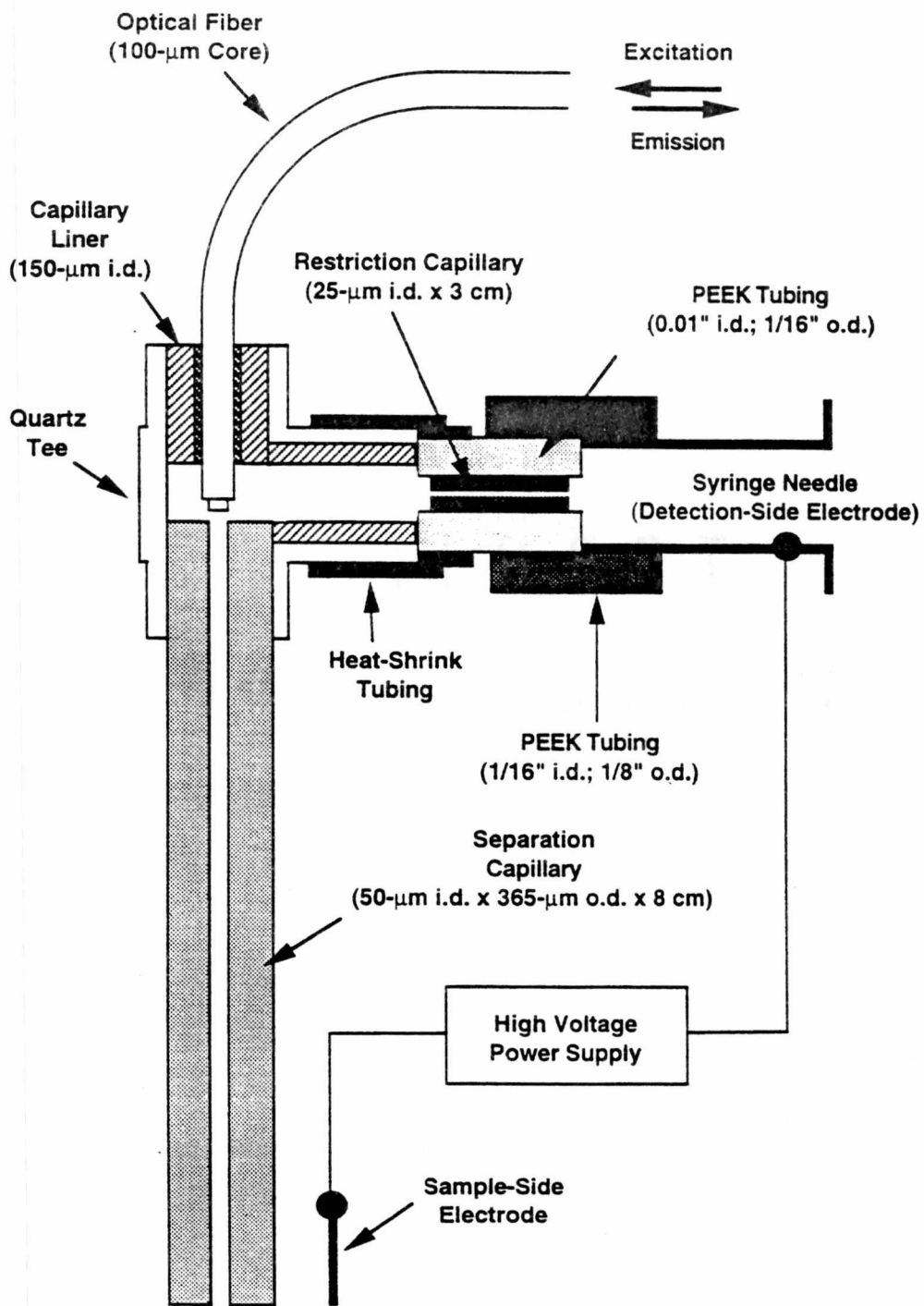
Figure 8.4. Schematic diagram of SBFOS Design C.

compounds) and the determination of air pocket sources during electrophoresis and flushing steps. As purchased, the "zero-volume" quartz tee was lined with 150-µm i.d./365-µm o.d. silica capillaries in each arm. The interior tips of these capillaries were precisely machined to form the zero dead volume union at the center of the tee. As shown in Figure 8.4, the capillary liner was removed from the sample inlet arm of the tee and replaced with the separation element (50-µm i.d./365-µm o.d. X 8-cm silica capillary). The 365-µm o.d. of the capillary formed a near perfect fit within the bore of the quartz tee and was cemented in place. The detection element, a 100-µm core, 0.22-NA optical fiber (Polymicro Technologies) was inserted in the opposing, capillary-lined arm of the tee. The 125-µm o.d. of the fiberoptic jacket formed a snug fit within the capillary liner. The third, capillary-lined arm of the tee was equipped with a syringe needle/restrictor capillary assembly.

The needle/restrictor capillary assembly was applied externally to the sensor tee. The GHF-restricting capillary, a 25-µm i.d. X 3 cm capillary, was cemented within the bore of a segment of 0.01" i.d. PEEK tubing (1/16" o.d.). The capillary-lined PEEK tubing was then cemented within a section of 1/16" i.d. PEEK tubing. A 16-gauge needle was cemented into the opposite end of the 1/16" i.d. tubing. The needle/restrictor capillary assembly was finally secured to the quartz tee with heat shrink tubing and epoxy. As with previous designs, the side arm needle served as the detection-side electrode. The sample-side electrode was a platinum wire submerged in the sample solution. Positive bias potentials were supplied to the sample-side electrode with a 20-kV power supply (Hipotronics).

Optics and Instrumentation

The optics and instrumentation varied slightly between various sensors and/or applications. These variations were in part due to the fact that studies were shared between laboratories at the University of Tennessee (UTK) and Oak Ridge National Laboratory (ORNL). Otherwise, variations were generally made to accommodate the excitation source required for a given application. All systems were based on a beam-splitting design previously developed to enable single-fiber transmission of both the excitation and analyte emission radiation (Tromberg et al., 1987, 1988; Alarie et al. 1990; Vo-Dinh et al., 1991; Bowyer et al., 1991).

Optical System I. Optical System I (ORNL) is illustrated in Figure 8.5. It was used with Sensor Designs A and B for the detection of fluorescence dyes. The 457.1-nm line (10 mW) of an argon ion laser (Coherent: Palo Alto, CA; Model Innova-70) was the excitation source. The laser beam was directed (nonfocused) through the hole in a plane mirror and into a 50X (0.30-NA) objective lens (Newport: Irvine, CA; Cat. No. L50X). The objective lens focused the excitation laser beam onto the optical fiber of the SBFOS. Efficient coupling of the laser beam to the sensor optical fiber was facilitated with an x-, y-, z-axis fiber positioner. The fiber transmitted both the laser excitation and sample fluorescence to and from the sensor, while the plane mirror served as a pseudo beamsplitter, oriented at 45° with respect to the excitation beam axis. The fluorescence signal from the SBFOS exited the fiber and was collimated by the objective lens. A majority of this collimated signal beam was deflected 90° off-axis towards a "relay" fiberoptic (600 μm core, 0.26-NA, Fiberguide Industries) by the beamsplitter. The "relay" fiber transmitted the signal to the detector. Prior to entering the detector aperture, the signal beam was filtered with a 480-nm "cut-on" filter to reject the
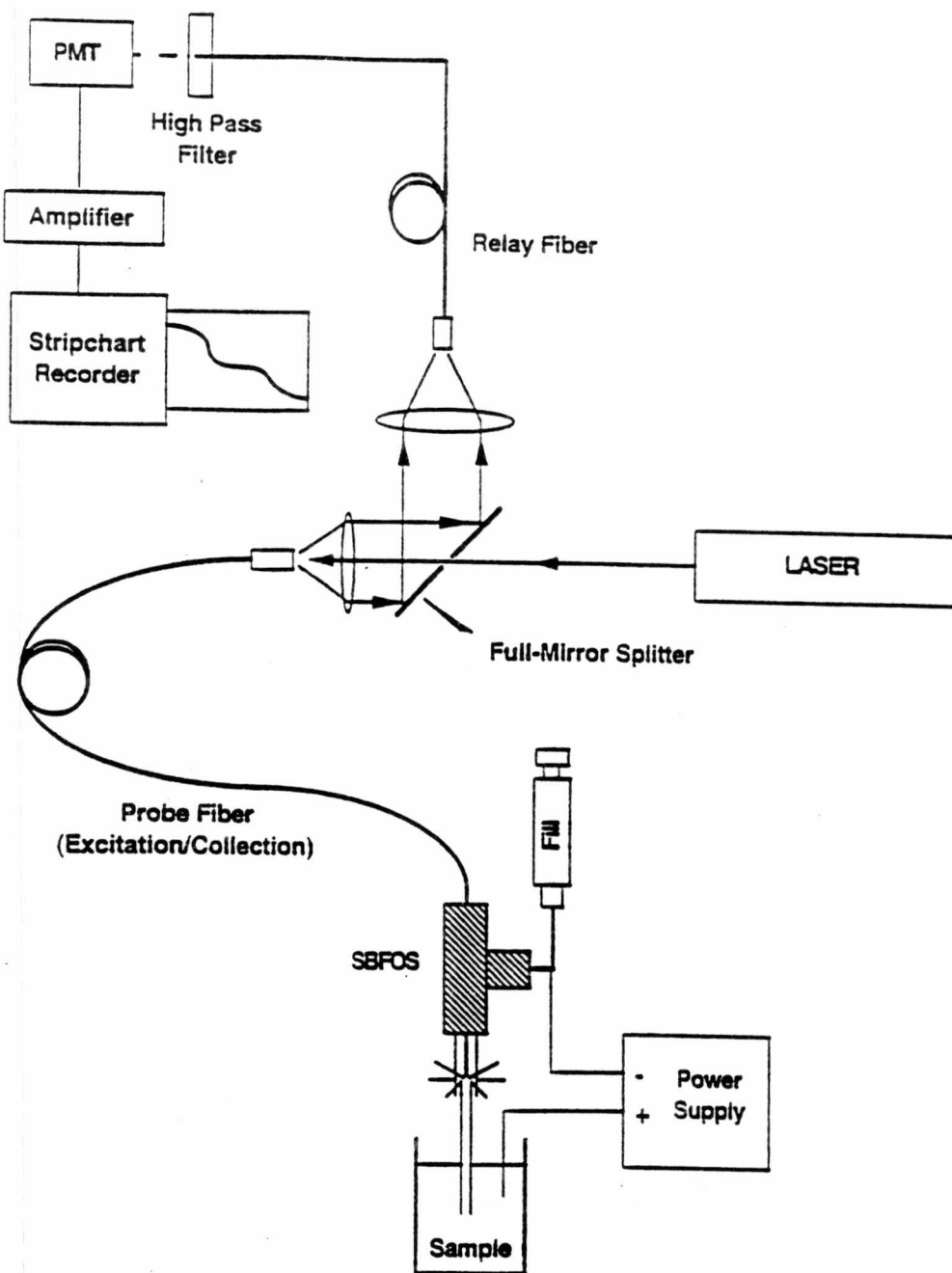
Figure 8.5. Schematic diagram of optical system I, used with SBFOS Designs A and B.

Source: M. J. Sepaniak, T. Vo-Dinh, D. L. Stokes, V. Tropina, and J. E. Dickens, *Talanta* **43**, 1889 (1996).

unwanted Rayleigh scatter and silica Raman scatter from the optical fiber (and possibly the separation capillary). The detector was a PMT (RCA: Lancaster, PA; Model IP-28) operated at 1000 V. Photocurrents from the PMT were amplified by a picoammeter (Keithley, Model 485) and electropherograms were directly recorded with a strip chart recorder (Kipp and Zonen: Delft, Netherlands; Model BD 40).

Optical System II. Optical System II (UTK) was used with Sensor Designs B and C for the detection of fluorescent dyes, organometallic complexes and derivatized amines. It was very similar to Optical System I, as shown in <u>Figure 8.5</u>, except that the "relay" optical fiber of Optical System I was omitted. The collimated signal beam diverted by the beamsplitter was focused directly onto the PMT by a conventional quartz lens. Because of the many applications pursued with this system, minor alterations of the general schematic were necessary to accommodate the different excitation sources. For example, the detection of fluorescent dyes was performed with the 543.5-nm line of a He-Ne laser, requiring a narrow excitation bandpass filter(543 nm). A conventional 1" f/2 lens was used to couple the laser beam with the sensor fiberoptic, and a 600-nm "cut-on" filter was used for isolation of analyte emission. The detection of organometallic complexes required the 325-nm line of a He-Cd laser (Omnichrome: Chino, CA; Series 74), operated at 20 mW intensity. This source necessitated a 325-nm laser bandpass filter, a quartz f/2 lens for coupling the laser beam to the SBFOS, and a 400-nm analyte emission filter. The 488-nm line of an air-cooled argon ion laser (Cyonics: San Jose, CA; Model 2201) was used for the analysis of derivatized amines, requiring a 488-nm bandpass filter and a 500-nm analyte emission "cut-on" filter. This study also involved the use of a 0.66-NA SBFOS optical fiber. A 40X, 0.65-NA objective lens was used to couple the laser beam to the optical fiber in this case. Otherwise, photocurrents from the PMT were amplified with a photometer (Pacific Precision Instruments: Concord,

298

CA), and electropherograms were recorded with the strip chart recorder (Kipp and Zonen).

Chemicals

All chemicals were purchased at the highest commercially available purity and used as received. The standard running buffer was a phosphate/borate-based solution which, unless otherwise stated in the results, was composed of 10 mM sodium phosphate, dibasic (J. T, Baker: Phillipsburg, NJ) and 6 mM sodium tetraborate (Fisher Scientific: Fair Lawn, NJ). The pH was ≈9. Water used to prepare the buffer solution was purified with a Waters Milli-Q+ filtration system. Depending on the application, the buffer solution was modified with various additives, including complexing reagents, surfactants, cyclodextrins and methanol.

The fluorescent dyes used for fundamental studies included Rhodamine 6G (Rhodamine 590) (Exiton: Dayton Ohio), sodium fluorescein (E. M. Science: Cherry Hill, NJ), and fluorescein isothiocyanate (FITC) (Sigma: St. Louis, MO). Dye solutions were generally prepared at ≈0.1 mM concentration in the standard running buffer solution. $MgSO_4$ and $CaSO_4$ (Baxter: Stone Mountain, GA), used for the metal ion studies, were prepared at 0.5 mM and 0.1 mM concentrations for $CaSO_4$ and $MgSO_4$, respectively. A sample of Big Limestone Creek was obtained from a site in Washington Co., TN, and used without further modification. On-column labeling of metal ions was accomplished with a complexing agent, 8-hydroxyquinoline-5-sulfonic acid (HQS) (Sigma), which was added to the standard running buffer at 2.5 mM concentration. Methylamine, ethylamine, and *n*-propylamine were all purchased from Fisher Scientific. The 7-chloro-4-nitrobenzofurazan (NBD-Cl) used to derivatize the amines was purchased

299

from Aldrich Chemical (Milwaukee, WI). Derivatization was performed by the simple mixing of 5 parts amines with 1 part NBD-Cl at room temperature, followed by 10x dilution in reagent grade methanol (Burdick and Jackson: Muskegon, MI). Stock solutions were stored in aluminum foil-wrapped glass vessels and refrigerated. Assuming complete derivatization, NBD-amine solutions ranged from 5×10^{-8} to 5×10^{-5} M, with dilutions being performed with the standard running buffer solution (unless otherwise stated in the discussions). The on-column standard running buffer for the separation of the derivatized amines contained 50 mM sodium dodecyl sulfate (SDS) (Sigma; 99%).

Sensor Operation Procedures

Sensor A. Prior to each measurement, the sensor was flushed, via syringe, with 0.1 M NaOH, followed by the standard running buffer solution. Flushing was performed through the side port of the brass tee joint which was, at that point, occupied by the unmodified syringe needle. Once flushing was complete, the normal needle was replaced with the modified GHF-restricting needle. Buffer filling was briefly continued through the GHF-restricting needle under high pressure. Once sensor filling was complete, the syringe was removed from the inlet needle, and the sensor was allowed to depressurize. Once pressure stabilization was visually confirmed (as demonstrated by ceased drop growth at the inlet of the separation capillary), the sensor was dipped into the sample for frontal mode operation.

Sensor B. The Design B SBFOS was flushed with the base and buffer solutions before each trial. First, the fiberoptic-housing fitting of the top port of the PEEK tee was loosened (but not removed). The 0.1 M NaOH was then injected (via syringe) through

300

the side port fitting (without the GHF-restricting capillary). Residual air in the void volumes of the tee joint was ejected through the top port. The top port fitting was then tightened, and base flushing was continued through the separation capillary. With the top port fitting loosened again, the buffer solution was injected, ejecting any residual base through the top port. Buffer flushing was continued through the capillary, with the top fitting retightened. The side-port, high-throughput fitting was then replaced with the fitting which housed the GHF-restricing capillary. A final, high-pressure, low-throughput buffer flush was performed with the top fitting loosened to allow ejection of air bubbles introduced during the installation of the GHF-restricting fitting. Again, the top fitting was retightened. After a sensor depressurization period, the SBFOS was dipped in the sample for frontal mode analysis.

Sensor C. Base and buffer flushing steps were performed before each trial. However, because of the permanent setting of the sensor components in the quartz tee by epoxy, all rinses had to be performed through the GHF-restricing capillary in the side port. The resulting low flow throughput necessitated longer sensor pretreatment times relative to the Designs A and B. Furthermore, no top-port bleeding was possible with this design. Consistent with previous designs, a syringe was used to flush the sensor; depressurization periods were allowed before each trial; and, all separations were performed with the frontal mode of operation.

RESULTS AND DISCUSSION

Fundamental Evaluations

SBFOS Design A. Incorporating CE for *in situ* optical detection offers the potential advantages of selectivity, versatility, reusability and sensitivity. However, the linear geometry associated with the general sensor design introduces major challenges in comparison conventional laboratory setups. Initially, the issue of GHF may be critical. When observed, the negative GHF can disrupt the "plug-like" flow profile of EOF, yielding a profile more like that illustrated in Figure 8.6, thus resulting in dramatic band dispersion (Grossman and Colburn, 1992). As a demonstration of the degree of dispersion that may be possible with the linear design of the SBFOS (without GHF-retricting measures), Figure 8.7 illustrates CZE electropherograms of a dye mixture of Rhodamine 6G (R6G), FITC and fluorescein (in order of elution). Both electropherograms were generated with a conventional laboratory system of 8-cm effective separation length; however, electropherogram B was acquired with the exit buffer reservoir elevated 8 cm relative to the inlet buffer reservoir (thus emulating the length of the SBFOS separation element). In comparison to electropherogram A (acquired with equal-height exit and entrance reservoirs- no GHF), the efficiency observed in electropherogram B is dramatically diminished. In addition, the presence of EOF-opposing GHF is manifested by the longer band elution times exhibited in electropherogram B. This effect of GHF can be offset by the application of elevated field strengths, as demonstrated by the following expression:

$$v_b = v_{hy} + v_{elec} = v_{hy} + (\mu_{eo} + \mu_e)E \qquad (8.1)$$

302
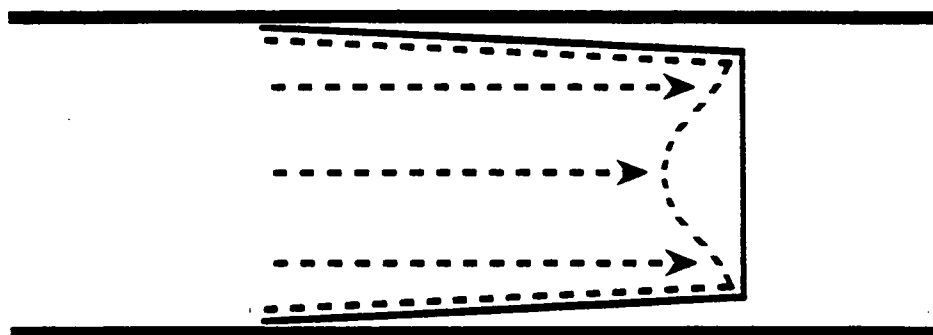
Figure 8.6. Conceptual illustration of the possible disruptive effect of gravity-driven hydrostatic flow on the "plug-like" profile of electroosmotic flow.
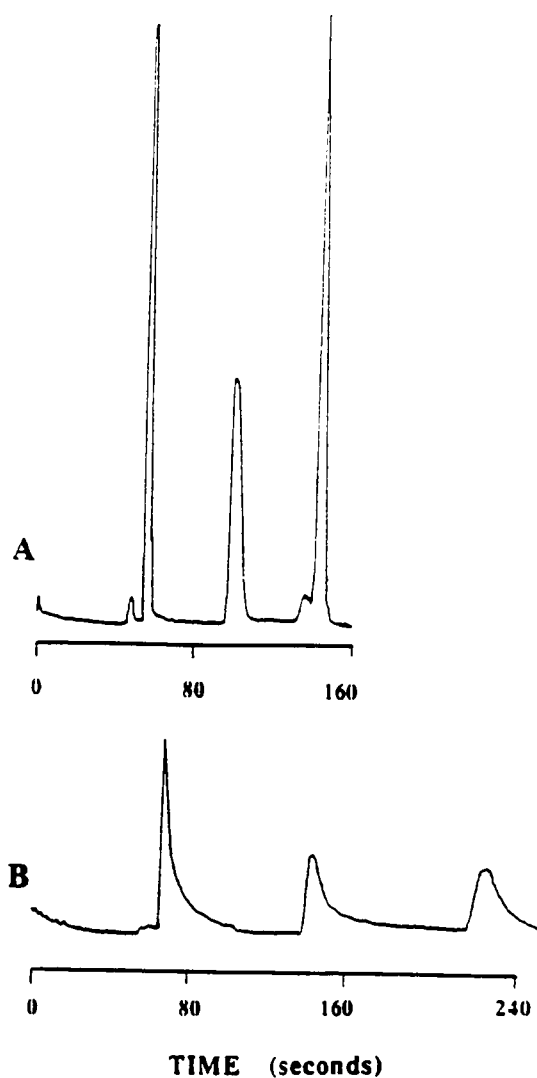
Figure 8.7. CZE separations of Rhodamine 6G, FITC, and sodium fluorescein performed via a conventional laboratory-based CE system with a) equal inlet and outlet buffer reservoir heights, and b) the outlet buffer reservoir height raised 8 cm relative to the inlet buffer reservoir. Conditions; 45-cm column, 8-cm effective length, 220 V/cm; absorbance at 500 nm.

Source: M. J. Sepaniak, T. Vo-Dinh, D. L. Stokes, V. Tropina, and J. E. Dickens, *Talanta* **43**, 1889 (1996).

304

where v_b is the total band velocity, v_{hy} is the GHF velocity, v_e is the electrophoretic flow velocity, μ_{eo} is the electroosmotic mobility, μ_{elec} is the analyte solute mobility, and E is the applied field strength.

It is clear from Equation 8.1 that the GHF velocity is independent of applied potential. However, elevated fields can produce joule heating and, hence, additional band dispersion. A GHF-restricting device was clearly needed. In SBFOS Design A, an auxiliary capillary of low permeability relative to the separation capillary was incorporated in hopes of minimizing GHF. This device was the "restrictor capillary", installed into the side port of Design A (illustrated in Figure 8.2). With an i.d. of 25-μm, this 1-cm segment of capillary should have reduced v_{hy} by a factor of 0.8.

Figure 8.8 illustrates the elution of a sharp bandfront observed for a frontal mode injection of fluorescein (10^{-4} M). Using the formula, $N = 16\left(\dfrac{T_r}{W}\right)^2$, a plate number of 8×10^3 was observed (> 10^5 plates/m), where W corresponds to the rise time of the bandfront between the baseline and the plateau, and T_r corresponds to the retention time. T_r was measured as the time elapsed between the application of the voltage and the point of half maximum intensity for the observed bandfront. However, the apparent T_r may have been larger than the true value due to a delayed introduction of sample onto the column resulting from residual pressure in the brass tee joint (see below). The plate count reported above may have therefore been overestimated.

Relatively sharp peaks were also observed using Design A for the separation of R6G (5 x 10^{-5} M) and fluorescein (5 x 10^{-5} M), as illustrated in Figure 8.9a. The resolution of this separation was greater than 5. Peak identities were confirmed by sample

305

$$N = 16(T_r/W)^2$$
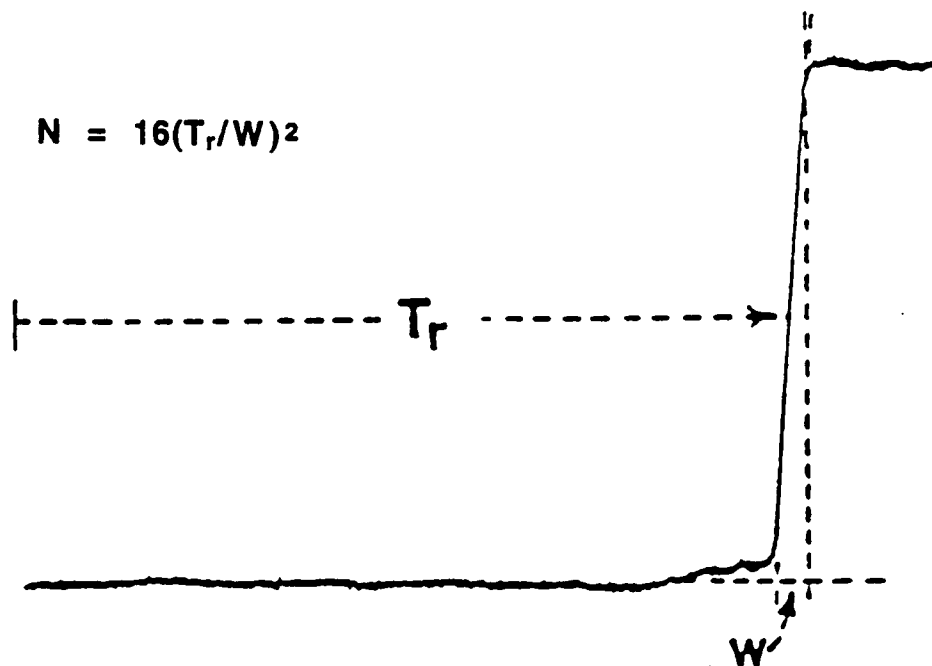
Figure 8.8. Frontal-mode CE electropherogram of sodium fluorescein (10^{-4} M) generated with SBFOS Design A operated at 500 V.

Source: D. L. Stokes, M. J. Sepaniak, and T. Vo-Dinh, *Biomed. Chromatogr.* 11, 187 (1997).
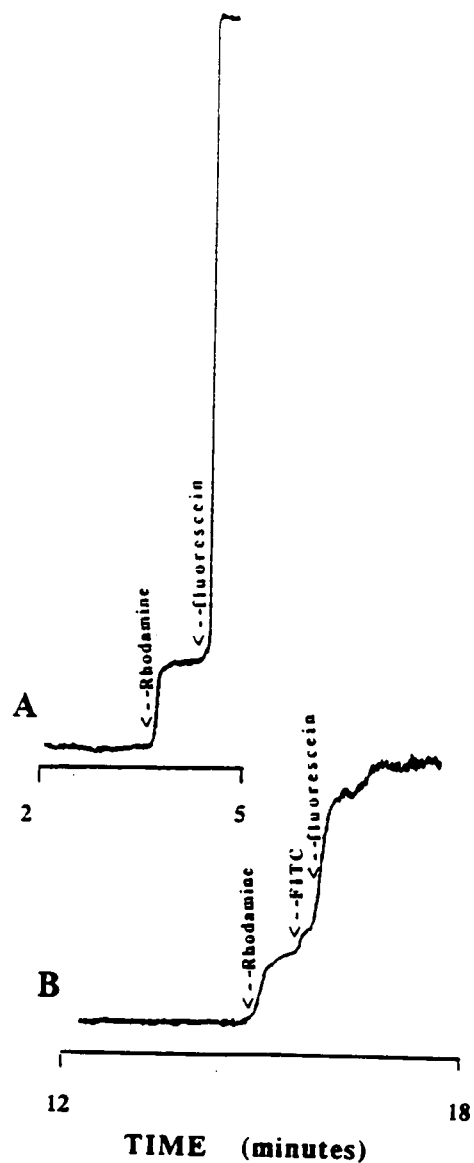
Figure 8.9. Frontal-mode CE electropherograms for mixtures of a) Rhodamine 6G and sodium fluorescein (both 5 $\times 10^{-5}$ M); and b) Rhodamine 6G (7 $\times$ 10^{-4} M), FITC (1 $\times$ 10^{-5} M), and sodium fluorescein (both 1 $\times 10^{-6}$ M), generated with SBFOS Design A operated at 500 V.

Source: D. L. Stokes, M. J. Sepaniak, and T. Vo-Dinh, *Biomed. Chromatogr.* **11**, 187 (1997).

307

spiking, and the elution order for the laser dyes was consistent with what would be expected, based on the charges of these solutes (positive and negative for R6G and fluorescein, respectively). When a mixture of R6G (7×10^{-5} M), FITC (1×10^{-5} M) and fluorescein (1×10^{-6} M) was injected in a separate experiment (Figure 8.9b), the additional FITC bandfront was observed to elute between the other two solutes. Unfortunately, the disparity in retention times of bands common to both Figures 8.9a and b reflect inadequate operational reproducibility. Both trials were performed with the same field strength.

GHF should be relatively consistent for a given system and, hence, does not explain the poor reproducibility. We therefore attribute the lack of retention time reproducibility to a variable hydrostatic pressure in the system. This pressure could be the result of residual pressure from the rinsing step or the expansion of gases trapped in the tee joint. For example, experimental observations have indicated that in the early stages of some separations, v_{hy} is very large. However, as the hydrostatic pressure is dissipated, v_{hy} diminishes to a point at which v_b becomes positive, and the separation begins. Migration rates probably increase throughout the separation as v_{hy} further decreases to the GHF limit (which has been reduced using the side port restrictor capillary). This uncontrollable process could explain the observed long and variable migration times for the fluorescent dyes.

The presence of void volume air pockets was an inherent complication of the large-volume of the brass tee joint. Another potential problem associated with the large volume was contamination of the running buffer due to inadequate flushing of the large-volume tee between trials. Carryover of sample solutes and variable pH conditions due to residual base were possible consequences. It was therefore concluded that a small-

volume tee would be a prudent modification in future designs. Yet another complication of the conductive brass tee joint was the possibility for the generating electrolysis gases within the tee joint, causing additional hydrostatic pressure in the closed system. A nonmetallic tee joint was therefore also sought for future designs.

Having discussed the issues of GHF and the possibility of hydrostatic pressure, one final aspect of SBFOS development which merits discussion is detection. Due to the small sample volumes common to CE, on-column detection is generally required to preserve the integrity of the separation. In this SBFOS design, however, detection is performed externally. Solutes elute into a void volume of the separation capillary housing where they are detected by the axially-configured optical fiber. This arrangement is analogous to the approach Huang *et al.* employed for the positioning of electrodes for electrochemical detection in CE (Huang *et al.*, 1991). While this streamline geometry is well suited for remote analysis, the introduction of dead volume can dramatically compromise the separation efficiency. Although a narrow diameter or tapered fiber could have been inserted into the capillary, placement of a large fiber next to the exit of the capillary was selected for stability. This option also minimized the possibility of multiple internal reflections of the excitation radiation within the bore of the separation capillary. For example, Benoit and Yappert have described a fiberoptic sensor that employs a capillary, functioning as a partially reflecting waveguide, to enhance selectivity (Benoit and Yappert, 1996). If such a waveguide effect were operative in the SBFOS, it would be expected to broaden bandfronts. In SBFOS Design A, by contrast, most of the divergent radiation from the relatively wide optical fiber (200-µm dia.) was excluded from the narrow bore (50-µm dia.) of the separation capillary. Furthermore, since an optical fiber will collect light most efficiently to only a distance of a few diameters from its tip, the off-column configuration merely probed the extremely small

space between the fiber and the capillary plus a sub-mm section of the separation capillary. Again, assuming no waveguide effect, the signal originating from within the capillary would have been insignificant compared to the signal in the void space. This condition permitted the observance of the sharp bandfronts demonstrated by Figures 8.8 and 8.9.

Nevertheless, the sharp bands are a surprising (albeit welcome) result considering the dead volume introduced by the space between the optical fiber and the separation capillary. In order to minimize the dead volume effect, the 250-μm i.d. capillary (as opposed to the large-volume tee joint) was used to house the junction between the axially arranged elements (see Figure 8.2). Even so, the dead volume must have been significant. For example, the entire volume of the 5-cm separation capillary could have been housed by a dead volume produced by a spacing of just two mm between the fiber and the separation capillary. The dramatic effect of spacing is demonstrated by the widely differing frontal mode electropherograms of R6G, shown in Figure 8.10. A relatively sharp bandfront at an elution time of 110 s is observed when the fiber is touching the capillary (Figure 8.10a). In sharp contrast, the bandfront is substantially broadened and the elution time is increased to greater than 1000 s when the fiber spacing is expanded to ≈ 1 mm.

On the other hand, a potential advantage of the increased spacing is an increase in detection sensitivity. As an illustration of this effect, a plot of relative fluorescence versus fiberoptic/capillary spacing is illustrated in Figure 8.11. Signals measured for this plot were generated by drawing a solution of fluorescein into the SBFOS with a syringe. As inferred from this plot, a nearly 300% increase in signal can be expected with a 1-mm spacing; therefore, a suitable compromise between efficiency and

310
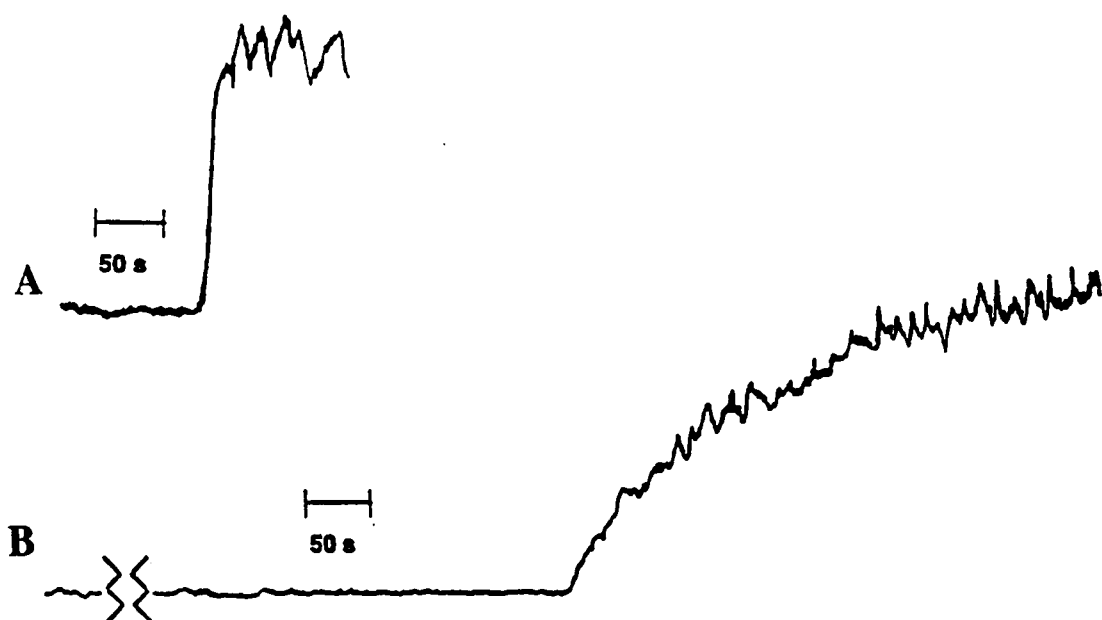
Figure 8.10. Frontal mode CE bandfronts for Rhodamine 6G generated with SBFOS Design B, operated at 4,000 V, with capillary/fiberoptic spacings of approximately a) 0 mm, and b) 1 mm.

Source: M. J. Sepaniak, T. Vo-Dinh, D. L. Stokes, V. Tropina, and J. E. Dickens, *Talanta* **43**, 1889 (1996).
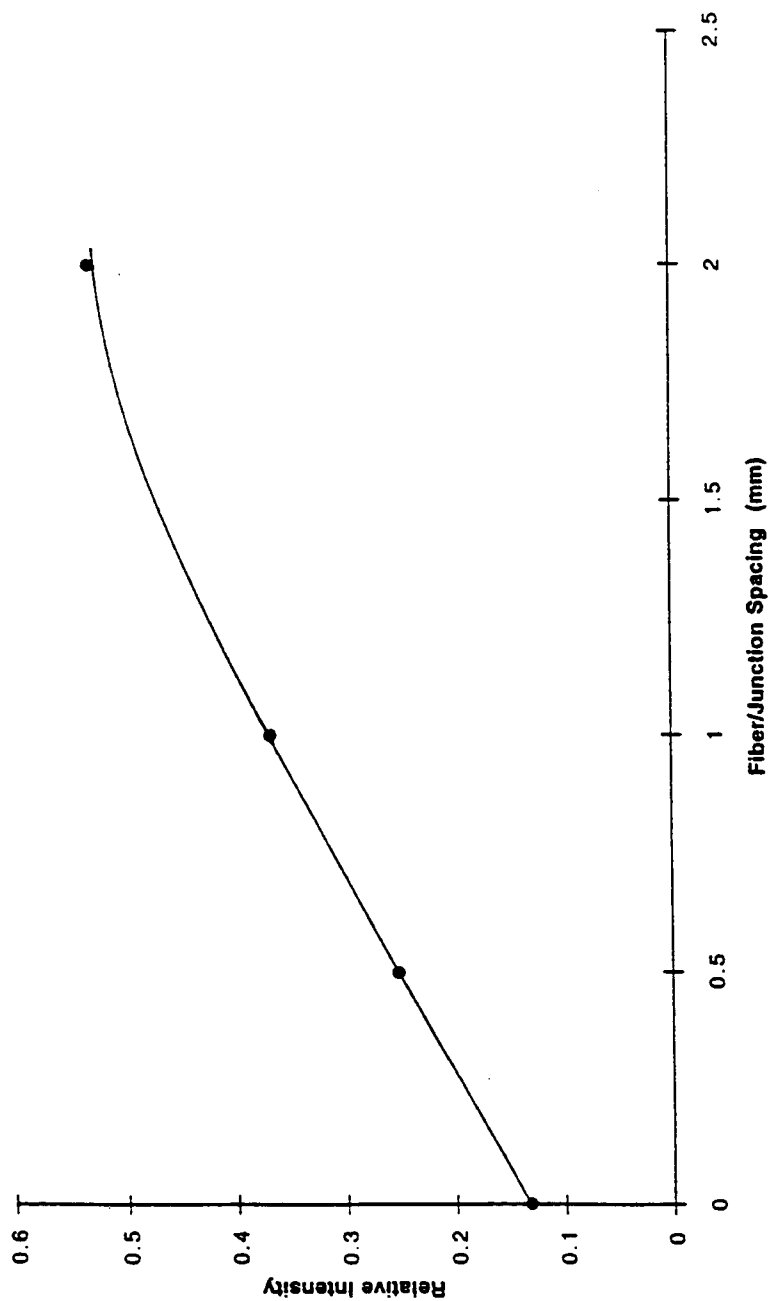
Figure 8.11. Fluorescence intensity plot for sodium fluorescein as a function of capillary/fiberoptic spacing in SBFOS Design A. The signal was generated by drawing a solution of fluorescein into the SBFOS by syringe.

Source: M. J. Sepaniak, T. Vo-Dinh, D. L. Stokes, V. Tropina, and J. E. Dickens, *Talanta* **43**, 1889 (1996).

detectability should be determined for a given application. In any case, it is clear from these results that stable positioning of the fiber relative to the capillary is imperative for reproducible performance in terms of efficiency, migration time and signal intensity. Unfortunately, slippage of the fiberoptic was occasionally observed with Design A. This variability could have been yet another factor in the poor reproducibility. In fact, the reproducibility was so poor that extensive fundamental studies of this design were bypassed as the development of a new design, SBFOS Design B, was quickly pursued.

SBFOS Design B. The salient feature of Design B was the low-volume, nonmetallic, PEEK tee joint. This modification addressed and minimized the major problems associated with Design A. For example, the nonmetallic tee enabled electrical isolation of the detection-side electrode from the vicinity of the capillary/fiberoptic junction, thereby preventing the formation of electrolysis gases within the tee. In addition, the detection-side electrode was positioned external to the side arm restrictor capillary, thus enabling gases formed at the electrode to escape into the atmosphere. The flangeless fittings permitted stable and reproducible positioning of the fiberoptic relative to the separation capillary. This feature, combined with the low volume of the tee, allowed efficient flushing of the sensor and expulsion of residual air pockets (especially since the flangeless fittings could be loosened for expulsion of bubbles and retightened without significantly altering the fiberoptic/capillary spacing). All of these factors combined to help minimize the variable trial-to-trial pressure-driven hydrostatic flow associated with Design A. As a result, much improved reproducibility was observed with Design B. For example, for five repetitive trials the RSD for retention times of R6G and fluorescein was observed to be less than 10% for various applied voltages in the 2000-2500 V range.

313

A possible disadvantage of Design B was the 500-μm bore of the tee joint which housed the junction between the fiberoptic and the separation capillary (see Figure 8.3). The increase in junction diameter, relative to the 250-μm diameter junction of Design A, could have exacerbated the dead volume effect of the spacing between the fiber and the capillary. For example, a Design B separation of R6G and fluorescein under optimum conditions is illustrated in Figure 8.12 (generated with Optical System I). In this case, the efficiency for the R6G band was only 3000 plates (in comparison to the possibly overestimated 8000 plates reported for Design A), even though the separation capillary length was increased from 5 to 8 cm. Nevertheless, an increased resolution of 7 was observed for this separation. The improved reproducibility was deemed to far outweigh any shortcomings of Sensor B relative to Sensor A.

The improved reproducibility furthermore enabled detailed fundamental evaluations of SBFOS Design B. For example, a voltage study was performed for the separation of R6G and fluorescein. The results are listed in Table 8.1, including observed current, solute band velocities with reproducibilities (N=5), efficiency, and resolution. It is noteworthy that the applied voltage was divided across the separation capillary, the restrictor capillary, and the fiber/capillary junction. Since the latter factor was not well defined, it was not possible to accurately assign a field strength to the separation capillary or to calculate solute or electroosmotic mobilities. The applied voltage was varied between 1500 V and 3000 V. Excessive and sporadic current was observed for the 3000 V trials, routinely causing the system to fail before data could be acquired. Conversely, the sensor functioned steadily at an applied voltage of 2500 V. However, the data in the table illustrate that the current increase relative to the 1500-V trials was considerably more than the expected 67% (Ohm's law predicts a linear relationship between potential and current, $E=IR$). This anomalous current, along with the decrease

314
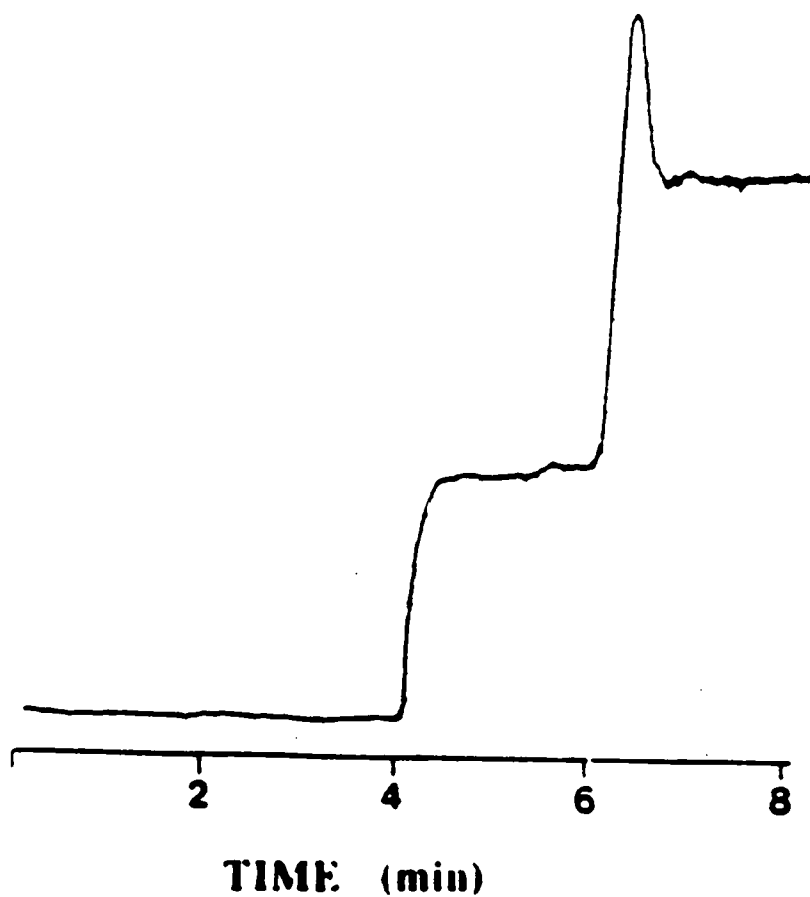
Figure 8.12. Frontal mode CE separation of Rhodamine 6G and sodium fluorescein (both 5 $\times 10^{-5}$ M), generated with SBFOS Design B operated at 1,500 V.

Source: M. J. Sepaniak, T. Vo-Dinh, D. L. Stokes, V. Tropina, and J. E. Dickens, *Talanta* **43**, 1889 (1996).

315

Table 8.1. Effect of applied voltage on separations of fluorescent dyes performed with SBFOS Design B

Voltage (v)	Current (µA)	Rhodamine 6G bandfront		Fluorescein bandfront	
		V_b (cm/min)	N	V_b (cm/min)	R_s
1500	90	1.1 (±9%)	≈3000	0.66 (±7%)	≈7
2500	250	1.8 (±18%)	≈1000	0.83 (±24%)	≈9

Source: M. J. Sepaniak, T. Vo-Dinh, D. L. Stokes, V. Tropina, and J. E. Dickens, *Talanta* **43**, 1889 (1996).

in bandfront sharpness (the efficiency decreased approximately by a factor of 3), indicated excessive thermal load due to joule heating at the higher applied voltage. The decreased reproducibility in solute band velocities observed for the higher applied voltage was probably due to a combination of heating effects and a lack of integrity in the conduction paths (perhaps due to periodic, highly localized boiling of the running buffer solution).

A GHF-restricting capillary was also used in this design, and the improved reproducibility of Design B allowed a more concrete evaluation of the effectiveness of the restrictor capillary. In this case, the 3-cm segment of 15-μm i.d. capillary should have reduced GHF by a factor of 4. Nevertheless, evidence of hydrostatic flow is apparent from the data in Table 8.1. For example, as the applied voltage is increased from 1500 to 2500 V the resolution increases despite a decrease in efficiency. This unusual behavior is the result of the differences in net mobility, $\mu_{eo} + \mu_e$, for the two bands. The net mobility of the fluorescein anion is nearly four times less than that of R6G cation (as determined from the conventional electropherogram of Figure 8.7). In the case of R6G, when the voltage is increases from 1500 to 3000 V, the band velocity nearly increases by the expected 67% (as predicted by Equation 8.1). Conversely, the impact of v_{hy} on v_b is much more significant for the fluorescein, as the corresponding increase in band velocity is much less than 67%. The net effect is a greater separation between the bandfronts of the two dyes at the higher applied voltage.

Having discussed the major challenges confronted in developing an effective SBFOS design, and having evaluated the measures taken to overcome them in Design B, it is now worthwhile to address some more subtle complications inherent with the frontal mode of operation. The frontal mode is compatible with remote, *in situ* analysis, a primary goal

317

of the SBFOS technology. However, this mode of operation can affect both the detection and separation characteristics of the SBFOS. For example, as each new bandfront elutes from the separation capillary, the baseline of the electropherogram increases along with the associated fluorescence noise. As a result, both the dynamic range and the detectability are limited with respect to the CZE mode of separation. Furthermore, the running buffer becomes displaced by the sample medium as the separation proceeds. Reagent depletion can occur at some point of frontal-mode CE separations depending on the EOF. For the simple case of natural ionic fluorophores which require no on-column derivatization or complexation for detection or electromigration, reagent depletion is not a complication. However, displacement of the running buffer by the sample medium can alter the EOF, thereby complicating retention time calibration. This problem can be accentuated for *in situ* analyses in which the ionic strength of the sample medium can differ from that of the running buffer. Because these fundamental studies were performed with dyes prepared in the running buffer solution, the potential complications of the frontal mode of operation were not severe enough to warrant discussion. This topic will be revisited in the "Applications" section of this chapter.

SBFOS Design C. The key salient feature of Design C was the "zero-volume" quartz tee. Like the PEEK tee of Design B, this nonmetallic tee enabled electrical isolation of the detection-side electrode. Relative to PEEK tee of Design B, the quartz tee reduced the bore diameter housing the fiber/capillary junction from 500 μm to approximately 365 μm, thereby reducing the dead volume of the junction spacing (though still not to the extent enabled with Design A). An additional advantage, particularly for fundamental studies, was the transparency of the tee joint. This feature permitted visual identification of the sources of problems encountered in previous designs, such as probable points of gas formation and collection. The transparent tee also enabled the

318

confirmation of the role of interior gases in the generation of hydrostatic pressure and unstable currents. Finally, visual inspection facilitated the determination and implementation of the proper positioning and spacing of sensor elements within the tee during fabrication. Another unique feature of Design C was the 100-μm core fiber. Otherwise, the 25-μm x 3-cm restrictor capillary should have decreased the GHF by a factor of 1.5. In general, all measures taken to enable the improved performance of Design B were also applied to Design C.

All fundamental evaluations of Design C were performed with Optical System II, and the 543.5-nm He-Ne laser source. Figure 8.13 illustrates the excellent reproducibility in both the retention times and intensities for 10^{-4} M R6G bandfronts generated by Design C. The operating potential was 1500 V. The RSDs for the retention times and band intensities were 6% and 5%, respectively. Furthermore, efficiencies in the 10,000-20,000 plate range were routinely observed for R6G bandfronts generated by this sensor. Because of these unsurpassed results, extensive fundamental evaluations were pursued.

A voltage study was performed for the 1000 V - 6500 V range, a much larger operation range than obtainable with previous designs. Figure 8.14 illustrates the observed current as a function of applied voltage. Each point represents an average of three trials. As demonstrated, Design C exhibited practically linear behavior in the 1000 to 5500 V range. The positive departure from linearity at higher voltages could have been the result of joule heating. This heating effect could have reduced the viscosity of the running buffer, thus increasing its conductivity. Another interesting feature of Figure 8.14 is the overlay of data from different dates. The compatibility of these data reflect commendable day-to-day reproducibility. In fact, a day-to-day reproducibility study

319
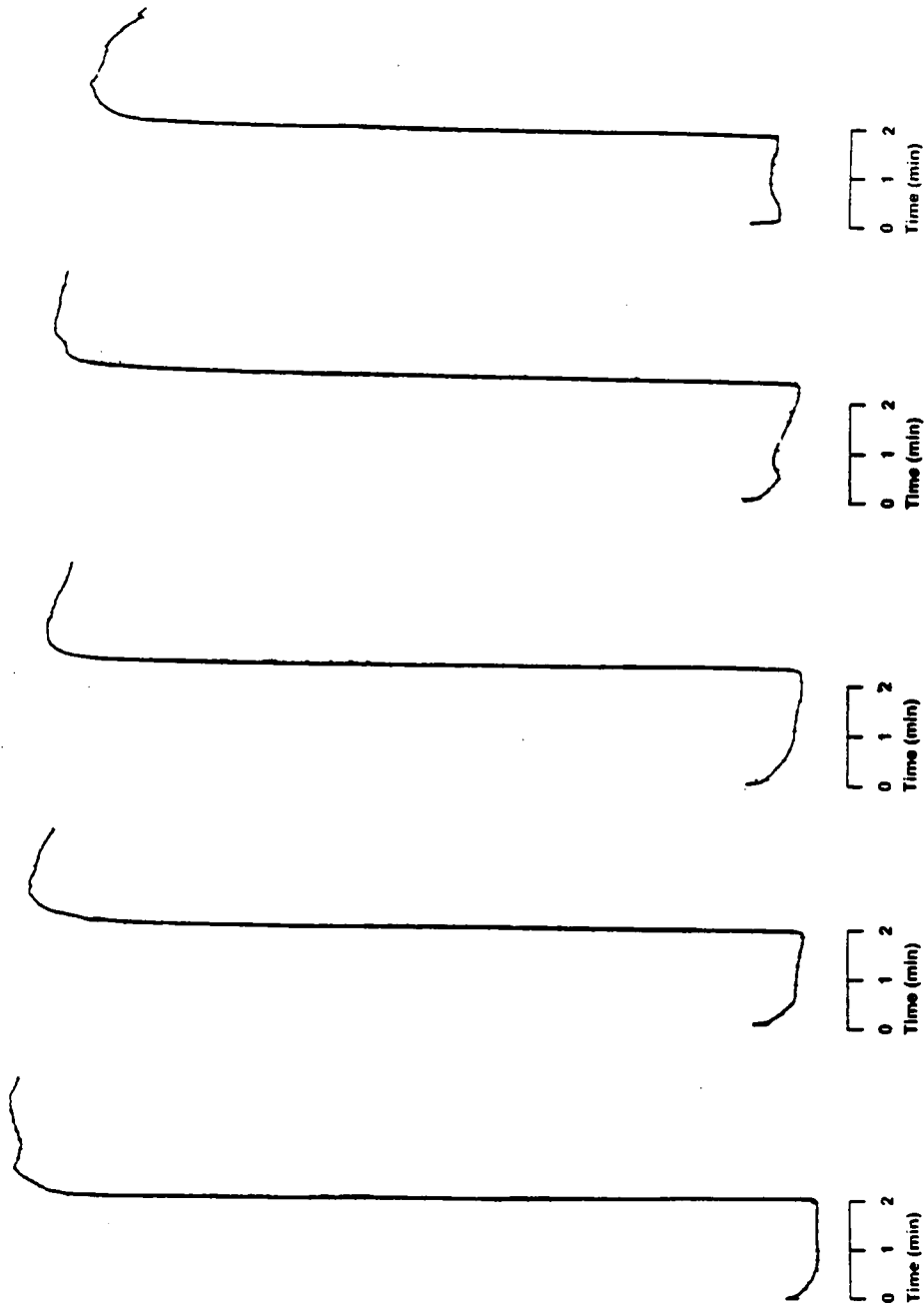
Figure 8.13. Repetitive frontal mode CE bandfronts for Rhodamine 6G (10^{-4} M) generated with SBFOS Design C, operated at 1,500 V, illustrating excellent reproducibilities for both retention times and bandfront intensities.
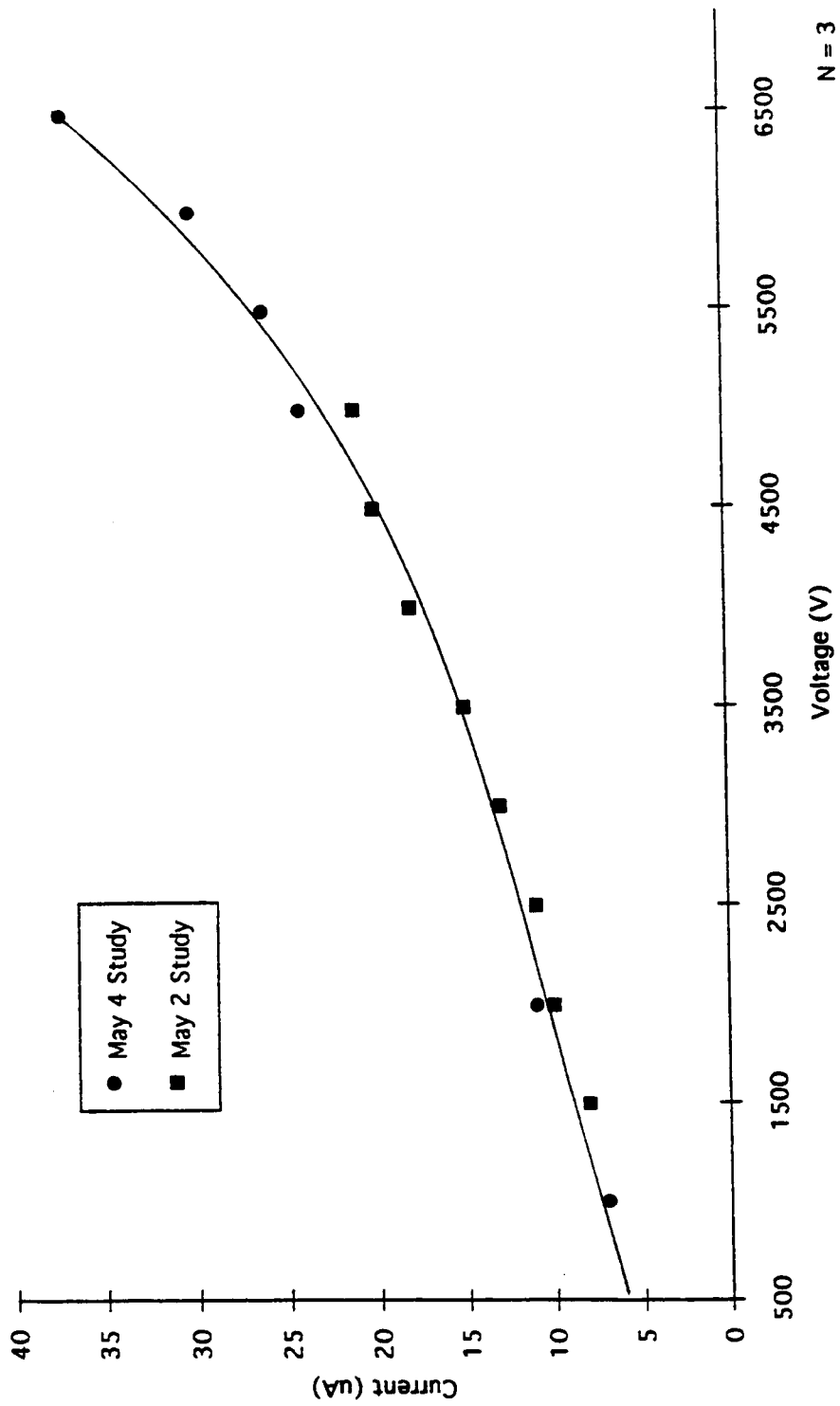
Figure 8.14. Plot of observed current as a function of potential applied to SBFOS Design C.

was performed over a 9-day period. The current was measured for an applied voltage of 2000 V. With three measurements acquired per day on six separate days, the RSD for the observed current was only 6%.

As a continuation of the voltage study, Figure 8.15 illustrates the bandfront elution times for Rhodamine-6G as a function of applied voltage. Linear behavior was not observed for the range investigated, as would have been expected according to Equation 8.1. On the other hand, the curve reflects the presence of a constant hydrostatic flow velocity, v_{hy}, which opposes the electrophoretic solute band velocity, v_{elec}. While v_{hy} is independent of the applied potential, v_{elec} (the sum of EOF velocity and solute migration velocity) ideally increases linearly with applied potential. If this behavior existed in this study, the constant v_{hy} would have become a more significant fraction of v_{elec} at the lower applied potentials, resulting in significantly longer band elution times than would have been expected in the absence of v_{hy}. In fact, a plot of the ratio of a $v_{hy}:v_{elec}$ as a function of applied potential would closely resemble the plot in Figure 8.15 if v_{hy} were constant, and if v_{elec} exhibited the linear behavior predicted by Equation 8.1. Regardless of the general lack of linearity, particularly in the 1000-2000 V range, the reproducibility of the sensor justifies elution time calibration based on the curve. For example, the curve is an overlay of data acquired on two separate days, yet data points (N=3) from both dates adhere well to the curve, even in the region of least linearity. In fact, a day-to-day reproducibility study was also performed for R6G bandfront elution times at an applied voltage of 2000 V over the 9-day period described above. Again, with three measurements acquired per day on six separate days, the RSD for the observed bandfront elution time was 20%.
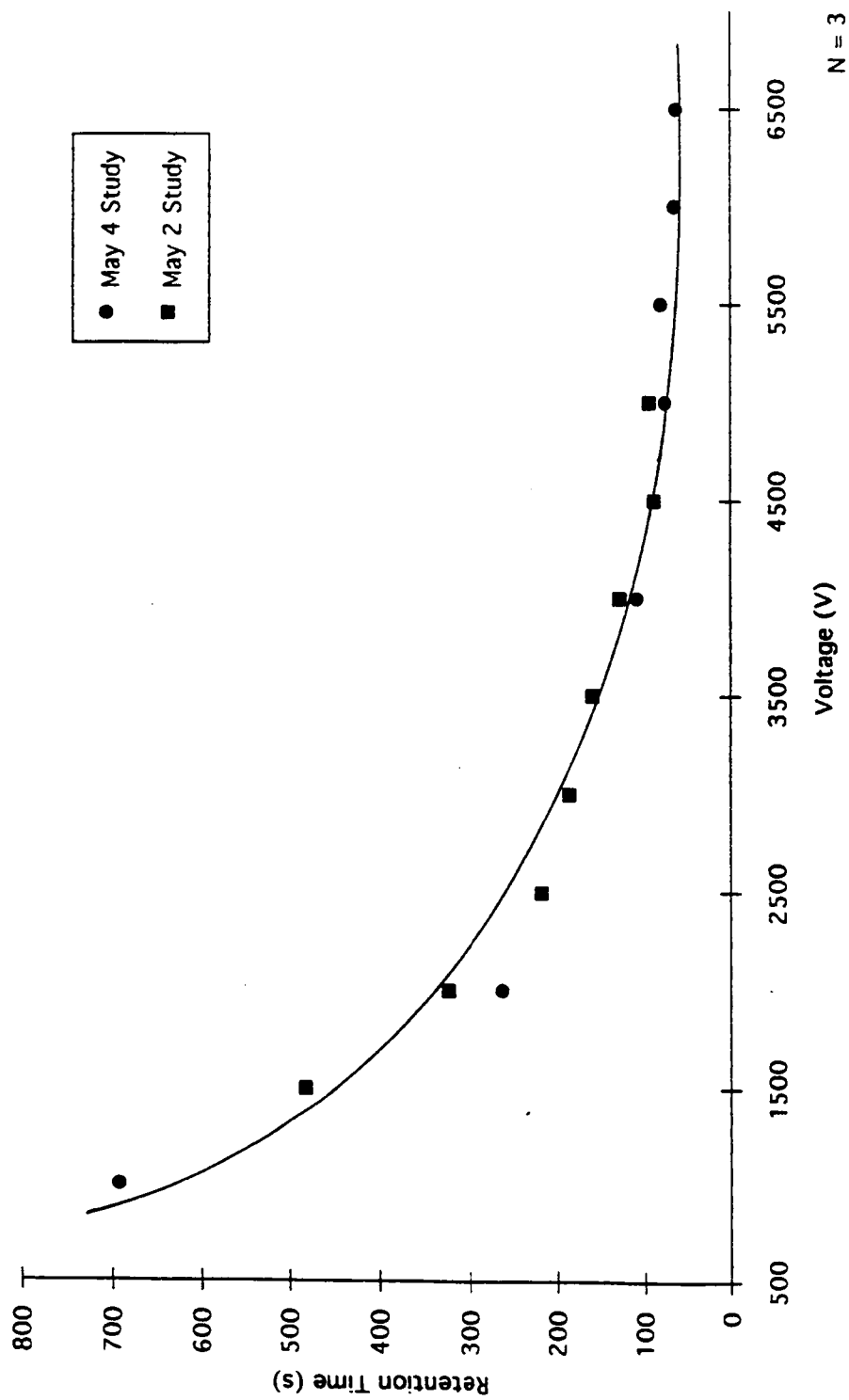
Figure 8.15. Plot of frontal-mode CE elution times for Rhodamine 6G (10^{-4} M) as a function of potential applied to SBFOS Design C.

323

As a demonstration of Design C separation capability, Figure 8.16 illustrates the electropherogram of a mixture of R6G (0.01 mM) and FITC (0.2 mM), generated with an applied potential of 6000 V. Although this applied field approached the upper limit of the useful operating potential range, sharp and fully-resolved bandfronts were observed, requiring a trial time of only 7 min. A voltage study was also performed for this dye mixture. The results are illustrated in Table 8.2, including band elution times, efficiencies, and currents. It is important to note that this study was performed on a different Design C sensor than that performed for the single-component (R6G) study discussed above. In this case, a 5-cm segment of 25-μm i.d. restrictor capillary was used. This factor may account for the generally lower currents observed relative to the previous voltage study, resulting from the increased resistance introduced by the longer restrictor capillary. Adhering to the discoveries cited in the SBFOS Design A evaluations, the generally longer elution times and decrease in efficiencies (up to 8000 plates) relative to the previous single-component study implies that this second Design C sensor had a larger fiberoptic/separation capillary junction spacing. Regardless of the variability in performance between the two Design C sensors, both sensors performed competitively with respect to the Design A and B sensors. While ideal for fundamental studies, some aspects of Design C made it impractical for field applications. For example, the quartz tee was relatively fragile and expensive. Furthermore, the permanent bonding of the sensor elements to the quartz tee made their replacement a difficult task. Breakage or failure of the detection capillary or optical fiber would often have rendered the quartz tee useless. For these reasons, Design B was selected for further applications studies.
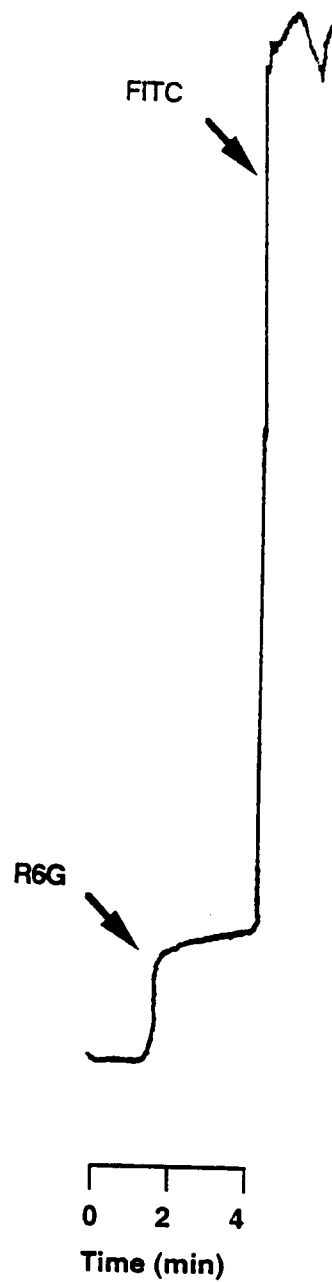
Figure 8.16. Frontal mode CE separation of Rhodamine 6G (0.01 mM) and FITC (0.2 mM), generated with SBFOS Design C operated at 6,000 V.

325

Table 8.2. Voltage study: separations of Rhodamine 6G (RG6) and FITC performed with SBFOS Design C

Voltage (V)	R6G			FITC			Current
	t_r (min)	(RSD)	N_{total} (RSD)	t_r (min)	(RSD)	N_{total} (RSD)	(±1 µA)
8000	1.12	(2.59%)	8000 (60%)	4.2	(18%)	200 (70%)	11.5
7000	1.35	(3.70%)	3400 (20%)	4.4	(7.0%)	300 (40%)	1 0
6000	1.81	(1.27%)	1800 (22%)	4.9	(6.1%)	500 (30%)	8.5
5000	2.41	(0.96%)	5000 (30%)	7.0	(1.7%)	500 (30%)	6.5
4000	3.37	(1.71%)	5000 (30%)	9.6	(2.1%)	690 (12%)	4.5
3000	4.93	(1.17%)	4200 (15%)	15.7	(0.64%)	1200 (29%)	2.5
2000	8.1	(3.7%)	4000 (44%)	30	(3.9 %)	1300 (44%)	1.5
1000	25	(N=1)	1500 (N=1)				

N=3

APPLICATIONS

A key advantage of the incorporation of CE in separations-based sensing is its versatility. A vast range of retention properties can be imparted on a single CE system by quick and easy modification of the running buffer with such additives as micelles, cyclodextrins, organic modifiers, metal ions, linear hydrophilic polymers, complexing ligands, crown ethers, and various zwitterionic substances (Terabe *et al.*, 1984; Holland and Sepaniak, 1993; Sepaniak *et al.*, 1992a; Grossman and Colburn, 1992; Nishi, 1997; Sarmini and Kenndler, 1997). As a result, a single CE-based SBFOS could potentially be used for separations of mixtures of both charged and neutral compounds ranging from small inorganic ions through large proteins and nucleotides. As a demonstration of the potential versatility of the CE-based SBFOS, several applications were pursued, including the separation and detection of nonfluorescent metal ions via on-column complexation with HQS, and the separation of neutral derivatized amines via micellar electrokinetic capillary chromatography.

Nonfluorescent Metals

A CE protocol previously developed for on-column labeling of metals with HQS (Swaile and Sepaniak, 1991a) has been adapted for use with the SBFOS. HQS is a non-fluorescent, bidentate ligand which undergoes a dramatic increase in quantum efficiency when complexed with a large number of metals. In addition to facilitating sensitive detection, the complexation conditions can be adjusted to affect the mobility of a metal ion (Swaile and Sepaniak, 1991a). The SBFOS strategy involves first flushing the sensor with a running buffer modified with an appropriate concentration of HQS. The magnitude of EOF is adjusted to outweigh the negative velocity of the anions. Upon

327

application of the electric field, the metal cations and the negative HQS molecules both migrate away from the positively-biased, sample-side electrode and towards the optical fiber; however, the HQS migration rate is much slower. The metal ions collide with the HQS molecules and form complexes. As a result of the complexation, the effective migration rate of the metal ion is reduced due to the reduced charge of the complex relative to the free metal. Furthermore, due to the large complex formation constants involved, an equilibrium is established which includes various forms of the metal complex. The dynamics of these processes influence the sharpness and shapes of the bandfronts, which migrate at rates characteristic of the metals.

Figure 8.17 is an electropherogram of a calcium/magnesium (in order of elution) sample generated with SBFOS Design B via on-column complexation with HQS. A 5-cm section of 25-μm i.d. capillary was used for GHF restriction. Optical System II was used with a He-Cd laser. The applied potential was 1500 V. As was previously discussed, *in situ* analysis with on-column complexation or derivatization can be complicated by reagent depletion or changes in column conditions as the sample medium displaces the running buffer. This application is one in which such complications can be significant. Nevertheless, no evidence of reagent depletion is demonstrated by the electropherogram in Figure 8.17. Although the separation time illustrated by this figure is quite long, this condition relaxes the nonequilibrium condition caused by the high complex formation constant. As a result, the bandfronts are very sharp (regardless of the long elution time). In any case, the wide separation between the metal ion bandfronts indicates that a shorter column could have been used to reduce the analysis time.

An SBFOS-generated electropherogram of a calcium-containing ground water sample is illustrated in Figure 8.18. Sensor conditions were the same as those for the previous

TIME (min)
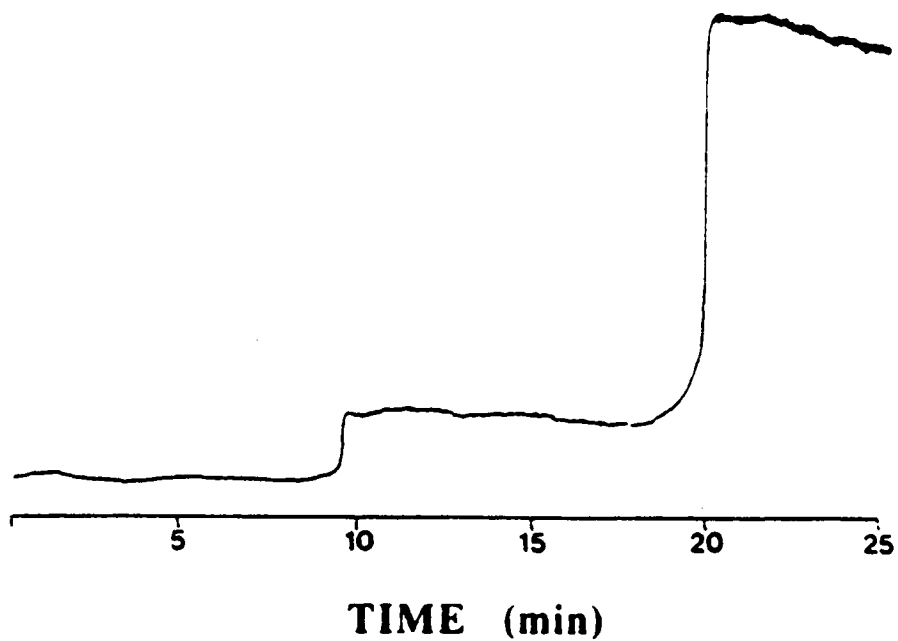
Figure 8.17. Frontal mode CE separation of calcium (0.5 mM) and magnesium (0.1 mM), generated with SBFOS Design B (1,500 V) via on-column complexation with 2.5 mM HQS.

Source: M. J. Sepaniak, T. Vo-Dinh, D. L. Stokes, V. Tropina, and J. E. Dickens, *Talanta* **43**, 1889 (1996).
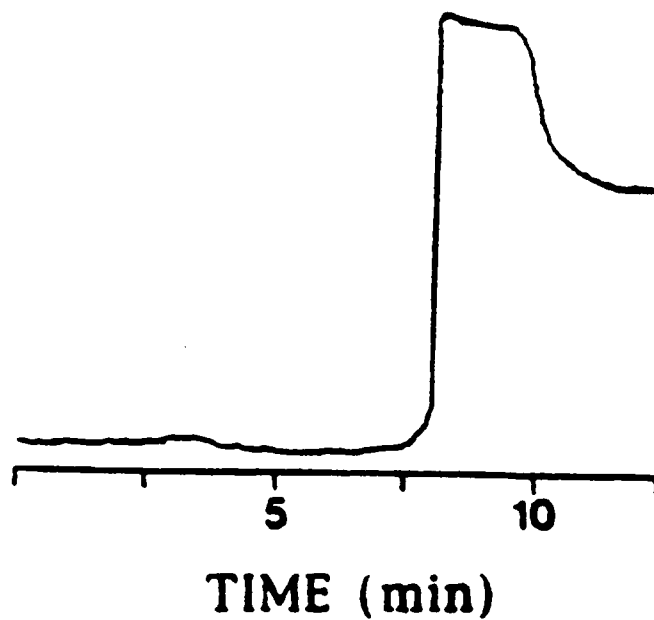
Figure 8.18. Frontal mode CE electropherogram of a calcium-containing groundwater sample, generated with SBFOS Design B (1,500 V) via on-column complexation with 2.5 mm HQS.

Source: M. J. Sepaniak, T. Vo-Dinh, D. L. Stokes, V. Tropina, and J. E. Dickens, *Talanta* **43**, 1889 (1996).

metal ion electropherogram, yet the calcium bandfront eluted sooner for the groundwater sample trial. This result could have been caused by the displacement of the reagent buffer by the sample medium, thereby possibly changing the pH or ionic strength of the solution within the capillary. Such changes can influence the EOF and hence result in varying elution times. Furthermore, a variation in ionic strength between the running buffer and the sample medium can lead to sample stacking. This condition may explain the dual-plateau shape of the calcium bandfront. Such effects were not observed in the previous metal ion separation because the sample was prepared in the running buffer solution (minus HQS).

Neutral Organic Compounds

As another demonstration of the versatility of the SBFOS technology, it was applied to the analysis of neutral compound mixtures which could not be separated with conventional CE conditions (unmodified buffer). This feat was accomplished via MECC with SDS. Focusing purely on the separation aspect of the SBFOS, pre-column derivatized amines were investigated first. The derivatization step was necessary to label the nonfluorescent amines with the fluorophore, NBD. Implementing a precolumn mode of derivatization, complications arising from reaction kinetics were bypassed. This procedure, though not amenable to *in situ* analyses, facilitated initial fundamental evaluations in terms of separation performance.

Neutral solutes are separated in MECC based on their distribution between the EOF-transported running buffer and the electrophoretically (negatively charged) micellar phase (Terabe *et al.*, 1984; Sepaniak *et al.*, 1992a). The distribution factor is formally referred to as the capacity factor, k'. Generally, solutes that are not solubilized by the

micelles should migrate with the same velocity as the EOF and elute at t_0. At the other extreme, completely solubilized solutes should migrate at the micelle velocity, thus eluting at time t_{mc}. The time span between t_0 and t_{mc} is the elution window for separation. The capacity factor can be expressed in terms of experimentally determined values, t_0, t_{mc}, t_r, as follows:

$$k' = \frac{t_r - t_0}{t_0 \left(1 - \left(\frac{t_r}{t_{mc}}\right)\right)} \qquad (8.2\ )$$

where t_r is the solute band retention time. Under ideal conditions, the retention time is expressed as a function of k':

$$t_r = \frac{L^2}{V(k'+1)[\mu_{mi}k' + \mu_{eo}]} \qquad (\ 8.3\ )$$

where μ_{mi} is the micellar electrophoretic mobility. This study was performed with SBFOS Design B, using a 5-cm x 25-μm i.d. restrictor capillary. As was pointed out in the fundamental evaluations of this design with fluorescent dyes, a constant hydrostatic flow velocity, v_{hy}, is associated with this design. A more accurate expression for t_r is therefore:

$$t_r = \frac{L^2}{V(k'+1)[\mu_{mi}k' + \mu_{eo}]} + \frac{L}{v_{hy}} \qquad (8.4)$$

Figure 8.19 illustrates frontal-mode separations of the derivatized amines, NBD-methylamine (0.4 mM), NBD-ethylamine (0.3 mM) and NBD-n-proplyamine (0.1 mM), with applied voltages of 2, 3, and 4 kV. Optical system II was used for detection with the 488-nm air-cooled argon ion laser. In spite of the potential efficiency-diminishing effect of v_{hv}, signals from each component were distinguished for all applied voltages illustrated by the figure. Furthermore, reagent depletion was not a factor in the separation of these compounds, even though the on-capillary SDS-laden buffer solution was being displaced by the sample medium (which did not contain SDS). Indeed, up to five-components have been resolved before reagent depletion using this system, thus demonstrating the feasibility of implementing MECC for *in situ* analysis with the SBFOS technology.

In contrast to all other sensors described in this chapter, this sensor utilized a 0.66-NA optical fiber. The greater light gathering capability should have yielded improved detection sensitivity. This system was thus selected for an LOD determination. As was discussed earlier, an inherent complication of the frontal mode of detection is a sacrifice in both linear dynamic range and detectability due to the fact that each bandfront contributes background and concomitant noise to subsequent bandfronts. To determine the extent of this effect for the SBFOS, LODs were determined for NBD-n-propyl amine as both a single component, and in the presence of the other two NBD-amines (at concentrations similar to that of the NBD-n-propyl amine). Calibration curves for the two experiments are illustrated in Figure 8.20. In spite of the possible complications of frontal mode detection, the linear dynamic range for both plots was more than 2 orders of magnitude. Furthermore, the LOD for both conditions was just under 80 nM,
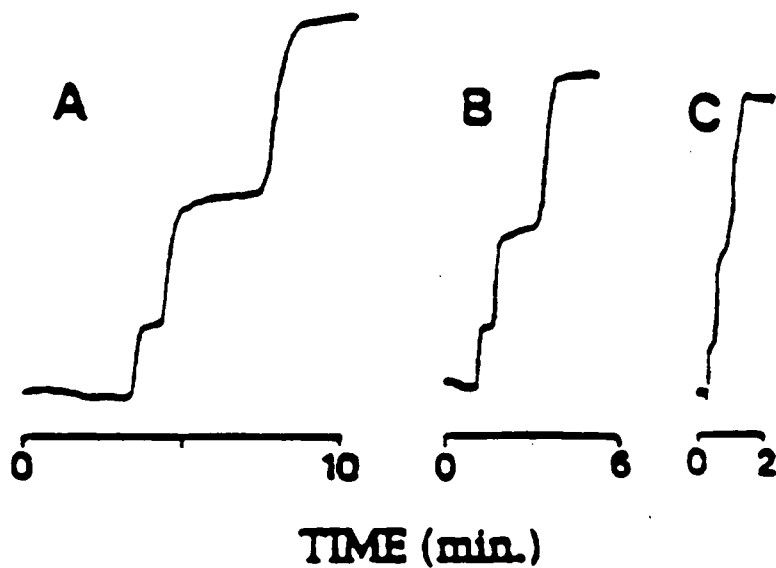
Figure 8.19. Frontal mode CE separations of a ternary mixture of the derivatized amines, NBD-methylamine (0.4 mM), NBD-ethylamine (0.3 mM), and NBD-*n*-propylamine (0.1 mM), generated with SBFOS Design B at applied voltages of a) 2,000 V, b) 3,000 V, and c) 4,000 V.

Source: M. J. Sepaniak, T. Vo-Dinh, V. Tropina, and D. L. Stokes, *Anal. Chem.* **69**, 3806 (1997).

334
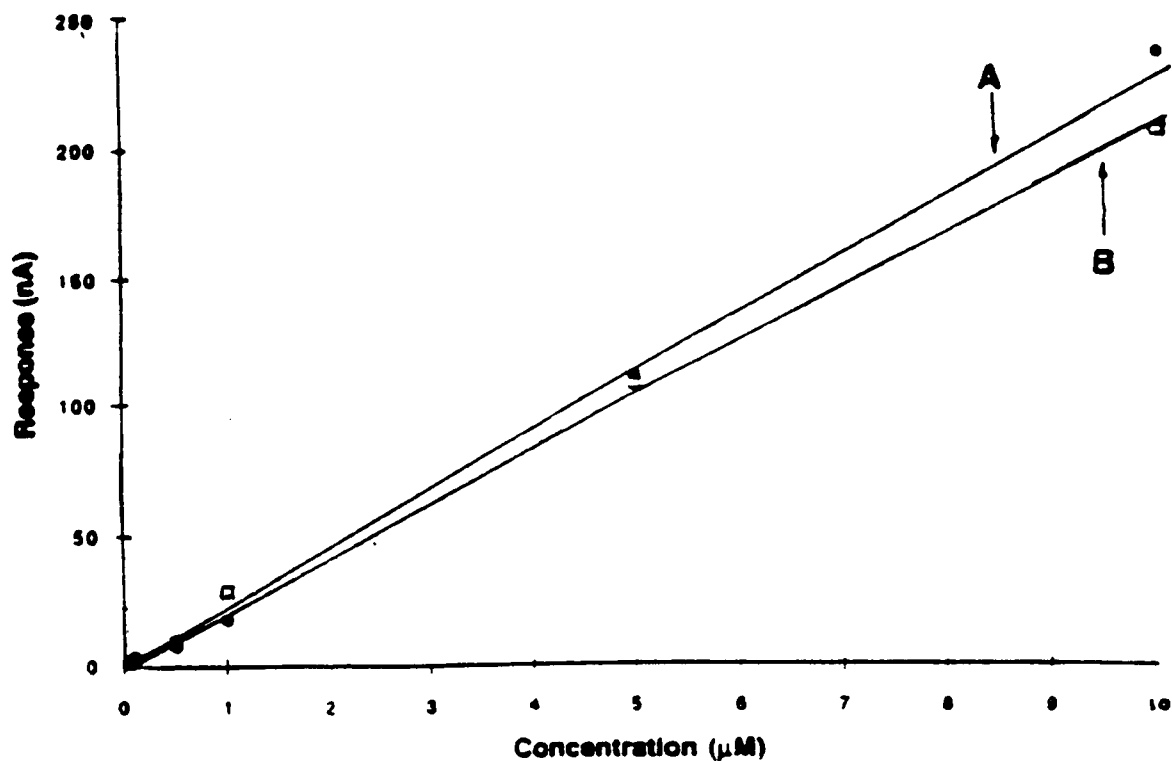
Figure 8.20. Calibration curve for the detection of NBD-*n*-propylamine in a) a single-component sample, and b) a ternary mixture sample (NBD-methylamine, -ethylamine, -*n*-propylamine), generated with SBFOS Design B at an applied potential of 2,500 V.

Source: M. J. Sepaniak, T. Vo-Dinh, V. Tropina, and D. L. Stokes, *Anal. Chem.* **69**, 3806 (1997).

335

assuming the minimum detectable concentration to yield a signal of 3 times the standard deviation of the noise.

MISCELLANEOUS MODIFICATIONS TO GENERAL DESIGNS

In closing this chapter, the following section briefly summarizes some minor modifications that were pursued, but either failed or were scarcely characterized. Nevertheless, they merit mention for continuing studies.

Coaxially-Applied GHF Restriction

A coaxially-arranged GHF-restriction design was investigated in order to preclude the need for the side arm restriction, thereby further streamlining the sensor. A schematic diagram of the design is illustrated in Figure 8.21. A 50-μm i.d./365-μm o.d. x 8-cm separation capillary was centered and cemented within a 520-μm i.d. capillary. A 200-μm core optical fiber was inserted into the opposite end of the large-bore capillary, placed against the elution end of the separation capillary, centered, and fixed in place by a silicate frit The silicate frit was formed *in situ* with a 2-W, 514-nm laser beam. Sephadex particles (20-80 μm dia.) were injected into the large bore capillary as a suspension pumped with a syringe. The porous frit blocked microparticles from the fiberoptic/separation capillary junction while allowing the liquids to flow on through the separation capillary.

This design never worked. Massive bubble formation was consistently observed in the region of the Sephadex particles upon application of electrical fields of any practical

Metallic Tee Upstream to Provide
Flow and Electrical Contact

Encasement
Capillary
(~ 500 μm i.d.)

Axial Flow

Axial Flow

hν

Optical Fiber
200 μm core

Variable Depth
Flow Restricting
Packing

In-Situ Sodium
Silicate Frit

Epoxy

Separation
Capillary
(360 μm o.d.)
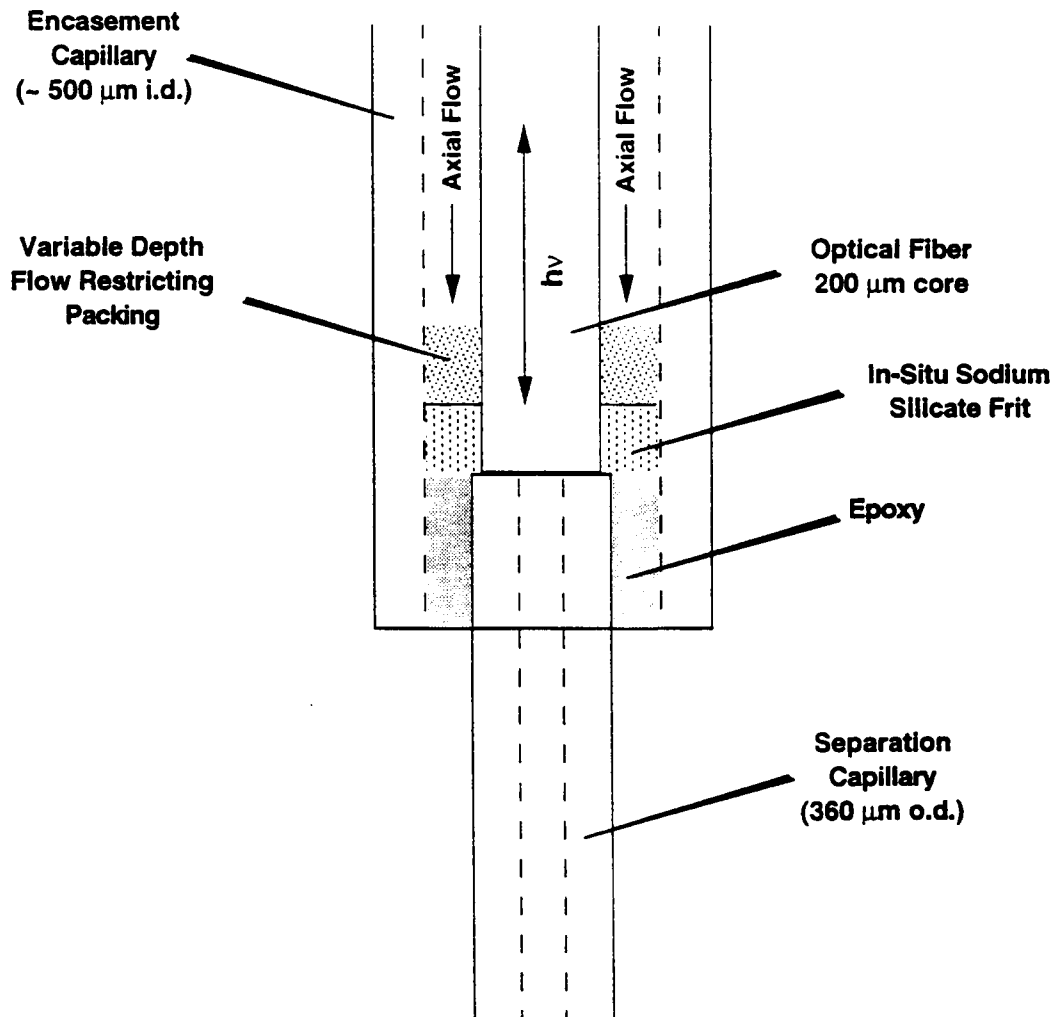
Figure 8.21. Coaxially-applied GHF restriction design for SBFOS.

337

magnitude. Perhaps the electric fields were concentrated at the microbody surfaces, thus causing localized joule heating.

Sample-Side Restriction

A sample-side restriction design for sample streamlining is illustrated in Figure 8.22. An 8-cm segment of 50-μm i.d/150-μm o.d. capillary was the separation capillary, while a 3-cm segment of 15-μm i.d./150-μm o.d. capillary served as the GHF-restricting capillary. The two capillaries were coupled within the bore of a 250-μm i.d. capillary. With the separation and restrictor capillaries in direct contact and centered, they were fixed in place with epoxy. The unaltered end of the separation capillary was coupled to the PEEK tee of SBFOS Design B, using the respective procedure described in the sensor fabrication section.

The sample-side detection design was tested with neutral FITC (0.1 mM), to confirm the reduction of GHF. A voltage study of the 5000-7000 V range was performed. The results are illustrated in Table 8.3. Five trials were performed at each voltage. While a nearly linear trend of current as a function of applied potential was observed, the corresponding band elution time trend was far from linear. Nevertheless, respectable reproducibility in terms of band elution time was observed. Unfortunately, fabrication of this design was difficult. The ideal union of the two capillaries would have required squarely polished tips and perfect alignment of the capillary bores. In reality, there was often a gap which introduced void volume and produced an air pocket in the housing sleeve during the high-pressure column pretreatment steps. This air pocket was exceedingly difficult to remove. This design was not extensively tested because of these factors.

To PEEK Tee

Ferrule

PEEK Tubing

Separation
Capillary
(50-μm i.d x
150-μm o.d. x 8 cm)

Junction
(250-μm i.d. sleeve)

Restrictor
Capillary
(15-μm i.d. x
150-μm o.d. x 3 cm)
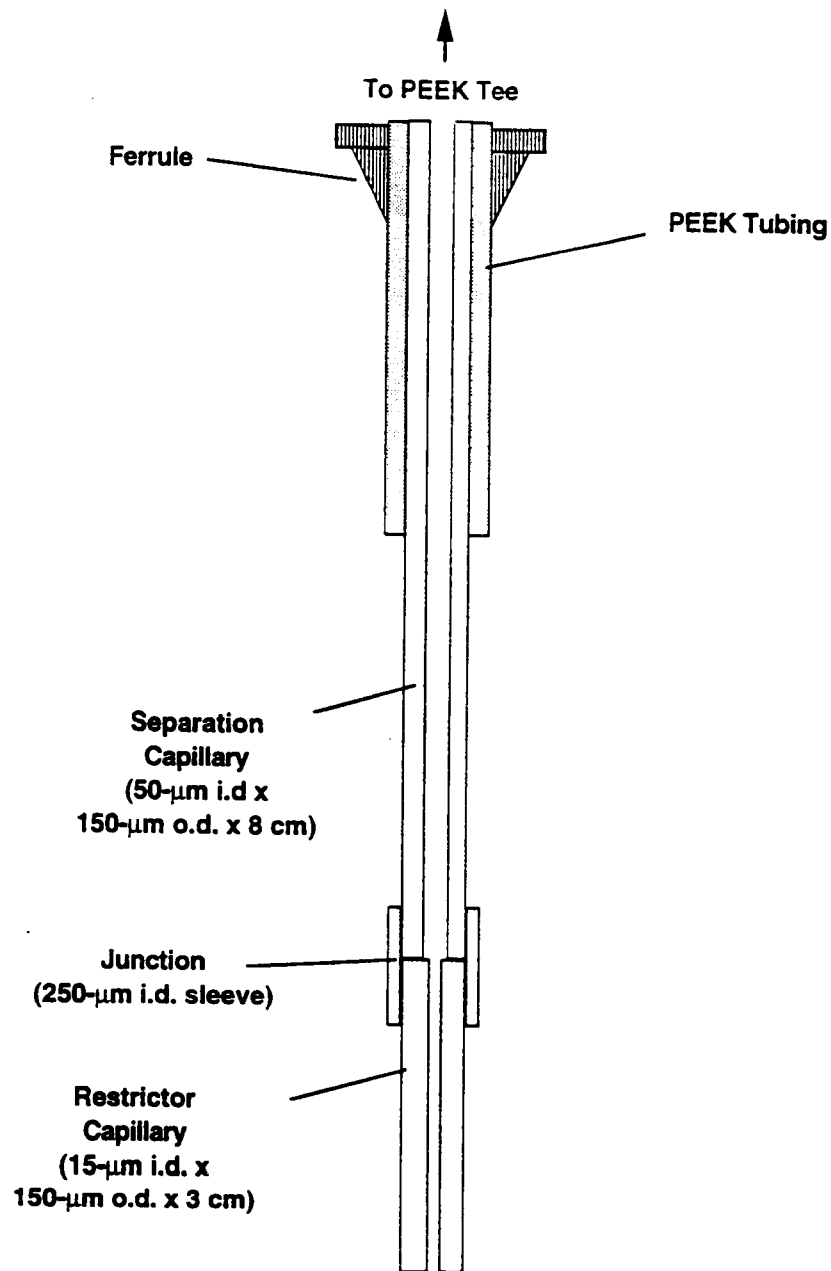
Figure 8.22. Sample-side GHF restriction design for SBFOS.

339

Table 8.3. Voltage study for sample-side restriction design

Voltage (V)	Current (µA)	t_r (min)	(RSD)	N_{total}	(RSD)
5000	5 ± 1	25	(7%)	3000	(30%)
6000	8 ± 1	10	(10%)	300	(40%)
7000	10 ± 1	7	(10%)	200	(30%)

N=5

340

Embedded Fiberoptic Configuration

All of the sensors described in this chapter have utilized an off-column mode of detection, thereby introducing a void volume which has been demonstrated to be dramatically affected by the spacing between the optical fiber and the separation capillary. In an attempt to eliminate the dead-volume factor in sporadic sensor performance and diminished efficiency, an embedded fiber design was investigated (Figure 8.23). In this modification of SBFOS Design C, the 50-µm i.d. separation capillary was replaced with a 10-cm x 75-µm i.d separation capillary. A 65-µm core fiberoptic (0.66-NA) was stripped of is jacket (0.6-0.8 cm), inserted through the opposite arm of the quartz tee joint, and very carefully inserted into the elution end of the separation capillary to a distance of 0.5 cm. All sensor elements were cemented in place as described for Design C fabrication.

As was previously discussed, a particular concern with the axial illumination is the possibility of a waveguide effect which can diminish the apparent efficiency of a separation by probing volumes extending deep into the capillary. Indeed, as a result of the embedded fiber geometry, the waveguide effect was observed for a frontal mode electropherogram of R6G, as evidenced by an initially gradual rise in the R6G bandfront. In addition, the band retention reproducibility was poor. It was very obvious, visually, that the bandfront migration rate typically decreased as the electrophoresis proceeded. Sometimes band migration even stopped. Pressure buildup due to flow restriction, applied coaxially to the optical fiber and in the immediate area of detection, could have been a newly introduced complication inherent with this design. Regardless of these drawbacks, a commendable separation of a derivatized amine mixture was generated with this new embedded fiber design, as illustrated in Figure 8.24.
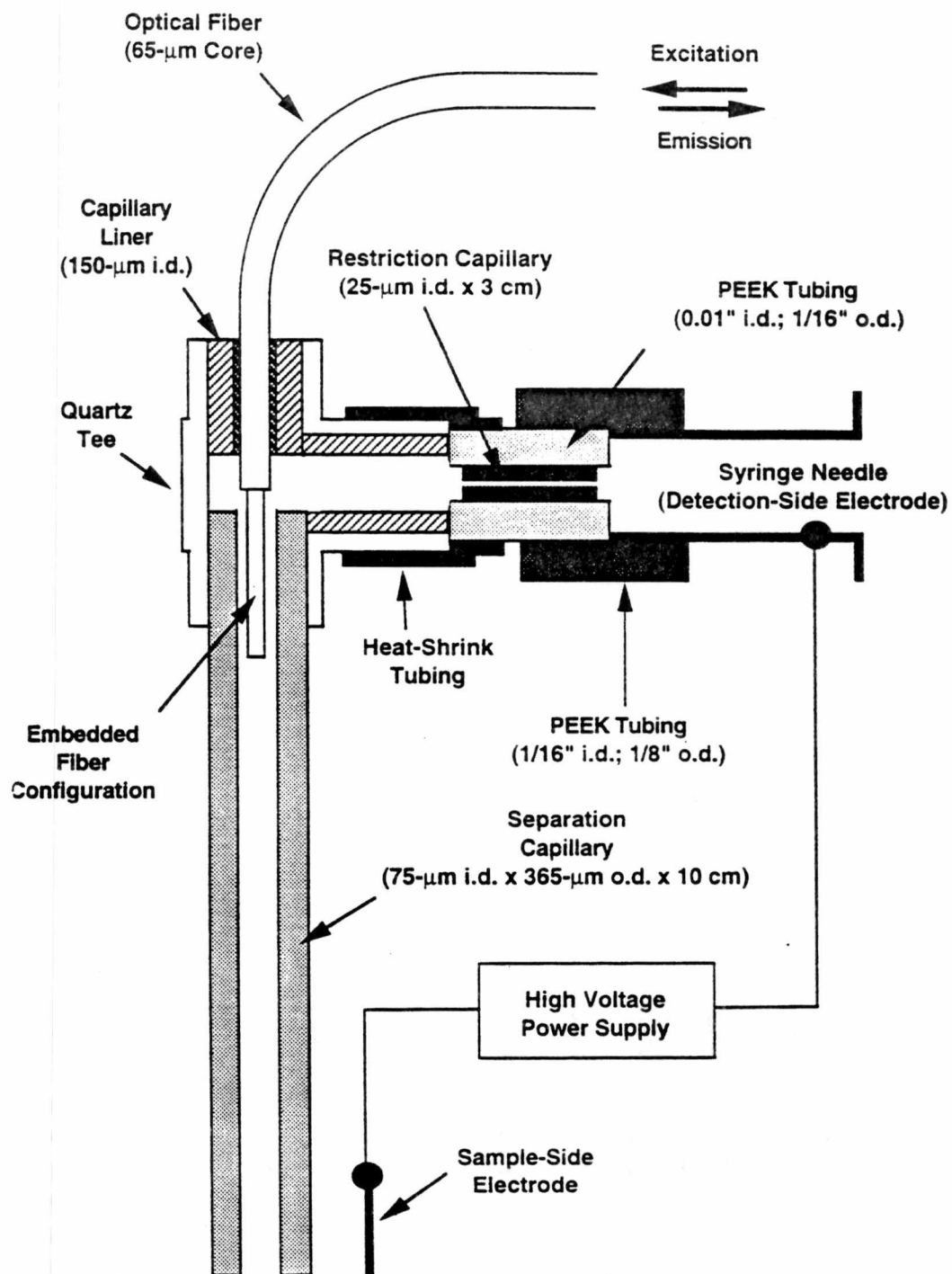
Figure 8.23. Embedded fiberoptic design for SBFOS.

342
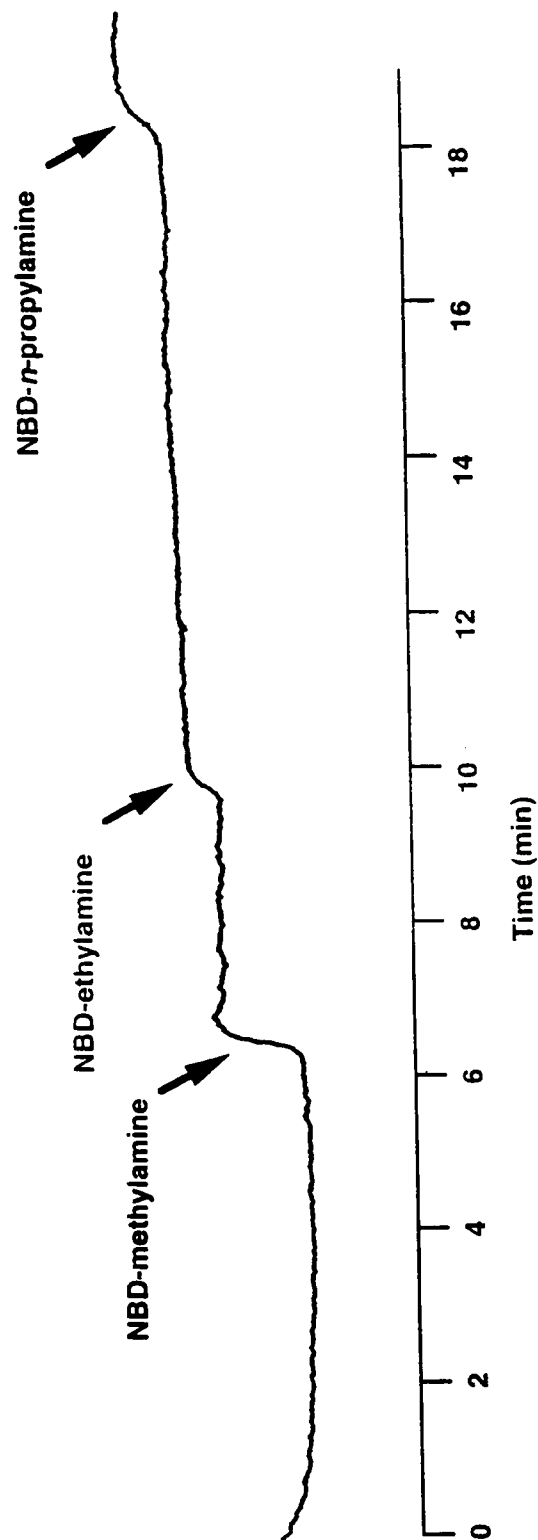
Figure 8.24. Frontal mode CE separations of a ternary mixture of the derivatized amines, NBD-methylamine (0.4 mM), NBD-ethylamine (0.3 mM), and NBD-*n*-propylamine (0.1 mM), generated with the embedded fiberoptic configuration of SBFOS Design C.

343

CHAPTER 9

DEVELOPMENT OF AN SBFOS FOR BIOANALYSIS

INTRODUCTION

While the prior focus of the SBFOS technology has been for *in-situ* environmental applications, the goal of this chapter is to introduce the SBFOS technology as a competitive technique for laboratory-based bioanalysis. CE has demonstrated wide-ranging successes in bioanalytical separations due largely to its combined unique characteristics of short analysis times, high efficiencies, and low sample volumes. Among its successes are the analyses of sequencing reactions (Ruiz-Martinez *et al.*, 1993; Swerdlow and Gesteland, 1990; Luckey *et al.*, 1991), restriction digests (Heiger *et al.*, 1990; Clark *et al.*, 1994; Zhang and Yeung, 1996b), protein-DNA interactions (Stebbins *et al.*, 1996) and PCR mixtures (Stalbom, 1994; Bianchi *et al.*, 1993; Kuypers *et al.*, 1993; Khrapko *et al.*, 1994). Indeed, CE has been speculated to be a valuable tool in the immense human genome project (Hunkapiller *et al.*, 1991; Smith, 1993).

The SBFOS technology shares the benefits of conventional CE for bioanalysis while providing the additional advantages of compactness, robustness and portability. Moreover, robotic automation with a range of motion limited only by the length of the fiberoptic should be possible. The sturdiness and ease of fabrication may permit the development of portable SBFOS arrays. Such arrays could serve as an attractive

alternative to cumbersome capillary bundles (Huang *et al.*, 1992; Wang *et al.*, 1996; Bashkin *et al.*, 1996; Anazawa *et al.*, 1996) or expensive microchips which typically require complicated out-of-house fabrication (Manz *et al.*, 1992; Wooley *et al.*, 1997).

The SBFOS sensor described herein is directed at the development of a sensor (and eventually a sensor array) for bioanalytical applications. This work stems from SBFOS designs reported in Chapter 8, but with modifications that are achievable in a laboratory environment and which minimize some previously reported problems (Sepaniak *et al.*, 1996; Stokes *et al.*, 1997; Sepaniak *et al.*, 1997). Among these modifications is a change from off-column to on-column LIF detection. This modification serves to eliminate separation-compromising detection dead volume, provide a uniform conduction path, and eliminate pockets which allow the formation or expansion of gas bubbles. Another modification is the elimination of GHF via dense size sieving media, thereby permitting sensor operation in virtually any orientation.

In light of these design modifications, significantly improved SBFOS performance is reported in this chapter, particularly in terms of band elution time reproducibility and efficiency. The sensor is applied to the analysis of a ϕX-174 *Hae*III DNA digest. The DNA fragments are labeled on-column with the intercalating dye, ethidium bromide, and detected via LIF. Two sieving matrices are investigated in these studies, polyethylene oxide (PEO) and methyl cellulose (MC), with comparable results in terms of both band elution time reproducibility (RSD < 5%) and efficiency (up to 2.5 million plates/m). Temporal analysis of ϕX-174 phage DNA digestion by the restriction enzyme, *Hae*III, is performed. Temporal characterization of DNA digest in near real-time can immensely reduce the time required for determining appropriate termination points and/or optimum reaction conditions for partial DNA digestion for cloning or other

345

applications(Stebbins *et al.*, 1997). The rate of labeling a protein digest with fluorescein isothiocyanate (FITC) and the effect that the labeling exhibits on separation behavior are also investigated.

EXPERIMENTAL

Chemicals

All chemicals were used as purchased from Sigma (St. Louis, MO, USA). Sieving matrices were based on Poly(ethylene oxide) (PE0), m.w. 2,000,000, and methyl cellulose, m.w. 100,000. Column coating chemicals included acrylamide, ammonium persulfate, N,N,N',N'-tetramethylethylenediamine (TEMED), and γ-methacryloxy-propyltrimethoxysilane (γ-MTMS). TRIS-boric acid-EDTA (TBE) buffers (pH=8.5) were prepared with tris(hydroxymethyl)aminomethane (TRIS), boric acid and ethylenediaminetetraacetic acid (EDTA). Other column treatment reagents included HCl, H_3PO_4, NaOH and acetone. DNA samples were prepared from φX-174 *Hae*III digest (390 μg/m), φX-174 phage DNA (10 u/ml), *Hae*III restriction enzyme (10 u/μl) and an incubation buffer (for digests). All aqueous solutions were prepared with water purified with a Milli-Q+ filtration system (Bedford, MA, USA).

Sensor Materials

Fused silica capillaries used for all separations (50 μm i.d. X 365 μm o.d.) and the optical fiber (155 μm core diameter X 195 μm o.d., 0.22-numerical aperture (NA))(FVP-155/165/195) used for sensor fabrication were purchased from

Polymicro Technologies (Phoenix, AZ, USA). The low volume Tefzel tee (Model P-632), associated flangeless fixtures, and PEEK tubing (0.020" i.d. X 1/16" o.d.) were all obtained from Upchurch Scientific (Oak Harbor, WA, USA). Devcon five minute epoxy was used for all cementing involved in sensor fabrication.

Sensor Fabrication

The new SBFOS design is demonstrated in Figure 9.1. Central to the design is the low-volume Tefzel tee which couples the optical fiber to the separation capillary and permits easy flushing of the sensor during pretreatment steps. The tee features three flangeless fittings for reproducible placement of the components, and 0.020" diameter channels extending from each fitting port to the center of the tee.

The 50-μm i.d. separation capillary was 17 cm in total length. A 1-cm detection window was burned in the polyamide capillary coating, by flame, at 10-cm from an end of the capillary (sample inlet end). Column pretreatment steps are described in a later section. The separation capillary was inserted through the two opposing arms of the tee (sample inlet and sensor pretreatment ports), positioned with the detection window at the center of the tee, and held in place by the flangeless fittings. Each flangeless fitting housed a ferrule which firmly held a section of the PEEK tubing. The separation capillary was cemented within the PEEK tubing of the pretreatment port fitting. The pretreatment port fitting also housed a stainless steel 16-gauge needle for flushing the sensor during pretreatment steps. The capillary outlet end, extending from the modified pretreatment port, was cemented within a stainless steel sleeve which served as the outlet-end electrode (ground). During operation, this electrode was inserted into small auxiliary reservoir- a 1.5-ml μ-centrifuge tube with a small hole drilled in the cap.

347
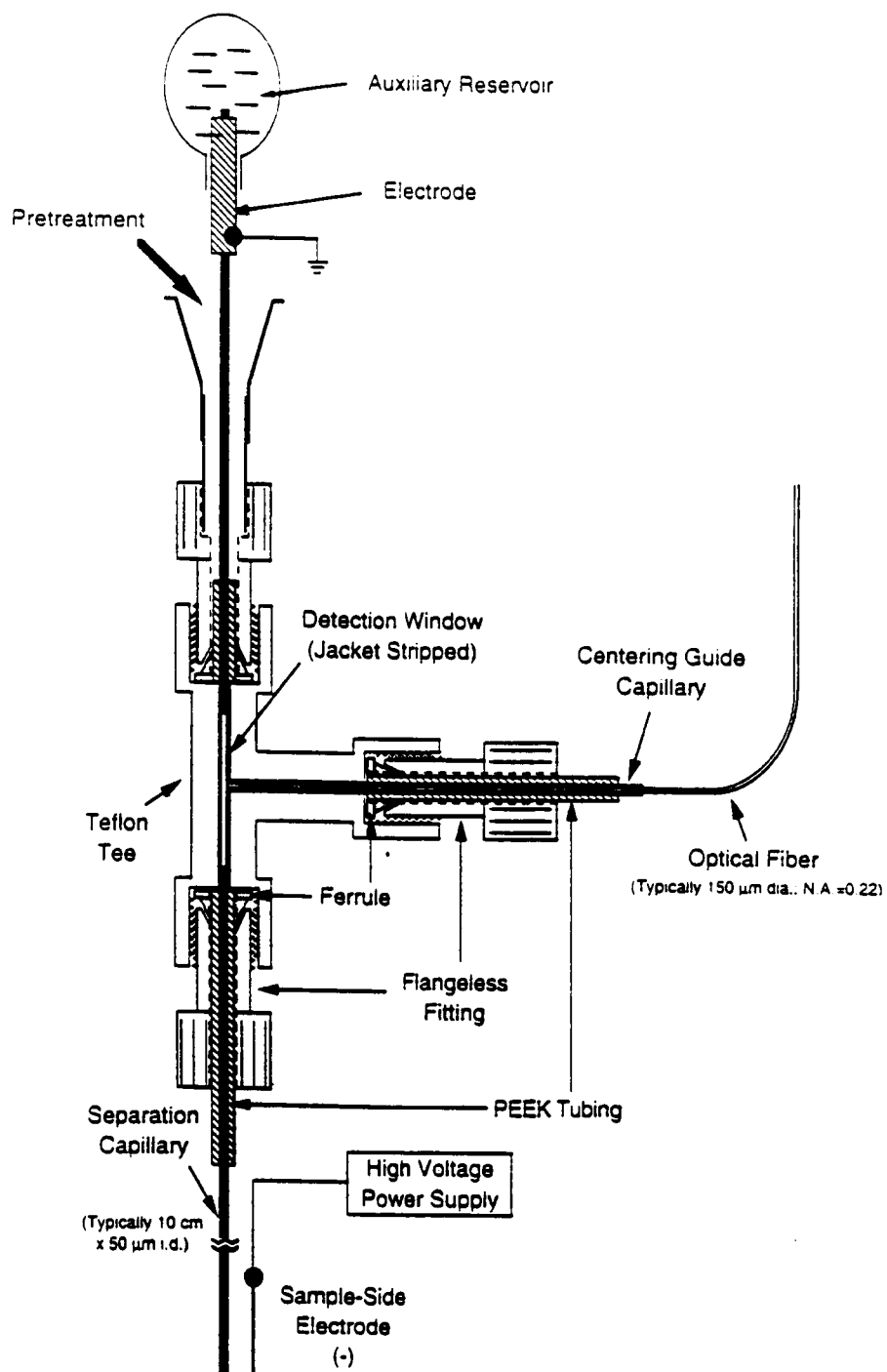
Figure 9.1. SBFOS design for bioanalysis featuring on-column detection.

Source: D. L. Stokes, M. J. Sepaniak, and T. Vo-Dinh, *Anal. Chim. Acta.* (1999) in press.

The high potential electrode (-) was a platinum wire placed in the sample solution or inlet reservoir. Electrophoretic fields were produced with a Hipotronics (Brewster, NY, USA) Model 840A high-voltage power supply.

The optical fiber, placed perpendicular to the axis of, and touching, the separation capillary, was centered in the side arm of the tee by the coaxial arrangement of a 4-cm section of section of 250-μm i.d. capillary (Polymicro Technologies) cemented within a 3-cm section of the PEEK tubing. The optical fiber was cemented within the 250-μm i.d. capillary while the PEEK tubing was held firmly in place by the ferrule. Prior to installation, a 0.5-m section of the optical fiber was cut using a sapphire cleaver (JDS Fitel, Inc.; Ottawa, Ontario, Canada) which provided suitable cuts to offset any further polishing. The jacket was stripped to a distance of approximately 1 cm from both ends of the optical fiber by flame.

Optical Train

The excitation source was the 514.5-nm line of Coherent Innova 70 argon ion laser (Palo Alto, CA, USA). A 25-mW power, measured at the laser aperture, was used for all trials. The beam splitting optical system external to the SBFOS has been described in Chapter 8. For wavelength selection in most of these studies, a SPEX 1403 double-grating spectrometer (Metuchen, NJ) equipped with a thermoelectrically-cooled PMT (C31034, Burle Industries, Lancaster, PA) was used. All slits were set at 3 mm for a bandpass of approximately 1 nm centered at 585 nm. A 1-m section of 600-μm core optical fiber (Fiberguide Industries, Sterling, NJ) was used to transmit the signal from the beamsplitting optics to the spectrometer. An f/2.5 lens was used to focus the signal from the beamsplitting optical system onto the 600-μm fiber (NA=0.22). A two-lens

349

system was used to efficiently couple the 600-μm optical fiber to the f/7.8 spectrometer. A fixed wavelength optical system that included a 10-nm bandpass filter (30%T, centered at 585 nm) to isolate emission was also used for some studies. The signal beam from the beamsplitting optics was focused directly onto a filter/PMT (Hamamatsu, R636) combo with a single f/3 lens. A bandpass filter, rather than a cut-on filter, was necessary to reject sensor fiber fluorescence background which becomes significant at 625 nm.

Running Buffer Preparations

All running buffer systems were based on pH 8.5 TBE buffer: 45 mM TRIS, 45 mM boric acid, and 1 mM EDTA. For PEO studies, a 2.0% solution of PEO in TBE was prepared using the procedure described by Fung and Yeung (Fung and Yeung, 1995; Clark *et al.*, 1995). A 0.5% solution was prepared daily from this stock solution in TBE. For methyl cellulose systems, a 1% methyl cellulose stock solution was prepared as previously described (Clark *et al.*, 1995). A 0.5% solution in TBE was prepared daily from this stock. All polymer solutions were degassed under vacuum before use in the sensor. Buffer reservoirs were loaded with the TBE buffer less the polymers for all studies.

Column Preparations

For the PEO-based system trials, bare 50 μm. i.d. fused silica capillary was installed in the SBFOS. All pretreatment reagents were flushed through the sensor column with a syringe affixed to the sensor pretreatment port illustrated in Figure 9.1. The capillary was first flushed with 1.0 N HCl, then filled with the 0.5% PEO solution, followed by the

2.0% PEO solution doped with 2.5 μM ethidium bromide. The column was filled with 0.1 N HCl when not in use.

For the methyl cellulose-based system trials, the fused silica capillary was first wall-coated with linear polyacrylamide, based on the procedure described by Hjerten (Hjerten, 1985), before being installed in the SBFOS. Detection windows were blazed in the exterior polyamide column coating prior to the wall-coating steps. Prior to each trial, the capillary was flushed with 10 mM H_3PO_4 for 3-5 min, then filled with ethidium bromide (2.5-μM)-doped methyl cellulose. The column was filled with 10 mM H_3PO_4 when not in use.

RESULTS AND DISCUSSION

Fundamental Evaluations: Reproducibility, Efficiency and Detectivity

Some subtle modifications have been implemented to prior SBFOS designs, which facilitate its use in a laboratory environment while preserving the compact size (see Figure 9.1). The sensor uses a linear section of separation capillary, which typically necessitates procedures for reducing gravity-driven hydrostatic flow and concomitant band dispersion (Chapter 7, Sepaniak et al., 1996; Stokes et al., 1997; Sepaniak et al., 1997). Small theoretical plate heights are especially critical to the compact nature of SBFOSs because relatively short separation capillaries (8-10 cm) are used. In conventional laboratory setups, hydrostatic flow is eliminated with an arched capillary geometry which allows equal-height entrance and exit buffer reservoirs. Such arrangements, however, are cumbersome and have very limited portability. The linear

351

design described herein, also featuring an integrated auxiliary exit buffer reservoir, has portability limited only by the sensing fiberoptic. The role of the inlet buffer reservoir is played at any given workstation. When the linearly-designed SBFOS is operated in a vertical geometry, hydrostatic flow is maximized and opposes EOF. While this effect can be offset to some degree by using high applied fields, the resulting current-induced joule heating can cause significant thermal dispersion. In previous designs for environmental applications, this complication was minimized by using a restriction capillary (Chapter 7).

In this work, a new sensor for bioanalytical applications in the laboratory environment has been developed. In these cases, size selective CE can be performed with an entangled polymer sieving matrix. With EOF minimized, the separation of the relatively large biomolecules results from a complex combination of differential migration rates and interactions with the sieving polymer matrix. For DNA analysis alone, at least 12 polymer matrices have been investigated (Barron *et al.*, 1996) which, with few exceptions, are highly viscous. Because viscous matrices can themselves minimize gravity-driven hydrostatic flow, this new sensor was designed without a restriction capillary.

PEO was selected as the separation medium for initial studies. In addition to being highly viscous, PEO permits the use of a bare silica column (Fung and Yeung, 1995). In contrast, coated columns typically have limited lifetimes and require some expertise in preparation. Simple, on-line preparation for DNA analysis with the possibility of long-term sensor use without capillary replacement are features making PEO particularly useful for exhaustive, initial sensor evaluations. Figure 9.2 illustrates PEO-based separations of φX-174 *Hae*III digest fragments acquired with horizontal and vertical
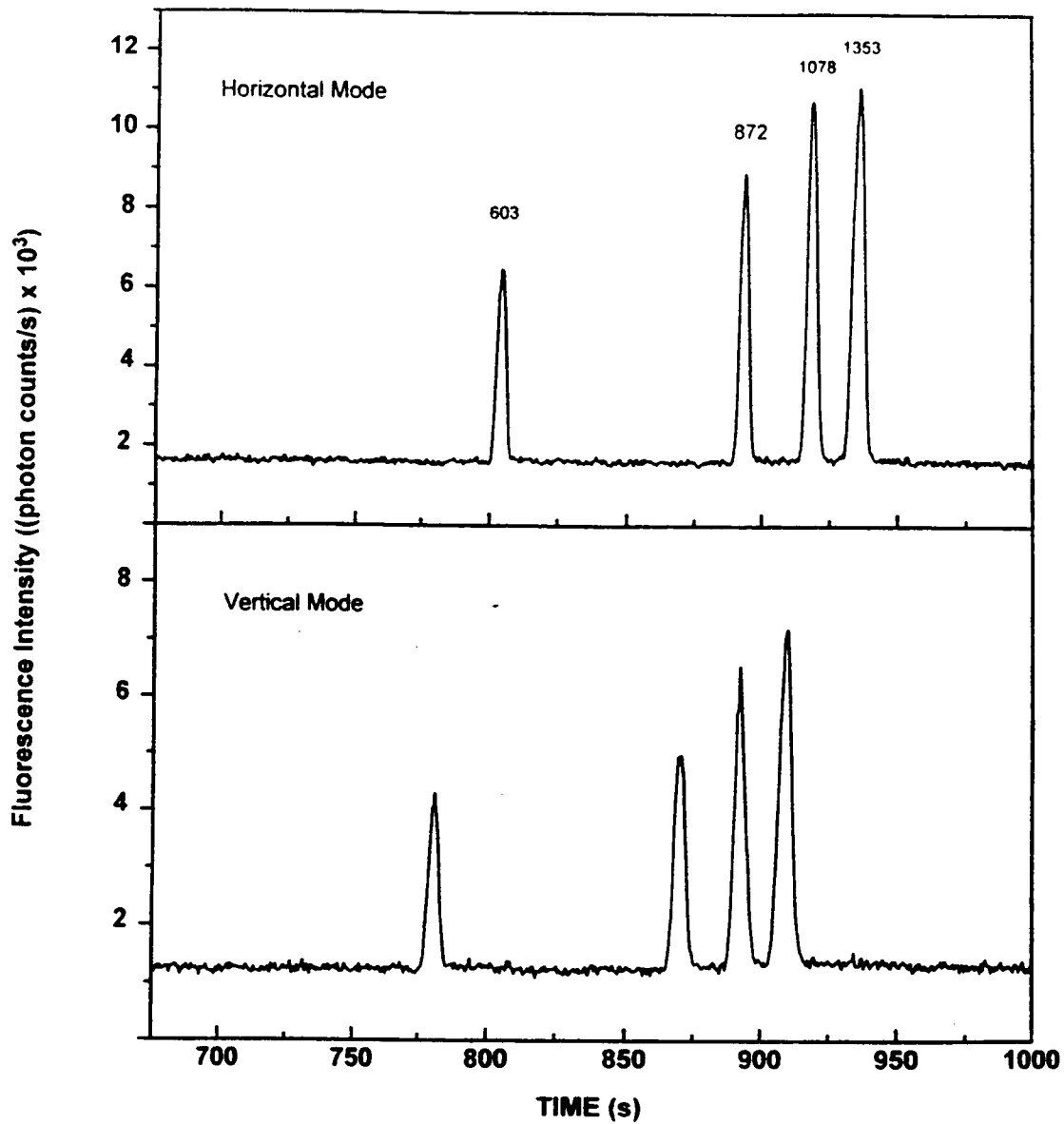
Figure 9.2. Comparison of CZE separations of the four largest fragments of a 10-µg/ml sample of φX-174 HaeIII DNA digest acquired with the SBFOS in horizontal and vertical modes of operation. Conditions: PEO matrix; injection: 88 V/cm for 10 s; running voltage: 118 V/cm.

Source: D. L. Stokes, M. J. Sepaniak, and T. Vo-Dinh, *Anal. Chim. Acta.* (1999) in press.

sensor orientations. In the vertical orientation, the exit (auxiliary) reservoir height was approximately +15 cm relative to the inlet reservoir. Nevertheless, band elution times and efficiencies were comparable for the two trials, indicating that gravity-driven hydrostatic flow was insignificant in virtually any sensor orientation. In fact, the bands were observed to elute slightly earlier for the vertical mode separation. This observation may be attributed to a variability in column wall conditions which could have resulted from incomplete expulsion of the highly viscous polymer matrix between trials.

In contrast to the previous work, the SBFOS designed for these studies employs a separation capillary that extends through the tee (see Figure 9.1) with both ends inserted into buffer reservoirs. This modification produces a more uniform path of electrical conductance and helps reduce the introduction of air bubbles during sensor flushing and filling steps. In addition, there are no void volume pockets within the sensor which can degrade reproducibility by trapping or allowing the expansion of bubbles. Finally, the on-column detection configuration with the fiber exterior to separation pathway eliminates other complications encountered with the off-column detection scheme used in the earlier works described in Chapter 7. In particular, earlier designs suffered from slight movement of the fiber during operation which degraded both band elution time reproducibility and efficiency. In this design, the position of the fiber should have no effect on band retention time reproducibility. Table 9.1 lists elution time reproducibility for four bands representing the full range of DNA fragment sizes. RSDs for all selected bands were 4% or less.

Efficiency is a critical parameter of CE when applied to biopolymer separations. Indeed, single base pair resolution is the ultimate goal for DNA sequencing. The on-column

354

Table 9.1. Retention times and reproducibilities of selected φx-174 bands obtained with the SBFOS designed for bioanalysis

Band No.	Number of Base Pairs	Trial 1	Trial 2	Trial 3	Average	RSD
1	72	420.0 s	412.5 s	425.0 s	420 s	2 %
4	234	521.0 s	540.0 s	540.0 s	520 s	3 %
8	603	739.0 s	763.5 s	763.5 s	740 s	4 %
11	1353	834.5 s	870.0 s	870.0 s	840 s	4 %

Source: D. L. Stokes, M. J. Sepaniak, and T. Vo-Dinh, *Anal. Chim. Acta.* (1999) in press.

detection configuration of this sensor promotes improved efficiency by eliminating the dead volume common to previous designs. The detection volume is defined by the i.d. of the capillary and the excitation/collection cone of the optical fiber. Using a 50-μm i.d. capillary and a 155-μm diam. core fiberoptic with 0.22 NA (acceptance angle of ~9 degrees when index matching gel is used to eliminate refraction at fiber-capillary boundary), the illuminated volume is estimated to be 0.4 nl when the optical fiber is placed against the capillary. Since the emission collection efficiency is relatively poor at the extremes of this illuminated volume, the true effective detection volume is somewhat less. Even at the best efficiency obtained in our work for DNA separations, 2.5 million plates/m, peak volumes exceed 1.5 nl for a 10 cm separation capillary. Thus it is expected that only under the best separation conditions will the on-column detection scheme have a noticeable (but small) effect on observed band variance. Actually, the detection integration time (1s) is a more limiting factor for the work described herein.

Typical CE/LIF systems approach the ideal detection scheme by focusing the laser beam for enhanced photon flux, and using a large-NA signal collection lens for high signal collection efficiency. In this SBFOS design, neither of these attributes is realized. A divergent beam impinges on the capillary from an optical fiber which, by contrast, has a relatively low NA. There is a potential compromise of sensitivity associated with the acceptable efficiency observed with the 0.22-NA optical fiber. Other complications arise from scattering and reflective losses of the signal at the air/capillary interface. Attempts to minimize this effect by using an index-matching gel between the fiber and the capillary have been unsuccessful thus far.

Conversely, it has been reported that the lens-like nature of the capillary wall can minimize radiative losses and improve collection efficiency when appropriate running buffers are used (Maystre and Bruno, 1992). This work was therefore performed without gel. Sensor detectivity was tested with a the fixed wavelength, bandpass filter-based optical system. Results are illustrated by Figure 9.3. For the 0.5 µg/ml sample, the final three DNA fragments (872, 1078, and 1353 b.p.) were detected with a S/N range of 15-20. Furthermore, nearly all fragment bands were distinguished from the noise with baseline resolution. The final three fragments were still observable for a 0.1 µg/ml sample, with a S/N of approximately 4-8. Additional improvement in signal can be expected with a wider-range bandpass filter.

Figure 9.4 illustrates a voltage optimization study performed with the SBFOS for the analysis of φX-174 HaeIII digest in the 1500-4000V range. Above 4000V, the sensor exhibited erratic current behavior, indicating possible bubbling in the polymer matrix (from current-induced joule heating). At 4000 V, full baseline resolution was observed for all but the 271 and 281 b.p. fragments with a total separation time of only 3 minutes. As demonstrated by the figure, however, full baseline resolution of all fragments was achievable only at the low-voltage extreme of 1500V, requiring a total separation time of over 20 minutes.

The PEO sieving matrix appeared to be optimized for the larger fragments as the smaller ones were somewhat distorted. Plots of migration time and current versus applied voltage showed modest nonlinearity at the higher voltages, indicating increased temperature and decreased viscosity at the higher fields. Likewise, efficiency peaked at a middle voltage value, perhaps indicating significant thermal dispersion at high fields and greater axial dispersion at low fields (e.g., the efficiencies for the 603 b.p. fragment

357
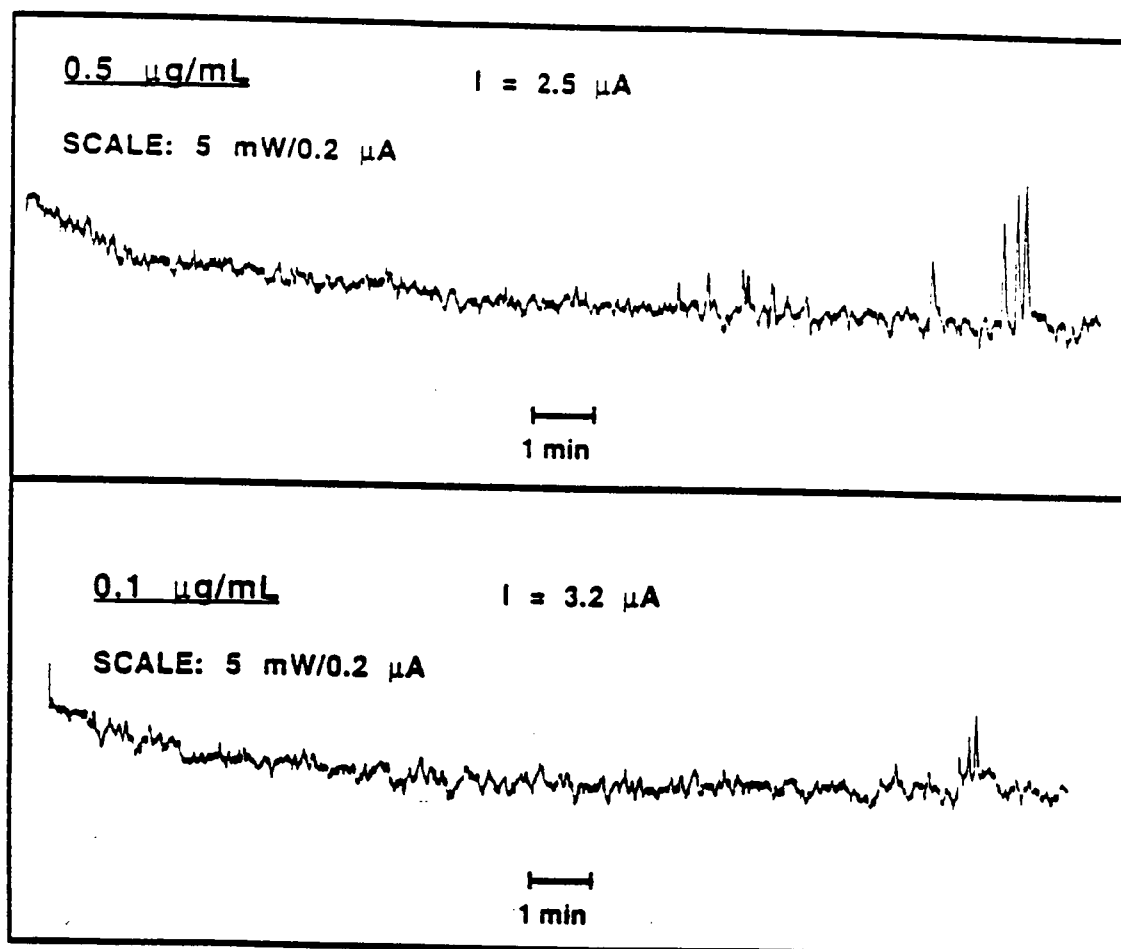
Figure 9.3. CZE separations of 0.5 and 0.1 µg/ml solutions of a φX-174 *Hae*III *DNA* digest acquired with a 10-nm bandpass at 585 nm (30%T) for improved detectivity. Conditions: PEO matrix; injection: 88. V/cm for 10 s; running voltage: 118 V/cm.

Source: D. L. Stokes, M. J. Sepaniak, and T. Vo-Dinh, *Anal. Chim. Acta.* (1999) in press.

Figure 9.4. Demonstration of an SBFOS voltage optimization study for the analysis of a φX-174 *Hae*III *DNA* digest when using a 2.0% PEO separation matrix, including CZE separations for applied electric fields of 235, 176, 118, 88 V/cm. Injection: 88 V/cm for 10 s.

Source: D. L. Stokes, M. J. Sepaniak, and T. Vo-Dinh, *Anal. Chim. Acta.* (1999) in press.

359

are 2.1, 2.3, 1.8, 1.4 million plates/m for 1500, 2000, 3000, and 4000 V, respectively). These results further support the claim that the potential hydrostatic flow and pressure complications cited in Chapter 8 had been minimized with this new design.

Applications

Temporal analysis of ϕX-174 digestion. Incomplete digests can provide the biochemical researcher with a large range of DNA fragments which can be isolated for cloning or other processes. While a target DNA fragment from incomplete digestion could be obtained through simple termination of a digestion via heat inactivation or phenol addition/extraction, the appropriate time for reaction termination is a critical parameter which can require an exhaustive number of time-consuming trials, especially when using conventional slab gel electrophoresis. It has been demonstrated in a previous work that CE can dramatically reduce the time required for the temporal characterization of DNA digests (Stebbins *et al.*, 1997). In the present work, a temporal analysis of ϕX-174 phage DNA digest by *Hae*III was performed with the SBFOS technology. As demonstrated by Figure 9.4, baseline resolution of all the fragments in the ϕX-174 phage DNA digest would typically require a 20-min separation time in addition to the 20 - 30-min column preparation time for each trial when using a PEO matrix. To conserve time, a surface-coated column was considered as an alternative to a bare column in this application. Typical column treatment times were less than 10 min when using a MC sieving matrix. Unfortunately, the column lifetimes were limited. The exhaustive sensor evaluations performed for the PEO system were therefore bypassed and those results were used as a cursory guide for the MC-based system. Figure 9.5 illustrates an electropherogram of a ϕX-174 digest acquired with a MC-loaded SBFOS.

360
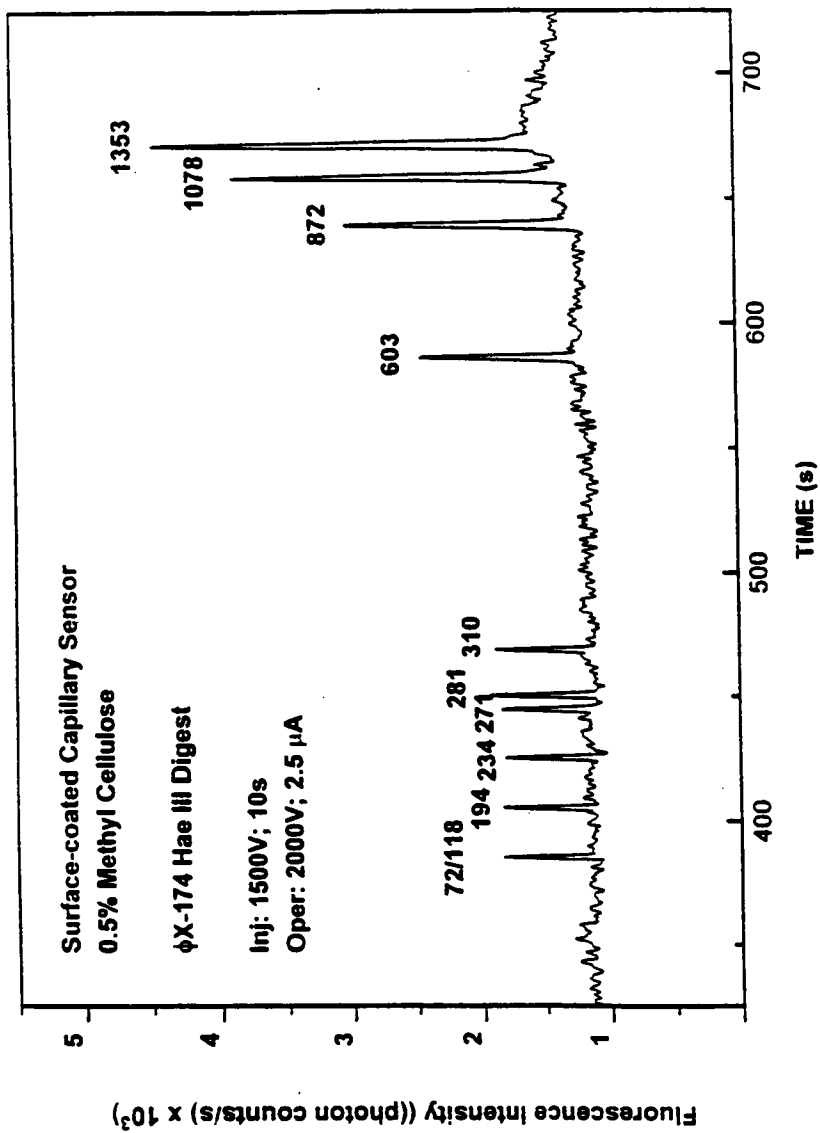
Figure 9.5. CZE separation of a 10 µg/ml φX-174 *HaeIII DNA* digest sample using a surface-coated capillary-based SBFOS and 0.5% methyl cellulose separation matrix, at an applied field strength of 118 V/cm. Injection: 88 V/cm for 10 s.

Source: D. L. Stokes, M. J. Sepaniak, and T. Vo-Dinh, *Anal. Chim. Acta.* (1999) in press.

Regardless of the similar separation parameters used for the two polymer matrices, full baseline resolution of the 271 and 281 b.p. fragments was observed in less than 12 minutes for the MC. As a cursory comparison with the PEO-loaded sensor, migration time reproducibility and efficiencies for selected bands were evaluated (N=3). Improved band elution time RSDs (less than 2%) and comparable efficiencies (up to 2.5 million plates/m) were observed with MC. Moreover, peak symmetry was good for all the fragments in the digest (compare Figures 9.4 and 9.5).

Figure 9.6 illustrates the results of the φX-174 digest temporal analysis performed with the MC-loaded sensor. Injection times relative to the beginning of the digestion reaction are provided above each electropherogram. While large intervals are reported between trials, the true temporal resolution was actually much higher; these electropherograms were selected to best represent the digestion process. Even at the large intervals illustrated by Figure 9.6a, the evolution of a complex intermediate electropherogram from a single-nicked plasmid band is observed prior to the emergence of the familiar completed digest pattern. Reaction-retarding steps were taken to produce this effect, including increasing the manufacturer's recommended concentration of phage DNA by 50% (1.5 u/ml) while decreasing the enzyme concentration by 50% (0.5 u/μl). The reaction mixture was also kept on ice for the first 270 minutes of the reaction. As demonstrated by the figure, the singly-cut plasmid DNA fragment of 5386 b.p. length was detected after 30 min at the cooled condition. After 80 min, a complex pattern of large DNA fragments was observed which is not characteristic of a complete digestion. A gradual disappearance of these intermediate fragments was observed in later trials, accompanied by the intensification of some characteristic complete digestion bands, such as the 234, 271, 281, 310, 603, 872, 1078, and 1353 b.p. bands.
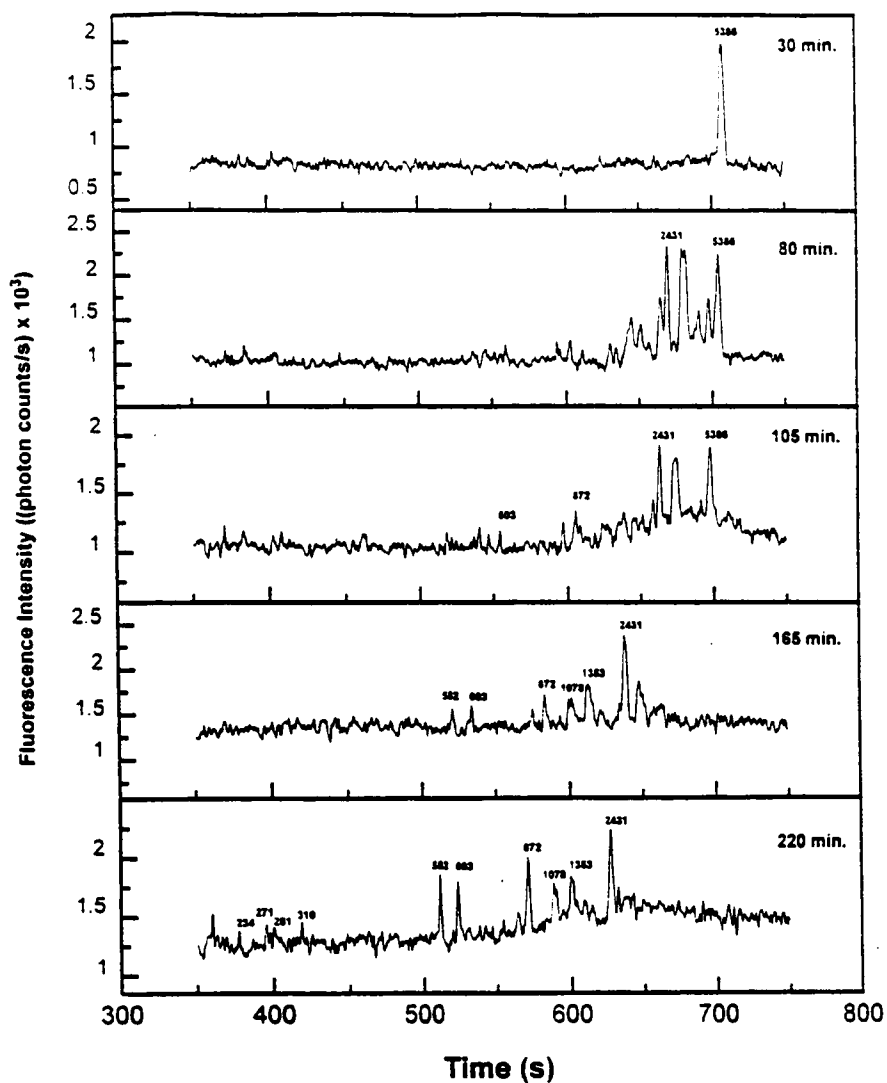
Figure 9.6a. Electropherograms depicting temporal analysis of φX-174 *Hae*III DNA digestion using surface-coated capillary-based SBFOS and a 0.5% methyl cellulose separation matrix for a) the first 220 minutes under ice-cooled reaction condition. Conditions: injection: 88 V/cm for 10 s; running voltage: 118 V/cm.

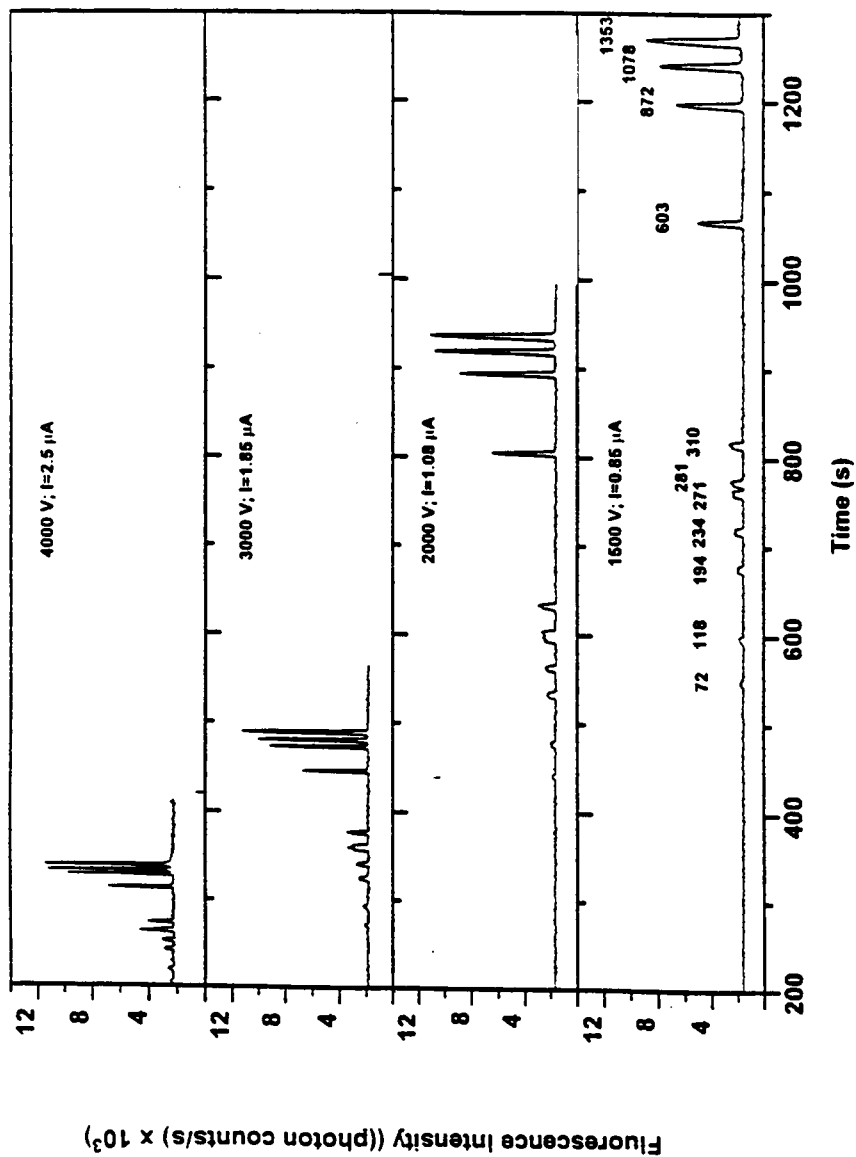Source: D. L. Stokes, M. J. Sepaniak, and T. Vo-Dinh, *Anal. Chim. Acta.* (1999) in press.
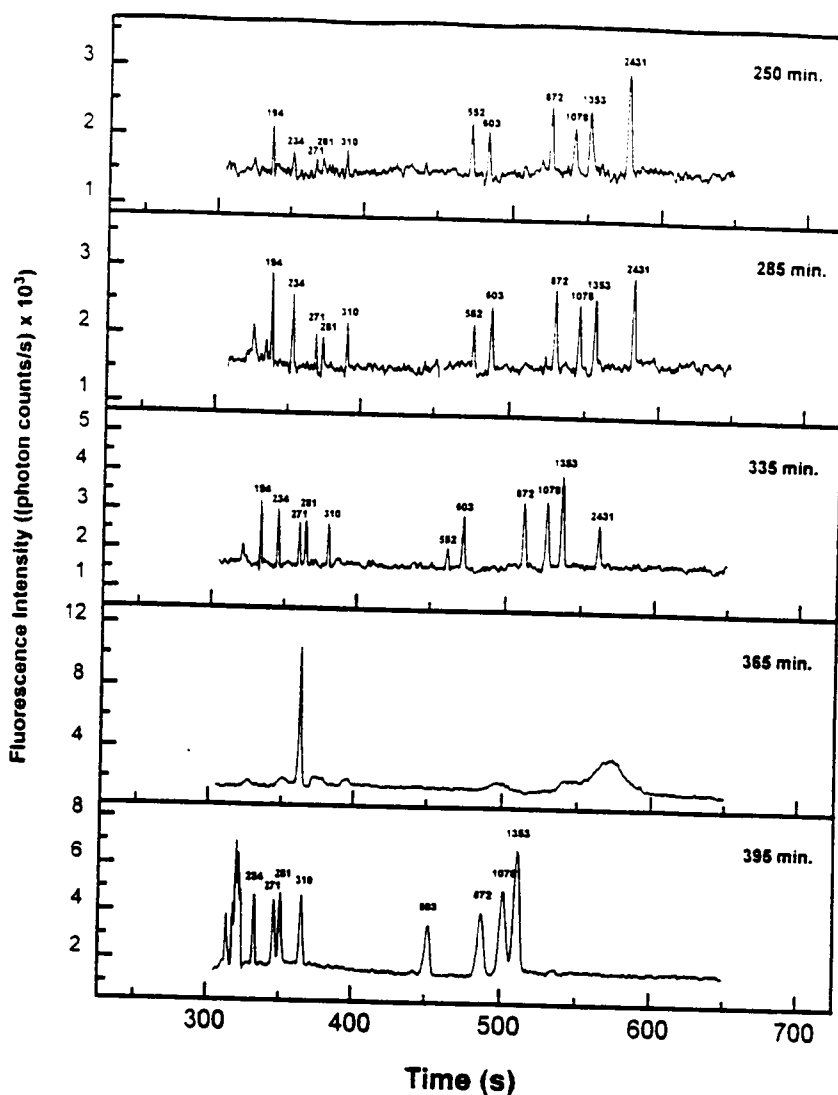
Figure 9.6b. Electropherograms depicting temporal analysis of ϕX-174 *Hae*III DNA digestion using surface-coated capillary-based SBFOS and a 0.5% methyl cellulose separation matrix for b) the final 395 minutes, with a room temperature reaction condition starting at 270 minutes. Conditions: injection: 88 V/cm for 10 s; running voltage: 118 V/cm.

Source: D. L. Stokes, M. J. Sepaniak, and T. Vo-Dinh, *Anal. Chim. Acta.* (1999) in press.

However, the intermediate 552 and 2431 b.p. fragments persisted through 220 min of digestion at the cooled condition.

Figure 9.6b illustrates an extension of the temporal study in which the digestion was warmed to room temperature after 270 min. At 285 min, the most salient feature was the decrease in the 552 b.p. band intensity relative to the 603 b.p. fragment. A corresponding increase in relative intensity of the daughter 271 and 281 b.p. fragments was likewise observed. After 335 min, a dramatic decrease in the 2431 intermediate fragment was finally observed, accompanied by a noticeable increase in the relative intensities of the daughter 1078 and 1353 b.p. bands. A major inherent disadvantage of the MC system is illustrated by the 365-min electropherogram. The failed separation was assumed to result from a degradation of the capillary wall coating. Regeneration of the column was attempted by flushing the sensor with 100 mM H_3PO_4. As demonstrated by the 395-min electropherogram, only partial regeneration was achieved. Nevertheless, the potential of the SBFOS in temporally characterizing DNA digestions and determining suitable termination times for desired DNA fragments has been demonstrated by this study.

Temporal study of myoglobin tryptic digest labeling process with FITC. As an additional example of bioanalytical potential, the SBFOS technology has been applied to the analysis of peptide mixtures. Furthermore, it has been used to monitor the dynamics of a peptide labeling process with FITC. Figure 9.7 illustrates electropherograms of a tryptic digest of myoglobin labeled with FITC. The five bands correspond to the five heaviest peptide fragments of the digest (the heaviest fragment eluting first). In this study, TBE solution was the running buffer and the sensor was operated in the horizontal mode. The sampling time relative to the initiation of the FITC
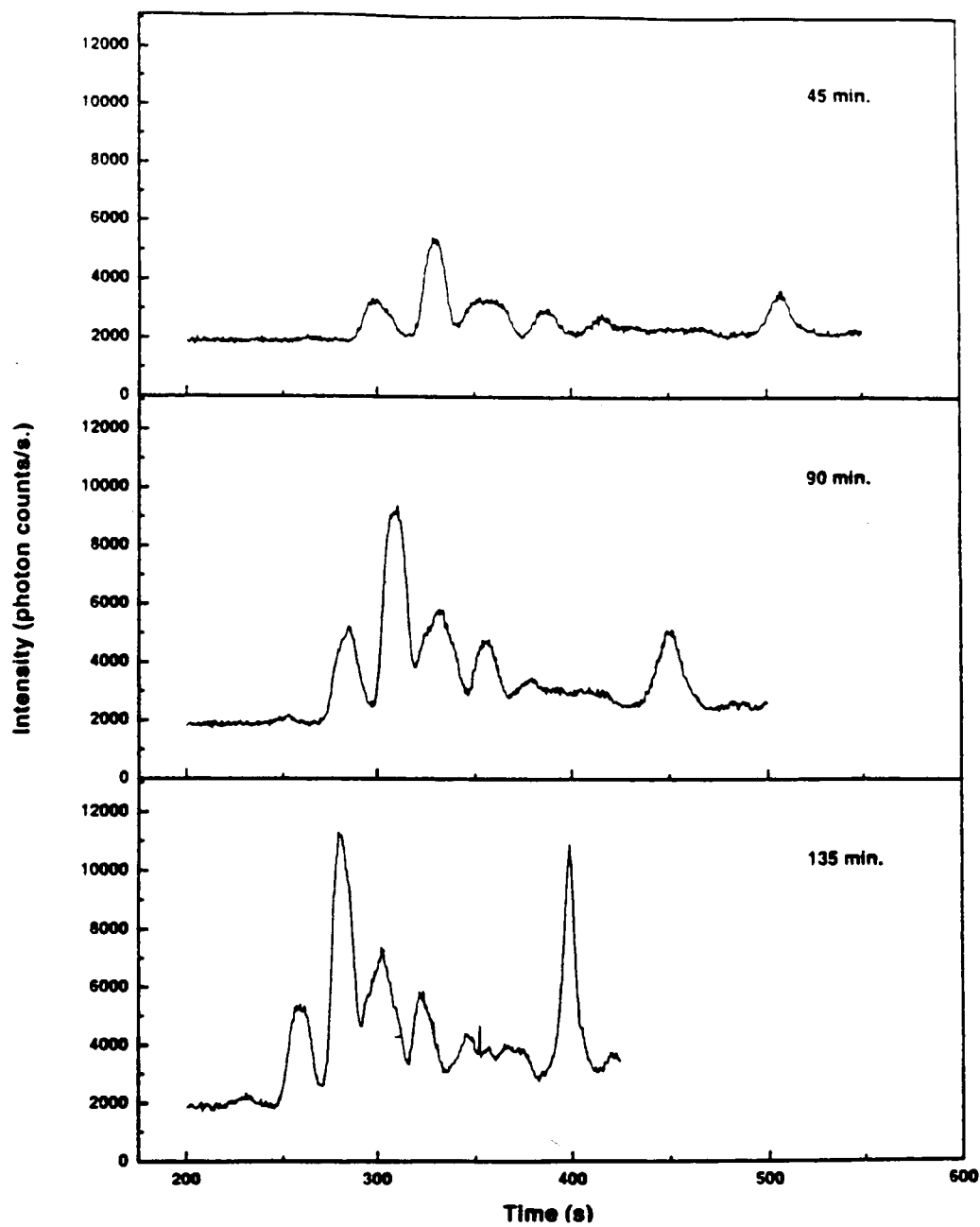
Figure 9.7. Electropherograms depicting temporal analysis of a myoglobin tryptic digest labeling process with FITC using the SBFOS with TBE running buffer via sampling at 45, 90 and 135 minutes.

366

labeling process is listed in the top right corner of each electropherogram. The concentration of the FITC for this reaction with a (50 µg/ml) myoglobin digest was approximately 50 µM.

As demonstrated by the figure, both band migration times and efficiencies were dependent on the sampling time relative to initiation of the FITC labeling process. The decreasing band migration times may be explained by the fact that, as the peptide fragments slowly reacted with the FITC, their masses became significantly increased. For example, peptide fragments of a tryptic digest of myoglobin may range from approximately 300 to 2000 Da, with corresponding residue numbers ranging from 1 to 17. The bands illustrated in Figure 9.7 are likely to be in the 1200 to 2000 Da range (10 - 17 residues). By comparison, the molecular weight of FITC is approximately 389 g/mol. While labeling at the terminal amine group of a peptide chain alone would significantly alter the mass of the migrating fragment in this mass range, there was also the likelihood of even further labeling at primary amine groups of various individual residues in the peptide chain. The increase in mass resulted in decreased migration velocity in opposition to the EOF, thus explaining the earlier elution times. As inferred above, there may be multiple labeling points on the peptide fragments, each with varying reaction dynamics. The process is complicated. The observed increase in efficiency with increasing sampling time could therefore be the result of increased homogeneity of the bands at greater sampling times. As this study demonstrates, the SBFOS technology may be used in optimizing reaction parameters or determining suitable endpoints for complicated peptide labeling processes.

CONCLUSION

This two-part study has demonstrated the feasibility of selective detection in remote analysis based on 1) surface-enhanced Raman scattering (SERS), and 2) separations-based fiberoptic sensing (SBFOS).

In the first part, TiO_2- and alumina-based substrates were developed which are easy to fabricate and are economical. They were applied to the detection of a variety of compounds of health and environmental interest at the trace concentration level. *In situ* analyses of complex samples were performed, including that of a mixture of structural isomers of phthalic acid. A 10-15% RSD has been routinely observed with these substrates. A silver island-based substrate has also been optimized and used for ultrasensitive detection (<100 molecules). The microparticle-based substrates have been readily integrated with fiberoptic sensors for remote SERS detection. Three fiberoptic SERS sensor systems have been developed. A SERS dosimeter for the detection of organic vapors has also been described in this work.

In the second part, a separations-based approach to selective, remote detection was demonstrated with the SBOFS technology. Several designs were introduced and evaluated, with the best designs yielding <10% RSDs in band elution times. The SBFOS technology offers flexibility and reusability. A single sensor was used for analyses of neutral organic compounds and nonfluorescent metals. The SBFOS was used also in bioanalytical applications. For example, a temporal analysis of a DNA digestion was performed.

BIBLIOGRAPHY

BIBLIOGRAPHY

Abler, J. K.; Reddy, K. R.; Lee, C. S. *J. Chromatogr. A* **759**, 139 (1997).

Adrian, F. J. *J. Chem. Phys.* **77**, 5302 (1982).

Akbarian, F.; Dunn, B. S.; Zink, J. I. *J. Phys. Chem.* **99**, 3892 (1995).

Akbarian, F.; Dunn, B. S.; Zink, J. I. *J. Raman Spectrosc.* **27**, 775 (1996).

Alak, A.; Vo-Dinh, T. *Anal. Chem.* **59**, 2149 (1987).

Alak, A.; Vo-Dinh, T. *Anal. Chim. Acta.* **206**, 333 (1988).

Alak, A.; Vo-Dinh, T. *Anal. Chem.* **61**, 656 (1989).

Alarie, J. P.; Bowyer, J.; Sepaniak, M.; Hoyt, A.; Vo-Dinh, T. *Anal. Chim. Acta* **236**, 237 (1990).

Alarie, J. P.; Stokes, D. L.; Sutherland, W. S.; Edwards, A. C.; Vo-Dinh, T. *Appl. Spectrosc.* **46**, 1608 (1992).

Albert, M.; Debusschere, L.; Demesmay, C.; Rocca, J. L. *J. Chromatogr., A.* **757**, 281 (1997). a

Albert, M.; Debusschere, L.; Demesmay, C.; Rocca, J. L. *J. Chromatogr., A.* **757**, 291 (1997). b

Albrecht, A. C. *J. Chem. Phys.* **34**, 1476 (1961).

Albrecht, M. G.; Creighton, J. A. *J. Am. Chem. Soc.* **99**, 5215 (1977).

Allred, C. D.; McCreery, R. L. *Appl. Spectrosc.* **44**, 1229 (1990).

Ambrose, W. P.; Goodwin, P. M.; Martin, J. C.; Keller, R. A. *Phys. Rev. Lett.* **72**, 160 (1994).

Anazawa, T.; Takahashi, S.; Kambara, H. *Anal. Chem.* **68**, 2699 (1996).

Angel, S.; Archibald, D. *Appl. Spectrosc.* **43**, 1097 (1989).

Angel, S. M.; Kulp, T. J.; Vess, T. M. *Appl. Spectrosc.* **46**, 1085 (1992).

Angel, S. M.; Carrabba, M.; Cooney, T. F. *Spectrochim. Acta A* **51**, 1779 (1995). a

Angel, S. M.; Cooney, F.; Skinner, H. T. *Proc. Europena Symp. Optics Env. Publ. Safety* (Munich), SPIE 2504, (1995). b

Angel, S. M.; Ridley, M. N.; Langry, T. L.; Kulp, T. J.; Myrick, M. L. *ACS Symp. Ser., 403 (Chem. Sens. Microinstrum.)* 345 (1989).

Archibald, D. D.; Lin, L. T.; Honigs, D. E. *Appl. Spectrosc.* **42**, 1558 (1988).

Arenas, J. F.; Marcos, J. I. *Spectrochim. Acta* **35A**, 355 (1979).

Aroca, R.; Kovaks, G. J. In: *Vibrational Spectra and Structure, Vol. 19*, Durig, J. R. (Ed.), Elsevier, Amsterdam, p.55, 1991.

Aroca, R.; Martin, F. *J. Raman Spectrosc.* **17**, 243 (1986).

Asher, S. A.; Flaugh, P.; Washinger, G. *Spectroscopy* **1**, 26 (1986).

Aussenegg, F. R.; Leitner, A.; Lippitsch, M. E. (Eds.) *Surface Studies with Lasers*, Springer, Berlin, 1983.

Banwell, C. N. *Fundamentals of Molecular Spectroscopy*, McGraw-Hill, New York, 1972.

Baraj, B.; Sastre, A.; martinez, M.; Spahiu, K. *Anal. Chim. Acta* **319**, 191 (1996).

Barber, P. W.; Chang, R. K.; Massoudi, H. *Phys. Rev. Lett.* **50**, 997 (1983). a

Barber, P. W.; Chang, R. K.; Massoudi, H. *Phys. Rev. B* **27**, 725 (1983). b

Barnes, M. D.; Ng, K. C.; Whitten, W. B.; Ramsey, J. M. *Anal. Chem.* **65**, 2360 (1993).

Barnes, M. D.; Whitten, W. B.; Ramsey, J. M. *Anal. Chem.* **67**, 418A (1995).

Barron, A. E.; Sunada, W. M.; Blanch, H. W. *Electrophoresis* **17**, 744 (1996).

Bartlett, J. R.; Cooney, R. P. In: *Spectroscopy of Inorganic-Based Materials*, Clark, R. J. H.; Hester, R. E. (Eds.), Wiley, Chichester, p.187 (1987).

Bashkin, J.; Bartosiewicz, M.; Roach, D.; Leong, J.; Barker, D.; Johnston, R. *J. Capillary Electrophor.* **3**, 61 (1996).

Behringer, J. In: *Molecular Spectroscopy, Vol. 2*, Barrow, R. F.; Long, D. A.; Millen, D. J. (Eds.), The Chemical Society, London, p. 100, 1974.

Beijersten, I.; Westerlund, D. *J. Chromatogr. A* **716**, 389 (1995).

Bello, J. M.; Narayanan, V. A.; Stokes, D. L.; Vo-Dinh, T. *Anal. Chem.* **62**, 2437 (1990).

Bello, J. M.; Stokes, D. L.; Vo-Dinh, T. *Anal. Chem.* **61**, 1779 (1989).

Bello, J. M.; Stokes, D. L.; Vo-Dinh, T. *Appl. Spectrosc.* **43**,1325 (1989).

Bello, J. M.; Stokes, D. L.; Vo-Dinh, T. *Anal. Chem.* **62**, 1349 (1990).

Bello, J. M.; Vo-Dinh, T. *Appl. Spectrosc.* **44**, 63 (1990).

Belton, P. S.; Wright, K. M. *Spectrochim. Acta*, **50A**, 689 (1994).

Benoit, V.; Yappert, M. C. *Anal. Chem.* **63**, 179 (1991).

Berthold, A.; Laserna, J. J.; Winefordner, J. D. *Appl. Spectrosc.* **41**, 1137 (1987).

Betzig, E.; Chichester R. J. *Science* **262**, 1422 (1993).

Bianchi, N.; Mischiati, C.; Feriotto, G.; Gambri, R. *Nucl. Acids Res.* **21**, 3595 (1993).

Bier, M., Ed. *Electrophoresis: Theory, Methods, and Applications, Vol. 1* Academic Press, New York, 1959.

Bier, M., Ed. *Electrophoresis: Theory, Methods, and Applications, Vol. 2* Academic Press, New York, 1967.

372

Bilhorn, R. B.; Epperson, P. M.; Sweedler, J. V.; Denton, M. B. *Appl. Spectrosc.* **41**, 1125 (1987).

Bilhorn, R. B.; Denton, M. B. *Appl. Spectrosc.* **43**, 1 (1989).

Bilhorn, R. B.; Denton, M. B. *Appl. Spectrosc.* **44**, 1538 (1990).

Birke, R. L.; Lombardi, J. R. In: *Advances in Laser Spectroscopy, Vol. 1*, Garetz, B.; Loombardi, J. R. (Eds.), Heyden, Philadelphia, p. 143, 1982.

Blokhintsev, D. I. *Principles of Quantum Mechanics*, Ally and Bacon, Boston, 1964.

Boero, F. J.; Roth, P. G. *Appl. Spectrosc.* **41**, 463 (1987).

Boisde, G.; Blanc, F.; Mauchien, P.; Perez, J. J. *Fiber Optic Chemical Sensors and Biosensors*, Wolfbeis, O. S. (Ed.), CRC Press, Boca Raton, FL, Vol 2 pp. 135-49 (1991).

Bowyer, J.; Alarie, J. P.; Sepaniak, M.; Vo-Dinh, T.; Thompson, R. *Analyst* **116**, 117 (1991).

Bristow, M. P. F. *Appl. Opt.* **18**, 952 (1979).

Buchberger, W. *Fresenius J. Anal. Chem.* **354**, 797 (1996).

Buncick, M. C.; Warmack, R. J.; Little, J. W.; Ferrell, T. L. *Bull. Am. Phys. Soc.* **29**, 129 (1984).

Burstein, E.; Chen, Y. J.; Chen, C. Y.; Lundquist, S.; Tosath, E. *Solid State Commun.* **29**, 567 (1979).

Campiglia, A. D.; Moreau, F.; Hueber, D. M.; Vo-Dinh, T. *Anal. Chim. Acta* **351**, 229 (1997).

Campion, A.; Woodruff, W. H. *Anal. Chem.* **59**, 1299A (1987).

Cao, P.; Moini, M. *J. Am. Soc. Mass Spectrom.* **8**, 561 (1997).

Carrabba, M. M.; Edmonds, R. B.; Raugh, R. D. *Anal. Chem.* **59**, 2559 (1987).

373

Carrabba, M . M.; Spencer, K. M.; Rich, C.; Rauh, R. D. *Appl. Spectrosc.* **44**, 1558 (1990).

Carron, K.; Mullen, K.; Lanouette, M.; Angersbach, H. *Appl. Spectrosc.* **44**, 63 (1990).

Carron, K.; Peiterson, L.; Lewis, M. *Environ. Sci. Technol.* **26**, 1950 (1992).

Chang, R. K.; Furtak, T. E. (Eds.) *Surface-Enhanced Raman Scattering*, Plenum, New York, 1982.

Chapman, D. L. *Phil. Mag.* **25**, 475 (1913).

Chen, C. -Y.; Morris, M. D. *Appl. Spectrosc.* **42**, 515 (1988).

Chen, M. C.; Tsai, S. D.; Chen, M. R.; et al. *Phys. Rev., B* **51**, 4507 (1995).

Cheng, Y. -F.; Dovichi, N. J. *Science* **242**, 562 (1988).

Chien, J. B.; Wallingford, R. A.; Ewing, A. G. *J. Neurochem.* **54**, 633 (1990).

Christensen, K. A.; Bradley, N. L.; Morris, M. D.; Morrison, R. V. *Appl. Spectrsoc.* **49**, 1120 (1995).

Chu, B. *Laser Light Scattering*, Academic Press, New York, 1974.

Clark, B. K.; Nickles, C. L.; Morton, K. C.; Kovac, J.; Sepaniak, M. J. *J. Microcol. Sep.* **6**, 503 (1994).

Clark, B. K.; Sepaniak, M. J. *J. Microcol. Sep.* **5**, 275 (1993).

Clark, B. K.; Vo-Dinh, T.; Sepaniak, M. J. *Anal. Chem.* **67**, 680 (1995).

Collins, R. J.; Nelson, D. F.; Schawlow, A. L.; Bond, W.; Garrett, C. G. B.; Kaiser, W. *Phys. Rev. Lett.* **5**, 303 (1960).

Cooney, T. F.; Skinner, H. T.; Angel, S. M. *Appl. Spectrosc.* **50**, 836 (1996). a

Cooney, T. F.; Skinner, H. T.; Angel, S. M. *Appl. Spectrosc.* **50**, 849 (1996). b

Cooper, J. B.; Fletcher, P. E.; Albin, S.; Vess, T. M.; Welch, W. T. *Appl. Spectrosc.* **49**, 1962 (1995).

Cooper, J. B.; Wise, K. L.; Jensen, B. J. *Anal. Chem.* **69**, 1973 (1997).

Cotton, T. M. In: *Spectroscopy of Surfaces*, Clark, R. J. H.; Hester, R. E. (Eds.), Wiley, New York, p. 91, 1988.

Cotton, T. M.; Brandt, E. S. In: *Physical Methods of Chemistry*, Wiley, New York, 1992.

Creighton, J. A. *Surf. Sci.* **173**, 665 (1986).

Creighton, J. A. In: *Spectroscopy of Surfaces*, Clark, R. J. H.; Hester, R. E. (Eds.), Wiley, New York, p. 37, 1988.

Davydov, A. S. *Quantum Mechanics*, Pergamon, Oxford, 1965.

de Bakker, C. J.; Fredericks. P. M. *Appl. Spectrosc.* **49**, 1766 (1995).

Deckert, V.; Kiefer, W. *Appl. Spectrosc.* **46**, 332 (1992).

Deckert, V.; Zeisel, D. Zenobi, R., Vo-Dinh, T. *Anal. Chem.* **70**, 2646 (1998).

Delonge, T.; Fouckhardt, H. *J. Chromatogr. A* **716**, 135 (1995).

De Olivera, W. A.; Narayanaswamy, R. *Talanta* **39**, 1499 (1992).

Desbene, P. L.; Morin, C. *J. Spectra Anal.* **25**, 15 (1996).

Deschaines, T. O.; Carron, K. T. *Appl. Spectrosc.* **51**, 1355 (1997).

Deyl, Z., Ed. *Electrophoresis: Survey of Techniques and Applications* Elsevier, Amsterdam, 1979.

Dickens, J. E.; Sepaniak, M. J. *J. Microcol. Sep.* **11**, 45 (1999).

Dirac, P. A. M. *Proc. Roy. Soc. London A* **114**, 710 (1927).

Djordjevic, N. M.; Ryan, K. *J. Liq. Chromatogr. Relat. Technol.* **19**, 201 (1996).

Djordjevic, N. M.; Widder, M.; Kuhn, R. *J. High Resolut. Chromatogr.* **20**, 189 (1997).

Dornhaus, R. In: *Springer Tracts in Modern Physics, Vol. 22*, Springer, Berlin, p.201, 1982.

Dornhaus, R.; Benner, R. E.; Chang, R. K.; Chabay, I. *Surf. Sci.* **101**, 493 (1980).

Efrima, S. In: *Modern Aspects of Electrochemistry, Vol. 16*, Conway, B. E.; White, R. E.; Bockris, O. M. (Eds.), Plenum, New York, p. 253 (1985).

Eigen, M.; Rigler, R. *Proc. Natl. Acad. Sci. USA* **91**, 5740 (1994).

Engert, C. T.; Michelis, T.; Kiefer, W. *Appl. Spectrosc.* **45**, 1333 (1991).

Enlow, P. D.; Buncick, M. C.; Warmack, R. J.; Vo-Dinh, T. *Anal. Chem.* **58**, 1119 (1986).

Everaerts, F. M.; Beckers, J. L.; Verheggen, Th. P. E. M. *Isotachophoresis: Theory, Instrumentation, and Applications* Elsevier, Amsterdam, 1976.

Ewing, A. G.; Wallingford, R. A.; Olefirowicz, T. M. *Anal. Chem.* **61**, 292A (1989).

Fed. Regist. **54**, 52158 (1989).

Figeys, D.; Ahmadzedeh, H.; Arriaga, E.; Dovichi, N. J. *J. Chromatogr., A* **744**, 325 (1996).

Flaugh, P. L.; O'Donnel, S. E.; Asher, S. A. *Appl. Spectrosc.* **38**, 847 (1984).

Fleischmann, M. J.; Hendra, P.J.; McQuillan, A. J. *Chem. Phys. Lett.* **26**, 163 (1974).

Fleischmann, M. J.; Graves, P. R.; Robinson, J. *J. Electroanal. Chem.* **182**, 87 (1985).

Foret, F.; Deml, M.; Kahle, V.; Bocek, P. *Electrophoresis* **7**, 430 (1986).

Fowler, W. K. *Amer. Lab.* **12**, 80 (1982).

Freeman R. G.; Grabar, K. C.; Allison, K. J.; Bright, R. M.; Davis, J. A.; Guthrie, A. P.; Hommer, M. B.; Jackson, M. A.; Smith, P. C.; Walter, D. G.; Natan, M J. *Science* **267**, 1629 (1995).

Fung, E. N.; Yeung, E. S. *Anal. Chem.* **67**, 1913 (1995).

Furtak, T. E.; Rayes, J. *Surf. Sci.* **93**, 351 (1980).

Furtak, T. E. In: *Advances in Laser Spectroscopy, Vol. 2*, Garrett, B. A.; Lobaradi, J. R. (Eds.), Wiley, New York, p.175, 1983.

Futamata, M. *Appl. Spectrosc.* **50**, 199 (1996).

Gaal, O.; Medgyesi, G. A.; Verczkey, K. *Electrophoresis in the Separation of Biological Macromolecules* Wiley-Interscience, Chichester, U. K., 1980.

Ganter, E.; Steinhart, D. *Fresenius, J. Anal. Chem.* **338**, 2 (1990).

Garrell, R. L. *Anal. Chem.* **61**, 401A (1989).

Gersten, J. I.; Nitzan, A. *J. Chem. Phys.* **73**, 3023 (1980).

Gilman, S. D.; Ewing, A. G. *Anal. Methods Instrum.* **2**, 133 (1995).

Goldstein, S. R.; Kidder, L. H.; Herne, T. M.; Levin, I. W.; Lewis, E. N. *J. Microsc. Oxfd.* **184**, 35 (1996).

Goudonnet, J. P.; Begun, G. M.; Arakawa, E. T. *Chem. Phys. Lett.* **92**, 197 (1982).

Gouy, G. *J. Phys. Radium* **9**, 457 (1910). a

Gouy, G. *Compt. Rend.* **149**, 654 (1910). b

Grossman, P. D.; Colburn, J. C., Eds. *Capillary Electrophoresis: Theory and Practice* Academic Press, New York, 1992.

Gupta, N.; Fell, N. F. *Talanta* **45**, 279 (1997).

Harris, D. C.; Bertolucci, M. D. *Symmetry and Spectroscopy*, Oxford University Press, New York, 1978.

Haumann, I.; Baechmann, K. *J. Chromatogr. A* **717**, 385 (1995).

Heard, F. J.; Manning, M. P. *Am. Ind. Hyg. Assoc. J.* **44**, 778 (1980).

Heaton, H. I. *Appl. Opt.* **36**, 6739 (1997).

Hecht, E. *Optics*, Addison-Wesley, Reading, 1987.

Heftmann, E. *Chromatography, 2nd Ed.* Reinhold, New York, Ch. 10, 1976.

Heiger, D. N.; Cohen, A. S.; Karger, B. L. *J. Chromatogr.* **516**, 33 (1990).

Hendra, P. J.; Ellis, G.; Cutler, D. J. *J. Raman Spectrosc.* **19**, 413 (1988).

Hester, R. E. In: *Raman Spectroscopy:Theory and Practice*, Szymanski (Ed.), Plenum Press, New York, 1967.

Heyns, J. B.; Sears, L. M.; Corcoran, R. C.; Carron, K. T. *Anal. Chem.* **66**, 1572 (1994).

Hill, W.; Wehling, B.; Gibbs, C. G.; Gutsche, C. D.; Klockow, D. *Anal. Chem.* **67**, 3187 (1995).

Hill, W.; Wehling, B.; Klockow, D. *Sensors and Actuators B* **18-19**, 188 (1994).

Hirschfield, T.; Chase, B. *Appl. Spectrosc.* **40**, 133 (1986).

Hjerten, S. *J. Chromatogr.* **347**, 191 (1985).

Hjerten, S.; Elenbring, K.; Kilar, F.; Liao, J. -L.; Chen, A. J. C.; Siebert, C. J.; Zhu, M. -D. *J. Chromatogr.* **403**, 47 (1987).

Hjerten, S.; Zhu, M. -D. *J. Chromatogr.* **346**, 265 (1985).

Hoffman, C. G.; Menzebach, H. U.; Oelichmann, B.; Schrader, B. *Appl. Spectrosc.* **46**, 568 (1992).

Holland, R. D.; Sepaniak, M. J. *Anal. Chem.* **65**, 1140 (1993).

Huang, X.; Gordon, M. J.; Zare, R. N. *J. Chromatogr.* **425**, 385 (1988).

Huang, X.; Pang, T. -K. J.; Gordon, M. J.; Zare, R. N. *Anal. Chem.* **59**, 2747 (1987).

Huang, X. C.; Quesada, M. A.; Mathies, R. A. *Anal. Chem.* **64**, 967 (1992).

Huang, X.; Zare, R. N.; Sloss, S.; Ewing, A. G. *Anal. Chem.* **63**, 189 (1991).

Hueber, D. M.; Stevenson, C. L.; Vo-Dinh, T. *Appl. Spectrosc.* **49**, 1624 (1995).

Hunkapiller, T.; Kaiser, R. J.; Koop, B. F.; Hood, L. *Science* **254**, 59 (1991).

Ibrahim, A.; Oldham, P.; Stokes, D. L.; Vo-Dinh, T. *J. Raman Spectrosc.* **27**, 887 (1996).

Ingle, J. D., Jr.; Crouch, S. R. *Spectrochemical Analysis*, Prentice Hall, Englewood Cliffs, NJ, p.2, 1988.

Isola, N. R.; Stokes, D. L.; Vo-Dinh, T. *Anal. Chem.* **70**, 1352 (1998).

Jeanmaire, D. J.; Van Duyne, R. P. *J. Electroanal. Chem.* **84**, 1 (1977).

Jennings, C.; Aroca, R.; Hor, A. M.; Loutfy, R. O. *Anal. Chem.* **56**, 2033 (1984).

Jones, W. R.; Soglia, J.; McGlynn, M.; Haber, C.; Reineck, J.; Krstanovic, C. *Amer. Lab.* **28**, 25 (1996).

Jorgenson, J. W. *Anal. Chem.* **58**, 743A (1986).

Jorgenson, J. W.; Lukacs, K. D. *Anal. Chem.* **53**, 1298 (1981).

Jorgenson, J. W.; Lukacs, K. D. *Science* **222**, 266 (1983).

Kambhampati, P.; Child, C. M.; Foster, M. C.; Campion, A. *J. Chem Phys.* **108**, 5013 (1998).

Keller, R. A.; Ambrose, W. P.; Goodwin, P. M.; Jett, J. H.; Martin, J. C.; Wu, M. *Appl. Spectrosc.* **50**, 12A (1996).

379

Kerker, M. *The Scattering of Light and Other Electromagnetic Radiation*, Academic Press, New York, 1969.

Kerker, M.; Blatchford, C. G. *Phys. Rev. B* **26**, 4052 (1982).

Kerker, M. *Acc. Chem. Res.* **17**, 271 (1984).

Kersey, A. D.; Dandridge, A. *IEEE Trans. Compon. Hybrids Manuf. Technol.* **13**, 137 (1990).

Khrapko, K.; Hanekamp, J. S.; Thinly, W. G.; Belenkii, A.; Foret, F.; Karger, B. L. *Nucl. Acids Res.* **22**, 364 (1994).

Kneipp, K. *Exp. Tech. Phys.* **38**, 1 (1990).

Kneipp, K.; Wang, Y.; Kneipp, H.; Perelman, L. T.; Itzkan, I.; Dasari, R. R.; Feld, M. *Phys. Rev. Lett.* **78**, 1667 (1997).

Kneipp, K.; Kneipp, H.; Deinum, G.; Itzkan, I.; Dasari, R. R.; Feld, M. *Appl. Spectrosc.* **52**, 175 (1998). a

Kneipp, K.; Kneipp, H.; Manoharan, R.; Hanlon, E. B.; Itzkan, I.; Dasari, R. R.; Feld, M. *Appl. Spectrosc.* **52**, 1493 (1998). b

Knoll, P.; Singer, R.; Kiefer, W. *Appl. Spectrosc.* **44**, 776 (1990).

Kradjel, C.; Fresenius, Z. *Anal. Chem.* **65**, 339 (1991).

Kramers, H. A.; Heisenburg, W. *Z. Physik* **31**, 681 (1925).

Kriz, D.; Ramstrom, O.; Svensson, A.; Mosbach, K. *Anal. Chem.* **67**, 2142 (1995).

Kuhr, W.; Yeung, E. S. *Anal. Chem.* **60**, 1832 (1988). a

Kuhr, W.; Yeung, E. S. *Anal. Chem.* **60**, 2642 (1988). b

Kurtz, I.; Dwelle, R.; Katzka, P. *Rev. Sci. Instrum.* **58**, 1996 (1987).

Kuypers, A. W. H. M.; Willems, P. M. W.; van der Schans, M. J.; Linssen, P. C. M.; Wessels, H. M. C.; de Bruijn, C. H. M. M.; Everaerts, F. M.; Mensinkk, E. J. B. M. *J. Chromatogr., B* **621**, 149 (1993).

Laserna, J. J.; Torres, E. L.; Winefordner, J. D. *Anal. Chim. Acta* **200**, 469 (1987)

Lacy, W. B.; Williams, J. M.; Wenzler, L. A.; Beebe, T. P., Jr.; Harris, J. M. *Anal. Chem.* **68**, 1003 (1996).

Lada, M. W.; Kennedy, R. T. *Anal. Chem.* **68**, 2790 (1996).

Lambeck, P. V. *Proc. SPIE Int. Soc. Opt. Eng. 1511 (Fiber-Opt Sens.:Eng. Appl.)*, 100 (1991).

Lee, P. C.; Meisel, D. *J. Phys. Chem.* **86**, 3391 (1982).

Lee, S. Y.; Heller, E. J. *J. Chem. Phys.* **71**, 4777 (1979).

Lee, Y. H.; Dai, S.; Young, J. P. *J. Raman Spectrosc.* **28**, 63S (1997).

Lee, Y. -T.; Whang, C. -W. *J. Chromatogr., A* **746**, 269 (1996).

Lerchi, M.; Bakker, E.; Rusterholz, B.; Simon, W. *Anal. Chem.* **64**, 1534 (1992).

Lewis, E. N.; Kalasinsky, V. F.; Levin, I. W. *Anal. Chem.* **60**, 2658 (1988).

Lewis, E. N.; Treado, P. J.; Levin, I. W. *Appl. Spectrosc.* **47**, 539 (1993).

Liao, P. F. In: *Surface-Enhanced Raman Scattering*, Chang, R. K.; Furtak, T. E. (Eds.), Plenum Press, New York, p. 379, 1982.

Lin, Q.; Zhang, R.; Liu, G. *J. Liq. Chromatogr. Relat. Technol.* **20**, 1123 (1997).

Linhardt, R. J.; Pervin, A. *J. Chromatogr., A* **720**, 323 (1996).

Long, D. A. *Raman Spectroscopy*, McGraw-Hill, New York, 1974.

Long, D. A.; Matterson, H. S.; Woodward, L. A. *Proc. Roy. Soc. London*, **224A**, 33 (1954).

Loo, B. H. *J. Phys. Chem.* **87**, 3003 (1983).

Lu, B.; Westerlund, D. *Electrophoresis* **17**, 341 (1996).

Luckey, J. A.; Drossman, H.; Kostichka, A. J.; Mead, D. A.; D'Cunha, J.; Norris, T. B.; Smith, L. M. *Nucl. Acids Res.* **18**, 4417 (1990).

Lund, P. A.; Smardzewski, R. R.; Terault, D. E. *Chem. Phys Lett.* **89**, 508 (1982).

Lyot, B. *C. R. Acad. Sci.* **197**, 1593 (1933).

Ma, J.; Li, Y.-S. *Appl. Spectrosc.* **48**, 1529 (1994).

Maiman, T. H. *Nature* **187**, 493 (1960).

Maiman, T. H.; Hoskins, R. H.; D'Haenens, I. J.; Asawa, C. K.; Evtuhov, V. *Phys. Rev.* **123**, 1151 (1961).

Malmstadt, H. V.; Franklin, M. L.; Horlick, G. *Anal. Chem.* **44**, 63A (1972).

Manz, A.; Harrison, D. J.; Werpoorte, E. M. J.; Fettinger, J. C.; Paulus, A.; Ludi, H.; Widmer, H. M. *J. Chromatogr.* **593**, 253 (1992).

Margalith, E.; Vo-Dinh, T. *Analusis* **23**, 45 (1995).

Masterson, H. J.; Sharp, G. D.; Johnson, K. M. *Opt. Lett.* **14**, 1249 (1989).

Mathies, R. A.; Peck, K.; Stryer, L. *Anal. Chem.* **62**, 1786 (1990).

Matsubara, N.; Terabe, S. *Methods Enzymol.* **270**, 319 (1996).

Mazereeuw, M.; Hofte, A. J. P.; Tjaden, U. R.; van der Greef, J. *Rapid Commun. Mass Spectrom.* **11**, 981 (1997).

McCreery, R. L.; Horn, A. J.; Spencer, J.; Jefferson, E. *J. Pharm. Sci.* **87**, 1 (1998).

Meier, M.; Wokaun, A. *Opt. Lett.* **8**, 58, (1983).

Meier, M.; Wokaun, A.; Vo-Dinh, T. *J. Phys. Chem.* **89**, 1843 (1985).

Michon, G. J.; Burke, H. K. *Dig. IEEE, Int. Solid State Circuits Conf.* **16**, 138 (1973).

Mikkers, F. E. P.; Everaerts. F. M.; Verheggen, Th. P. E. M. *J. Chromatogr.* **169**, 11 (1979).

Miller, C. M.; Mettler, S. C. White, I. A. *Opt. Eng. (NY)* **28**, 363 (1991).

Moerner, W. E. *Science* **265**, 46 (1994).

Moerner, W. E.; Kadar, L. *Anal. Chem.* **61**, 1217A (1989).

Moody, R. L.; Vo-Dinh, T.; Fletcher, W. H. *Appl. Spectrosc.* **41**, 966 (1987).

Moreau, F.; Moreau, S. M.; Hueber, D. M.; Vo-Dinh, T. *Appl. Spectrosc.* **50**, 1295 (1996). a

Moreau, F.; Hueber, D. M.; Vo-Dinh, T. *Instrum. Sci. Tehnol.* **24**, 179 (1996). b

Morris, H. R.; Hoyt, C. C.; Miller, P.; Treado, P. F. *Appl. Spectrosc.* **50**, 805 (1996).

Morse, P. M. *Phys. Rev.* **34**, 57 (1929).

Moskovitz, M.; DiLella, D. P. In: *Surface-Enhanced Raman Scattering*, Chang, R. K.; Furtak, T. E. (Eds.), Plenum, New York, p. 243, 1982.

Moskovits, M. *Rev. Mod. Phys.* **57**, 783 (1985).

Mourey, T.; Carpenter, A. P.; Siggia, S.; Lane, A. *Anal. Chem.* **48**, 1592 (1976).

Mueller, D.; Jelinek, I.; Opekar, F.; Stulik, K. *Electroanalysis* **8**, 722 (1996).

Mullen, K. I.; Carron, K. T. *Anal. Chem.* **63**, 2196 (1991).

Mullen, K.; Wang, D.; Crane, L.; Carron, K. *Anal. Chem.* **64**, 930 (1992).

Murray, C. A.; Dierker, S. B. *J. Opt. Soc. Am. A* **3**, 2151 (1986).

Myers, A. B.; Mathies, R. A. In: *Biological Applications of Raman Spectroscopy, Vol. 2*, Wiley, New York, p.1, 1987.

Myrick, M. L.; Angel, S, M, *Appl. Spectrosc.* **44**, 565 (1990).

Myrick, M. L.; Angel, S. M.; Desiderio, R. *Appl. Opt.* **29**, 1333 (1990).

Myseis, K. J. *Introduction to Colloid Chemistry* Interscience, New York, Ch. 15-16, 1976.

Narayanan, V. A.; Begun, G. M.; Stokes, D. L.; Sutherland, W. S.; Vo-Dinh, T. *J. Raman Spectrosc.* **23**, 281 (1992).

Narayanan, V. A.; Bello, J. M.; Stokes, D. L.; Vo-Dinh, T. *Analusis* **19**, 307 (1991).

Newmann, C. D.; Bret, G. G.; McCreery, R. L. *Appl. Spectrosc.* **46**, 262 (1992).

Ng, K. C.; Whitten, W. B.; Arnold, S.; Ramsey, J. M. *Anal. Chem.* **64**, 2914 (1992).

Nguyen, D. C.; Keller, R. A. *Anal. Chem.* **59**, 2158 (1987).

Ni, F.; Sheng, R.; Cotton, T. M. *Anal. Chem.* **62**, 1958 (1990).

Nie, S.; Chiu, D. T.; Zare, R. N. *Science* **266**, 1018 (1994).

Nie, S.; Emory, S. R. *Science* **275**, 1102 (1997).

Nishi, H. *J. Chromatogr., A* **780**, 243 (1997).

Nishi, H.; Terabe, S. *J. Chromatogr., A* **735**, 3 (1996).

Norris, J. O. W. *Analyst* **114**, 1359 (1989).

Nussberger, S.; Foret, F.; Hebert, S. C.; Karger, B. L.; Hediger, M. A. *Biophys. J.* **70**, 998 (1996).

Oguri, S.; Fujiyoshi, T.; Miki, Y. *Analyst* **121**, 1683 (1996).

Olivares, J. A.; Nguyen, N. T.; Yonker, C. R.; Smith, R. D. *Anal. Chem.* **59**, 1230 (1987).

Orrit, M.; Bernard, J. *Phys. Rev. Lett.* **65**, 2716 (1990).

Orrit, M.; Bernard, J.; Personov, R. *J. Phys. Chem.* **97**, 10256 (1993).

Orwar, O.; Fishman, H. A.; Ziv, N. E.; Scheller, R. H.; Zare, R. N. *Anal. Chem.* **67**, 4261 (1995).

Otsuka, K.; Terabe, S. *Methods Mol. Biol.* **52**, 125 (1996).

Otto, A. *Surf. Sci.* **75**, 1392 (1978).

Otto, A. *Appl. Surf. Sci.* **6**, 309 (1980).

Otto, A. In: *Light Scattering in Solids, Vol. IV*, Cardona, M.; Güntherodt, G. (Eds.), Springer, Berlin, 1983.

Otto, A.; Mrozek, I.; Grabhorn, H.; Akermann, W. *J. Phys. Condens. Mattter* **4**, 1143 (1992).

Otto, A., Timper, J.; Billman, J.; Kovaks, G.; Pockrand, I. *Surf. Sci.* **92**, L55 (1980).

Pagannone, M.; Fornari, B.; Mattei, G. *Spectrochim. Acta* **43**, 621 (1987).

Pal, A.; Stokes, D. L.; Alarie, J. P.; Vo-Dinh, T. *Anal. Chem.* **67**, 3154 (1995).

Palmes, E. D. *Proc. Symp. Assessing Ind. Hig. Monit. Needs Coal Convers. Oil Shale Ind.* 203 (1979).

Pandey, P. K.; Schatz, G. C. *J. Chem. Phys.* **80**, 2959 (1984).

Panitz, J.-C.; Zimmermann, F.; Fischer, F.; Hafner, W.; Wokaun, A. *Appl. Spectrosc.* **48**, 454 (1994).

Parker, S. F.; Williams, K. P. J.; Hendra, P. J.; Turner, A. J. *Appl. Spectrosc.* **42**, 796 (1988).

Pauling, L.; Wilson E. B. Jr. *Introduction to Quantum Mechanics, with Applications to Chemistry*, McGraw-Hill, New York, 1935.

Peck, K.; Stryer, L.; Glazer, A. N.; Mathies, R. A. *Proc. Natl. Acad. Sci. USA* **86**, 4087 (1989).

Pelletier, M. J. *Appl. Spectrosc.* **44**, 1699 (1990).

Pelletier, M. J.; Reeder, R. C. *Appl. Spectrosc.* **45**, 765 (1991).

Pelletier, M. J. *Appl. Spectrosc.* **46**, 395 (1992).

Pemberton, J. E. In: *Electrochemical Interfaces: Modern Techniques for In-Situ Characterization*, Abruna, H. D. (Ed.), VCH Verlag Chemie, Berlin, 1991.

Pemberton, J. E.; Sobocinski, R. L. *J. Am. Chem. Soc.* **111**, 432 (1989).

Pentoney, S. L., Jr.; Huang, X.; Burgi, D. S.; Zare, R. N. *Anal. Chem.* **60**, 2625 (1988).

Persson, B. N. J. *Chem. Phys. Lett.* **82**, 56 (1981).

Pettinger, B.; Wenneng, U.; Wetzel, H. *Surf. Sci.* **101**, 409 (1980).

Piletsky, S. A.; Piletskaya, E. V.; Elskaya, A. V.; Levi, R.; Yano, K.; Karube, I. *Anal. Lett.* **30**, 445 (1997).

Placzek, G. In: *Handbuch der Radiologie*, Marx, E. (Ed.), Akademische Verlagsgesekkschaft, Leipzig, p. 205, 1934.

Plocek, J.; Novotny, M. V. *J. Chromatogr. A.* **757**, 215 (1997).

Pockrand, I. *Surface-Enhanced Raman Vibrational Studies at Solid/Gas Interfaces*, Springer, Berlin, 1984.

Pretorius, V.; Hopkins, B. J.; Schieke, J. D. *J. Chromatogr.* **99**, 23 (1974).

Puppels, G. J.; Huizinga, A.; Krabbe, H. W.; de Boer, H. A.; Gijsbers, G.; de Mul, F. F. M. *Rev. Sci. Instrum.* **61**, 3709 (1990).

Puppels, G. J.; de Grauw, C. G.; te Plate, M. B. J.; Greve, J. *Appl. Spectrosc.* **48**, 1399 (1994).

Raman, C. V. *Indian J. Phys.* **2**, 387 (1928). a

Raman, C. V. *Nature* **121**, 619 (1928). b

Raman C. V.; Krishnan, K. S. *Nature* **121**, 711 (1928). a

Raman C. V.; Krishnan, K. S. *Nature* **121**, 501 (1928). b

Ramsey, R. S.; McLuckey, S. A. *J. Microcolumn Sep.* **7**, 461 (1995).

Rao, C. N. R.; Venkataraghavan, R. *Spectrochim. Acta* **18**, 541 (1962).

Rasetti, F. *Nuovo Cimento* **9**, 261 (1930).

Rassi, Z. E.; Postlewait, J.; Mechref, Y.; Ostrander, G. K. *Anal. Biochem.* **244**, 283 (1997).

Ren, J.; Li, B.; Deng, Y.; Cheng, J. *Talanta* **42**, 1891 (1995).

Rice, C. L.; Whitehead, R. J. *J. Phys. Chem.* **69**, 4017 (1965).

Ritchie, R. H. *Phys. Rev.* **106**, 879 (1957).

Rose, D. R., Jr.; Jorgenson, J. W. *J. Chromatogr.* **447**, 117 (1988).

Ruiz-Martinez, M. C.; Berka, J.; Belenkii, A.; Foret, F.; Miller, A. W.; Karger, B. L. *Anal. Chem.* **65**, 2851 (1993).

Ruperez, A.; Laserna, J. J. In: *Modern Techniques in Raman Spectroscopy*, Laserna, J. J. (Ed.), Wiley, New York, 1996.

Sabbaghzadeh, J.; Buell, W.; Holder, J.; Fink, M. *Appl. Phys. B* **60**, S261 (1995).

Saito, M.; Kikiuchi, K. *Opt. Rev.* **4**, 527 (1997).

Sarmini, K.; Kenndler, E. *J. Chromatogr., A* **792**, 3 (1997).

Schaeffer, S.; Gareil, P.; Dezael, C.; Richard, D. *J. Chromatogr. A.* **740**, 151 (1996).

Schatz, G. C.; Van Duyne, R. P. *Surf. Sci.* **101**, 425 (1980).

Schatz, G. C. *Acc. Chem. Res.* **17**, 370 (1984).

387

Schrader, B. In: *Infrared and Raman Spectroscopy: Methods and Applications*, Schrader, B. (Ed.), VCH Verlagsgesellschaft mbH, Weinheim, 1995.

Schulte, A. T.; Lenk, T. J.; Hallmark, V. M.; Rabolt, J. F. *Appl. Spectrosc.* **45**, 325 (1991).

Schwab, S. D.; McCreery, R. L. *Anal. Chem.* **56**, 2199 (1984).

Schwab, S. D.; McCreery, R. L.; Gamble, F. T. *Anal. Chem.* **58**, 2486 (1986).

Seidel, B. S.; Steinle, E.; Faubel, W.; Ache, H. J. *Proc. SPIE-Int. Soc. Opt. Eng.* **2836**, 283 (1996)

Sepaniak, M. J.; Cole, R. O.; Clark, B. K. *J. Liq. Chromatogr.* **15**, 1023 (1992). b

Sepaniak, M. J.; Swaile, D. F.; Cole, R. O.; Powell, A. C. in *Capillary Electrophoresis: Theory and Practice*, Grossmann, P. D.; Colburn, J. C. (Eds.), Academic Press, New York, pp. 159-189, 1992. a

Sepaniak, M. J.; Tromberg, B.; Vo-Dinh, T. *Prog. Anal. Spectrosc.* **11**, 481 (1988).

Sepaniak, M. J.; Vo-Dinh, T.; Stokes, D. L.; Tropina, V.; Dickens, J. E. *Talanta* **43**, 1889 (1996).

Sepaniak, M. J.; Vo-Dinh, T.; Tropina, V.; Stokes, D. L. *Anal. Chem.* **69**, 3806 (1997).

Shera, E. B.; Seitzinger, N. K.; Davis, L. M.; Keller, R. A.; Soper, S. A. *Chem. Phys. Lett.* **174**, 553 (1990).

Shihabi, Z. K. *J. Chromatogr., A* **744**, 231 (1996).

Shipp, W. S.; Biggins, J.; Wade, C. W. *Rev. Sci. Instrum.* **47**, 565 (1976).

Siiman, O.; Bumm, L. A.; Callaghan, R.; Blatchford, C. G.; Kerker, M. *J. Phys. Chem.* **87**, 1014 (1983).

Sims, G. R.; Denton, M. B. In: *Multichannel Image Detectors, Vol. 2.* Talmi, Y. (Ed.), ACS Symposium Series 236, Washington, D. C., Chapt. 5, 1983.

Singh, R. B.; Mukul, M.; Sharma, S. K. *Indian J. Phys.* **62B**, 556 (1988).

Smith, L. M. *Science* **262**, 530 (1993).

Smith, R. D.; Olivares, J. A.; Nguyen, N. T.; Udseth, H. R. *Anal. Chem.* **60**, 436 (1988).

Smith, W. H. *Publ. Astron. Soc. Pac.* **99**, 1344 (1987).

Smith, W. H.; Smith, K. M. *Expir. Astron.* **1**, 329 (1991).

Soper, S. A.; Kuwana, T. *Appl. Spectrosc.* **43**, 1180 (1989).

Sprunt, J. C.; Jayasooriya, U. A. *Appl. Spectrosc.* **51**, 1410 (1997).

Sqalli, O.; Plaza, P.; Jouan, M.; Dao, N. Q. *Analusis* **19**, 115 (1991).

Stalbom, B. M.; Torven, A; Lundberg, L. G. *Anal. Biochem.* **217**, 91 (1994).

Staller, T. D.; Sepaniak, M. J. *Instrum. Sci. Technol.* **23**, 235 (1995).

Stebbins, M. A.; Hoyt, A. M.; Sepaniak, M. J.; Hurlburt, B. K. *J. Chromatogr., B* **683**, 77 (1996).

Stebbins, M. A.; Schar, C. R.; Peterson, C. B.; Sepaniak, M. J. *J. Chromatogr. B* **697**, 181 (1997).

Stern, O. *Z. Elektrochem.* **30**, 508 (1924).

Stevenson, C. L.; Vo-Dinh, T. In: *Modern Techniques in Raman Spectroscopy*, Laserna, J.J. (Ed.), John Wiley and Sons, Chichester, 1996.

Stokes, D. L.; Alarie, J. P.; Vo-Dinh, T. *Proc. SPIE-Int. Soc. Opt. Eng.* 2504 (Environmental Monitoring and Hazardous Waste Site Remediation), 552 (1995).

Stokes, D. L.; Narayanan, V. A.; Vo-Dinh, T. *Anal. Chim. Acta.* (1999) in press.

Stokes, D. L.; Sepaniak, M. J.; Vo-Dinh, T. *Anal. Chim. Acta.* (1999) in press.

Stokes, D. L.; Vo-Dinh, T.; Sepaniak, M. J. *Biomed. Chromatogr.* **11**, 187 (1997).

Stokes, D. L.; Vo-Dinh, T. *Sensor Actuat. B-Chem.* (1999) in press.

Suh, J. S.; Dilella, D. P.; Moskovits, M. *J. Phys. Chem.* **87**, 1540 (1983).

Sutherland, W. S.; Alarie, J. P.; Dtokes, D. L.; Vo-Dinh, T. *Instrum. Sci. Technol.* **22**, 231 (1994).

Sutherland, W. S.; Alarie, J. P.; Edwards, A.; Tran, K. C.; Hurwitz, M.; Selph, W.; Margalith, E.; Vo-Dinh, T. *Analusis* **23**, 45 (1995).

Swaile, D. F.; Sepaniak, M. J. *Anal. Chem.* **63**, 179 (1991). a

Swaile, D. F.; Sepaniak, M. J. *J. Liq. Chromatogr.* **14**, 869 (1991). b

Sweedler, J. V.; Bilhorn, R. B.; Epperson, P. M.; Sims, G. R.; Denton, M. B. *Anal. Chem.* **60**, 282A (1988).

Sweedler, J. V. *Crit. Rev. Anal. Chem.* **24**, 59 (1993).

Swerdlow, H.; Gesteland, R. *Nucl. Acids Res.* **18**, 1415 (1990).

Takahashi, S.; Ahn, J. S.; Asaka, S.; Kitagawa, T. *Appl. Spectrosc.* **47**, 863 (1993).

Talmi, Y. *Anal. Chem.* **47**, 658A (1975).

Tang, J.; Albrecht, A. C. Developments in the Theories of Vibrational Raman Intensities. In: *Raman Spectroscopy,* Szymanski, H. A. (Ed.), Plenum Press, New York, p. 33, 1970.

Terabe, S.; Otsuka, K.; Ichikawa, K.; Tsuchiya, A.; Ando, T. *Anal. Chem.* **56**, 111 (1984).

Thompson, W. R.; Pemberton, J. E. *Anal. Chem.* **66**, 3362 (1994).

Tiselius, A. *Trans. Faraday Soc.* **33**, 524 (1937).

Tobias, R. S. *J. Chem. Educ.* **44**, 2 (1967).

Tobin, M. C. *J. Opt. Soc. Am.* **49**, 850 (1959).

Tobin, M. C. *Laser Raman Spectroscopy*, Chemical Analysis Series, Elving and Kolthoff (Ed.), Wiley Interscience, New York, 1971.

Treado, P. J.; Levin, I. W.; Lewis, E. N. *Appl. Spectrosc.* **46**, 553 (1992) a

Treado, P. J.; Levin, I. W.; Lewis, E. N. *Appl. Spectrosc.* **46**, 1211 (1992) b

Tromberg, B.; Sepaniak, M. J.; Alarie, J. P.; Vo-Dinh, T.; Santella, R. *Anal. Chem.* **60**, 1901 (1988).

Tromberg, B.; Sepaniak, M., Vo-Dinh, T.; Griffin, G. *Anal. Chem.* **59**, 1226 (1987).

Tsang, J. C.; Avouris Ph.; Kirtley, J. R. *J. Chem. Phys.* **79**, 493 (1983). a

Tsang, J. C.; Avouris Ph.; Kirtley, J. R. *J. Electron Spectrosc. Relat. Phenom.* **29**, 172 (1983). b

Tsang, J. C.; Avouris Ph.; Kirtley, J. R. *Chem. Phys. Lett.* **94**, 172 (1983). c

Tsang, J. C.; Demuth, J. E.; Sanda, P. N.; Kirtley, J. R. *Chem. Phys. Lett.* **71**, 54 (1980).

Ueba, H.; Ichimura, S.; Yamada, H. *Surf. Sci.* **119**, 433 (1982).

van de Hulst, H. C. *Light Scattering by Small Particles*, Dover, New York, 1981.

Van Duyne, R. P.; Hulteen, J. C.; Treichel, D. A. *J. Chem. Phys.* **99**, 2101 (1993).

Venkatachalam, R. S.; Boerio, F. J.; Roth, P. G. *J. Raman Spectrosc.* **19**, 281 (1988).

Virtanen, R. *Acta Polytech. Scand. Chem. Incl. Metall. Ser.* **123**, 1 (1974).

Vo-Dinh, T. *Environ. Sci. Technol.* **19**, 997 (1985).

Vo-Dinh, T. Surface-Enhanced Raman Spectroscopy, In: *Chemical Analysis of Polycyclic Aromatic Hydrocarbons*, Vo-Dinh, T. (Ed.), Wiley, New York, 1989.

Vo-Dinh, T. In: *Photonic Probes of Surfaces*, Halevi, P. (Ed.), Elsevier, New York, 1995. a

Vo-Dinh, T. *Sensor Actuat. B-Chem.* **29**, 183 (1995). b

Vo-Dinh, T. *Trends Anal. Chem.* **17**, 557 (1998).

Vo-Dinh, T.; Alak, A.; Moody, R. L. *Spectrochim. Acta B* **415**, 605 (1988).

Vo-Dinh, T.; Alarie, J. P.; Johnson, R.; Sepaniak, M. J.; Santella, R. *Clin. Chem.* **37**, 532 (1991).

Vo-Dinh, T.; Hiromoto, M. Y. K.; Begun, G. M.; Moody, R. L. *Anal. Chem.* **56**, 1667 (1984).

Vo-Dinh, T.; Houck, K.; Stokes, D. L. *Anal. Chem.* **33**, 3379 (1994).

Vo-Dinh, T.; Meier, M.; Wokaun, A. *Anal. Chim. Acta* **181**, 139, (1986).

Vo-Dinh, T.; Miller, G. H.; Bello, J.; Johnson, R.; Moody, R. L.; Alak, A; Fletcher, W. H. *Talanta* **36**, 227 (1989).

Vo-Dinh, T.; Stokes, D. L. *Appl. Spectrosc.* **47**, 1728 (1993).

Vo-Dinh, T.; Stokes, D. L. *Rev. Sci. Instrum.* **65**, 3766 (1994).

Vo-Dinh, T.; Wild, U. P. *Appl. Opt.* **12**, 1286 (1973).

Vo-Dinh, T.; Wild, U. P. *Appl. Opt.* **13**, 2899 (1974).

Wachs, T.; Sheppard, R. L.; Henion, J. *J. Chromatogr., B: Biomed. Appl.* **685**, 335 (1996).

Walbroehl, Y.; Jorgenson, J. W. *J. Chromatogr.* **315**, 135 (1984).

Waldron, K. C.; Li, J. *J. Chromatogr. B: Biomed. Appl.* **683**, 47 (1996).

Wallace, L. A.; Ott, W. R. *J. Air Pollut. Control Assoc.* **32**, 601 (1982).

Wallingford, R. A.; Ewing, A. G. *Anal. Chem.* **59**, 1762 (1987).

Wallingford, R. A.; Ewing, A. G. *Anal. Chem.* **60**, 258 (1988).

Wang, P.; Giese, R. W. *Anal. Biochem.* **230**, 329 (1995).

Wang, Y.; McCreery, R. L. *Anal. Chem.* **61**, 2647 (1989).

Wang, Y.; Wallin, J. M.; Ju, J.; Sensabaugh, G. F.; Mathies, R. A. *Electrophoresis* **17**, 1485 (1996).

Weitz, D. A.; Moskovits, M; Creighton, J. A. In: *Chemical Structure at Interfaces*, Hall, R. B.; Ellis, A. B. (Eds.), VCH, Berlin, p.197, 1986.

Whitten, W. B.; Ramsey, J. M.; Arnold, S.; Bronk, B. V. *Anal. Chem.* **63**, 1027 (1991).

Wilkerson, C. W.; Goodwin, P. M.; Ambrose, W. P.; Martin, J. C.; Keller, R. A. *Appl. Phys. Lett.* **62**, 2030 (1993).

Wilson, E. B. , Jr.; Decius, J. C.; Cross, P. C. *Molecular Vibrations: The Theory of Infrared and Raman Vibrational Spectra*, McGraw-Hill, New York, 1955.

Wokaun, A.; Gordon, J. P.; Liao, P. F. *Phys. Rev. Lett.* **48**, 957 (1982).

Wokaun, A. In: *Solid State Physics, Vol. 38*, Ehrenreich, H.; Seitz, F.; Turnbull, D. (Eds.), Academic Press, New York, p.223, 1984.

Wood, R. W. *Nature* **122**, 349 (1928).

Wood, T. H.; Klein, M. V. *Solid State Commun.* **35**, 263 (1980).

Wooley, A. T.; Sensabaugh, G. F.; Mathies, R. A. *Anal. Chem.* **69**, 2181 (1997).Shamsi, S. A.; Danielson, N. D. *J. Chromatogr. A* **739**, 405 (1996).

Wu, Z.; Tong, W. G. *J. Chromatogr. A* **757**, 215 (1997).

Xie, X. S.; Dunn, R. C. *Science* **265**, 361 (1994).

Xu, J.; Ma, Y. *J. Microcolumn Sep.* **8**, 137 (1996).

Xu, X.- H.; Yeung, E. S. *Science* **275**, 1106 (1997).

Yamada, H. *Appl. Spectrosc. Rev.* **17**, 227 (1981).

Yang, B.; Morris, M. D.; Owen, H. *Appl. Spectrosc.* **45**, 1533 (1991).

Yu, M.; Dovichi, N. J. *Anal. Chem.* **61**, 37 (1989).

Zeisel, D.; Deckert, V.; Zenobi, R.; Vo-Dinh, T. *Chem. Phys. Lett.* **283**, 381 (1998).

Zeman, E. J.; Schatz, G. C. *J. Phys. Chem.* **91**, 634 (1987).

Zhang, C. -X.; Thormann, W. *Anal. Chem.* **68**, 2523 (1996).

Zhang, L.; Yeung, E. S. *J. Chromatogr. A* **734**, 331 (1996). a

Zhang, N. Y.; Yeung, E. S. *Anal. Chem.* **68**, 2927 (1996). b

Zhao, J.; McCreery, R. L. *Appl. Spectrosc.* **50**, 1209 (1996).

Zhu, R.; Kok, W. T. *Anal. Chem.* **69**, 4010 (1997).

Zimba, C. G.; Rabolt, J. F. *Appl. Spectrosc.* **45**, 162 (1991).

VITA

David L. Stokes was born in Syracuse, New York on November 9, 1965. He spent his formative years in Georgetown Delaware, where he graduated from Sussex Central High School in June, 1983. He entered The University of the South (Sewanee, Tennessee) in August, 1983, where he was awarded a Bachelor of Science Degree in Physics (broad science). He entered a productive interim period as a research associate with Dr. Tuan Vo-Dinh at Oak Ridge National Laboratory (ORNL), where his efforts were focused towards the development of practical technologies implementing surface-enhanced Raman scattering (SERS). He entered graduate school at the University of Tennessee, Knoxville, in August of 1993. While there, he majored in analytical chemistry as a part-time student under Professor Michael J. Sepaniak. His graduate work, performed at both UTK and ORNL (under Dr. Tuan Vo-Dinh) involved the development of remote chemical sensors based on SERS and separations-based fiberoptic sensing (SBFOS). He officially received his doctoral degree in analytical chemistry in December, 1999.

He is currently working under Dr. Tuan Vo-Dinh as a post-doctoral fellow at ORNL, where he continues to be involved in the development of chemical sensors for bioanalytical applications.